
**Universidad Pontificia Comillas de Madrid**
**Escuela Técnica Superior de Ingeniería (ICAI)**

**Instituto de Investigación Tecnológica (IIT)**

# Control of VSC-HVDC multi-terminal systems to improve angle stability in hybrid HVAC/HVDC electrical transmission systems

Thesis submitted for the Degree of Doctor of Philosophy (Modelling of Engineering Systems)

**Author:** Francisco Javier Renedo Anglada

**Supervisors:** Prof. Dr. Aurelio García Cerrada
Prof. Dr. Luis Rouco Rodríguez

March 5, 2018

Madrid, Spain

# CONSTANCIA REGISTRAL DEL TRIBUNAL DEL ACTO DE LA DEFENSA DE TESIS DOCTORAL

**TÍTULO:** Control of VSC-HVDC multi-terminal systems to improve angle stability in hybrid HVAC/HVDC electrical transmission systems

**AUTOR:** Francisco Javier Renedo Anglada

**DIRECTOR:** Prof. Aurelio García Cerrada
Prof. Luis Rouco Rodríguez

**TUTOR-PONENTE:**

**DEPARTAMENTO:** Instituto de Investigación Tecnológica (IIT)

**FACULTAD O ESCUELA:** Escuela Técnica Superior de Ingeniería (ICAI)

**Miembros del Tribunal Calificador:**

**PRESIDENTE:** Prof. Julio García Mayordomo **Firma:**

**VOCAL:** Prof. Oriol Gomis Bellmunt **Firma:**

**VOCAL:** Prof. Enrique Acha **Firma:**

**VOCAL:** Dr. Ignacio Egido Cortés **Firma:**

**SECRETARIO:** Dr. Francisco Miguel Echavarren Cerezo **Firma:**

**Fecha de lectura:**

**Calificación:**

# Summary

The aim of this doctoral thesis was to investigate control strategies in Voltage Source Converter - High Voltage Direct Current (VSC-HVDC) multi-terminal systems (VSC-MTDC, for short) to improve angle stability in hybrid HVAC/HVDC grids (under large and small disturbances).

The work was motivated by the growing interest of transmission system operators (TSOs) in various parts of the world on this technology. Electrical systems tend to be operated in increasingly stressed conditions (AC lines closer to their stability limits, transmission of large amount of power over long distances and less inertia, among others), which make angle stability a key limiting factor. Meanwhile, future electrical systems are expected to have an ever-increasing number of electronic power converters, such as renewable generators interfaced by power converters, FACTS devices and point-to-point and multi-terminal HVDC systems. Furthermore, hybrid HVAC/VSC-HVDC transmission systems are being considered to facilitate the integration of a large amount of renewable generation and to interconnect different countries in different parts of the world. The main application of any VSC-HVDC system will be power transmission. Nevertheless, due to the fast control of the active and reactive power injections of the VSCs stations, VSC-HVDC multi-terminal systems, when installed, seem to be an attractive alternative to help improving angle stability.

Previous work has shown that, indeed, VSC-MTDC systems can improve angle stability of electrical power systems significantly using suitable control strategies. All those strategies had in common the use of global-but-difficult-to-implement measurements, namely, the speed of all the generators of the system and the speed of the centre of inertia (COI). This thesis investigates control strategies based on "global-but-practical" measurements for (a) transient stability improvement and for (b) power-oscillation damping.

First of all, control strategies for P and the Q injections of the VSCs using the weighted-average frequency (WAF) of the converter stations of the

VSC-MTDC system have been proposed to improve transient stability. The results presented in this thesis have shown that large and small-signal angle stability can be improved significantly using the proposed control strategies and their implementation is easier than previous approaches that require a Wide Are Measurement System (WAMS) with the masurements of the speeds of all the generators of the system in real time.

Due to the promising results obtained for transient stability, supplementary controllers for power-oscillation damping (POD), using the same signals, were also investigated, showing that the WAF could also be useful for this purpose. A coordinated-design algorithm based on eigenvalue sensitivities was used to design the POD controllers of the VSC-MTDC system.

The following conclusions have been obtained from the results of this thesis:

- The proposed strategy P-WAF (for P injections of the VSCs) improves transient stability significantly. It uses the weighted-average frequency of the AC terminals of the VSC-MTDC system.

- The proposed strategy Q-WAF (for Q injections of the VSCs) also improves transient stability significantly. It uses the weighted-average frequency of the AC terminals of the VSC-MTDC system.

- The proposed local strategy Q-LWAF (for Q injections of the VSCs) improves transient stability significantly. It behaves very much like strategy Q-WAF, but it requires local measurements, only.

- The proposed POD controllers (for P and/or Q injections of the VSCs) damp inter-area oscillations successfully. The coordinated-design algorithm allows the POD controllers to damp a required set of modes, obtaining the required damping ratios.

# Agradecimientos

Esta tesis doctoral ha sido posible gracias a la colaboración de muchas personas que merecen su agradecimiento.

En primer lugar, a mis supervisores, Aurelio García Cerrada y Luis Rouco, por su confianza, apoyo, la dirección de la tesis y sus enseñanzas en sistemas eléctricos, sistemas HVDC y estabilidad de sistemas eléctricos.

Muchas gracias a Aurelio García Cerrada por haberme dado la oportunidad de trabajar en el Instituto de Investigación Tecnológica (IIT), por haberme transmitido sus conocimientos en sistemas HVDC y modelado de este tipo de sistemas. Por haberme guiado, por haberme enseñado rigurosidad y a perseguir los problemas; y por su confianza en mi.

Muchas gracias a Luis Rouco por los conocimientos que me transmitió en sistemas eléctricos y en estabilidad, por su supervisión, por ayudarme a mejorar constantemente, por enseñarme a distinguir los temas importantes; y por su confianza en mi.

A Lukas Sigrist e Ignacio Egido, por su ayuda y colaboración en el desarrollo del modelo de PSS/E, por compartir sus conocimientos de sistemas eléctricos conmigo y por haberme ayudado cuando lo he necesitado.

A Luis Díez Maroto, por su ayuda en sistemas eléctricos y por compartir las ideas de su tesis relacionadas con el uso de medidas globales de la velocidad del centro de inercia, que motivaron el uso de la frequencia media en las estaciones convertidoras de un sistema VSC-MTDC para los controles de estabilidad transitoria propuestos en esta tesis.

A Javier Roldán y Miguel Ochoa, por sus enseñanzas en sistemas de control y electrónica de potencia, y por su ayuda en general.

A Paco Echavarren, por ayudarme en temas de sistemas eléctricos siempre que acudí a su puerta.

A Silvia Sanz Verdugo, de Red Eléctrica de España (REE), por su colaboración en el desarrollo del modelo de PSS/E y en el proyecto ESP-LIDER.

A Behzad Kazemtabrizi, por haberme acogido en el departamento de

ingeniería de la Universidad de Durham (Reino Unido) durante mi estancia de investigación y por la fructífera colaboración en la investigación desarrollada allí.

A Elena Saiz, Inmaculada Saboya, Laura Casado, Quanyu Zhao, María Antolín, Kai Doenges, Jose María Bobadilla y Javier García González, por su ayuda/colaboración cuando lo he necesitado.

A Ahmad Bin-Ibrahim, Carlos Ferrandón y Omar Kobt, por haber tenido discusiones interesantes y útiles de ingeniería con ellos.

A Isabel Tamudo, Marisa Sánchez, Cristina Ruiz y Julián Martín, ya que su trabajo siempre ha facilitado el mío.

A Tomás Gómez San Román, Enrique Lobato y Fidel Fernández Bernal, por su confianza en mi.

A Juan Luis Zamora y Ramón Rodríguez Pecharromán, por los conocimientos de control que me enseñaron hace años.

A Javier Muñoz García, Mario Castro, Rodolfo Cuerno, Esteban Moro, José Cuesta y Froilán Martínez Dopico por sus enseñanzas en matemáticas aplicadas. En particular, a Javier por la supervisión de mi tesis de master. A Cristina Sánchez Rebollo por el apoyo mútuo en nuestra etapa del master en Ingeniería Matemática en la Universidad Carlos III de Madrid.

A los miembros del tribunal de esta tesis, por haber aceptado evaluarla: los profesores Julio García Mayordomo, Oriol Gomis Bellmunt, Enrique Acha, Ignacio Egido y Francisco Echavarren. También, a los profesores Behzad Kazemtabrizi, Luis Fernández Beites, Joaquín Pedra Durán y Lukas Sigrist por el tiempo dedicado en la revisión de esta tesis

A Carlos Jaureguízar (de NOESIS AF), Orlando Izquierdo, David Trebolle y Jesús Beloso (de Gas Natural Fenosa) y Luis Murciano (de Boslan Ingeniería y Consultoría), por haberme hecho madurar profesionalmente en mis dos primeros trabajos.

A mis compañeros del IIT durante estos años, que trabajan en distintos grupos, pero que han sido importantes: María, Mercedes, Aurora, Eva, Andrea, Antonio, Fer, João, Diego, Rodrigo, Alessandro, Renato, Álvaro, Adrián, Peyman, Luis, Alejandro y muchos más.

Al Instituto de Investigación Tecnológica (IIT) de la Escuela Técnica Superior de Ingeniería (ICAI) de la Universidad Pontificia Comillas de Madrid.

A mis padres, Maite y Javier, por todo el cariño y apoyo en toda mi vida, y por haberme incentivado a estudiar. Sin su soporte no hubiese llegado hasta aquí. A mi hermano Jaime, por haber compartido diversas aficiones: desde la ingeniería hasta el tenis. También, muchas gracias a Iole.

A mis abuelos/as, Carmen, Ana, Sebastián y Jaime.

A Joselina Fernandes y a Vini, por su cariño y hospitalidad.

A Irene y a Marcos.

A mis amigos/as ajenos a este trabajo académico (de Chile y de España), que siempre han sido un pilar importante en mi vida, siempre he podido contar con ellos en los momentos buenos y malos y se que siempre van a estar allí. No escribo nombres, ya que ellos saben quienes son.

A mi compañera de vida, Camila, por estar siempre al lado en los momentos buenos y malos; por hacerme que tenga ilusión cada día; y por darme fuerzas para seguir adelante.

Finalmente, me gustaría agradecer al Ministerio de Economía y Competitividad del Gobierno de España y a la Comunidad de Madrid por la financiación de los proyectos de investigación que han financiado esta tesis doctoral:

- Electrónica de potencia en el sistema eléctrico para la integración de energías renovables (ESP-LIDER) (ref. IPT-2011-0844-920000), financiado por el Ministerio de Ciencia e Innovación y el Ministerio de Economía y Competitividad, Gobierno de España.

- Herramientas de simulación y análisis para el estudio de la operación y la optimización de sistemas híbridos HVDC-VSC multiterminal/HVAC (ref. ENE2014-57760-C2-1-R), financiado por el Ministerio de Economía y Competitividad, Gobierno de España.

- Programa de redes eléctricas inteligentes en la Comunidad de Madrid (PRICAM) (ref.S2013/ICE-2933), financiado por la Comunidad de Madrid, España.

# Contents

# List of Tables

# List of Figures

# Acronyms

**FACTS:** Flexible alternating current transmission system.

**HVAC:** High voltage alternating current.

**HVDC:** High voltage direct current.

**LCC:** Line conmutated converter.

**MTDC:** Multi-terminal HVDC system.

**P-LF:** Active-power control strategy based on local measurements of the frequency at the converter station.

**POD:** Power-oscillation damping.

**P-WAF:** Active-power control strategy based on the weighted-average frequency.

**Q-LF:** Reactive-power control strategy based on local measurements of the frequency at the converter station.

**Q-LWAF:** Reactive-power control strategy based on the estimation of the weighted-average frequency using local measurements.

**Q-WAF:** Reactive-power control strategy based on the weighted-average frequency.

**SSA:** Small-signal analysis

**TSO:** Transmission system operator.

**VSC:** Voltage source converter.

**WAF:** Weighted-average of the frequencies measured at the AC terminals of a VSC-MTDC system.

**WAMS:** Wide-area measurement system.

# Chapter 1

# Introduction

## 1.1 HVAC and HVDC transmission

Electrical energy systems all over the world are been urged to incorporate an ever-increasing amount of energy from renewable sources. Sometimes, these sources are distributed and located close to the consumption points but they may also be in remote sites far from consumer centres. For example, one of the targets of the European Union by 2050 is to reduce the greenhouse gas emissions by 80-95 % (compared to 1990 levels) [1] and this is expected to require the generation of, at least, 20 % to 27 % of its electricity from renewable sources by 2020 and 2030, respectively [2, 3]. Europe has plans to include a large amount of offshore wind power from the North Sea [4], which will require energy transmission through submarine cables over relatively long distances. Furthermore, Europe also plans an increase in solar photovoltaic generation and an increase of the contribution in solar energy from neighbouring contries.

The increase in transmission capability with conventional High Voltage Alternating Current (HVAC) long lines is often limited by technical aspects which can be tackled with High Voltage Direct Current (HVDC) transmission [5, 6]. Several point-to-point HVDC links are already in operation all around the world (see Table 5 of [7]). The most relevant applications of HVDC transmission are:

- Transmission of large amounts of power over long distances.
- Transmission through isolated cables (underground/submarine) over middle-to-long distances.

- Interconnection of asynchronous power systems.

For example, the transmission of bulk power over long HVAC lines is limited due to stability limits and losses, while the transmission over isolated HVAC cables is limited due to the shunt capacitance of the cables.

Initially HVDC installations are still more expensive than their HVAC counterparts due to the cost and losses of the electronic power converters required, unless the line exceeds a certain distance (known as the break-even distance). Beyond this distance the need for reactive-power compensation and the losses of the line in AC offset the cost associated with the converter stations. The break-even distance is drastically reduced if submarine or underground cables have to be used, due to the important reactive power associated with the cable. Although the break-even distance depends on many different variables (including social and political issues), it can be as short as 50 km when cables are used.

Technical difficulties, environmental concerns, renewable resource integration, the need for grid upgrading, etc... have favoured proposals for building a European HVDC grid (known as "Supergrid" [8]) in order to (a) deal with the intermittence of renewable generation [4,8,9] and (b) facilitate the massive integration of offshore wind energy through submarine cables [10–12]. An HVDC supergrid must be based on a multi-terminal solution: a set of more than two power converters with their DC terminals connected to a common HVDC grid, as shown in Fig. 1.1. A meshed multi-terminal HVDC grid is preferred rather than a set of single point-to-point HVDC links to increase the reliability of the system while reducing the number of converters, which are the most expensive and lossy components of an HVDC system.

HVDC supergrids in Europe would ease, for example, the integration of a large amount of offshore wind energy, mainly form the North Sea, and the integration of solar energy from neighbouring countries across the Mediterranean. Furthermore, grid-expansion plans in Europe also include the interconnection to the currently asynchronous Baltic Energy Market [13], which is something that would also require the use of HVDC. Figure 1.2 [1] shows some possible topologies for an HVDC pan-European Supergrid, proposed by Airctricity [8], Desertec [15] and "Friends of the supergrid" [14].

[1] Figs. 1.2-(a), 1.2-(b) and 1.2-(c) were obtained from [14], [8] and [15], respectively

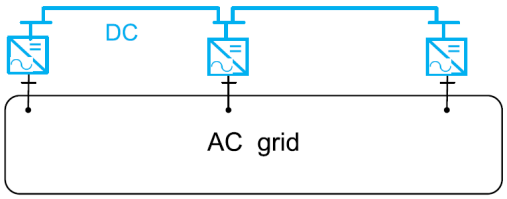


Figure 1.1: Multi-terminal HVDC system.


(a) (b) (c)

Figure 1.2: Supergrids proposed by (a) Friends of the Supergrid (DC lines in dark green), (b) Airtricty (DC lines in orange) and (c) Desertec (DC lines in red).

HVDC tenchnology can be based on:

1. Current Source Converters (CSC), also known as Line Conmutated Converters (LCC)

2. Voltage Source Converters (VSC) [2]

In LCC-HVDC tenchnology, the converters use thyristors, whilst VSC converters need switches with turn-off capability such as Insulated Gate Bipolar Transistors (IGBTs). Point-to-point LCC-HVDC and VSC-HVDC links are shown in Fig. 1.3.

The best option for a multi-terminal HVDC system (MTDC, for short) is VSC-HVDC technology [5], which presents some advantages for this purpose in comparison with classic LCC-HVDC technology, mainly: the voltage level of the DC grid is constant, each converter controls reactive power independently and in both directions at the AC side, the converters introduce lower levels of current harmonics than those with LCC technology, the connection to weak grids is possible, the supply to passive grids is also possible and it has black start capability. On the other hand, LCC-HVDC technology is much more mature than VSC technology, and LCC converters have less losses and higher DC-voltage and power ratings than VSC converters. A comparison between LCC-HVDC and VSC-HVDC technologies is provided in Table 1.1 [5,12,16–23]. A complete description of VSC-MTDC technology and its applications can be found in references such as [6,24,25].

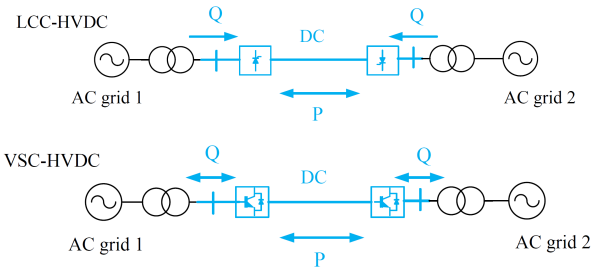


Figure 1.3: Point-to-point LCC-HVDC and VSC-HVDC links.

[2] In [16], the term voltage-sourced converters (VSC) is used instead, to emphasise that the DC link voltage must remain constant. However, the term used here is more widespread.

Table 1.1: LCC-HVDC and VSC-HVDC technologies. *: only possible with series capacitor. **: only possible with full-bridge MMC.

| | **LCC-HVDC** | **VSC-HVDC** |
|---|---|---|
| **Maturity** | many examples (1954-) | few examples (1997-) |
| **max. $P_N$ to date** | 7200 MW | 1000 MW |
| **max. DC voltage to date** | ±800 kV | ±320 kV |
| **max. distance to date** | 2375 km | 970 km |
| **$P$ direction** | DC-voltage polarity | DC-current direction |
| **Power control** | fast | very fast |
| **Cables** | expensive: mass-impregnated oil-filled to allow changes on the DC-voltage polarity | cheap: XLPE |
| **Converter losses** | 0.7-0.8 % | 0.9-1.7 % |
| **Reactive power** | the converters consume Q | bi-directional Q control at each converter |
| **Connection to weak grids** | limited* | full |
| **Connection to passive grids** | no | yes |
| **Connection to asynchronous AC grids** | yes | yes |
| **Black start** | no | yes |
| **Current harmonics** | high content | low content |
| **Converter current limit during DC faults** | yes | difficult** |
| **Cost (today)** | low | high |
| **HVDC multi-terminal** | difficult | easy |

The latest VSC technology developed is the Modular Multilevel Converter (MMC) [26, 27] and the main manufacturers already have commercial products for VSC-HVDC using this technology: Siemens [18], ABB [20] and Alstom Grid (now General Electric (GE)) [21]. A state of the art of VSC-HVDC technology can be found in [19] and in [22]. However, for the time being, there still are many obstacles for a VSC-HVDC supergrid. Among others [5, 7],

- The technology for HVDC breakers is far from being mature.
- DC grids need new protection strategies.
- Technical standards must be developed for DC grids.
- The interaction between new DC grids and existing AC ones (impact on power flows, controllability, stability, etc.) must be investigated thoroughly.
- Power flow and voltage control in the DC grid must be addressed.
- Who would actually operate this supergrid in the present "multi-zonal" environment with liberalised markets must be studied.
- The magnitude of the investment and the rate of return are still open questions.

Nevertheless, although a large-scale supergrid cannot be expected in the next few years, VSC-HVDC links or multi-terminal systems are already being built or have been built and are having some impact on traditional AC power systems.

## 1.2 Main objective of this thesis

The scenario described above leads to a picture of a stressed electrical system, with transmission of large amounts of power over long distances, with conventional generation but also with a large amount of renewable energy interfaced through electronic generators. Solutions to tackle the coming challenges include Flexible AC Transmission Systems (FACTS) [28, 29], HVDC systems and energy storage systems. Among them, HVDC stands out as a technology with a high potential for application in transmission systems [30]. In fact, two-terminal links (mainly of LCC type) have already proved to be very useful for the flexible operation of power systems. More recently, however, the

application of multi-terminal VSC-HVDC systems have raised a number of concerns and many of them still need a great deal of research.

It is clear that the main purpose of a VSC-HVDC grid must be related to energy harvesting and transmission over long distances (often using cables) but many other features of this type of systems can be used simultaneously to contribute to a more flexible power system. Among many other possibilities, this thesis will focus on:

- the potential of multi-terminal VSC-HVDC systems to improve angle stability of hybrid HVAC/HVDC grids while maintaining flexible power flow control.

A previous step before any type of analysis regarding hybrid HVAC/HVDC systems is to have appropriate simulation tools and models [23]. Hence, another target of this work has been to provide:

- a comprenhensive analysis and further development of software tools for power-flow calculation and dynamic simulation for hybrid HVAC/VSC-HVDC systems.

The state of the art of angle stability of hybrid HVAC/HVDC systems will be further reviewed in Section 1.3 and the identified research niche will be taken further towards the proposed PhD work. The available simulation tools for power-flow calculation and dynamic simulation of hybrid HVAC/HVDC systems will be analysed and summarised in Section 1.4.

## 1.3 Angle stability

According to the IEEE/CIGRE Joint Task Force on Stability Terms and Definitions, **angle stability** is defined as [31] *the ability of synchronous machines of an interconnected power system to remain in synchronism after being subjected to a disturbance.*

Angle stability can be classified into two types [31]:

- **Large-disturbance (or transient) stability**: *the ability of the power system to maintain synchronism when subjected to a severe disturbance, such as a short circuit on a transmission line. The resulting system response involves large excursions of generator rotor angles and is influenced by the nonlinear power-angle relationship.*

- **Small-disturbance (or small-signal) stability**: *the ability of the power system to maintain synchronism under small disturbances. The disturbances are considered to be sufficiently small so that the system of equations can be linearised for analysis purposes.*

It is well known that angle stability can be improved with generators, FACTS and HVDC systems, by means of suitable control actions affecting the electromagnetic load torque of the synchronous machines of the system. Along this line, the main features of VSC-HVDC multi-terminal technology which make it a promising option for angle stability improvement against both, large and small disturbances, are:

- Fast control of the active-power (P) injections of the VSC stations.
- Fast control of the reactive-power (Q) injections of the VSC stations.

In this thesis, control strategies for P and Q injections of the converters in VSC-MTDC systems to improve angle stability will be analysed. The grid codes for hybrid HVAC/HVDC systems already require supplementary controllers in the VSCs stations for ancillary services (frequency support, synthetic inertia and power-oscillation damping) or Fault Ride Through Capability (FRT) [32]. Therefore, the implementation of supplementary control strategies for angle stability improvement would require a very small additional investment.

### 1.3.1 Transient stability

Transient stability is a key limiting factor when HVAC transmission of bulk power over long distances takes place [33–35]. The time constants for transient stability simulation are in the range of 0.1-10 s [36]. Transient stability studies try to avoid events like the recent one in Turkey (31-03-2015) [37]. Initially, four long 400-kV lines were already out of service and the Turkish grid was heavily loaded. Then, another 400-kV line was disconnected because of over-loading and this produced the loss of synchronism between the Western and the Eastern areas of the Turkish Electric System, resulting in the blackout of the whole system 12 s later.

In this thesis, control strategies (supplementary controllers) for the active- and reactive-power injections in VSC-MTDC systems for transient stability improvement will be considered. A general scheme for supplementary control strategies for P and Q injections of the VSC stations is depicted in Fig. 1.4, where, for example, the TSO's P and Q set points are $p_s^0$ and $q_s^0$ and the

supplementary set-point values for the P and Q injections are represented by $\Delta p_s^{ref}$ and $\Delta q_s^{ref}$, respectively.[3] Using supplementary controllers, P and Q injections are modulated during the transient, only, therefore the pre-fault operating point of the VSC stations remains unchanged.

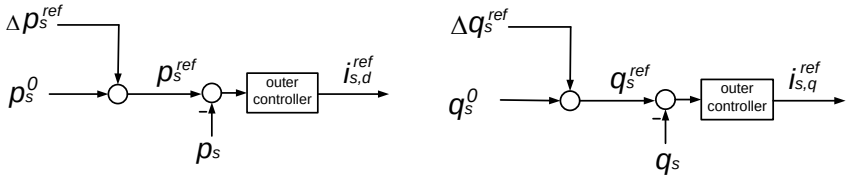


(a) (b)

Figure 1.4: (a) P control and (b) Q control.

Control strategies in VSC-MTDC can use (a) local measurements, i.e., each converter can modulate its P and/or Q injections using measurements available at the converter station, or (b) global measurements, i.e., each converter can modulate its P and/or Q injections using measurements from other parts of the system, in addition to those available at the point of coupling.

A brief review of the previous research on P- and Q-control strategies in VSC-MTDC systems for transient stability improvement is presented now, although a much thorough review will be presented in Chapters 3 and 4, respectively.

Many examples in the literature show that transient stability can be improved by controlling P through LCC-HVDC links [38–44] and VSC-HVDC links [43,45–48]. In a point-to-point HVDC link, the active-power controlled by one converter station is supplied/evacuated by the other station. However, P control in a VSC-MTDC system is a more complicated problem than before and coordination among the converter stations is required. More recently, references [49–51] have shown that supplementary controllers for the active power at each terminal of a VSC-MTDC system using global measurements can improve power system transient stability. However, they have the disadvantage that a Wide Area Measurements System (WAMS) is required to obtain the speed of all the generators in real time. The question that arises is whether transient stability could be improved by using less demand-

[3]For the explanation of the rest of variables in Fig. 1.4, see Chapters 3 and 4

ing measurements, such as local measurements or global measurements only at the converter stations.

Regarding, Q control, several references show that transient stability can also be improved by appropiate control strategies for Flexible AC Transmission Systems (FACTS), such as Static Var Compensators (SVCs) or static synchronous compensators (STATCOMs) [52,53]. In all these cases the controllers act upon the reactive power injected into the grid. Since each VSC converter of a VSC-MTDC system is able to control the reactive-power injection independently and in both directions, the potential of suitable reactive-power control strategies to improve transient stability seems to be enormous. To the best of the PhD candidate's knowledge, the coordination of the reactive power of the converters in a VSC-MTDC system for this purpose has only recieved attention before in [49]. Nevertheless, the approach in that reference requires the use of a WAMS with the speeds of all the generators available. In addition, some relevant aspects to be able to understand the role of the reactive-power modulation were omitted (for example, the reactive-power injections obtained by simulation are not shown). The work reported here has investigated this issue in more detail and alternatives using local and global measurements obtained from the VSC stations of the system have been proposed and analysed.

Summarising, the following control strategies in VSC-MTDC systems for transient stability improvement will be proposed in this PhD thesis:

1. P injections:
    - P-WAF (global): In this strategy, each VSC modulates its P injection proportionally to its frequency error, using the weighted-average frequency of the VSC-MTDC system as frequency set point.
    - P-LF (local): This strategy tries to mimic strategy P-WAF, but using local measurements obtained at the AC side of each converter.
2. Q injections:
    - Q-WAF (global): Similarly to P-WAF, VSCs modulate their Q injections proportionally to their frequency error, also using the weighted-average frequency of the VSC-MTDC system as frequency set point. Although, with the opposite sign used in strategy P-WAF.

- Q-LWAF (local): This control law tries to mimic strategy Q-WAF, but using local measurements. The weighted-average frequency is estimated using local measurements together with an auxiliary active-power control strategy (P-LF).

The proposed control strategies will be described in Chapters 3-5. Results will show that strategies P-WAF, Q-WAF and Q-LWAF produce significant improvements on transient stability and the mesurement system (all the frequencies read by the VSC-MTDC system or the local frequency of each VSC) is much easier to implement than the ones used in previous studies (the speeds of all the the generators of the system). Strategy P-LF will show some important limitations for transient stability improvement, but will prove to be useful to obtain global information of the VSC-MTDC by using local measurements in strategy Q-LWAF.

**Transient-stability assessment**

Transient stability will be analised theoretically and by non-linear time-domain simulation. Lyapunov theory will be used to analyse the stability of the power system when using the proposed control strategies, following the guidelines given in [54]. Simplified models of the power system were used, including the non-linear dynamics of the generators, but using classical models and neglecting their controllers and the operation limits of the devices. Although Lyapunov analysis gives useful insight into the behaviour of the system, the non-linearities caused by the operation limits of the converters, for example, may play a relevant role in transient stability.

Therefore, it is essential to investigate the system's behaviour by simulation in realistic scenarios, including detailed electromechanical models of the generators and VSC converters.

Transient stability will be evaluated computing the critical clearing time (CCT), which is defined as the maximum time that a fault can stay before been cleared without loss of synchronism and it is often used as an indicator of transient stability margin [55]. In general, when a short circuit occurs in an HV transmission line, its primary protection opens the breaker within 30-100 ms after the fault (first zone distance relay) and the backup protection will open 250-400 ms after the fault detection, if the primary protection fails (second zone distance relay). The minimum CCTs admissible in a power system can vary depending on the country [56], but a common practice is to ensure that the CCTs are greater than 150 ms [57–59].

### 1.3.2 Small-signal stability

In small-signal stability, the dynamic equations of the system can be linearised and stability will be assessed looking at the eigenvalues of the system. In multi-machine systems, the eigenvalues of interest for angle stability are the electromechanical modes, which are associated to the angles and speeds of the synchronous machines. Electromechanical oscillations can be [33]: (a) inter-area modes, which involve groups of generators within the system oscillating against each other (in the frequency range 0.1-0.7 Hz) or (b) local modes, which involve oscillations between close-by generators (in the frequency range 0.7-2 Hz). A comprehensive analysis of inter-area modes in North America transmission system, using field measurements recorded in Phasor Measurement Units (PMUs) can be found in Chapter 10 of [60]. Furthermore, inter-area oscillations in Continental Europe electrical system were reported in [61].

One of the most cost-effective and widely used ways to damp electromechanical oscillations is to include Power System Stabilisers (PSSs) in some generators of the system [62, 63]. Nevertheless, supplementary controllers for power-oscillation damping can also be implemented in FACTS [64–67], wind farms [68, 69] or HVDC systems [70]. Since the control in electronic power converters is much faster than in synchronous generators, if electronic devices (e.g. FACTS) are properly placed, they can be an attractive option for power oscilllation damping.

Recent publications have proposed supplementary controllers for power-oscillation damping (POD) in VSC-MTDC systems [71–77], showing promising results. Those strategies will be discussed in detail in Chapter 7. As in the transient stability case, the use of wide-area signals may bring benefits to the performance of damping controllers [75]. This has motivated the research on new damping controllers using global measurements, but without requiring a WAMS, very much in the line of the control strategies proposed to improve transient stability.

Regarding small-signal angle stability:

1. This thesis investigates whether the control strategies proposed to improve transient stability can also damp electromechanical modes.

2. This thesis proposes control strategies to modulate P and Q injections of the VSC stations of a VSC-MTDC system tailored to damp power oscillations. The design based on the difference between the frequency at the AC side of each of the VSC stations ($\omega_j$) and the weighted-average

frequency ($\bar{\omega}$) is explained in detail. Fig. 1.5 depicts the strategy proposed for power-oscillation damping, where the input of the controllers of VSC $j$ will be given by $y_j = \bar{\omega} - \omega_j$. The proposed controllers will be explained in detail in Chapter 7.

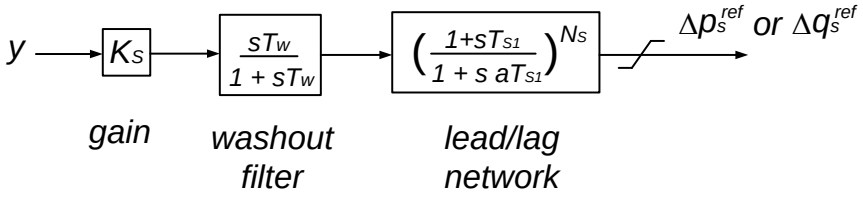


Figure 1.5: POD controller using P or Q injections of the VSCs.

**Small-signal stability assessment**

The system will be linearised and the damping of electromechanical modes will be evaluated using eigenvalue analysis and frequency-domain methods [78–80]. The procedure can be summarised as follows:

1. A steady-state operating point is calculated by solving a power flow.
2. The non-linear differential equations of the power system are linearised around the operating point and a state-space model is obtained.
3. The eigenvalues and eigenvectors of the system matrix are computed.
4. The participation factors of each system state variable on each eigenvalue are calculated, in order to identify the electromechanical modes.
5. The response of the system is confirmed by time-domain simulation.

## 1.4 Modelling and simulation tools for hybrid HVAC / VSC-HVDC systems

Dynamic simulation of power systems can be divided into (a) electromechanical simulation, which neglects some fast dynamics and is suitable for large power systems with a good deal of conventional generators, and (b) electromagnetic simulation, which uses more detailed models and is appropriate to test the control system of the devices and to analyse fast transients.

For angle stability analysis in conventional power systems with VSC-MTDC systems, electromechanical simulation of hybrid HVAC/HVDC systems will be used. Nevertheless, several simulation tools have been used here: power-flow algorithms to obtain the initial operating point and electromagnetic simulation to validate the electromechanical models. Different types of simulation and simulation tools available for hybrid HVAC/VSC-HVDC systems will be summarised in this section. The simulation tools used in this PhD project will be described in detail in Chapter 2.

For the purpose of this thesis, one can classify computer-aided tools as follows.

- Steady-state or power-flow calculations
  - To obtain viable operating points of the system.
- Dynamic simulation
  - Non-linear time-domain simulation
    - Electromagnetic transient simulation (EMT) is used to analyse fast transients in power systems. The time constants of interest are between $10^{-7} - 10^{-2}$ s. Typical applications of EMT simulation are [81, 82]: insulation coordination studies (over-voltages due to lightning and energisation), transient recovery voltage studies, harmonic studies and electronic power devices (and their interaction with the power system). Depending on the application, different types of EMT models should be used:
      - Average models: These models only take into account the first harmonic (50 or 60 Hz) and they are suitable for power system studies or to study the stability of the main control loops of electronic converters.

- Switching models: These models represent the switches of the power converters and they are used for more detailed studies (e.g. harmonics or to study the behaviour of semiconductor devices).
- Real-time simulators: These tools are intended for very fast simulation of electrical systems combined with hardware devices (this situation is often called Hardware-in-the-loop or HIL simulation). The differential equations must be solved in several computer cores working in parallel (parallel computing).

* Electromechanical simulation or root-mean-square simulation (RMS) is concerned with the electromechanical dynamics of the electrical machines and it covers time constants from 0.1-10 s [36]. In this type of simulation, dynamic models of the generators, excitation systems and prime governors are used while the dynamics of the AC lines are assumed to be instantaneous and they are represented by impedances.

– Small-signal analysis (SSA)

* Electromagnetic approach: where a linearised version of EMT average models are used to analyse the stability of systems in which fast dynamics are of interest. For example, the stability of a converter connected to the grid or the stability of the DC grid in a hybrid AC/DC system.
* Electromechanical approach: where RMS models are linearised and used to analyse the stability of large power systems, in which the dynamics of interest are the electromechanical oscillations.

A summary of the applicability of different simulation tools is reported in Tables 1.2-1.5.

PSS/E software has been used for power-flow calculation and electromechanical simulation of hybrid HVAC/VSC-HVDC systems in this work. Since PSS/E does not offer VSC-MTDC models within its libraries, the power-flow algorithm and the dynamic models for VSC-MTDC systems had to be developed and are reported in this thesis. The tool developed has been validated against an electromagnetic model in Simulink + SimPowerSystems and the results have also been compared to those obtained with PowerFactory. This study is described in Chapter 2. The resulting PSS/E tool has been used for

Table 1.2: Simulation tools for power-flow calculation in AC/DC grids.

| Tool (Power flow) | type | large systems | AC/DC grids |
|---|---|---|---|
| PSS/E | commercial | yes | user defined |
| PowerFactory | commercial | yes | yes |
| EUROSTAG | commercial | yes | yes |
| MatACDC | open source | yes | yes |
| PSAT | open source | yes | user defined |
| SimPowerSystems | commercial | no | user defined |

Table 1.3: Simulation tools for EMT simulation of AC/DC grids, including real-time simulators. Type: C=commercial, F=free.

| Tool (EMT) | type | large systems | average models | switching models | real time sim. | AC/DC systems |
|---|---|---|---|---|---|---|
| Simulink | C | no | yes | no | no | yes |
| PowerFactory | C | yes | yes | yes | no | yes |
| SimPowerSystems | C | no | yes | yes | no | yes |
| PSCAD | C | no | yes | yes | no | yes |
| EMTP-RV | C | yes | yes | yes | no | yes |
| RTDS | C | yes | yes | yes | yes | yes |
| eMEGAsim | C | yes | yes | yes | yes | yes |
| HYPERSIM | C | yes | yes | yes | yes | yes |

Table 1.4: Tools for non-linear time-domain electromechanical simulation of AC/DC grids. Type: C=Commercial, OS=Open source and free.

| Tool (RMS) | type | large systems | AC/DC systems |
|---|---|---|---|
| PSS/E | C | yes | used defined |
| PowerFactory | C | yes | yes |
| EUROSTAG | C | yes | yes |
| PSAT | OS | yes | user defined |
| MatDyn | OS | yes | yes |
| SimPowerSystems | C | no | user defined |

Table 1.5: Tools to small signal-stability analysis of AC/DC grids. Type: C=Commercial, OS=Open source and free.

| Tool (SSA) | type | approach | large systems | AC/DC systems |
|---|---|---|---|---|
| PSS/E | C | Electromechanical | yes | no |
| PowerFactory | C | Electromechanical | yes | yes |
| EUROSTAG | C | Electromechanical | yes | yes |
| SMAS3/SSST | C | Electromechanical | yes | user defined |
| PSAT | OS | Electromechanical | yes | user defined |
| Simulink | C | Electromagnetic | no | yes |
| PSCAD | C | Electromagnetic | no | yes |

non-linear time-domain electromechanical simulation of hybrid HVAC/VSC-HVDC systems when studying transient stability with the control strategies proposed in this work.

Models of VSC-MTDC systems have been included in SSST, which is a Matlab-based tool for small-signal analysis of large power systems, developed by the Institute for Research in Technology (IIT) of Comillas Pontifical University. Small-signal analysis of test cases of hybrid HVAC/VSC-HVDC system has been carried out with SSST and the results have been compared with those provided by PowerFactory. This study is described in Chapter 6. SSST has also been used for small-signal analysis of the control strategies proposed in this work (Chapter 7).

## 1.5 Outline of the thesis

In Chapter 1 (this one), the motivation of the thesis, a review of previous work in key areas and the identification of the niche for research are presented.

In Chapter 2, the models for power-flow calculation and electromechanical simulation of VSC-MTDC systems are described and the implementation in PSS/E is discussed. Chapter 2 also includes the validation of those models, which will be used for simulation in the rest of the thesis.

Active-power control strategies for transient stability improvement (P-LF and P-WAF) are proposed and analysed in Chapter 3. Reactive-power control stragies for transient stability (Q-WAF) are proposed and analysed in Chapter 4. A communication-free control strategy for transient stability improvement, for the reactive-power injections of the VSC stations (Q-LWAF), is proposed and described in Chapter 5. Control strategies proposed in chapters 3-5 are the main contributions of the thesis regarding transient stability.

In Chapter 6, a generalised model for small-signal angle stability analysis of hybrid HVAC/VSC-HVDC systems is proposed and validated. The proposed linearised model will be used to analyse power-oscillation damping. Chapter 6 provides the guidelines of the proposed model, but the details of the formulation are reported in Appendix D. The model proposed in Chapter 6 will be used for small-signal stability analysis of the control strategies proposed in this thesis.

In Chapter 7, control strategies for power-oscillation damping are analysed. First of all, the capability of the control strategies proposed in Chapters 3-5 to damp electromechanical oscillations is analysed. Finally, specific controllers for power-oscillation damping are designed using coordinated-design methods. The analysis and control strategies proposed in Chapter 7 are the main contributions of the thesis regarding small-signal angle stability.

Finally, the conclusions and contributions of this thesis and suggestions for further research are reported in Chapter 8.

Several appendices have also been included, to cover useful details that may be spared in a first reading, but will be needed to reproduce the results shown in the main body of this document.

# Chapter 2

# Modelling of VSC-MTDC systems in PSS/E

## 2.1 Introduction

This chapter describes the implementation of a simulation tool for power-flow calculation and dynamic simulation of VSC-HVDC multi-terminal systems (VSC-MTDC) in PSS/E (a widely used commercial simulation tool for large power systems [83]), which has been used to analyse rotor-angle stability.

Power-flow calculation is used to obtain the steady-state operating point of a power system: the bus voltages and the power flows through the lines and transformers are obtained, by using as input data the generation and demand [55]. Power-flow calculation is an essential tool for transmission system operators (TSOs) for planning and operation of the power system. In this thesis, the power-flow algorithm is only used to obtain the initial operating point for dynamic simulation. Results of the stability analysis will be reported in the following chapters.

The rest of this chapter is organised as follows. A review of the state of the art on modelling and simulation of VSC-MTDC systems is presented in Section 2.2. The sequential AC/DC power-flow algorithm implemented in PSS/E is described in Section 2.3. The dynamic model for VSC-MTDC systems implemented in PSS/E is described in Section 2.4. The power-flow algorithm and the dynamic model are validated in sections 2.5 and 2.6, respectively. Results for the Cigré Nordic32A system with an embedded VSC-MTDC, using the proposed PSS/E tool, are shown in Section 2.7. Finally, a summary of the chapter is presented in Section 2.8 .

## 2.2 Review of previous work

AC/DC power-flow algorithms can be classified into unified and sequential methods. The former solves the power-flow equations of the AC and DC grids together, whereas the latter has an external iteration in which the AC and DC power flows are calculated sequentially. In general, unified methods have better numerical stability but sequential methods can be incorporated to existing AC power-flow tools without modifying the equations of the AC power flow. Several steady-state models for AC/DC power-flow calculation with VSC-MTDC systems have been reported in the literature, using unified methods [84–88] and sequential methods [89–95]. The most general approaches are the unified algorithms proposed in [86–88] and the sequential ones proposed in [91,93,95], which are valid for hybrid AC/DC systems with an arbitrary topology and they include all the components of VSC stations (converters and filters), converter losses and converter limits. The unified algorithms of [86,87] have been coded with Matlab while the software used to implement the unified algorithm of [88] was not specified in the paper. In [91, 93], the sequential algorithms have been implemented in Matlab + Matpower [96]. The work in [91] culminated in the first open-source code for power-flow calculation of AC/DC grids: MatACDC [97].

Dynamic simulation of power systems can be divided into [36] (a) electromechanical simulation, which neglects some fast dynamics and is suitable for large-scale power systems, and (b) electromagnetic simulation, which uses more detailed models and it is appropriate to investigate fast transients and to test the control system of the devices used.

Regarding VSC-MTDC systems, a generalised model for electromechanical transient simulation has been proposed and implemented in MatDyn (see [98] and [99]) and was later improved in [100]. Similar models were used in [101], using PSAT [102], and in [50,75,103,104], using PowerFactory (DigSilent) [105]. A different modelling approach was proposed in [106] including, explicitly, the modulation index of the VSCs. The electromechanical models of [50,75,99–101,103,104,106–110] have in common that they represent the VSC stations of different technologies (e.g. 2-level VSC converters or Modular Multilevel Converters (MMC)) in the same way and only the relevant dynamics of the VSCs for electromechanical simulation are modelled. Nevertheless, the work in [111] explores the impact of MMC systems on the dynamic behaviour of the system using a fairly detailed model of the converter stations, concluding that the actual energy control loop implemented may show in the overall behaviour of the systems. The study in [111] also

concludes that, if the reference of the energy loop of the MMC is chosen proportionally to the DC voltage, simplified electromechanical models of the VSC stations (e.g. as in [99]) present a reasonable accuracy, regardless the technology of the VSCs.

Several electromagnetic models have been presented in [112–119]. Recently, a hybrid electromechanical and electromagnetic simulator for VSC-HVDC systems has been proposed in [120]: it includes fast dynamics into transient stability models, by using different time steps. A comprehensive guide for the development of VSC-HVDC models with different level of detail can be found in [121, 122].

PSS/E does not have available VSC-MTDC models within its libraries and only a VSC-HVDC point-to-point model is offered. In this work, a steady-state VSC-MTDC tool for power-flow calculation and an electromechanical VSC-MTDC tool suitable for non-linear time-domain simulation, have been developed for PSS/E. The tool follows the guidelines of type 6 model of [121, 122] for electromechanical simulation and it has been (a) validated against a detailed electromagnetic model in Matlab + Simulink + SimPowerSystems [123] which includes the switching of 3-level power converters and (b) against an electromechanical model in PowerFactory.

Two VSC-MTDC PSS/E user-defined models for electromechanical simulation have been published recently: [107] (improved in [108]) and [109]. Both models are based on similar ideas to those behind the model proposed in this thesis. All of them are valid for hybrid AC/DC grids with arbitrary topology, although they present some differences. The fast dynamics of the inner current controllers are modelled with great detail in [109], they are assumed instantaneous in [107, 108] and they are approximated by a first order system in this thesis. The results in [108, 109] illustrate, by simulation, that the dynamics of the inner controller are fast in comparison with the dynamics of rest of the system, justifying the use of a simple model. This approximation can lead to ignore the internal AC-voltage limit of the VSCs. However, this limit is taken into account here by re-computing the current set points if the limit is reached. In [107,108] and in the model proposed here, the DC grid is modelled with all its components (capacitors, resistances and inductances) whilst in [109], inductances are eliminated because they only contribute to fast time constants. Converter losses are neglected in [107, 108] and approximated in [109]. In this work, converter losses are calculated using a quadratic function of the AC current as in [124, 125]. The treatment of converter losses of [107, 108] and [109] simplifies the power flow algorithm, but is not as general as the approach given here.

The model proposed in [107], [108] was validated against an electromagnetic simulator in [120], and the results showed good agreement. The model proposed in [109] was validated against PSCAD (an electromagnetic simulator [126]) and similar results seemed to be obtained with the electromechanical and electromagnetic tools although the scale used to show the results is not sufficiently detailed. The validation carried out in this thesis will clearly show good agreement between the electromechanical model proposed and an electromagnetic model, within the frequency range of interest.

## 2.3 AC/DC power-flow algorithm

The initial operating point for dynamic simulation will be obtained from the AC/DC power-flow algorithm. The per-unit system used for the AC/DC power-flow calculation is described in Appendix B.

The ideas behind VSC modelling for power-flow analysis are depicted in in Fig. 2.1 [99, 100, 127]. Each converter is connected to the AC grid and to the DC grid. The AC side is modelled by a voltage source $\bar{e}_c = e_c\angle\delta_c$ coupled to the AC bus $s$ ($\bar{u}_s = u_s\angle\delta_s$) through a phase reactor, a capacitor and a transformer ($\bar{z}_c = r_c + j\omega L_c$, $\bar{z}_f = -j1/(\omega C_f)$ and $\bar{z}_{tf} = r_{tf} + j\omega L_{tf}$, respectively). The capacitor, $C_f$, is a low-pass filter to compensate the current harmonics of the VSC station at its value will depend on the technology of the converters. For example, MMC stations will require small low-pass filters or they could be even eliminated [128]. The DC side of the converter is seen by the DC grid as a current injection $i_{dc}$. AC and DC sides are related by the energy conservation principle and the losses at the VSC station, $p_{loss}$, are calculated using a quadratic function of the converter AC current (rms), $i_c$, as proposed in [124]:

$$p_c + p_{dc} + p_{loss} = 0, \qquad p_{loss} = a + b \cdot i_c + c \cdot i_c^2, \tag{2.1}$$

A current-controlled VSC station is able to control (a) the active power injected into the AC grid, $p_s$, or the DC voltage, $u_{dc}$, and (b) the reactive power injected into the AC grid, $q_s$, or the modulus of the AC voltage, $u_s$. A general VSC-MTDC system with $n$ converters and $n_L$ DC lines is considered. For the power-flow analysis, it is assumed that one converter controls the voltage of the DC grid (DC-slack bus) and all the others control the active power. The sequential algorithm proposed in [91] has been used in this work, since it can be easily implemented in only-AC tools, such as PSS/E, without modifying the AC power-flow algorithm. Hence, the use

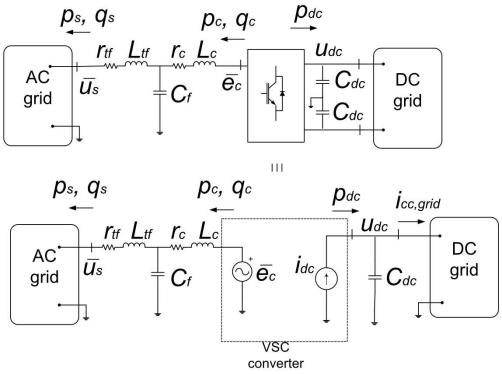


Figure 2.1: VSC-station modelling.

of VSC-MTDC systems can be easily explored using existing cases of large HVAC systems. The algorithm runs as follows:

1. The $k$-th external iteration starts. An initial guess of the active power injected into the AC grid by the DC-slack converter ($p^{(k)}_{s,n_s}$, where $n_s$ is the index of the DC-slack bus). If available, the results for iteration $k-1$ are used.

2. An AC power flow is calculated (calling PSS/E) by taking the variables of the current external iteration $k$ as the initial state (or an initial guess, if started from scratch). All the VSC stations are seen as PQ or PV buses from the AC grid (at the s-bus in Fig. 2.2), depending whether they are controlling the reactive power or the AC voltage. The specified active-power injections of the non-slack converters are constant during the external iteration, whilE the specified active power of the DC slack is allowed to vary during the external iteration ($p^{(k)}_{s,n_s}$). Therefore, this is a traditional AC power flow problem with a single AC-slack bus (a generator of the AC grid).

3. The AC/DC coupling for each converter is solved: $p^{(k)}_{c,i}$ (at c-bus in Fig. 2.2) is calculated from the s-bus data, taking into account the connection impedance. Also, the power injected by the VSC into the DC grid ($p^{(k)}_{dc,i}$) is calculated, by calculating the converter losses and by using Eq. (2.1).

4. The DC power flow is solved for the DC grid (see Fig. 2.2). A Newton-

Raphson algorithm has been used in this work. The DC-slack bus specifies the fixed DC voltage ($u^0_{dc,n_s}$) and the rest of DC buses specify the active-power injections ($p^{(k)}_{dc,i}$, which are known data for the DC power flow, but are updated at each iteration $k$, as described in the previous point). DC voltages are obtained together with the power of the DC slack ($p^{(k)}_{dc,n_s}$).

5. DC-slack iteration ($\ell$): A new value of $p^{(k+1)}_{s,n_s}$ is obtained, iteratively, from $p^{(k)}_{dc,n_s}$ taking into account the converter losses [91] (Fig. 2.2):

   (a) Initial value: $p^{(\ell=0)}_{c,n_s} = p^{(k)}_{c,n_s}$.

   (b) Solve the branch $s, n_s - c, n_s$ (Fig. 2.1, for the DC-slack bus $n_s$) with the data: $u_{s,n_s}$, $\delta_{s,n_s}$, $q_{s,n_s}$ and $p^{(\ell)}_{c,n_s}$ (Newton-Raphson method).

   (c) Obtain the new value of $p^{(\ell+1)}_{c,n_s}$ with $p_{dc,n_s}$ and $p_{loss,n_s}(i^{(\ell)}_{c,n_s})$ using (2.1).

   (d) If $|p^{(\ell+1)}_{c,n_s} - p^{(\ell)}_{c,n_s}| < \epsilon$, stop; if not, make $\ell = \ell + 1$ and return to step b). The output is $p^{(k+1)}_{s,n_s}$.

6. Convergence test: If $|p^{(k+1)}_{s,n_s} - p^{(k)}_{s,n_s}| < \epsilon$: stop and if not, make $k = k+1$ and return to step 1).

The main script was coded in Python and it calls PSS/E at each external iteration $k$ to solve the AC power flow. The DC power flow and the DC-slack iteration scripts were also coded in Python. The solution of the AC/DC power flow can later be used by PSS/E as the initial operating point for dynamic simulation.

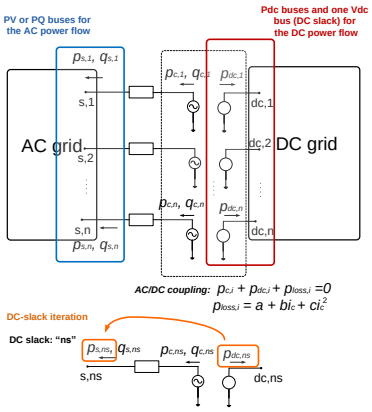


Figure 2.2: AC/DC power flow.

## 2.4 Dynamic model

The dynamic model for VSC-MTDC systems to be used in PSS/E was intended for electromechanical dynamic simulation, which covers time constants from 0.01 s to 10 s [36]. Electromechanical models of a power system take into account the slow dynamics of synchronous machines, their controllers and other devices, while the AC branches are assumed to be quasi-static. The model was split into converter models and the DC-grid model.

The dynamic model for VSC-MTDC systems must satisfy the time-step requirements for electromechanical simulation. Typical values for the time steps used are 0.1-10 ms, being 1 ms a commonly used value. Therefore, the electromechanical model of a VSC-MTDC system must be the result of a tradeoff between accuracy and computational time. The base values for the AC/DC per-unit system are the same as those used for the power-flow calculation and they are described in Appendix B.

The simplifications of the model will now be summarised and the scenarios in which these types of models can be used will be discussed:

- VSC stations

  The VSCs are represented according to type-6 models of [122] (electromechanical type). The closed-loop systems of the current controllers are modelled as first-order systems, the outer controllers are modelled in detail, the dynamics of the Phase Locked Loop (PLL) is neglected

and the VSC electromechanical model used is independent of the technology, which means that some dynamics of MMC technology are neglected. It is reasonable to use these simplifications for transient stability studies, since (a) the transients of interest take about 0.5-15s and (b) VSCs must have a good response of the inner and outer control loops to be able to provide supplementary modulation for angle stability improvement, by manipulating the set points of the outer controllers.

- DC grids

  The most important dynamics of the DC grids are the equivalent capacitances of the VSCs [129], therefore they are included in the model at every DC bus. The dynamics of the DC lines are faster and reduced-order models have been used for electromechanical simulation neglecting their shunt capacitances and inductances [109], whilst other approaches included them using lumped $\pi$ models [99, 100, 107, 108]. The latter choice has been used in this thesis, with the purpose of capturing the interaction between supplementary controllers, DC-voltage droop and the DC-grid dynamics. Notice that this modelling approach requires lower time steps for time-domain simulation (i.e. 0.1 ms). Meanwhile, recent studies have shown that the accuraccy of the models for the DC cables can be improved using higher-order models [130, 131], by introducing additional series and parallel branches. However, no significant impact is expected in transient stability studies.

- Connection to weak grids

  Several publications have analysed the control of VSC-HVDC systems connected to weak grids [132–136]. In these scenarios, the control of the VSC stations is more difficult and simplified models as, the ones used in this thesis, should not be used [136, 137]. Instead, electromagnetic models or more detailed electromechanical models (including the details of the inner and outer controllers and the PLL) would be more appropriate. The connection of VSCs to weak grids is left out of the scope of this thesis: it would never be reasonable to implement supplementary control strategies for angle stability improvement in VSCs which have difficulties with the outer control system.

This modelling approach captures the relevant dynamics for electromechanical simulation, while using a reasonable time step. Time steps of 0.1 ms have been used for dynamic simulation of hybrid HVAC/VSC-HVDC systems in

this thesis. If larger time steps are required, then the inner-current loop must be assumed instantaneous and the DC lines must be modelled as resistances (neglecting the inductances and the shunt capacitances). The latter simplifications would have small impact on transient stability studies, since the dynamics of interest are much slower.

### 2.4.1 VSC station model

Regarding the VSC model shown in Fig. 2.1: the connection impedance of the VSC station and the rest of the AC grid were assumed to be quasi-static. The VSC station is controlled using vector control, where the AC voltage is aligned with the $d$-axis: $\bar{u}_s = u_s + j0$. Hence, the active and reactive-power injections of the VSC station are $p_s = u_s i_{s,d}$ and $q_s = -u_s i_{s,q}$.

Active and reactive power are controlled with an inner current loop and with an outer control loop [99]. The inner current loop time constants (1-10 ms [23]) are much faster than the time constants of the synchronous machines and their controllers and they have been approximated by a first-order system, as shown in Fig. 2.3, where $i_{s,d}^{ref}$, $i_{s,q}^{ref}$ are the current set points. Instantaneous current loops are used in [107,108] but the approach here adds some flexibility.

Either the active power $p_s$ or the DC voltage $u_{dc}$ is controlled with the d-axis current $i_{s,d}$ using Proportional-Integral (PI) controllers, as depicted in Figure 2.4a. Similarly, the q-axis current is used to control either the reactive power or the AC-voltage modulus (Fig. 2.4b). The time constants of the outer loops are between 1 ms and 100 ms [23].

The converter model was implemented with the operating limits for active and reactive power: $P_{max}$, $P_{min}$, $Q_{max}$, $Q_{min}$ and with the maximum current limit $i_{s,max}$, which can be set to d-axis priority, q-axis priority or equal priority [107]. The maximum output AC voltage of a VSC station depends on the DC voltage and the maximum modulation index ($e_{c,max} = m_{max} u_{dc}$) [100]. This limit is also taken into account: if $e_c^{ref} > e_{c,max}$, the current set-point values are re-calculated using $e_{c,max} \angle \delta_c^{ref}$ as internal voltage, as depicted in Fig. 2.3.

### 2.4.2 HVDC-grid model

The dynamic model of the HVDCgrid (or simply DC grid, for short) includes the VSC stations, the capacitors and the cables, following the guidelines of [99]. The input signals of the system are the current injections, $\boldsymbol{I_{dc}} =$

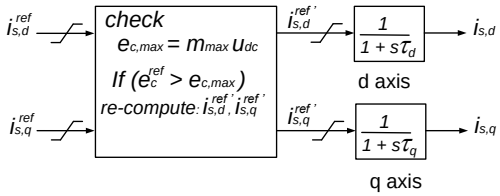


Figure 2.3: Approximation of the inner current loop.

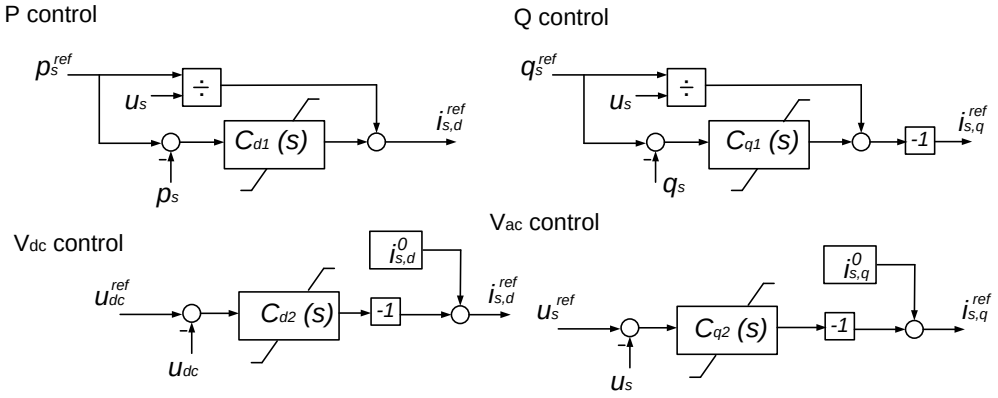


(a) d-axis. (b) q-axis.

Figure 2.4: Outer controllers. $C_x(s) = K_{P,x} + K_{I,x}/s$ where $x = d1, d2, q1, q2$.

$(i_{dc,i}) \in \mathbb{R}^{n\times 1}$, which model the DC side of the converters. The DC cables are represented by an equivalent $\pi$-model, with resistance $r_{dc,ij}$, inductance $L_{dc,ij}$ and shunt capacitance $C_{cc,ij}$ (Fig. 2.5). An equivalent capacitor at each DC bus is used to model the capacitor of the converter, $C_{VSC,i}$, and the capacitance of the DC cables, $C_{cc,ij}/2$, as depicted in Fig. 2.6:

$$C_{dc,i} = C_{VSC,i} + \sum_{j\neq i} \frac{C_{cc,ij}}{2} \tag{2.2}$$

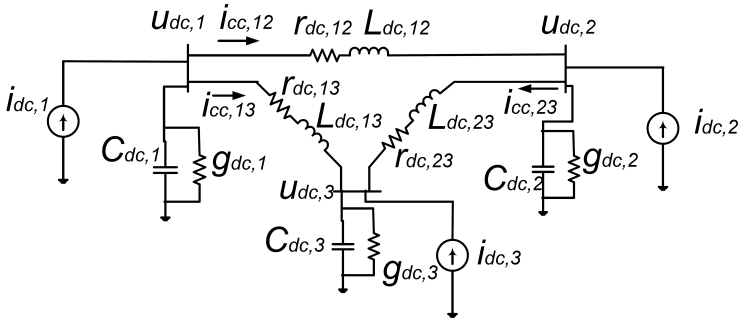


Figure 2.5: Dynamic model of the DC grid.

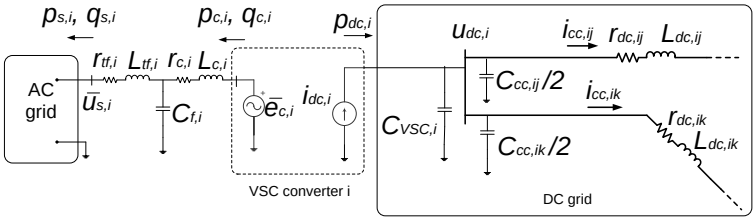


Figure 2.6: Model of the VSC stations and the DC grid.

The model also includes a shunt conductancek, $g_{dc,i}$, at every DC bus, which can be used to model resistive loads. The state variables of the system are the voltages at the DC buses, $\boldsymbol{U_{dc}} = (u_{dc,i}) \in \mathbb{R}^{n\times 1}$, and the currents through the DC lines, $\boldsymbol{I_{cc}} = (i_{cc,\ell}) \in \mathbb{R}^{n_L\times 1}$ . Therefore, the differential

equations for the DC grid are [99]:

$$\boldsymbol{C_{dc}}\frac{d\boldsymbol{U_{dc}}}{dt} = -\boldsymbol{G_{dc}}\boldsymbol{U_{dc}} - \boldsymbol{A_c}\boldsymbol{I_{cc}} + \boldsymbol{I_{dc}} \tag{2.3}$$

$$\boldsymbol{L_{dc}}\frac{d\boldsymbol{I_{cc}}}{dt} = \boldsymbol{A_c^T}\boldsymbol{U_{dc}} - \boldsymbol{R_{dc}}\boldsymbol{I_{cc}} \tag{2.4}$$

$$\text{where:} \quad \boldsymbol{G_{dc}} = \text{diag}(g_{dc,i}),\ \boldsymbol{C_{dc}} = \text{diag}(C_{dc,i}) \in \mathbb{R}^{n\times n} \tag{2.5}$$

$$\boldsymbol{R_{dc}} = \text{diag}(r_{dc,\ell}),\ \boldsymbol{L_{dc}} = \text{diag}(L_{dc,\ell}) \in \mathbb{R}^{n_L\times n_L} \tag{2.6}$$

and $\boldsymbol{A_c} = (a_{i\ell}) \in \mathbb{R}^{n\times n_L}$ is the incidence matrix of the DC grid, whose elements are:

$$a_{i\ell} = \begin{cases} +1 & \text{if line } \ell \text{ is defined leaving node } i. \\ -1 & \text{if line } \ell \text{ is defined entering node } i. \\ 0 & \text{if line } \ell \text{ is not connected to node } i. \end{cases} \tag{2.7}$$

### 2.4.3 AC/DC coupling

AC and the DC sides of each VSC $i$ are coupled by the energy conservation principle (2.1). At each time step, AC and the DC systems are updated sequentially and $p_{dc,i}$ is obtained from $p_{c,i}$. The currents injected by the VSC stations into the DC grid are calculated as:

$$i_{dc,i} = \frac{p_{dc,i}}{u_{dc,i}} = \frac{-(p_{c,i} + p_{loss,i})}{u_{dc,i}} \quad \forall i = 1,\ldots,n \tag{2.8}$$

### 2.4.4 Control of the VSC-MTDC system

The most common control options for VSC-MTDC systems are [138, 139]: (a) centralised control, in which one converter controls its DC voltage and all the others control their active power injected into the AC grid and (b) distributed control, in which the DC-voltage control is shared among a set of converters, with the so-called DC-voltage droop. In the distributed control scheme, the active-power set point of each VSC station reads [100]:

$$p_{s,i}^{ref}(t) = p_{s,i}^0 - \frac{1}{k_{dc,i}}(u_{dc,i}^0 - u_{dc,i}(t)) \tag{2.9}$$

where $p_{s,i}^0$ and $u_{dc,i}^0$ are the active-power injection and the DC voltage of the $i$-th VSC at the steady-state operating point, respectively.

The design of the DC-voltage droop constants ($k_{dc,i}$) must ensure (a) the stability of the system, (b) the steady-state active-power contribution of each converter to the DC-voltage control and (c) the maximum steady-state DC-voltage deviations. Several studies have already addressed the design of the DC-voltage droop constants in VSC-MTDC systems [100, 101, 113, 117, 138, 140, 141].

### 2.4.5 Implementation in PSS/E

The VSC-MTDC model has been coded in FORTRAN as a PSS/E user-defined model. User-defined models in PSS/E can be "generator-type", "governor-type", "exciter-type" or "stabiliser-type" models, among others. At the end, user-defined models are subroutines with certain characteristics. For example, a "generator-type" model injects current into the grid, but "governor" or "exciter" types can be used to manipulate variables of other models of the system even if they are really not modelling a true governor or a true excitation system. A user-defined model of a VSC-MTDC system must fit with the flexibility of PSS/E software.

The proposed VSC-MTDC model consists of $n$ "generator-type" models for the converters and one "governor-type" model for the DC grid. DC-voltage droop control or controllers for ancillary services could have been included in the VSC models but, for flexibility, they were implemented in independent models which change the set-point values for the converter models. Along these lines, the DC-voltage control has been implemented as an "exciter-type" model that changes the active-power set point of the converters according to (2.9). Supplementary control strategies for angle stability improvement have been included in the simulation tool in very much the same way.

## 2.5 Validation of the AC/DC power flow algorithm

In this Section, the AC/DC power-flow algorithm implemented in PSS/E is validated against MatACDC tool [97], which for the time being is the only open-source tool for power-flow calculation of AC/DC systems.

The test system considered for the validation is composed of `case5_stagg` (AC grid) and `case5_stagg_MTDCslack.m` (DC grid) of MatACDC, which is shown in Fig. 2.7. The data of this test system are reported in Section A.1 and the specified variables of the VSCs for the power flow read:

- VSC1: Mode $P_s - Q_s$, con $P^0_{s,1} = -60$ MW y $Q^0_{s,1} = -40$ MVAr.
- VSC2: Mode $U_{dc} - U_s$, con $u^0_{dc,2} = 1$ p.u y $u^0_{s,2} = 1$ p.u.
- VSC3: Mode $P_s - Q_s$, con $P^0_{s,3} = 35$ MW y $Q^0_{s,3} = 5$ MVAr.

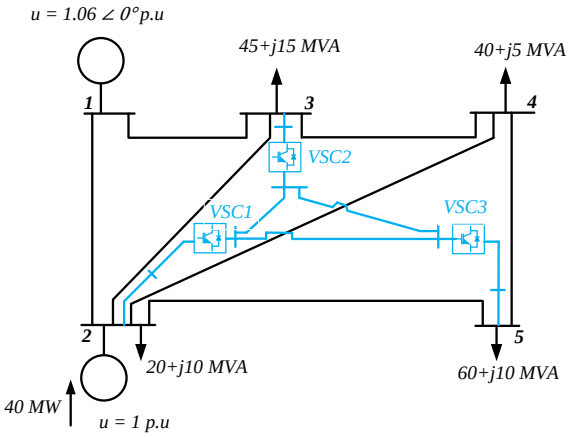


Figure 2.7: Leuven test system.

The tolerance for the mismatches of the net P and Q injections for the AC power flow was set to $10^{-3}$ p.u. (default value in PSS/E), while the tolerance for P mismatches for the DC power flow was set to $10^{-4}$ p.u. The net mismatches at the non-slack AC and DC buses obtained with the AC/DC power-flow algorithm in PSS/E are reported in Table 2.1, illustrating the convergence of the power flow.

The results of the AC/DC power flow obtained with MatACDC tool and with the PSS/E tool developed in this thesis are included in Tables 2.2-2.5, showing very good agreement.

Hence, the sequential algorithm for power-flow calculation of AC/DC systems in PSS/E has been validated.

Table 2.1: Results of the AC/DC power flow using the proposed PSS/E tool. Mismatches at the non-slack AC and DC buses.

| AC bus | $p^{sp} - p^{calc}$ (p.u) | $q^{sp} - q^{calc}$ (p.u) |
|---|---|---|
| 2 | $3.16 \times 10^{-6}$ | $1.73 \times 10^{-6}$ |
| 3 | $-0.16 \times 10^{-6}$ | $-0.31 \times 10^{-6}$ |
| 4 | $0.98 \times 10^{-6}$ | $-1.39 \times 10^{-6}$ |
| 5 | $-6.25 \times 10^{-6}$ | $-5.28 \times 10^{-6}$ |
| DC bus | $p_{dc}^{sp} - p_{dc}^{calc}$ (p.u) | - |
| 1 | $-2.05 \times 10^{-10}$ | - |
| 3 | $1.72 \times 10^{-5}$ | - |

Table 2.2: Results of the AC/DC power flow. AC grid.

| | PSS/E (proposed) | | MatACDC | |
|---|---|---|---|---|
| bus | $u$ (p.u) | $\delta$ (deg) | $u$ (p.u) | $\delta$ (deg) |
| 1 | 1.0600 | 0.000 | 1.0600 | 0.000 |
| 2 | 1.0000 | -2.383 | 1.0000 | -2.383 |
| 3 | 1.0000 | -3.894 | 1.0000 | -3.895 |
| 4 | 0.9960 | -4.260 | 0.9960 | -4.262 |
| 5 | 0.9908 | -4.149 | 0.9908 | -4.149 |

Table 2.3: Results of the AC/DC power flow. VSC stations.

| Modelo | PSS/E (proposed) | | | MatACDC | | |
|---|---|---|---|---|---|---|
| Converter | 1 | 2 | 3 | 1 | 2 | 3 |
| AC bus | 2 | 3 | 5 | 2 | 3 | 5 |
| $P_s$ (MW) | -60.00 | 20.78 | 35.00 | -60.00 | 20.76 | 35.00 |
| $Q_s$ (MVAr) | -40.00 | 7.13 | 5.00 | -40.00 | 7.14 | 5.00 |
| $u_s$ (p.u) | 1.000 | 1.000 | 0.991 | 1.000 | 1.000 | 0.991 |
| $\delta_s$ (deg) | -2.383 | -3.894 | -4.149 | -2.383 | -3.895 | -4.149 |
| $P_c$ (MW) | -59.92 | 20.78 | 35.02 | -59.92 | 20.76 | 35.02 |
| $Q_c$ (MVAr) | -32.63 | -0.64 | -0.37 | -32.63 | -0.65 | -0.37 |
| $e_c$ (p.u) | 0.890 | 1.007 | 0.995 | 0.890 | 1.007 | 0.995 |
| $\delta_c$ (deg) | -13.017 | -0.650 | 1.442 | -13.017 | -0.655 | 1.442 |

Table 2.4: Results of the AC/DC power flow. DC buses.

| | PSS/E (proposed) | | MatACDC | |
|---|---|---|---|---|
| bus DC | $u_{dc}$ (p.u) | $P_{dc}$ (MW) | $u_{dc}$ (p.u) | $P_{dc}$ (MW) |
| 1 | 1.0079 | 58.6518 | 1.0079 | 58.6274 |
| 2 | 1.0000 | -21.9254 | 1.0000 | -21.9013 |
| 3 | 0.9978 | -36.1856 | 0.9978 | -36.1856 |

Table 2.5: Results of the AC/DC power flow. DC branches.

| | PSS/E (proposed) | | MatACDC | |
|---|---|---|---|---|
| línea DC | $P_{cc,ij}$ (MW) | $P_{cc,ij}$ (MW) | $P_{cc,ij}$ (MW) | $P_{cc,ij}$ (MW) |
| 1-2 | 30.6821 | -30.4411 | 30.6648 | -30.4242 |
| 1-3 | 27.9697 | -27.6887 | 27.9625 | -27.6816 |
| 2-3 | 8.5157 | -8.4969 | 8.5228 | -8.5040 |

## 2.6 Validation of the dynamic model

The dynamic model developed in PSS/E was compared with a detailed electromagnetic model in Matlab + Simulink and with an electromechanical model in PowerFactory. A guideline for modelling VSC-MTDC systems in PowerFactory can be found in [103].

The test case consists of three infinite grids coupled synchronously with HVAC lines and a 3-terminal VSC-HVDC system, as shown in Fig. 2.8. The parameters are shown in Table A.6 of Section A.2. The test case considered is a simple extension of test system `power_hvdc_vsc` provided by Matlab + Simulink + SimPowerSystems [142]. A time step of $\Delta t = 0.1$ ms was used for electromechanical simulation in PSS/E and PowerFactory, while a time step of $\Delta t = 7.4$ $\mu$s was used for electromagnetic simulation in SimPowerSystems.

Converters VSC1 and VSC3 control their active-power injections, while VSC2 controls the DC voltage. All VSCs control their reactive-power injections. The VSC stations in Matlab were simulated using the models available in example `power_hvdc_vsc` provided by Matlab: three-level neutral point clamped (NPC) VSC stations controlled with single-phase carrier-based sinusoidal pulse width modulation (SPWM).

The initial steady-state point of the VSC-MTDC system is:

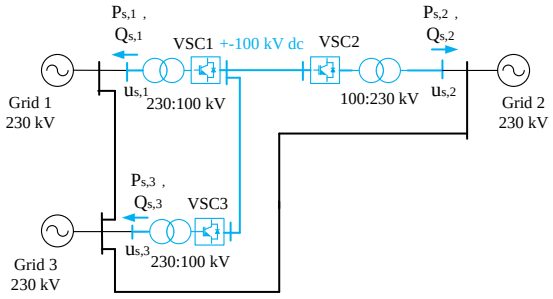


Figure 2.8: Test system for validation.

- VSC1 (s,1): $P^0_{s,1} = -100$ MW and $Q^0_{s,1} = 0$ MVAr.
- VSC2 (s,2): $u^0_{dc,2} = 1$ p.u and $Q^0_{s,2} = 0$ MVAr (DC-slack).
- VSC3 (s,3): $P^0_{s,3} = -50$ MW and $Q^0_{s,3} = 0$ MVAr.

The following step changes were simulated:

- From $u^{ref}_{dc,2} = 1$ p.u to $u^{ref}_{dc,2} = 1.05$p.u at $t = 1$ s.
- From $P^{ref}_{s,1} = -100$ MW to $P^{ref}_{s,1} = -50$MW at $t = 1.5$ s.
- From $Q^{ref}_{s,2} = 0$ MVAr to $Q^{ref}_{s,2} = -50$MVAr at $t = 3$ s.

Results obtained with each tool are compared in Fig. 2.9 showing good agreement within the scope of each simulator. Only the results obtained with Simulink spresent a high-frequency ripple, due to the electronic power switches.

Therefore, the proposed PSS/E model for electromechanical simulation of VSC-MTDC systems has been validated.

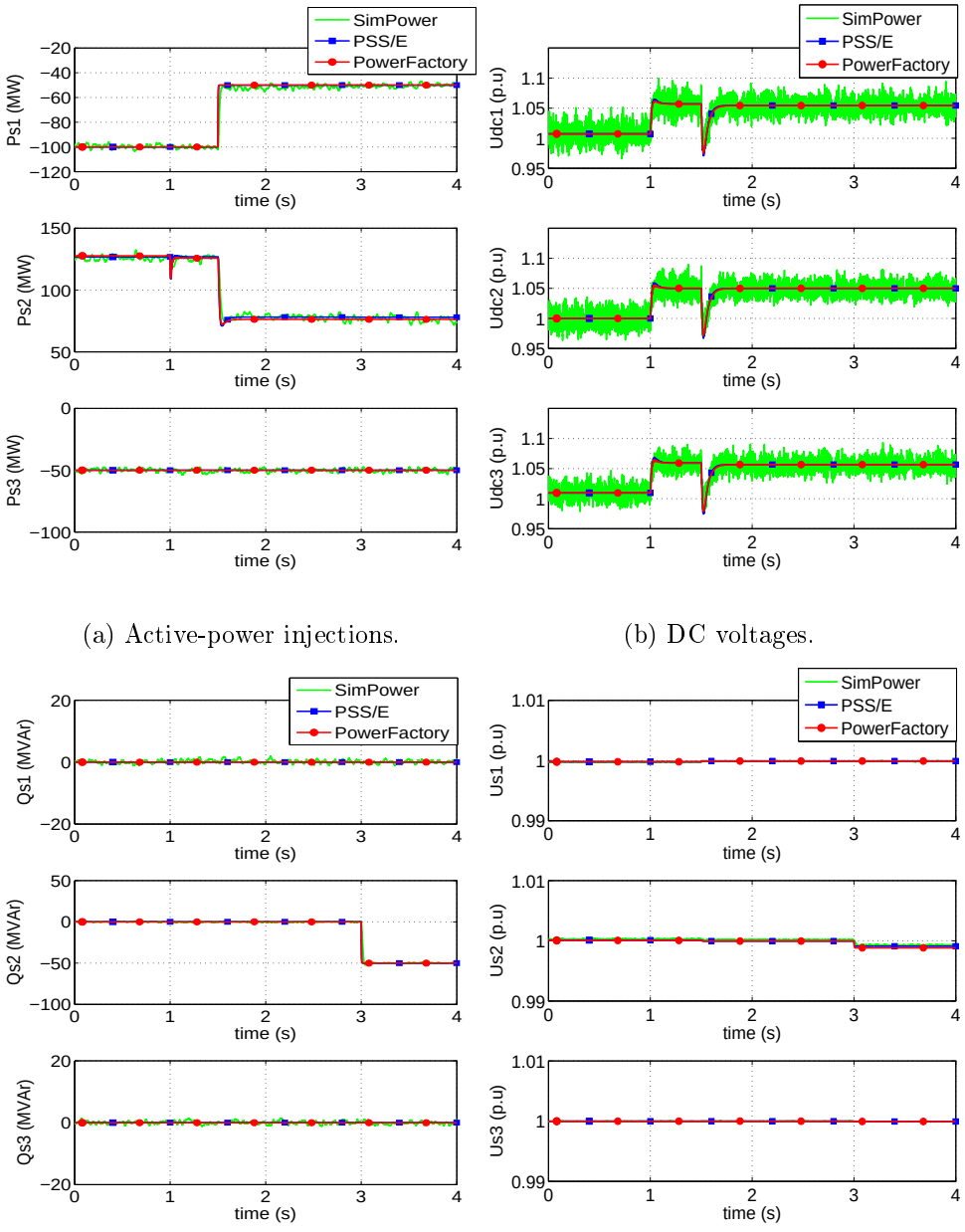


(a) Active-power injections.

(b) DC voltages.

(c) Reactive-power injections.

(d) AC voltages.

Figure 2.9: Validation of the VSC-HVDC multi-terminal model.

## 2.7 Case study

A 3-terminal VSC-MTDC system built into the modified Cigré Nordic32A system [143] has been simulated (see Fig. 2.10). This system will be used in this thesis for angle stability analysis. The test system is described in Section A.3.1 (operating point A) of the Appendix. The parameters of the converters and the DC grid were similar to those in [114,124] (see Table A.8 of Section A.3). The time step for dynamic simulation was set to 0.1 ms.

The initial steady-state specified operating points of the converters were:

- VSC1: $P^0_{s,1} = -350$ MW and $Q^0_{s,1} = 0$ MVAr ($P_s - Q_s$).
- VSC2: $P^0_{s,2} = 500$ MW and $u^0_{s,2} = 1$ p.u ($P_s - U_s$).
- VSC3: $u^0_{dc,3} = 1$ p.u and $Q^0_{s,3} = 100$ MVAr ($U_{dc} - Q_s$).

The initial steady state of the AC/DC grid is obtained by the power-flow calculation and is reported in Table 2.6 whilst the control modes of the converters during the dynamic simulation are summarised in Table 2.7. VSC2 controls its active-power injection and its AC-voltage magnitude to constant values. The DC-voltage control is shared by converters 1 and 3 using a DC-voltage droop control strategy. They inject the active power demanded by VSC2, into the DC grid. A droop constant of $k_{dc,i} = 10$ % was used for each VSC (in p.u's with respect to the rating of the converters). VSCs 1 and 3 also control their reactive-power injections to constant values.

Table 2.6: Power flow solution. Converters and DC grid.

| Converter | 1 | 2 | 3 |
|---|---|---|---|
| AC bus, DC bus | 4012, dc1 | 4044, dc2 | 4062, dc3 |
| $P_s$ (MW), $Q_s$ (MVAr) | -350.0, 0.0 | 500.0, 15.8 | -190.8, 100.0 |
| $u_s$ (p.u), $\delta_s$ (deg) | 1.006, 1.21 | 1.000, -46.59 | 1.016, -41.81 |
| $P_c$ (MW), $Q_c$ (MVAr) | -349.8, 20.69 | 500.5, 58.59 | -190.7, 107.69 |
| $e_c$ (p.u), $\delta_c$ (deg) | 1.007, -2.17 | 1.007, -41.73 | 1.033, -43.60 |
| $P_{loss}$ (MW) | 12.8 | 13.9 | 12.0 |
| DC grid | | | |
| DC bus, type | 1, Pdc | 2, Pdc | 3, Udc |
| $u_{dc}$ (p.u) | 1.00053 | 0.99769 | 1.00000 |
| $P_{dc}$ (MW) | 336.99 | -514.36 | 178.74 |
| DC branch | 1-2 | 1-3 | 2-3 |
| $P_{cc,ij}$, $P_{cc,ji}$ (MW) | 284.3, -283.5 | 52.7, -52.7 | -230.9, 231.4 |

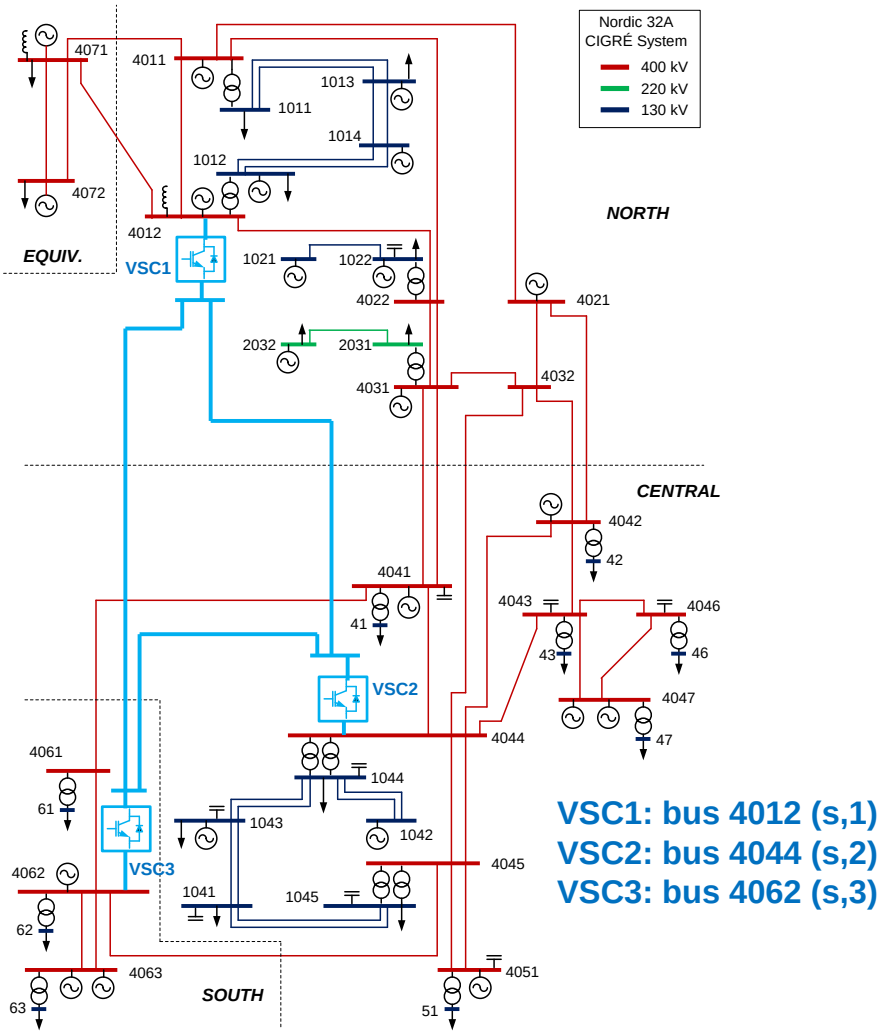


Figure 2.10: Nordic 32A system with an VSC-MTDC system.

Table 2.7: Converter Control Modes for dynamic simulation.

| Converter | Control mode $d$ | Control mode $q$ |
|---|---|---|
| VSC1 | $P_s - U_{dc}$ droop | $Q_s$ constant |
| VSC2 | $P_s$ constant | $U_s$ constant |
| VSC3 | $P_s - U_{dc}$ droop | $Q_s$ constant |

### 2.7.1 Set-point change

A set-point change from $P_{s,2}^{ref} = 500$ MW to $P_{s,2}^{ref} = 600$ MW at $t = 1$ s. Fig. 2.11 shows the active power injected by the VSC stations into the AC grid ($P_{s,i}$) and the DC voltages ($u_{dc,i}$), Fig. 2.12 shows the reactive-power injections ($Q_{s,i}$) and the AC voltages ($u_{s,i}$). The active-power flows through the DC lines are shown in Fig. 2.13.

VSC2 changes its active-power injection, as requested, while the DC voltage is maintained close to its set point (differences are due to the droop control) (Fig. 2.11). VSC1 and VSC3 change their active-power injections according to the droop control, to maintain the power balance in the DC grid; and the power flows through the DC lines change accordingly.

Finally, VSC2 controls its AC voltage to 1 p.u , while VSC1 and VSC3 maintain a constant reactive-power injection (Fig. 2.12).

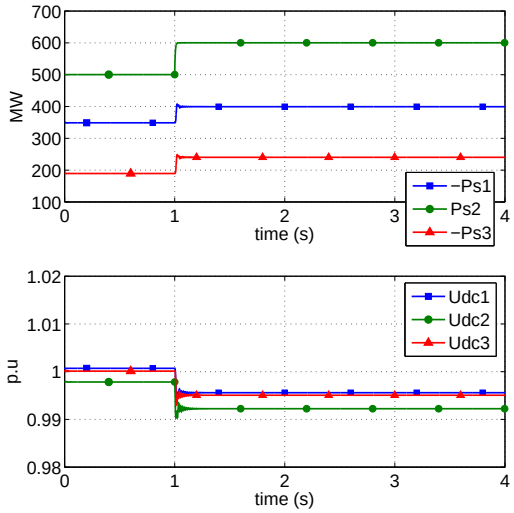


Figure 2.11: P injections and DC voltages. (The signs of $P_{s,1}$ and $P_{s,3}$ were changed).

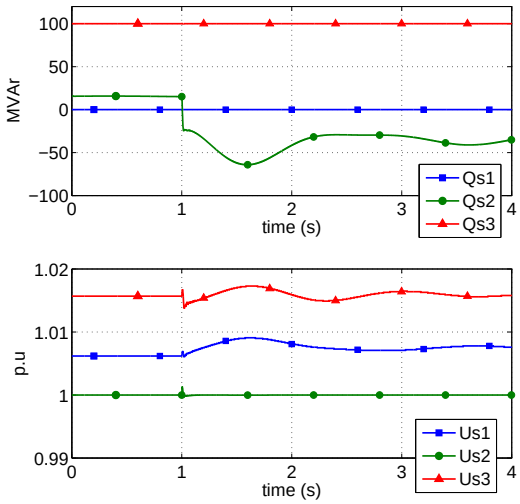


Figure 2.12: Q injections and AC voltages (and detail).

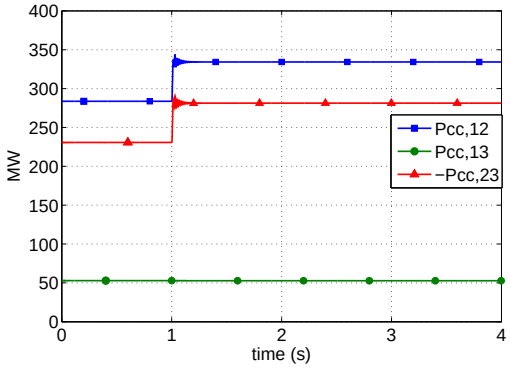


Figure 2.13: P flows through the DC lines. (The sign of $P_{cc,23}$ was changed).

### 2.7.2 Fault simulation

At $t = 0.2$ s, a short circuit occurs at bus 4012 in line 4012-4022 and it is cleared by disconnecting the line 130 ms later. Fig. 2.14 shows the active-power injections and the DC voltages ; Fig. 2.15 shows the reactive-power injections ($Q_{s,i}$) and the AC voltages ($u_{s,i}$). The different time frames of the AC and DC system dynamics can be clearly seen in Figs. 2.14 and 2.15: the transients of the AC voltages (and the reactive-power injection of VSC2, which varies to control the AC voltage) take several seconds while the transients of the DC voltages last some milliseconds. Different time scales are used to represent the results in Figs. 2.14 and 2.15 in order to have a reasonable resolution for each variable.

During the short circuit, the AC voltage of bus 4012 drops to zero, VSC1 reaches its current limit (see Fig. 2.16, which shows the magnitude of the converter currents ($i_{s,i}$), in p.u referred to the converter's rating) and no active or reactive power can be injected by VSC1 (Figs. 2.14 and 2.15). After the fault clearing, VSC1 is able to control the active- and reactive-power injections successfully. VSC3, which is far from the fault, does not reach its current limit and it is able to supply the required active power for DC-voltage control during the fault and maintains its reactive-power injection during the simulation. VSC2 does not reach the current limit either and controls its active power successfully. However, when controlling its AC voltage to 1 p.u, the reactive power occasionally reaches its upper limit (Fig. 2.15). The control of the AC voltage of VSC2 can be appreciated clearly in plot at the bottom of Fig. 2.15, where the AC voltages at the PCC are represented in a shorter time span. The contingency also provokes oscillations in the DC voltages (Fig. 2.14).

Hence, results of sections 2.7.1 and 2.7.2 show that a VSC-MTDC system can be plugged into a large case in PSS/E, using the proposed tool for power-flow calculation and electromechanical simulation.

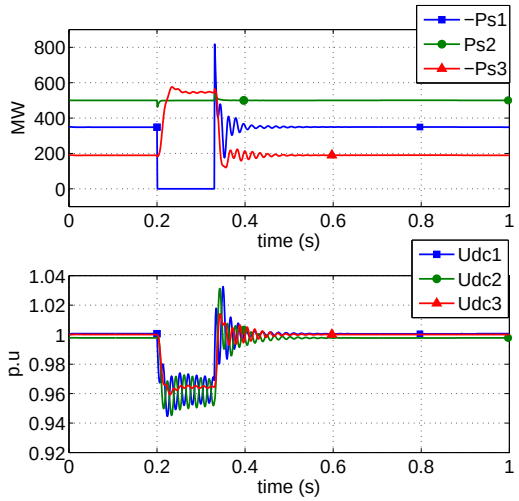


Figure 2.14: P injections and DC voltages. (The signs of $P_{s,1}$ and $P_{s,3}$ were changed).

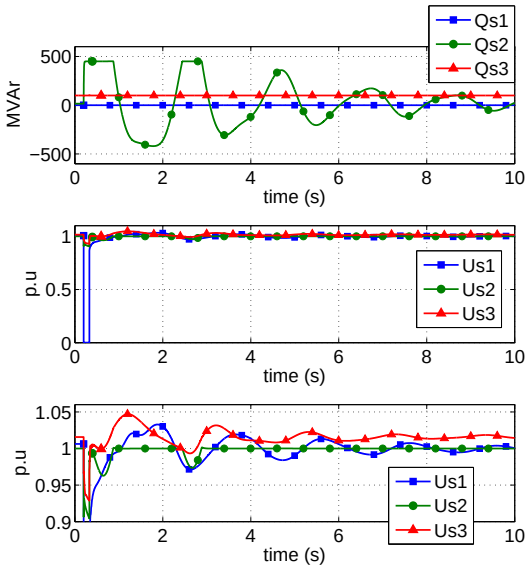


Figure 2.15: Q injections and AC voltages (and detail).

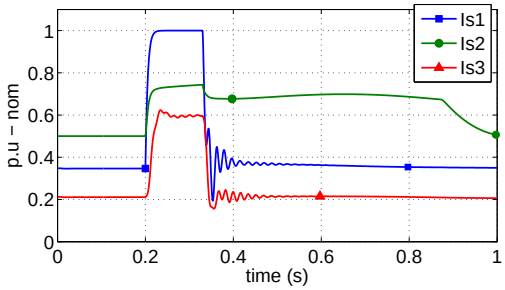


Figure 2.16: Converter currents (magnitude in nominal p.u.).

## 2.8 Summary

This chapter can be summarised as follows:

- A PSS/E tool for power-flow calculation and dynamic simulation of large AC/DC grids with VSC-MTDC systems has been presented. To date, PSS/E does not include such a model within its libraries. The procedure used makes it possible to easily add a DC grid to any existing large AC case in PSS/E.
- The sequential algorithm for power-flow calculation of hybrid AC/DC systems with VSC-MTDC systems, implemented in PSS/E, has been validated against MatACDC.
- The dynamic model for VSC-MTDC systems in PSS/E proposed in this chapter has been validated against a detailed electromagnetic model in Matlab + Simulink + SimPowerSystems and against an electromechanical model in PowerFactory (DigSilent).
- The flexibility of the proposed model has been illustrated simulating a 3-terminal VSC-HVDC system built into the Cigré Nordic32A test system.

# Chapter 3

# Active-power control strategies for transient stability improvement

## 3.1 Introduction

This chapter proposes a control strategy for the active-power (P) injections of the VSC stations in VSC-MTDC systems to improve transient stability. In the proposed strategy, each VSC uses frequency measurements from all the VSC stations of an MTDC system. This chapter also discusses the use of local, global (at the VSC stations) or global (WAMS, such as the speeds of the generators) measurements in control stratregies for transient stability improvement.

The rest of the chapter is organised as follows. Section 3.2 presents a review of previous work on P control strategies in VSC-MTDC systems for transient stability improvement. Section 3.3 describes P control strategies for transient stability improvement. Section 3.4 details a theoretical analysis of the control strategies. Section 3.5 tests the performance of the control strategies by means of electromechanical time-domain simulation. The effect of the communication latency on the performance of the proposed control strategy is analysed in Section 3.6. Finally, the conclusions are reported in Section 3.7.

## 3.2 Review of previous work

In multi-machine systems, large disturbances will cause the separation of the rotor angle of some machines with respect to some others during the transient. If the contingency is severe enough, synchronism will be lost, leading to cascade failures (i.e. disconnection of generators due to their under- or over-speed protections, line tripping or load shedding, among others) wich could cause a blackout of the system. It is well known that control strategies in generators, FACTS and HVDC systems can help to improve transient stability. Control strategies in either of these systems can use (a) local measurements or (b) global measurements. If chosen appropriately, global measurements are richer than local measurements because they inform of the global behaviour of the system. However, they require a communication system and signals will be subject to communication delays.

Transient stability has been traditionally addressed, locally, by controlling the electromagnetic torque of synchronous generators [33] with fast automatic voltage regulators (AVR). Control of the mechanical power would also be, theoretically, possible for this purpose but it is slow in traditional generators except in steam turbines with fast valving [33]. However, in modern VSC-MTDC systems, the active-power injections of the VSC stations can be controlled fast, which makes these type of systems a very attractive alternative to improve transient stability.

Previous publications have shown that transient stability can be, indeed, improved by using suitable active-power control strategies for point-to-point VSC-HVDC links [43, 45–48]. The work in [45] proposed to modulate the active power of a VSC-HVDC link (placed in parallel with an AC line) according to a non-linear function, containing the product of the cosine of the angle difference between both terminals of the link and the sign of the frequency difference between both terminals. The derivation of this control law was not explained in the paper, but simulation results in a small test system showed that the rotor angle response is improved when implementing this control strategy. Ref. [46] analysed a system with two asynchronous AC areas connected by a VSC-HVDC link and it showed that the Critical Clearing Time (CCT) of a short circuit in one of the two AC areas could be increased by using an emergency power-reversal control in the VSC-HVDC link, in order to evacuate active power from the faulted area. Although only the case of two asynchronous areas was analysed, similar conclusions could be expected if the two AC areas were synchronous.

The work in [47] proposed the control of the active power through the

VSC-HVDC link proportionally to the frequency difference between the two ends of the link. Under a contingency, the link would extract active power from the AC terminal with higher frequency to inject it to the part of the system with lower frequency. The idea behind this strategy is to try to slow down the generators close to the VSC station which sees the highest frequency and to accelerate the generators close to the terminal which sees the lowest frequency. The results presented in [47] confirmed the effectivness of this approach.

More recently, [48] proposed a control strategy to coordinate several point-to-point VSC-HVDC links for transient stability improvement, based on a model-based predictive controller and using measurements of the speeds of all the generators of the systems. The controller tries to pull together the generators of the system by introducing the square of the speed deviation of each generator with respect to the speed of the centre of inertia (COI) in the cost function of the model-based predictive control algorithm.

In [43], the active power through a VSC-HVDC link was controlled proportially to the frequency deviation of the terminals, as in [47], and this was compared with the case of constant active power through the link. Reactive-power control and the impact of the current limiter priority were also analysed, showing that reactive-power control could also be attractive for transient stability improvement.

In a point-to-point VSC-HVDC link, the coordination of the two converter stations is bound by the fact that all the energy entering the link through one end has to leave through the other end. Meanwhile, in VSC-MTDC systems, how the converters are coordinated to improve transient stability (or to provide any other ancillary service) while maintaining a zero net energy balance in the DC system is a more complicated problem. Recently, some publications have explored active-power control in VSC-MTDC systems for transient stability improvement [49–51, 144].

The work in [49] showed that supplementary Lyapunov-based control strategies for the active- and reactive-power injections at each terminal of an VSC-MTDC system connecting two areas can improve angle stability, after a fault in one of the areas. In these controllers, the supplementary power to be injected by each VSC is computed by using a linear combination of the speeds of all the synchronous generators in both areas. However, the improvements are not quantified.

A much more thorough study is presented in [50] where also a Lyapunov-based control strategy for an MTDC system is used to improve power system transient stability. The performance of the algorithm is evaluated computing

the critical clearing times (CCT) for some faults. In [50], a fixed amount of active power is injected (evacuated) into (from) the AC grid by each VSC if the input signal of the controller is above (below) a threshold. The input signal depends on the deviation of the speeds of the generators with respect to the speed of the COI (see Subsection 3.3.3). An alternative control strategy (using the frequency deviation between two terminals of the VSC-MTDC) is also investigated, but better results were obtained using the speed of the COI.

More recently, an active-power control strategy based on siliding mode robust control was proposed in [51]. In this control strategy, each converter requires the speed of the COI and the mechanical and electrical power measurements of all the generators of the system to compute the supplementary active-power reference. Simulation results show that transient stability is improved by using this strategy, but the improvements were not quantified.

Reference [144] proposed active-power set-point adjustments (corrective actions) in VSC-MTDC systems to improve transient stability: when a fault is detected, the VSC stations change their P set points to reduce the angle deviations of a set of critical AC tie lines. Set-point adjustement methods (as in [144]) are different to supplementary control strategies (as in [49–51]). In the former, the post-fault steady-state set points of the VSC stations are changed, while, in the latter, the control actions of the VSC stations only act during the transients, without modifying the post-fault set points. This thesis only focuses on supplementary control strategies.

Clearly, the control strategies proposed in [49], [50] and [51] require a Wide Area Measurement System (WAMS).

In this chapter, a new active power control strategy based on the frequency measurements in all the VSC stations of the MTDC system is proposed to improve transient stability. In comparison to [49], [50] and [51], the global data used here are much easier to obtain, since each VSC has always available the frequency at its AC side (e.g. using a PLL), for synchronisation purposes, and it could be communicated to all the others in different ways. In fact, point-to-point VSC-HVDC links already in service have a communication system between their terminals [145].

Besides, an active-power control strategy using local measurements at each converter station will also be investigated in this chapter, as an alternative to the one based on global measurements in all the converter stations. This local control strategy is based on the ideas for frequency control presented in [146] and [147]. The purpose of exploring the use of local measurements is to evaluate if reasonable improvements on transient stability could

be obtained avoiding any type of communication system. Moreover, even if better results were obtained using global measurements, reliable local control strategies could always be used as backup for global control strategies.

## 3.3 Control strategies

The active-power (P) injections of the converters in VSC-MTDC systems ($p_{s,i}$) must be coordinated in order (a) to achieve the desired operating point and (b) to control the DC voltage of the HVDC grid (see [138, 139]). As discussed in [139], a DC-voltage droop is more appropriated for large HVDC grids than the use of a single DC slack. In addition to the DC-voltage control, converters can be coordinated to provide ancillary services to the AC grid, such as frequency support [146–152] or to improve rotor-angle stability under small [71–76] or large disturbances [49–51]. These applications can be tackled by adding supplementary terms to the set point of the outer controllers of the converters.

The set point for the active-power injection of each converter $i$ into the AC system can be written as:

$$\begin{aligned} p_{s,i}^{ref}(t) &= p_{s,i}^{0} - \frac{1}{k_{dc,i}}(u_{dc,i}^{0} - u_{dc,i}(t)) + \Delta p_{s,i}^{ref}(t) \\ &= p_{s,i}^{0} + \underbrace{\Delta p_{s,i}^{ref,DC}(t) + \Delta p_{s,i}^{ref}(t)}_{\Delta p_{s,i}^{*}(t)} \end{aligned} \tag{3.1}$$

where the first term ($p_{s,i}^{0}$) is the active-power injection of the VSC in the operating point established by the TSO, the second term ($\Delta p_{s,i}^{ref,DC}$) implements the DC-voltage droop controller ($u_{dc,i}^{0}$ is the voltage at the DC side of the converter at the operating point) and the third term ($\Delta p_{s,i}^{ref}$) is an additional supplementary set point for transient stability improvement. Besides, $u_{dc,i}$ is the measured DC voltage and $k_{dc,i}$ is the DC-voltage droop constant.

The scheme proposed for the frequency-based P controller of a converter is shown in Figure 3.1, where $\omega$ is the frequency at the AC bus of the VSC (each VSC to be controlled), $\omega^{*}$ is the frequency set point, $k_P$ is the proportional gain, $\Delta p_{max}$ is the power limit value, $T_f$ is the time constant of a low-pass filter used to eliminate noise from the frequency measurements (100 ms is recommended by [153]) and $T_w$ is the time constant of a washout filter used to avoid power modulation under steady-state frequency offsets (1-20 s,

according to [33]).

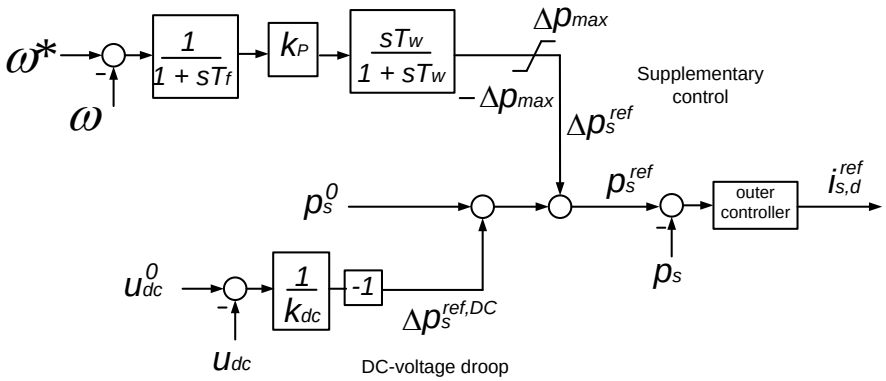


Figure 3.1: Supplementary frequency-based control.

Based on Fig. 3.1, two control strategies for transient stability improvement are proposed in this chapter. They differ only in the way in which the frequency set point $\omega^*$ is calculated before it is compared to the actual AC frequency of the converter station:

- A global control strategy that uses a weighted average of the frequencies measured at the AC side of the VSC stations of the MTDC system (P-WAF, for short).
- A local control strategy that uses the nominal frequency of the system (P-LF, for short).

Moreover, results with the strategy in [50] (also based in global measurements) will be compared with those of the proposed one as a kind of benchmark.

### 3.3.1 Weighted-average frequency control strategy (P-WAF)

It is implementated as in Fig. 3.1 using:

$$\omega_i^* = \bar{\omega} = \sum_{k=1}^{n} \alpha_k \omega_k, \quad \text{with} \quad \alpha_k \in [0,1] \text{ and } \sum_{k=1}^{n} \alpha_k = 1. \tag{3.2}$$

where $\omega_k$ is the frequency at the AC bus of VSC $k$. The design of $\alpha_k$ is postponed to Section 3.4.1.

The idea behind this control strategy is to evacuate (inject) active power from the AC terminals of the VSC-MTDC where the frequency is above (below) the weighted average. The philosophy is somehow similar to the one behind the use of the COI speed in [50], but using only the measurements of the frequency at each AC bus of the VSC-MTDC system which is more practical: these measurements are always available at each VSC for synchronisation purposes. The proposed control strategy extends to multi-terminal VSC-HVDC systems the approach of [47], which modulates the active power of a VSC-HVDC link proportionally to the frequency difference between the two terminals.

Strategy P-WAF was mainly motivated by the results of [154–156], which showed that the speed of the COI could be used with advantages when controlling the excitation of synchronous generators to improve transient stability.

It should be noticed that if the VSC-MTDC system were embedded in a meshed grid, the washout filter in Fig. 3.1 would not be necessary, because a frequency offset would be cancelled, eventually. Nevertheless, a washout filter is still recommended, in case that the frequency offsets of the measurements system of each converter station are different.

### 3.3.2 Local frequency control strategy (P-LF)

Based on the local frequency control scheme proposed in [146, 147] for frequency support, a local control scheme is used here for transient-stability support. It is implemented as in Fig. 3.1 making:

$$\omega_i^* = \omega_0 = 1 \text{ p.u.} \tag{3.3}$$

This control strategy has the advantage that each VSC only uses local measurements to calculate its set point. Meanwhile, the balance between the power entering or leaving the DC grid will be maintained, ultimately, by the DC-voltage droop control, as detailed in [146,147].

It should be notice that strategy P-LF, which is devoted for angle-stability support, has certain similarities to control schemes for frequency support [146, 147] (i.e. frequency droop). The difference is that strategy P-LF has a washout filter $T_w$, which ensures that the controller does not act against steady-state frequency deviations.

### 3.3.3 Time optimal control Lyapunov function (TO-CLF)

Time Optimal Control Lyapunov's Function (TO-CLF) strategy was proposed in [50] and it is described in this subsection because it will compared with the proposed strategies (P-WAF and P-LF).

In strategy TO-CLF, the following value is calculated for each converter VSC-$j$ in the VSC-MTDC system:

$$\phi(j) = -\sum_{\forall k} b_{P,jk} \left(\omega_{G,k} - \omega_{COI}\right) \tag{3.4}$$

where $b_{P,jk}$ accounts for the effect of a power injection using VSC-$j$ on the speed of the generator $k$ ($\omega_{G,k}$) (see Eq. (C.8) of Section C.2, of the Appendix) and $\omega_{COI}$ is the speed of the COI of the AC system (see Section C.2).

Station VSC-$j$ would inject a fixed supplementary amount of active power $\Delta p_{max,j}$ into the AC system according to:

$$\Delta p_{s,j}^{ref} = \begin{cases} +\Delta p_{max,j} & \text{if } \phi(j) > +\epsilon \\ -\Delta p_{max,j} & \text{if } \phi(j) < -\epsilon \\ 0 & \text{otherwise} \end{cases} \tag{3.5}$$

where $\pm\epsilon$ and $\Delta p_{max,j}$ are parameters to be designed.

A direct measurement of the speed of all generators is used for feedback and, unlike the two previous strategies, the controller is not a proportional one but a non-linear one of the so-called "bang-bang" type. In [50], one converter of the VSC-MTDC controls the DC voltage (DC-slack bus) while the rest participate in the control strategy. In order to avoid the overload of the DC-slack converter, a linear optimisation problem is solved at each time step to redistribute the active-power set points.

## 3.4 Theoretical analysis of the control strategies

### 3.4.1 Interaction between the AC-side control and the DC-voltage droop

The interaction between control strategies P-WAF and P-LF and the DC-voltage droop control will now be studied analytically with the following assumptions:

- the dynamics of the DC grid have been neglected since they are much faster than the dynamics of the AC system (i.e. the DC grid has been modelled as an aggregated capacitor),
- the limits of the converters and their controllers are not taken into account and
- the controllers in Fig. 3.1 are working within their frequency bandwidth and the filters (for the frequency measurement and the washout) can be neglected.

Strategy TO-CLF is not included here because it uses a sufficiently large slack converter in the VSC-MTDC system to always maintain a constant DC value.

If a steady-state active-power imbalance occurs in the VSC-MTDC system, the converters with DC-voltage droop control will change their active power in order to maintain the DC voltage. If the DC-voltage change is similar in all terminals, the contribution of each converter will be approximately proportional to the relative droop gain of each converter ($g_i$), as shown in [101]. Moreover, since the dynamics of the VSC-MTDC system are much faster than the dynamics of the AC system [23], slow changes in the active-power supplementary references of the converters will be reached almost instantaneously, leading to:

$$\Delta p_{s,i}^{ref,DC} \simeq -g_i \underbrace{\left( \sum_{k=1}^{n} \Delta p_{s,k}^{ref} \right)}_{\Delta p_{total}^{ref}}, \quad g_i = \frac{1/k_{dc,i}}{\sum_{k=1}^{n} 1/k_{dc,k}} \tag{3.6}$$

**Strategy P-WAF**

According to Fig. 3.1, within the bandwidth of the controller and if no limits are reached, the supplementary reference using strategy P-WAF is:

$$\Delta p_{s,i}^{ref} \simeq k_{P,i}(\omega_i^* - \omega_i) = k_{P,i}(\bar{\omega} - \omega_i) \tag{3.7}$$

Hence, the total active-power supplementary reference can be manipulated as:

$$\begin{aligned}
\Delta p_{total}^{ref} = \sum_{k=1}^{n} \Delta p_{s,k}^{ref} &\simeq \sum_{k=1}^{n} k_{P,k}(\bar{\omega} - \omega_k) \\
&= \Big(\sum_{k=1}^{n} k_{P,k}\Big)\Big(\bar{\omega} - \sum_{k=1}^{n} \frac{k_{P,k}}{\sum_{j=1}^{n} k_{P,j}}\omega_k\Big) \\
&= \Big(\sum_{k=1}^{n} k_{P,k}\Big)\Big(\sum_{k=1}^{n} \alpha_k\omega_k - \sum_{k=1}^{n} \frac{k_{P,k}}{\sum_{j=1}^{n} k_{P,j}}\omega_k\Big) \\
&= \Big(\sum_{k=1}^{n} k_{P,k}\Big) \sum_{k=1}^{n} \Big(\alpha_k - \frac{k_{P,k}}{\sum_{j=1}^{n} k_{P,j}}\Big)\omega_k
\end{aligned} \tag{3.8}$$

Eq. (3.8) shows that if the weights in (3.2) verify

$$\alpha_k = \frac{k_{P,k}}{k_{P,T}}, \;\; k_{P,T} = \sum_{j=1}^{n} k_{P,j}, \tag{3.9}$$

the total supplementary reference change in the VSC-MTDC system will be $\Delta p_{total}^{ref} = 0$ in (3.8), yielding $\Delta p_{s,i}^{ref,DC} \simeq 0$ in (3.6). In other words, there is no change in the DC voltage during the transients and, therefore, if the operating limits are not reached, low impact of the DC-voltage droop control on the performance of this power control strategy is expected. Notice that the gains in (3.6) and (3.2) must be referred to the same p.u base values.

**Strategy P-LF**

Assuming again that the controller is within its bandwidth and no limits are reached, the supplementary reference using strategy P-LF is $\Delta p_{s,i}^{ref} \simeq k_{P,i}(\omega_0 - \omega_i)$. Hence, the total active-power supplementary reference can be

manipulated as:

$$\begin{aligned}\Delta p^*_{s,i} &= \Delta p^{ref}_{s,i} + \Delta p^{ref,DC}_{s,i} \\ &\simeq \Delta p^{ref}_{s,i} - g_i\Big(\sum_{k=1}^{n} \Delta p^{ref}_{s,k}\Big) \\ &= k_{P,i}(\omega_0 - \omega_i) - g_i\Big[\sum_{k=1}^{n} k_{P,k}(\omega_0 - \omega_k)\Big] \\ &= g_i k_{P,T} \sum_{k=1}^{n} \frac{k_{P,k}}{k_{P,T}}\omega_k - k_{P,i}\omega_i + k_{P,i}\omega_0 - g_i k_{P,T}\omega_0\end{aligned} \tag{3.10}$$

Using $\bar{\omega}$ from (3.2), with the weights defined in (3.9):

$$\Delta p^*_{s,i} \simeq k_{P,i}(\bar{\omega} - \omega_i) + (\omega_0 - \omega_i)(k_{P,i} - g_i k_{P,T}) \tag{3.11}$$

which shows that, if $k_{P,i} = g_i k_{P,T}$ is verified and there is no saturation, strategies P-WAF and P-LF produce the same contribution of $\Delta p^*_{s,i}$. However, in the latter, the contribution of the DC-voltage droop is not zero. In P-LF a DC-voltage droop control is mandatory.

Finally, the conditions that the gains in strategy P-LF must verify to produce the same behaviour as strategy P-WAF ($k_{P,i} = g_i k_{P,T}$) are:

$$\frac{k_{P,i}}{\sum_{j=1}^{n} k_{P,j}} = \frac{1/k_{dc,i}}{\sum_{j=1}^{n}(1/k_{dc,j})} = \alpha_i \tag{3.12}$$

Notice that the conditions in (3.12) mean equal relative gains for the AC and DC side control strategies.

### 3.4.2 Lyapunov-based stability analysis

Lyapunov theory can be used to prove that the control strategies P-WAF and P-LF improve power system transient stability (see Appendix C). A similar analysis for strategy TO-CLF was reported in [50]. The same assumptions used in Subsection 3.4.1 are now used here.

A power system with VSCs can be written as a set of differential-algebraic equations ($\dot{\boldsymbol{x}} = \boldsymbol{F}(\boldsymbol{x}, \boldsymbol{z})$, $\boldsymbol{0} = \boldsymbol{H}(\boldsymbol{x}, \boldsymbol{z})$), using a power-injection model for each VSC, as shown in [47,54]. Using the implicit theorem, if $\partial \boldsymbol{H}/\partial \boldsymbol{z}$ is non-singular, the system is locally equivalent to a set of differential equations and

can be written as [47,54]:

$$\dot{\boldsymbol{x}} = \boldsymbol{f}(\boldsymbol{x}) \tag{3.13}$$

To start with, the VSCs are considered to be injecting a constant (uncontrolled) power and [54] and [47] show that an energy function ($\mathcal{V}(\boldsymbol{x})$, for short), such as those studied in [34, 157], can be written for the system in (3.13) and it satisfies the necessary and sufficient conditions for the stability of the system at an operating point $\boldsymbol{x}_0$: $\mathcal{V}(\boldsymbol{x}) > 0$ if $\boldsymbol{x} \neq \boldsymbol{x}_0$, $\mathcal{V}(\boldsymbol{x}_0) = 0$, and $\dot{\mathcal{V}}(\boldsymbol{x}) \leq 0$ in the neighbourhood of $\boldsymbol{x}_0$ [158]. A function $\mathcal{V}(\boldsymbol{x})$ that verifies the stability conditions is said to be a Lyapunov's function.

The system with controlled VSCs (power injections are allowed to vary) is written as [47,50,54]:

$$\dot{\boldsymbol{x}} = \boldsymbol{f}(\boldsymbol{x}) + \boldsymbol{g}(\boldsymbol{x})\boldsymbol{u} \tag{3.14}$$

where $\boldsymbol{f}(\boldsymbol{x})$ includes constant power injections by the VSCs and $\boldsymbol{u}$ is the control strategy to be implemented in the VSC stations.

If the energy function $\mathcal{V}$ used before for the uncontrolled system is proposed as a Lyapunov's function candidate for the controlled system, it will satisfy $\mathcal{V} \geq 0$ and its derivative will depend on the control law used. The derivative of this function reads [47,54]:

$$\dot{\mathcal{V}} = \nabla\mathcal{V} \cdot \dot{\boldsymbol{x}} = \overbrace{\nabla\mathcal{V} \cdot \boldsymbol{f}(\boldsymbol{x})}^{\dot{\mathcal{V}}_{unctr}} + \overbrace{\nabla\mathcal{V} \cdot \boldsymbol{g}(\boldsymbol{x})\boldsymbol{u}}^{\dot{\mathcal{V}}_{ctr}} \tag{3.15}$$

where $\dot{\mathcal{V}}_{unctr}$ is equal to the derivative with the uncontrolled system and it is proved to be $\dot{\mathcal{V}}_{unctr} \leq 0$ [47]. Therefore, if the control law for the VSCs satisfies $\dot{\mathcal{V}}_{ctr} \leq 0$, too, the system in (3.14) can be said to be stable. Reference [47] writes $\dot{\mathcal{V}}_{ctr}$ for a two-VSC system using a structure preserving model for the power system (see Section C.3 of the Appendix), and generalising for $n$ VSCs of an MTDC system, one can write:

$$\dot{\mathcal{V}}_{ctr} = \sum_{i=1}^{n} \Delta p_{s,i}(\omega_i - \omega_{COI}) \tag{3.16}$$

### Analysis of the investigated control strategies

Including the weighted-average frequency in (3.16), assuming that all the VSCs participate in the control strategy and no reactive power is modulated,

one has:

$$\dot{\mathcal{V}}_{ctrl} = \sum_{i=1}^{n} \Delta p_{s,i}(\omega_i - \bar{\omega}) + (\bar{\omega} - \omega_{COI}) \sum_{i=1}^{n} \Delta p_{s,i} \tag{3.17}$$

- Strategy P-WAF

  In this control strategy, inside the bandwidth of the controller, the total active-power change of each converter is given by: $\Delta p_{s,i} = \Delta p^*_{s,i} = k_{P,i}(\bar{\omega} - \omega_i)$. Replacing this expression in (3.17) and taking into account that $\sum_{i=1}^{n} \Delta p_{s,i} = 0$ when using this control strategy (with $\alpha_i = k_{P,i}/k_{P,T}$):

$$\dot{\mathcal{V}}_{ctrl} \quad = \quad -\sum_{i=1}^{n} k_{P,i}(\bar{\omega} - \omega_i)^2 \leq 0 \tag{3.18}$$

  which proves that strategy P-WAF makes $\mathcal{V}$ in (3.15) a Lyapunov's function.

- Strategy P-LF

  If $k_{P,i} = g_i k_{P,T}$, strategies P-LF and P-WAF have the same behaviour (see Section 3.4.1), and $\dot{\mathcal{V}}_{ctrl} \leq 0$. Therefore, strategy P-LF also makes $\mathcal{V}$ in (3.15) a Lyapunov's function.

### 3.4.3 Limitations of the theoretical analysis

The theoretical analysis carried out in subsections 3.4.1 and 3.4.2 gives a useful insight into the performance of strategies P-WAF and P-LF. However, the non-linearities caused by the operating limits, for example, which may be relevant when studying transient stability, were not taken into account. Furthermore, (3.6) and (3.11) imply that the DC-voltage droop controllers detect instantaneously the voltage variation produced by the active power modulation like if the DC link were a single equivalent capacitor. However, the DC system consists of lines/cables with resistances and inductances, too. Therefore, the above control strategies will now be investigated by simulation in realistic scenarios, including all the converter limits and DC-side inductances and resistances.

## 3.5 Results

This section contains an investigation of the different control strategies for transient stability improvement described in Section 3.3, in case of different faults. The control strategies have been tested and compared by simulation using the PSS/E model for VSC-MTDC systems presented in Chapter 2.

The case study consists in the modified Cigré Nordic 32A grid [159] with a 3-terminal VSC-HVDC system described in Section A of the Appendix. In order to consider a more heavily loaded case, the load in the central area has been increased in 580 MW (operating point B of Section A). The initial operating point of the VSC-MTDC system is also reported in Section A. The system has been simulated using a time step of $\Delta t = 0.1$ ms.

The following control strategies have been compared:

- DC0: No supplementary control (only DC-voltage droop).
- P-LF: Local frequency control (and DC-voltage droop).
- P-WAF: Weighted-average frequency control (and DC-voltage droop).

The parameters used for the control strategies (see Fig. 3.1) are $k_{P,i} = 200$ p.u, $T_{f,i} = 0.1$ s, $T_{w,i} = 15$ s, $\Delta p_{max,i} = 1$ p.u, $\alpha_k = 1/n$ and $k_{dc,i} = 0.1$ p.u. Gains are in p.u., referred to the converters' ratings.

Additionally, some results with strategy TO-CLF have been included for comparison with the P-WAF (both using global measurements). In this case, VSC1 and VSC2 control their P injections, while converter VSC3 is the DC slack. Parameters of TO-CLF were set by engineering judgement to $\epsilon = 0.001$ p.u. and $\Delta p_{max,i} = 380$ MW (0.38 p.u.). The performance of TO-CLF is strongly dependent of the value of $\Delta p_{max,i}$ which, if chosen as small as in [50], could not cope with the severe fault investigated below. Therefore, this value was increased up to the maximum value of $\Delta p_{max,i}$ that produces the best results.

### 3.5.1 Fault I: Severe fault

A symmetrical short circuit was applied to line 4031-4041a (at bus 4041) (see Fig. A.3 of Appendix A) at $t = 1$ $s$ and it was cleared by tripping both circuits of the corridor (4031-4041a and b) after 390 ms (Fault I). Initially, each circuit carried 726.29 MW and, therefore, the event was extremely severe. Two representative generators have been chosen to plot the results: G4012 (North area) and G4062 (South area).

The rotor-angle difference between the chosen machines is shown in Fig. 3.2. Synchronism is lost when no supplementary control strategy is implemented (DC0) or when using the local supplementary control strategy (P-LF). Only, strategies P-WAF, proposed in this work, and TO-CLF proposed in [50] succeed in maintaining synchronism.

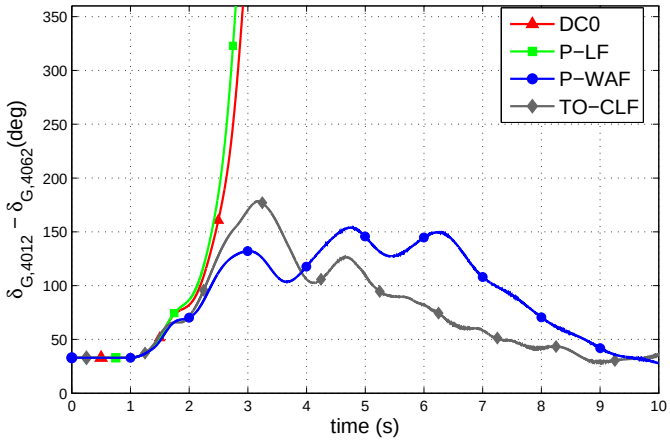


Figure 3.2: Generator angles: Fault I cleared after 390 ms.

Active-power injections of the converters and the DC-voltages are shown in Figs. 3.3 and 3.4, respectively. Using strategy P-WAF, the converters modulate their P injections comparing the weighted-average frequency with the frequency measured at each converter station. The frequencies measured at each station and the weighted frequency using strategy P-WAF are shown in Fig. 3.5. Strategy P-LF performs worse than P-WAF because the DC voltages (Fig. 3.4) at the VSC stations in the former soon reach their limit (1.1 p.u.) and active-power injections are locked by the DC-voltage control. Meanwhile, if strategies P-WAF and TO-CLF are used, only very small DC-voltage fluctuations can be seen.

Finally, the critical clearing times (CCTs) obtained for Fault I with control strategies DC0, P-LF, P-WAF and TO-CLF are 105 ms, 115 ms, 390 ms and 410 ms, respectively. Clearly, for this severe fault, strategy P-WAF improves transient stability, significantly, in the system considered, and works much better than strategies DC0 and P-LF. The best performance is obtained with strategy TO-CLF although the CCT is close to the one obtained

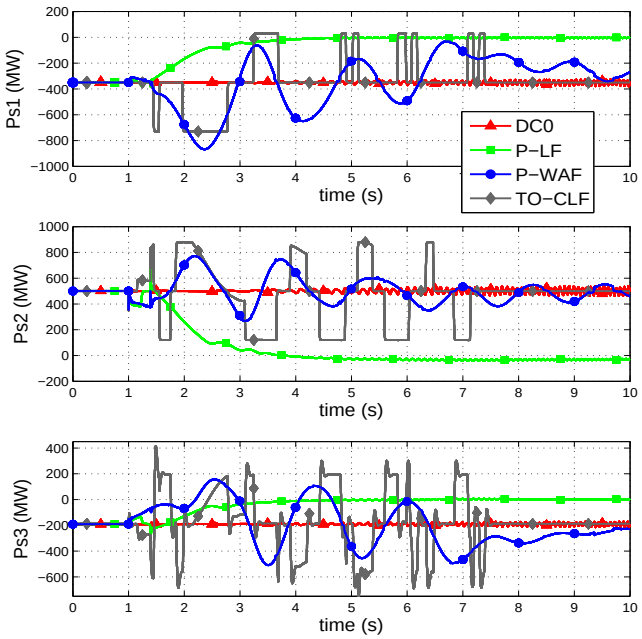


Figure 3.3: Fault I cleared after 390 ms. P injections ($P_{s,i}$)

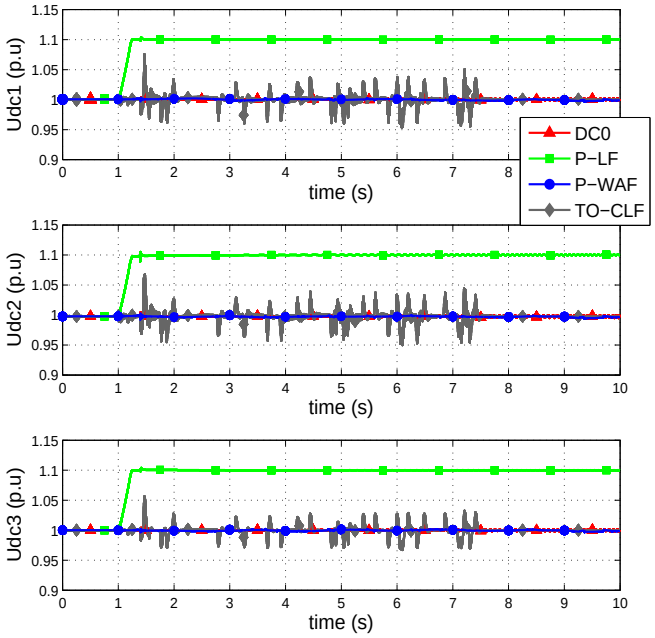


Figure 3.4: Fault I cleared after 390 ms. DC voltages ($u_{dc,i}$)

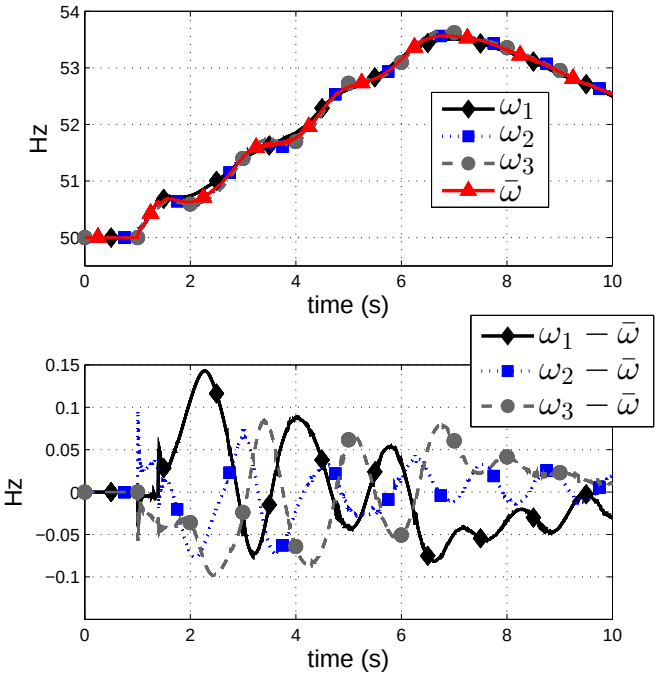


Figure 3.5: Fault I cleared after 390 ms (P-WAF). Weighted-average frequency (WAF), VSC-station frequencies and frequency deviations with respect to the WAF.

by P-WAF. However, strategy P-WAF is much easier to implement thant strategy TO-CLF, because in the fomer each VSC uses the weighted-average frequency and its frequency measurement, whilst in the latter the converters need the speeds of all the generators of the system.

The input signal of strategy P-WAF is much easier to implement than the input signal of strategy TO-CLF. The effect of the bang-bang limit on the performance of TO-CLF was investigated in Fault I using the CCTs obtained (see Table 3.1). If $\Delta p_{max,i}$ is too high, the performance deteriorates, because current limits can be reached and the active-power modulation is limited to prevent the saturation of the DC slack.

Table 3.1: TO-CLF: effect of the bang-bang saturation parameter.

| Fault I | DC0 | TO-CLF | | | |
|---|---|---|---|---|---|
| $\Delta p_{max,i}$ (MW) | - | 100 | 200 | 380 | 400 |
| CCT (ms) | 105 | 207 | 287 | 410 | 376 |

### 3.5.2 Fault II: Less severe fault

In order to understand better the behaviour of strategies P-LF and P-WAF when the DC-voltage limits are not reached, a less severe fault has also been simulated: a three-phase short circuit is placed in line 4012-4022, at bus 4012 (where VSC1 is connected), and is cleared by disconnecting the line after 120 ms (Fault II, for short). The rotor-angle difference is shown in Fig. 3.6 and the active power and DC-voltages of the converters are plotted in Fig. 3.7. The system's synchronism can be maintained even without taking any action: a different stable equilibrium point is reached without the faulted line.

The case with the largest rotor-angle differences is when no supplementary control is implemented (DC0). During the fault, converter VSC1 can not inject active power with none of the three alternatives because its current limit is reached. After the fault is cleared, the active-power injection of each converter in strategies P-LF and P-WAF is modulated producing a damping effect on the rotor-angle oscillations. In fact, active-power injections of the converters are remarkably similar with these two control strategies (Fig. 3.7) and they produce, apparently, the same effect on the generators' dynamics (unlike in the case of Fault I), as predicted in Section 3.4.1. However, strategy P-LF shows larger DC voltage variations than those shown by strategy

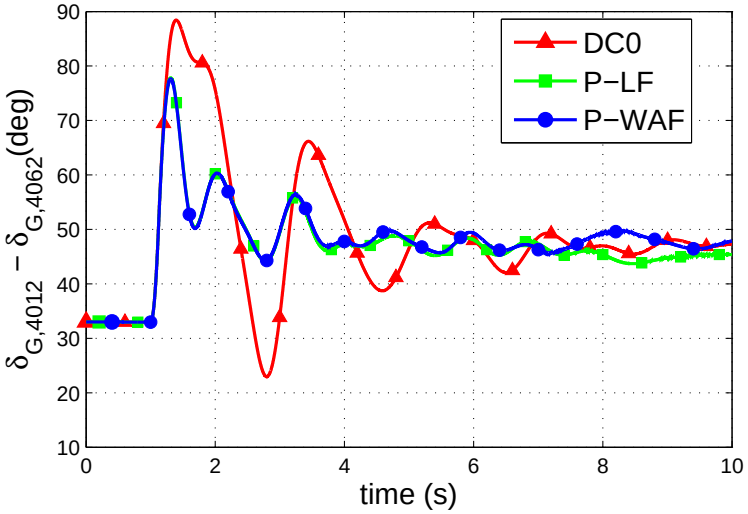


Figure 3.6: Generator angles. Fault II cleared after 120 ms.

P-WAF although DC voltages are within limits in both (right-hand side of Fig. 3.7).

The critical clearing times obtained for Fault II are 188 ms, 218 ms and 224 ms, using strategies DC0, P-LF and P-WAF, respectively. Thus, for Fault II, better results are obtained with strategy P-WAF than those obtained with strategy P-LF.

The most important conclusion drawn from this simulation is that strategy P-LF can produce a similar response to strategy P-WAF, if no limits are reached, even if the former uses local measurements only. However, as seen in Section 3.5.1, when using strategy P-LF, severe faults will produce important fluctuations in the DC voltages, provoking that the converters reach their DC-voltage limits and jeopardising the performance of strategy P-LF.

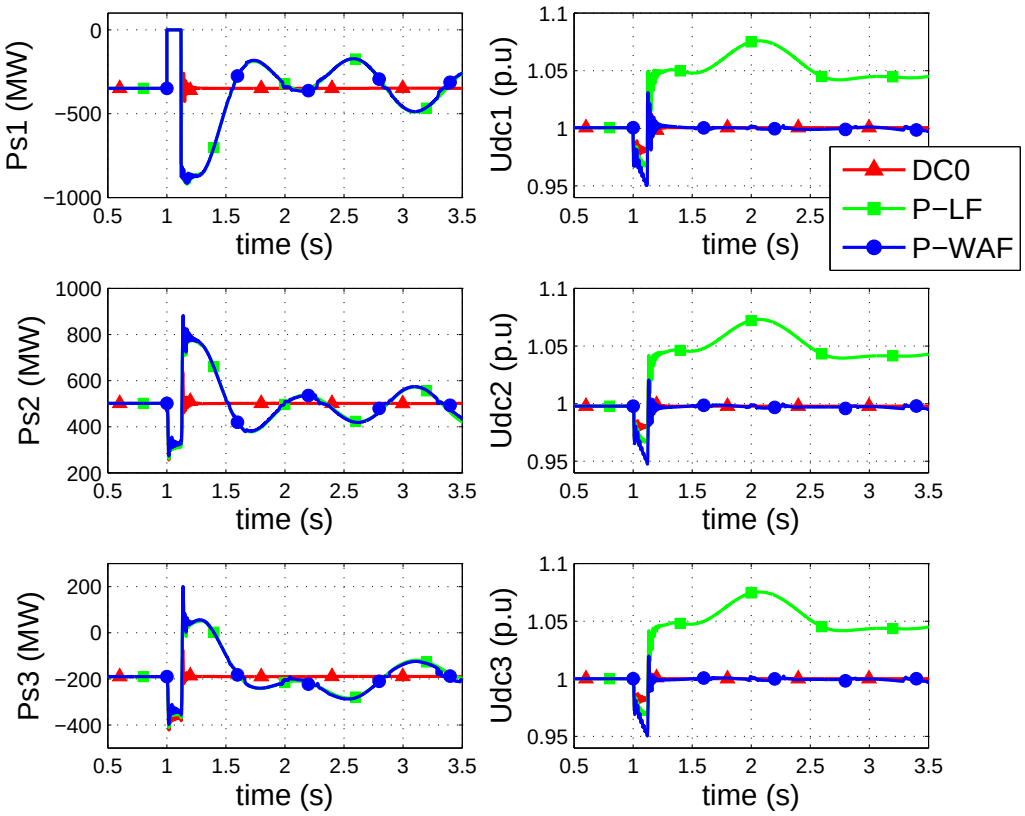


Figure 3.7: Fault II cleared after 120 ms. P injections and DC-voltages.

### 3.5.3 Critical clearing times

The critical clearing times (CCTs) have been calculated for the set of contingencies described in Table 3.2. The CCTs obtained for each contingency are given in Table 3.3.

Clearly, CCTs can be increased significantly by implementing strategy P-WAF and the results are nearly-always better than in the base case (DC0) or using strategy P-LF. Although, naturally, the numerical results obtained change with the fault simulated. For example, the CCT of Fault I can be increased substantially using P-WAF strategy, while the CCT of Fault III is almost the same in all cases. In the latter, active-power modulation in the VSC-MTDC system cannot prevent loss of synchronism in generator 1021, which is close to the point of the short circuit. In Fault IV, the CCT obtained with P-LF is lower than the one obtained with DC0. This problem can be avoided by rducing the controller gain or saturating the supplementary reference, as will be discussed in Subsection 3.5.4.

Finally, it has to be underlined that no fault was found with longer CCT in the base case (DC0) than the one obtained using strategy P-WAF.

Table 3.2: Fault description.

| | Short circuit at line $i-j$ | close to bus | clearing |
|---|---|---|---|
| Fault I | 4031-4041a | 4041 | Lines 4031-4041a&b disconnected |
| Fault II | 4012-4022 | 4012 | Line disconnected |
| Fault III | 4012-4022 | 4022 | Line disconnected |
| Fault IV | 4032-4044 | 4044 | Line disconnected |
| Fault V | 4011-4022 | 4011 | Line disconnected |

### 3.5.4 Impact of the control parameters

In view of (3.18), higher values of $k_{P,i}$ in both strategies P-WAF and P-LF should produce better results. In theory, a larger saturation band ($\pm\Delta p_{max,i}$) will also be more beneficial. However, as seen in the simulations, the active-power modulation can produce DC-voltage fluctuations, which are critical specially in strategy P-LF. Therefore, gains and saturation parameters should be carefully tuned.

Table 3.4 shows the CCTs for faults of Table 3.2, using strategies P-WAF

Table 3.3: Critical clearing time (CCT) for different faults.

| Fault (ms) | DC0 CCT (ms) | P-LF CCT (ms) | P-WAF CCT (ms) |
|---|---|---|---|
| Fault I | 105 | 115 | 390 |
| Fault II | 188 | 218 | 224 |
| Fault III | 237 | 241 | 240 |
| Fault IV | 390 | 306 | 824 |
| Fault V | 205 | 229 | 235 |

and P-LF, respectively, with different values of $k_{P,i}$ and $\pm\Delta p_{max,i}$. Tables 3.4 and 3.5 show that, in general, much better results can be obtained with strategy P-WAF than with strategy P-LF, in agreement with the simulations of the previous sections.

Table 3.4: Effect of parameters $k_{P,i}$ and $\Delta p_{max,i}$ of P-WAF.

| P-WAF | CCT (ms) | | | | |
|---|---|---|---|---|---|
| $k_{P,i}$ (p.u) ($\Delta p_{max,i} = 1$ p.u) | 0 | 50 | 200 | 500 | 1000 |
| Fault I | 105 | 211 | 390 | 525 | 555 |
| Fault II | 188 | 212 | 224 | 125 | 181 |
| Fault III | 237 | 239 | 240 | 241 | 241 |
| Fault IV | 390 | 568 | 824 | 802 | 794 |
| Fault V | 205 | 225 | 235 | 213 | 210 |
| $\Delta p_{max,i}$ (p.u) ($k_{P,i} = 200$ p.u) | 0 | 0.1 | 0.2 | 0.5 | 1.0 |
| Fault I | 105 | 237 | 332 | 390 | 390 |
| Fault II | 188 | 199 | 210 | 224 | 224 |
| Fault III | 237 | 239 | 240 | 240 | 240 |
| Fault IV | 390 | 440 | 512 | 818 | 824 |
| Fault V | 205 | 214 | 224 | 235 | 235 |

Using strategy P-WAF, if a large gain of $k_{P,i} = 500$ p.u is chosen for all VSCs, the CCT of Fault I increases significantly (from 105 ms in DC0 case to 525 ms). However, for the same gain, the CCT of Fault II decreases from 188 ms to 125 ms, because the current limiter blocks VSC1 and the active-

power imbalance in the DC grid is so large that the DC-voltage reaches its limit. This problem can by tackled saturating the controller. For example, if $k_{P,i} = 500$ p.u and $\Delta p_{max,i} = 0.5$ p.u, the CCT of Fault II is 218 ms. Nevertheless, gains $k_{P,i} < 500$ p.u are recommended. Good results have been obtained with $k_{P,i} = 200$ p.u.

If the saturation parameter is reduced, the effect of strategy P-WAF on angle stability will be less significant, as expected. Nevertheless, a significant improvement can be obtained also when the saturation bandwidth is small ($\Delta p_{max,i} = 0.2$ p.u).

Table 3.5: Effect of parameters $k_{P,i}$ and $\Delta p_{max,i}$ of P-LF.

| P-LF | CCT (ms) | | | | |
|---|---|---|---|---|---|
| $k_{P,i}$ (p.u) ($\Delta p_{max,i} = 1$ p.u) | 0 | 50 | 200 | 500 | 1000 |
| Fault I | 105 | 204 | 115 | 70 | 62 |
| Fault II | 188 | 212 | 218 | 208 | 201 |
| Fault III | 237 | 239 | 241 | 240 | 235 |
| Fault IV | 390 | 437 | 306 | 300 | 300 |
| Fault V | 205 | 225 | 229 | 221 | 216 |
| $\Delta p_{max,i}$ (p.u) ($k_{P,i} = 200$ p.u) | 0 | 0.1 | 0.2 | 0.5 | 1.0 |
| Fault I | 105 | 106 | 109 | 109 | 115 |
| Fault II | 188 | 191 | 193 | 202 | 218 |
| Fault III | 237 | 239 | 239 | 239 | 241 |
| Fault IV | 390 | 390 | 390 | 391 | 306 |
| Fault V | 205 | 207 | 209 | 217 | 229 |

In strategy P-LF, results deteriorate when $k_{P,i} > 50$ p.u due to the fluctuation of the DC-voltage, which can reach its limits if the fault is severe enough (recall Section 3.5.1). Limiting the supplementary reference ( $\pm\Delta p_{max,i}$) can prevent this problem, but no improvements on the CCTs can be obtained. Only if $k_{P,i}$ is very low, some marginal improvements can be achieved. For example, Table 3.5 shows that, if $k_{P,i} = 50$ p.u, the CCT of Fault I improves from 105 ms to 204 ms.

## 3.6 The effect of communication latency

The impact of communication latency on the performance of strategy P-WAF has been investigated. For this purpose, the frequency at each terminal $i$ measured by converter $j$ has been assumed to be delayed as:

$$\omega_i^j = \omega_i e^{-\tau_{ij}s} \text{ with } \tau_{ij} = \tau_{ij}^0 + \tau_{ij}^X \tag{3.19}$$

where $\tau_{ij}^0$ is a constant value ($\tau_{ii}^0 = 0$ for $i = j$) and $\tau_{ij}^X$ is a stochastic random variable (which changes over time) with a triangular distribution centred at zero with upper and lower limits $\pm\Delta\tau$. The delay has been implemented in PSS/E by using a second-order Padé's approximation.

The value of the delays will depend on the communication technology and on the computation time of the signal. Despites those factors, realistic values for the communication delays in wide area control systems are below 110 ms, according to [160].

Communication latency provokes that the frequency set point is computed with delayed measurements of frequencies at the AC side of the converters. This could lead to a situation in which the total active-power commanded by strategy P-WAF is not zero any more: $\sum_{i=1}^{n} \Delta p_{s,i}^{ref}(t) \neq 0$. The DC-voltage control scheme of the VSC-MTDC will compensate this imbalance and the performance of the system will also depend on how the DC voltage is controlled. Therefore, the impact of the comunication delays on strategy P-WAF will be analysed in the following cases:

- Strategy P-WAF with distributed DC-voltage control (as done so far).
- Strategy P-WAF with centralised DC-voltage control (In this case VSC1 and VSC2 modulate their P injections according to strategy P-WAF, whilst VSC3 is the DC-slack converter).

Notice that when using strategy P-WAF with centralised DC-voltage control, the converters which modulate their active-power injections should not have the DC-voltage droop term in Fig. 3.1.

### 3.6.1 Communication latency and strategy P-WAF with distributed DC-voltage control

Results of Fault I cleared after 300ms, using strategy P-WAF and considering different communication delays are shown in Figs. 3.8 and 3.9. The rotor-angle difference between generators G4012 and G4062 obtained for each case

proves that the communication latency have a small negative impact on the performance of strategy P-WAF (Fig. 3.8) and similar active-power modulation is produced for delays below 300 ms (Fig. 3.9a). Synchronism is lost when the delays are $\tau_{ij} = 350 \pm 20$ ms, which are beyond reaslistic values. The time response of the DC voltages in Fig. 3.9b shows that the longer the communication delays, the larger the DC-voltage fluctuations are. In fact, the DC-voltage upper limit of the three converters is reached when $\tau_{ij} = 350 \pm 20$ ms. The DC-voltage droop also plays a role in the performance of strategy P-WAF when the control signals have communication latency. In strategy P-WAF, the communication delays will provoke that the frequency set point (weighted average frequency) is computed wrongly (e.g. see Fig. 3.10). One of the consequences is that control strategy P-WAF is not ensuring $\sum_{i=1}^{n} \Delta p_{s,i}^{ref} = 0$ anymore. However, the converters also react under that power imbalance, due to the DC-voltage droop scheme. Results in Fig. 3.8 shown that this interplay attenuates the negative effect of the communication latency on the system performance, but the DC-voltage fluctuations increase (Fig. 3.9b). If one or more converters reach their DC-voltage limits, control strategy P-WAF would not work properly any more.

The CCTs obtained for the faults described in Table 3.2, using strategy P-WAF with communication latency, are reported in Table 3.6. Results confirm that reasonable improvements are obtained with strategy P-WAF. The delays have more impact in some faults than in others. For example, no negative impact of the communication delays on the CCT of Fault II was observed, whilst more noticiable reduction of the CCTs of Faults I and IV was observed. As discussed above, the impact of the communication latency is reduced by the DC-voltage droop control and the critical factor is whether any DC-side converter voltage reaches its operation limits and this depends on the fault type and duration.

Since the DC-voltage fluctuations are the result of the imbalance caused by the communication latency when using strategy P-WAF and its interaction with the DC-voltage droop control, a question that arises naturally is whether this effect could be mitigated by limiting the supplementary reference provided by strategy P-WAF (i.e. $\Delta p_{max,i}$ of Fig. 3.1). The CCTs of the same faults described before but obtained using strategy P-WAF setting the saturation parameter to $\Delta p_{max,i} = 0.35$ p.u (350 MW) for different delay values are shown in Table 3.7. By limiting the P supplementary set point, the negative impact of the communication latency seems to be attenuated for some faults. For example, if $\Delta p_{max,i} = 1$ p.u, delays of $250 \pm 20$ ms reduce the CCT of Fault IV from 824 ms to 309 ms (which is smaller than

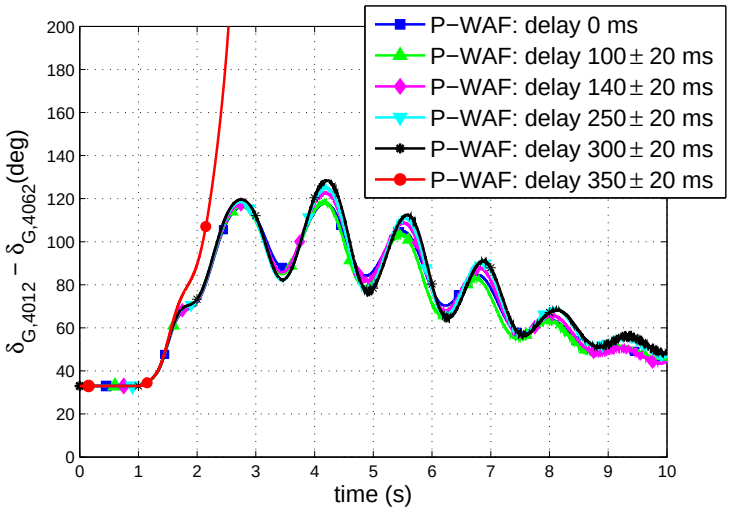


Figure 3.8: P-WAF with DC-voltage droop. Fault I cleared after 300 ms. Generator angle difference.

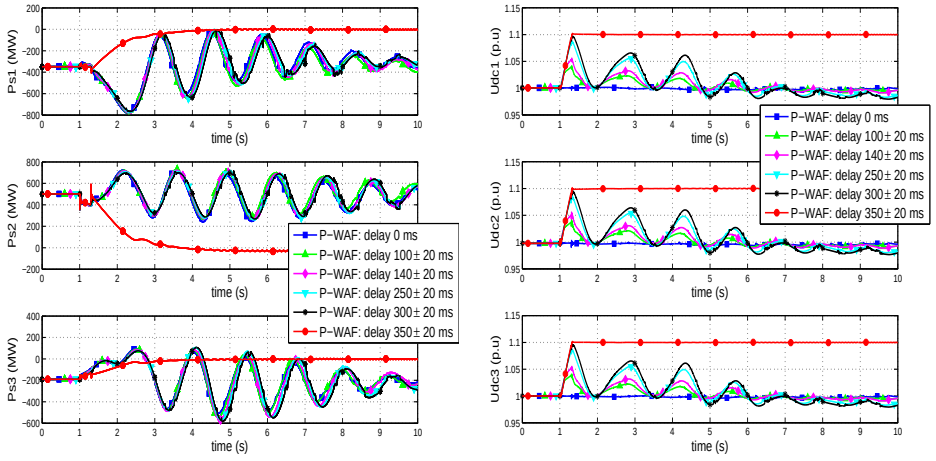


(a) P injections ($P_{s,i}$) (b) DC voltages ($u_{dc,i}$)

Figure 3.9: P-WAF with DC-voltage droop. Fault I cleared after 300 ms.

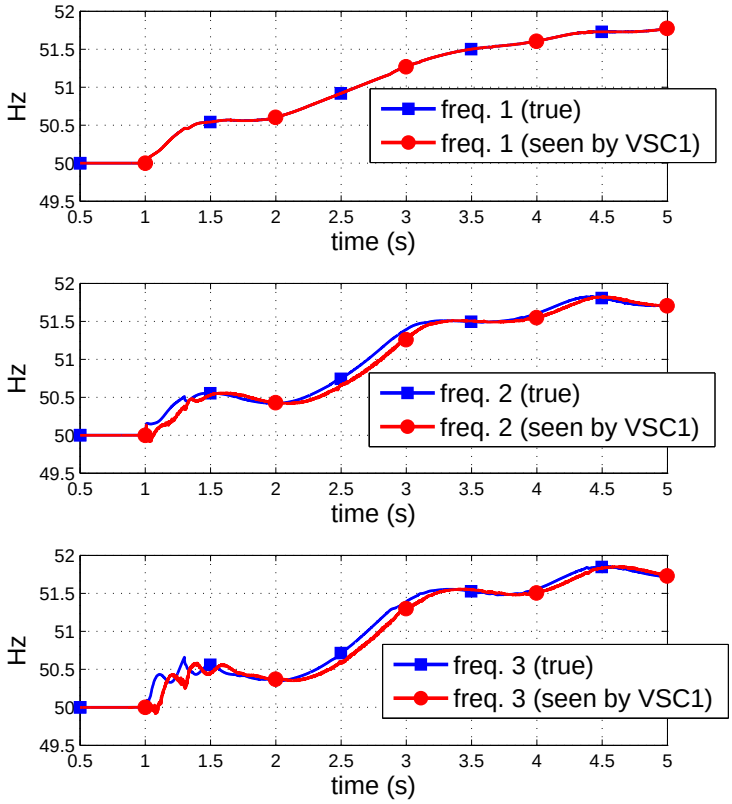


Figure 3.10: P-WAF with DC-voltage droop control. Fault I cleared after 300 ms. Frequencies seen by VSC1 for the computation of the frequency set point when the communication latency is $100 \pm 20$ ms.

the one obtained in the base case: 390 ms). Whereas, if $\Delta p_{max,i} = 0.35$ p.u, the CCT of Fault I is reduced from 613 to 588 ms. However, for other faults, no significant differences when reducing $\Delta p_{max,i}$ were observed. Finally, it is worth pointing out that, in general, the CCTs obtained with strategy P-WAF with $\Delta p_{max,i} = 0.35$ p.u tend to be shorter than the ones obtained with $\Delta p_{max,i} = 1$ p.u because, in the former case, the control action of the converters is limited.

Table 3.6: CCTs. P-WAF with DC-voltage droop.

| Fault | DC0 | P-WAF delay=0 | with 50ms ±10ms | delay 100ms ±20ms | 200ms ±20ms | 250ms ±20ms | 300ms ±20ms | 350ms ±20ms |
|---|---|---|---|---|---|---|---|---|
| | CCT (ms) | CCT (ms) | CCT (ms) | CCT (ms) | CCT (ms) | CCT (ms) | CCT (ms) | CCT (ms) |
| Fault I | 105 | 390 | 390 | 388 | 382 | 375 | 336 | 299 |
| Fault II | 188 | 224 | 224 | 224 | 227 | 228 | 228 | 228 |
| Fault III | 237 | 240 | 240 | 240 | 240 | 240 | 240 | 240 |
| Fault IV | 390 | 824 | 823 | 823 | 375 | 309 | 308 | 308 |
| Fault V | 205 | 235 | 235 | 235 | 237 | 237 | 237 | 237 |

Table 3.7: CCTs. P-WAF with saturation $\Delta p_{max,i} = 0.35$ p.u. (P-WAF with DC-voltage droop).

| Fault | DC0 CCT (ms) | P-WAF delay=0 CCT (ms) | with $100 \pm 20$ms CCT (ms) | delay $250 \pm 20$ms CCT (ms) | $350 \pm 20$ms CCT (ms) |
|---|---|---|---|---|---|
| Fault I | 105 | 362 | 339 | 307 | 272 |
| Fault II | 188 | 224 | 224 | 214 | 206 |
| Fault III | 237 | 241 | 240 | 239 | 239 |
| Fault IV | 390 | 613 | 606 | 588 | 583 |
| Fault V | 205 | 235 | 235 | 223 | 216 |

### 3.6.2 Communication latency and strategy P-WAF with centralised DC-voltage control

In this case, VSC1 and VSC2 have strategy P-WAF implemented (without DC-voltage droop), whilst VSC3 controls the DC-voltage of the DC grid. In order to avoid the overloading of the DC-slack converter (VSC3), the supplementary set point of VSC 1 and 2 have been limited to $\Delta p_{max,i} = 0.35$ p.u.

Results for Fault I cleared after 300 ms when using strategy P-WAF subject to different communication delays are shown in Figs. 3.11 and 3.12. The time response of the rotor angle difference of generators G4012 and G4062 is shown in Fig. 3.11, to illustrate that, when using a centralised DC-voltage control scheme, transient stability deteriorates greatly due to communication delays (see Fig.3.8 for comparison to the case with distributed DC-voltage control). With centralised DC-voltage control, communication delays of $200 \pm 20$ ms cause instability for this fault.

P injections of the converters and the DC voltages are shown in Figs 3.12a and 3.12b, respectively. Unlike with the DC-voltage droop control, using a centralised scheme the communication delays do not cause significant DC-voltage deviations (see Fig. 3.12b), because VSC3 is in charge of controlling the DC voltage. For the same reason, the active-power imbalance introduced by the communication delays when computing the supplementary active-power set point of VSC 1 and 2 is compensated only by VSC3. Therefore, the control actions commanded by strategy P-WAF are more inaccurate with the presence of communication latency and therefore the negative impact is more important.

The CCTs of the same faults as before (described in Table 3.2) when using strategy P-WAF and a centralised DC-voltage control are depicted in Table 3.8. In this case, the CCTs deteriorate more than when using strategy P-WAF with DC-voltage droop control, although still signifcant improvements can be obtained with communication latency as big as $200 \pm 20$ ms.

Table 3.8: CCTs. P-WAF with centralised DC-voltage control (VSC3 is the DC slack).

| Fault | DC0 | P-WAF delay=0 | with 50ms ±10ms | delay 100ms ±20ms | 140ms ±20ms | 200ms ±20ms | 250ms ±20ms | 300ms ±20ms |
|---|---|---|---|---|---|---|---|---|
| | CCT (ms) | CCT (ms) | CCT (ms) | CCT (ms) | CCT (ms) | CCT (ms) | CCT (ms) | CCT (ms) |
| Fault I | 105 | 357 | 349 | 321 | 301 | 281 | 272 | 272 |
| Fault II | 188 | 219 | 219 | 220 | 221 | 220 | 218 | 218 |
| Fault III | 237 | 241 | 241 | 241 | 241 | 241 | 241 | 241 |
| Fault IV | 390 | 632 | 600 | 507 | 473 | 453 | 353 | 318 |
| Fault V | 205 | 232 | 232 | 232 | 232 | 232 | 232 | 231 |

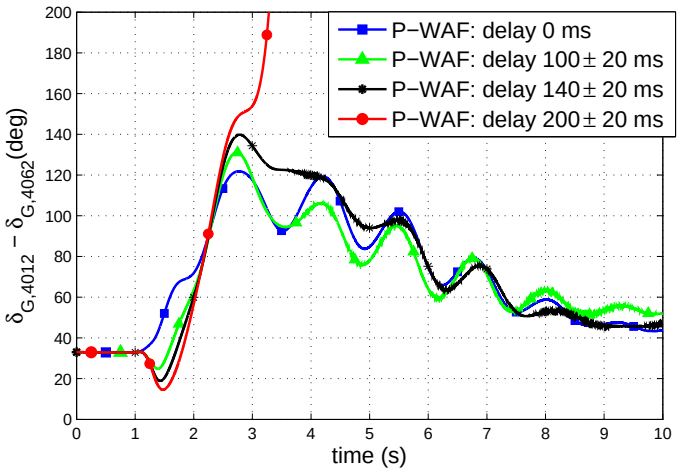


Figure 3.11: P-WAF with centralised DC-voltage control (VSC3 is the DC slack). Fault I cleared after 300 ms. Generator angle difference.

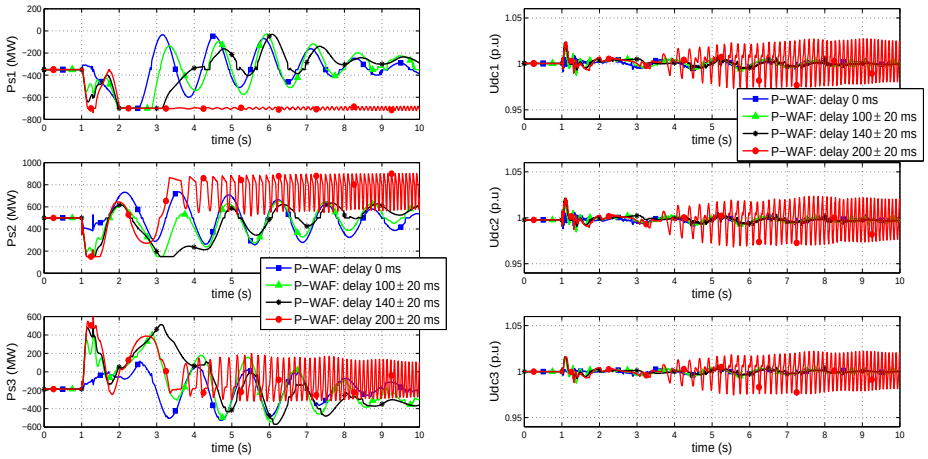


(a) P injections ($P_{s,i}$) (b) DC voltages ($u_{dc,i}$)

Figure 3.12: P-WAF with centralised DC-voltage control (VSC3 is the DC slack). Fault I cleared after 300 ms.

### 3.6.3 Discussion

The analysis carried out for the communication latencies can be summarised as follows:

- Significant improvements on transient stability can be obtained with strategy P-WAF even with communication delays higher than realistic values for this application. For example, strategy P-WAF still increase the CCTs of all the faults analysed when the communication delays are as big as $200 \pm 20$ ms.
- The negative impact of communication latency is attenuated by using strategy P-WAF with a distributed DC-voltage control scheme, instead of P-WAF with a centralised DC-voltage control scheme.
- With communication delays, the interaction between strategy P-WAF and the DC-voltage droop control causes DC-voltage fluctuations, which could be bounded by limiting the supplementary active-power set point.

## 3.7 Conclusions

The results presented in this chapter have shown that:

- The proposed strategy P-WAF improves transient stability significantly.
- The advantage of the proposed strategy P-WAF with respect to previous ones for VSC-MTDC systems is that it uses global measurements which are much easier to implement: it uses the weighted-average frequency of the AC terminals of the VSC-MTDC system, while previous approaches require measurements of the speeds of all the generators of the system.
- In general, higher gains in strategy P-WAF produce better results, although converter limits must be considered. A compromise must be reached. Good results were obtained with $k_{P,i} = 200$ p.u.
- The impact of the communication latency on strategy P-WAF is very small.
- The improvements on transient stability produced by local strategy P-LF are very limited, since the DC-voltage fluctuations jeopardise the performance of this control strategy.

# Chapter 4

# Reactive-power control strategies for transient stability improvement

## 4.1 Introduction

This chapter proposes a control strategy for the reactive-power (Q) injections of the VSC stations in VSC-MTDC systems to improve transient stability. In this strategy, each VSC uses frequency measurements from all the VSC stations of a VSC-MTDC system.

The rest of this chapter is organised as follows. A review of the state of the art on reactive-power control strategies in VSC-MTDC systems for transient stability improvement is presented in Section 4.2. The proposed Q control strategy is described in Section 4.3. A theoretical analysis of the proposed control strategy is provided in Section 4.5. The proposed Q control strategy is tested by numerical simulation in Section 4.5. The impact of the communication latency is analysed in Section 4.6. Section 4.7 compares P and Q modulation for transient stability improvement. Finally, Section 4.8 presents the conclusions of the chapter.

## 4.2 Review of previous work

As discussed in Chapter 1, transient stability can be improved controlling the electromagnetic torque of synchronous generators [33] which, basically, can be done controlling the voltage throughout the electrical grid. Traditionally,

this could only be achieved by controlling the excitation of generators or with fixed shunt capacitors [33]. However, the development of power electronics for flexible AC transmission systems (FACTS) in the last two decades has made it possible to use more flexible solutions such as static var compensators (SVCs) or (above all) static compensators based on VSCs (STATCOMs) [52, 53, 161].

Examples of transient stability improvement with FACTS can be found in [52] and [53]. The former derives a reactive-power control strategy for STATCOMs using Lyapunov theory. The performance of the proposal was verified by simulation in a single machine connected to an infinite bus (SMIB system) but its behaviour in a multi-machine system was not investigated. Reference [53] proposed a hybrid discontinuous/continuous control strategy for SVCs and STATCOMs. The complement to the set point of the controlled variable is raised to its maximum value during the first swing and, afterwards, it is made proportional to the speed deviation of a near-by machine. Transient stability is improved in SMIB and multi-machine systems, although further improvement may be expected using global measurements [154].

In VSC-HVDC systems (either point-to-point or multi-terminal) each converter is able to control the reactive-power injection independently and some publications have already explored reactive-power control in connection to transient stability. For example, in [48], the active- and reactive-power injections of multiple VSC-HVDC point-to-point links are coordinated for transient stability improvement. A model predictive control based on the speeds of all the generators of the system with respect to the COI speed is used. A similar approach was used in [162] to coordinate HVDC links and series FACTS, for transient stability improvement. The work reported in [43] studied the impact of active- and reactive-power control strategies for VSC-HVDC links on transient stability. Traditional constant reactive power and constant AC voltage strategies were first analysed, but the reactive-power modulation using the average of the frequencies at both ends to estimate the COI speed, showed better results. It is worth pointing out that the coordination of reactive-power injections of several FACTS devices or point-to-point VSC-HVDC links is equivalent to the coordination of the reactive-power injections of a VSC-MTDC system, since they are independent in each VSC.

To the best of the author's knowledge, the coordination of the reactive power of the converters in an VSC-MTDC system for this purpose has only been studied in [49], in which a VSC-MTDC system interconnecting two asynchronous AC areas is used with a Lyapunov-based control law for, both,

the active- and the reactive-power injections. Regarding the reactive-power modulation, which is the focus of this chapter of the thesis, [49] calculates the supplementary reactive-power command using the speed deviation of each generator of the two areas with respect to the ideal and constant synchronous speed, requiring an extensive global measurement system. In addition, it is difficult to evaluate the damping contribution of the reactive-power modulation, since the reactive-power injections of the VSCs are not plotted in the paper.

More recently, a local fast voltage support control at the VSC stations of an MTDC system was proposed in [163] to improve transient stability. This controller consists of a supplementary reactive-power set point that increases if the AC voltage at the PCC drops. Although it is clear that this strategy helps to slow down the generators which are close to the converter station, further improvements may be expected using some kind of global measurements.

The analysis in [43, 48, 162] for HVDC links and the work in [49] for VSC-MTDC systems, show that the use of global measurements (the speed of all generators with or without calculating the speed of the COI speed) for reactive-power control strategies can improve transient stability. However, given the difficulty of measuring the speed of all generators in the system, this chapter proposes a coordinated control strategy using, only, the frequencies measured at the VSC stations (already available for synchronisation). The approach is similar to the one proposed in the previous chapter for the active-power injections (P-WAF), but, in this case, the weighted-average frequency is used to modulate the reactive-power injections. The use of this set of measurements was motivated by the good results obtained in the previous chapter and by the good results obtained in [43] modulating the reactive-power injections of a point-to-point VSC-HVDC link using the frequency average of both ends of the link. The results will show that, with this approach, the Critical Clearing Times (CCTs) for various faults can be increased significantly.

## 4.3 Control strategies

In VSC-MTDC systems, the reactive-power (Q) injections of the converters can be controlled independently because there is no “reactive power" in the DC grid. The converters can control their Q injections or AC-voltages to constant values or, similarly to the active-power control, supplementary set

points can be included in the outer control loop to provide ancillary services. In this work, Q supplementary controllers for transient stability improvement are studied. The Q set point of converter $i$, including its supplement, can be written as:

$$q_{s,i}^{ref}(t) = q_{s,i}^{0} + \Delta q_{s,i}^{ref}(t) \tag{4.1}$$

where $q_{s,i}^{0}$ is the reactive power at the operation point and $\Delta q_{s,i}^{ref}$ is the supplementary Q reference.

The frequency measured at each terminal of the VSC-MTDC is proposed here to control the Q injection of each converter according to the general approach depicted in Figure 4.1, where $\omega$ is the frequency at the AC bus of the converter, $\omega^*$ is the frequency reference, $k_Q$ is the proportional gain, $\Delta q_{max}$ is the Q limit of the supplementary reference, $T_f$ is the time constant of a low pass filter used to eliminate noise from the frequency measurements and $T_w$ is the parameter of a washout filter.

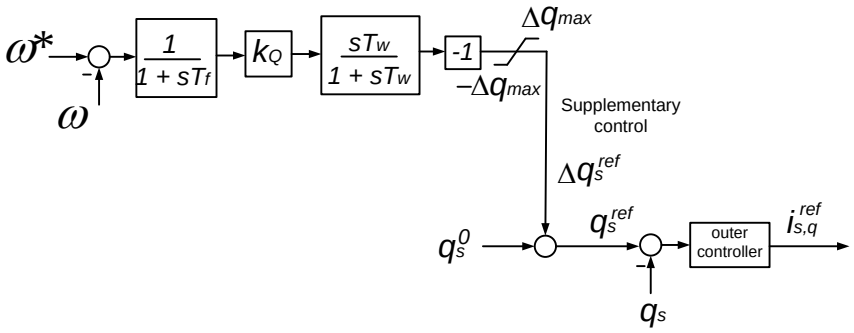


Figure 4.1: Control for the reactive-power injection of a VSC.

Two Q-control strategies for transient stability improvement will be analysed and compared:

- A new global control strategy using the weighted-average of the frequencies measured at the AC terminals of the VSC-MTDC system (Q-WAF, for short).

- A local frequency control strategy (Q-LF, for short).

### 4.3.1 Strategy Q-WAF

In this alternative, each converter modulates its reactive-power injection with the scheme showed in Figure 4.1, using a frequency set point as:

$$\omega_i^* = \sum_{k=1}^{n} \alpha_k \omega_k \tag{4.2}$$

where $\omega_k$ is the frequency of the AC bus of converter $k$, $\alpha_k \in [0,1]$ and $\sum_{k=1}^{n} \alpha_k = 1$. Therefore, each converter of the VSC-MTDC system will inject (or consume) reactive power if its frequency is above (or below) the weighted average in (4.2). This should reduce the electromagnetic torque applied to those synchronous machines below the reference speed (even if they are already accelerating) while increasing the electromagnetic torque to those above the reference speed (even if they are decelerating). This idea was motivated by the results obtained in [43,48,154] and by the good results obtained in the previous chapter, using the weighted-average frequency of the VSC-MTDC to modulate the active-power injections of the converters.

### 4.3.2 Strategy Q-LF

Alternatively, the Q injection of each converter could be modulated proportionally to its frequency deviation (local) with respect to the nominal frequency (avoiding communications). Therefore, $\omega_i^* = 1$ p.u. in Fig. 4.1: if the measured frequency rises, each converter will inject reactive power seeking to increase the electromagnetic torque seen by the system generators.

## 4.4 Theoretical analysis of the control strategies

Lyapunov theory will be used to analyse the performance of the reactive-power control strategies theoretically. In Chapter 3, Lyapunov theory was already used to analyse the proposals for active-power modulation. In that case, a structure-preserving model was used to represent the power system in the theoretical analysis, using suitable energy functions already available as Lyapunov's function candidates. Using that type of models was straightforward, since they include frequency-dependent loads and the VSCs were represented in the same way (as active-power injections which could modulate their active-power output as a function of frequency). Unfortunatelly, those models do not allow frequency-dependent reactive-power injections. There-

fore, they cannot be used directly to carry out a Lyapunov-based stability analysis of the reactive-power modulation of the converters of a VSC-MTDC system. Alternatively, a classical reduced network model of the power system will be used for this analysis (see Section C.2 of the Appendix for details). It will prove to be useful for this analysis (in spite of its simplicity).

The following assumptions were accepted for the theoretical analysis:

- The reactive-power injections of the converters are assumed to be controlled instantaneously, since their dynamics are much faster than the dynamics of the synchronous generators.
- Limits of the converters are not taken into accout.
- A reduced grid model with classical representation of the synchronous generators is used.

These hypotheses make it possible to analyse the impact of the reactive-power injections of the VSC-MTDC stations on the synchronous machines while using relatively simple equations. Nevertheless, some of the simplifications considered may have an impact on transient stability. For example, the operating limits of the converters may be reached often when large disturbances occur. Therefore, the performance of the control strategies will also be evaluated by simulation in Section 4.5, by using detailed electromechanical models of the VSC-MTDC system, the generators and their controllers, including limits.

### 4.4.1 Power system model

Usually, for stability analysis purposes, the power system is represented using a reduced network model, with a classical model for the generators, and with VSCs being modelled as power injections [47, 54, 164]. Hence:

$$\dot{\tilde{\boldsymbol{\delta}}}_{\boldsymbol{G}} = \tilde{\boldsymbol{\omega}}_{\boldsymbol{G}} \tag{4.3}$$

$$\dot{\tilde{\boldsymbol{\omega}}}_{\boldsymbol{G}} = \boldsymbol{M}^{-\mathbf{1}}[\boldsymbol{P} - \boldsymbol{P_e} + \frac{P_{COI}}{M_T}\boldsymbol{M}] \tag{4.4}$$

where:

- $\tilde{\boldsymbol{\delta}}_{\boldsymbol{G}}$ and $\tilde{\boldsymbol{\omega}}_{\boldsymbol{G}} \in \mathbb{R}^{n_G \times 1}$ are vectors with the rotor angles and speeds of the generators, respectively, all referred to the COI ($\tilde{\delta}_{G,i} = \delta_{G,i} - \delta_{COI}$ and $\tilde{\omega}_{G,i} = \omega_{G,i} - \omega_{COI}$). The number of generators of the system is $n_G$.

- $\boldsymbol{M} = \text{diag}(M_k) \in \mathbb{R}^{n_G \times n_G}$ is a diagonal matrix with the moments of inertia of the generators.

- $\boldsymbol{P}$ and $\boldsymbol{P_e} \in \mathbb{R}^{n_G \times 1}$ are vectors containing the net mechanical power and the electrical power injections of the generators, respectively.

- $M_T = \sum_{k=1}^{n_G} M_k$ and $P_{COI} = \sum_{k=1}^{n_G} (p_k - p_{e,k})$. Subscript $k$ refers to each generator.

The effect of P and Q injections of the VSC-MTDC system (inputs) can be included implicitly in the expression of the electrical power vector $\boldsymbol{P_e}$, following the guidelines given in [50]:

$$\boldsymbol{P_e} = \boldsymbol{P_e^{nc}} + \boldsymbol{B_P \Delta P_s} + \boldsymbol{B_Q \Delta Q_s} \tag{4.5}$$

where $\boldsymbol{P_e^{nc}}$ is the electrical power vector without P and Q modulation and:

- $\boldsymbol{B_P} \in \mathbb{R}^{n_G \times n}$ accounts for the effect of the active-power modulation $\boldsymbol{\Delta P_s}$ of the VSCs on the electrical power vector $\boldsymbol{P_e}$ and $n$ is the number of VSCs of the MTDC system.

- $\boldsymbol{B_Q} \in \mathbb{R}^{n_G \times n}$ accounts for the effect of the Q modulation $\boldsymbol{\Delta Q_s}$ of the VSCs on the electrical power vector $\boldsymbol{P_e}$.

Matrix $\boldsymbol{B_Q} = (b_{Q,ki})$ can be decomposed as:

$$\boldsymbol{B_Q} = \boldsymbol{M_Q B_{Q,T}} \tag{4.6}$$

where $\boldsymbol{M_Q} \in \mathbb{R}^{n_G \times n}$ is a dimensionless matrix and $\boldsymbol{B_{Q,T}} = \text{diag}(b_{Q,T,i})$ is a diagonal matrix containing the sum of all the elements of each column of matrix $\boldsymbol{B_Q}$ ($b_{Q,T,i} = \sum_{k=1}^{n_G} b_{Q,ki}$).

In inductive systems, such as HVAC grids, the elements of matrix $\boldsymbol{B_Q}$ are non negative if the machines are generating active power, which means that a positive Q injection in one bus contributes to raise the voltages of the system, provoking the rise of the electromagnetic torque seen by the generators. As mentioned previously, the effect of the Q injections of the converters on the different generators is contained in matrix $\boldsymbol{B_Q}$ and matrix $\boldsymbol{M_Q} = (m_{Q,ki})$ weights the effect of the Q injection of each VSC converter $i$ on the electrical power of each generator $k$. The decomposition in (4.6) will be useful for the analysis that follows.

### 4.4.2 Lyapunov-based stability analysis

Lyapunov's theory is used for stability analysis (see Section C.1 of Appendix C). For the theoretical analysis, the dynamics of the power injections of the VSCs are assumed instantaneous, since their time constants (1-100 ms) are much faster than the electromechanical oscillations (1-10 s):

$$\boldsymbol{\Delta P_s} \simeq \boldsymbol{\Delta P_s^{ref}}, \quad \boldsymbol{\Delta Q_s} \simeq \boldsymbol{\Delta Q_s^{ref}}, \tag{4.7}$$

where $\boldsymbol{\Delta P_s^{ref}}$ and $\boldsymbol{\Delta Q_s^{ref}}$ are the vectors containing the P and Q set points. $\boldsymbol{\Delta P_s} = \mathbf{0}$ and $\boldsymbol{u} = \boldsymbol{\Delta Q_s}$ to consider Q control, only.

#### Uncontrolled system

Without control, the input vector is set to zero: $\boldsymbol{u} = \boldsymbol{\Delta Q_s} = \mathbf{0}$. Refs. [34, 47, 54] showed that the uncontrolled system is stable and the following energy function of the system is a Lyapunov's function [34,50]:

$$\mathcal{V} = \frac{1}{2}\sum_{k=1}^{n_G} M_k \tilde{\omega}_{G,k}^2 - \sum_{k=1}^{n_G} p_k \tilde{\delta}_{G,k} - \sum_{k=1}^{n_G-1}\sum_{l=k+1}^{n_G} e_k e_l b_{kl} \cos(\tilde{\delta}_{G,k} - \tilde{\delta}_{G,l}) + C_0 \tag{4.8}$$

where $b_{kl}$ is the transfer susceptance between generators $k$ and $l$, $e_i$ is the internal voltage of each generator, $\tilde{\delta}_{G,i}$ is the rotor angle of generator $i$ and $\tilde{\omega}_{G,i}$ is the speed of generator $i$. $C_0$ is used to make $\mathcal{V} = 0$ at the operating point.

For the uncontrolled system, the derivative of $\mathcal{V}$ is equal to zero: $\dot{\mathcal{V}}_{unctr} = 0$ [34].

#### Controlled system

The energy function of the uncontrolled system (4.8), used for the controlled system, will have a derivative (3.15) with $\dot{\mathcal{V}}_{ctr}$ given by:

$$\dot{\mathcal{V}}_{ctr} = -\tilde{\boldsymbol{\omega}}_{\boldsymbol{G}}^{\boldsymbol{T}} \boldsymbol{B_Q} \boldsymbol{\Delta Q_s} = -(\boldsymbol{M_Q^T}\tilde{\boldsymbol{\omega}}_{\boldsymbol{G}})^{\boldsymbol{T}} \boldsymbol{B_T} \boldsymbol{\Delta Q_s} \tag{4.9}$$

Stability will be guaranteed if $\boldsymbol{\Delta Q_s}$ makes $\dot{\mathcal{V}}_{ctr} \leq 0$.

### 4.4.3 Discussion of the control strategies

#### Q-WAF

Within the bandwidth of the controllers:

$$\boldsymbol{\Delta Q_s} = \boldsymbol{K_Q}\hat{\boldsymbol{\omega}}_{\boldsymbol{C}} = \boldsymbol{K_Q}(\boldsymbol{\omega_C} - \bar{\omega}\mathbf{1}) \tag{4.10}$$

where $\hat{\boldsymbol{\omega}}_{\boldsymbol{C}} \in \mathbb{R}^{n\times 1}$ is the vector of the frequency deviations at the AC side of the converters with respect to the weighted-average frequency ($\bar{\omega}$), $\boldsymbol{K_Q} = \text{diag}(k_{Q,i}) \in \mathbb{R}^{n\times n}$ is the gain matrix and $\mathbf{1} \in \mathbb{R}^{n\times 1}$ is a column vector filled with ones. Manipulating $\dot{\mathcal{V}}_{ctr}$ in (4.9) to include the weighted-average frequency explicitly, gives:

$$\dot{\mathcal{V}}_{ctr} = \underbrace{-(\boldsymbol{M_Q^T}\hat{\boldsymbol{\omega}}_{\boldsymbol{G}})^T\boldsymbol{B_{Q,T}}\boldsymbol{\Delta Q_s}}_{\dot{\mathcal{V}}_{ctr,A}} + \underbrace{(\omega_{COI} - \bar{\omega})\mathbf{1}^T\boldsymbol{B_{Q,T}}\boldsymbol{\Delta Q_s}}_{\dot{\mathcal{V}}_{ctr,B}} \tag{4.11}$$

where $\hat{\boldsymbol{\omega}}_{\boldsymbol{G}} = \boldsymbol{\omega_G} - \bar{\omega}\mathbf{1}$ and $\mathbf{1} \in \mathbb{R}^{n_G\times 1}$ represents a column vector filled with ones.

In general, the relationship between the generator speeds and the bus frequencies is nonlinear and hard to obtain explicitly and an approximation will be used to be able to continue with the analysis. Since matrix $\boldsymbol{B_Q} = \boldsymbol{M_Q}\boldsymbol{B_{Q,T}}$ measures the effect of the Q injections of the VSCs on the electrical power of the generators, it will also be used to approximate the frequencies at the AC terminals of the VSC-MTDC system ($\hat{\boldsymbol{\omega}}_{\boldsymbol{C}}$) as a function of the generator speeds: $\hat{\boldsymbol{\omega}}_{\boldsymbol{C}} \simeq \boldsymbol{M_Q^T}\hat{\boldsymbol{\omega}}_{\boldsymbol{G}}$. Therefore, since $\boldsymbol{\Delta Q_s} = \boldsymbol{K_Q}\hat{\boldsymbol{\omega}}_{\boldsymbol{C}}$ in strategy Q-WAF, (4.11) leads to:

$$\dot{\mathcal{V}}_{ctr} \simeq \underbrace{-\hat{\boldsymbol{\omega}}_{\boldsymbol{C}}^{\boldsymbol{T}}(\boldsymbol{B_{Q,T}}\boldsymbol{K_Q})\hat{\boldsymbol{\omega}}_{\boldsymbol{C}}}_{\dot{\mathcal{V}}_{ctr,A}} + \underbrace{(\omega_{COI} - \bar{\omega})\mathbf{1}^T(\boldsymbol{B_Q}\boldsymbol{K_Q})\hat{\boldsymbol{\omega}}_{\boldsymbol{C}}}_{\dot{\mathcal{V}}_{ctr,B}} \tag{4.12}$$

Since $\boldsymbol{B_{Q,T}}$ and $\boldsymbol{K_Q}$ are non-negative diagonal matrices, $\dot{\mathcal{V}}_{ctr,A}$ is a (negative) quadratic form of $\hat{\boldsymbol{\omega}}_{\boldsymbol{C}}$ and, hence, it is non-positive. Unfortunately, the sign of $\dot{\mathcal{V}}_{ctr,B}$ will be, in general, unknown. However, $\dot{\mathcal{V}}_{ctr,B}$ is a linear function of $\hat{\boldsymbol{\omega}}_{\boldsymbol{C}}$ whilst $\dot{\mathcal{V}}_{ctr,A}$ is a quadratic function of the same variable. Therefore, the absolute value of the former is expected to be smaller than the one of the latter (above all for large deviations of the frequency with respect the weighted-average frequency $\hat{\boldsymbol{\omega}}_{\boldsymbol{C}}$ which implies large modulation $\boldsymbol{\Delta Q_s}$). Furthermore, since the weighted-average value of the converter frequencies

$\bar{\omega}$ and $\omega_{COI}$ can be expected to change more slowly than the converter output frequencies. It can also be expected that $(\bar{\omega} - \omega_{COI})$ will grow more slowly than $|\hat{\boldsymbol{\omega}}_{\boldsymbol{C}}|$ (and $|\boldsymbol{\Delta Q_s}|$). Hence, $\dot{\mathcal{V}}_{ctr,B}$, even if positive, should never outweigh the negative value of $\dot{\mathcal{V}}_{ctr,B}$. Besides, if possible, the weights $\alpha_k$ should be calculated so that $\bar{\omega} \simeq \omega_{COI}$ and, therefore, $\dot{\mathcal{V}}_{ctr,B} \simeq 0$. Under these circumstances, the total $\dot{\mathcal{V}}_{ctr}$ will be non-positive too and the control strategy Q-WAF would improve transient stability.

The approximation $\hat{\boldsymbol{\omega}}_{\boldsymbol{C}} \simeq \boldsymbol{M}_{\boldsymbol{Q}}^{\boldsymbol{T}} \hat{\boldsymbol{\omega}}_{\boldsymbol{G}}$ used to derive (4.12) from (4.11) calculates the frequency at the AC side of each converter station $i$ as a function of the speeds of the generators, asigning a weight $m_{Q,ki}$ to the speed of each generator $k$:

$$\hat{\omega}_i \simeq \hat{\omega}_i^{est} = \sum_{k=1}^{n_G} m_{Q,ki} \hat{\omega}_{G,k} \tag{4.13}$$

This assumption only gives a rough approximation of the frequencies at the AC side of the converters, based on intuition. Simulation results support this assumption, but it could not be proved theoretically. Although the accuracy of this approximation may be questionable, it has been observed, from simulation results, that the sign the frequency deviation of a VSC converter with respect to the weighted-average frequency has almost always the same sign as the approximation given by (4.13). Hence, the expression of the derivative $\dot{\mathcal{V}}_{ctr}$ (4.11) can be written again, assuming strategy Q-WAF and without including the approximation, as:

$$\dot{\mathcal{V}}_{ctr} = \underbrace{-(\hat{\boldsymbol{\omega}}_{\boldsymbol{C}}^{\boldsymbol{est}})^T (\boldsymbol{B_{Q,T} K_Q}) \hat{\boldsymbol{\omega}}_{\boldsymbol{C}}}_{\dot{\mathcal{V}}_{ctr,A}} + \underbrace{(\omega_{COI} - \bar{\omega}) \mathbf{1}^T (\boldsymbol{B_Q K_Q}) \hat{\boldsymbol{\omega}}_{\boldsymbol{C}}}_{\dot{\mathcal{V}}_{ctr,B}} \tag{4.14}$$

where $\hat{\boldsymbol{\omega}}_{\boldsymbol{C}}^{\boldsymbol{est}} = \boldsymbol{M}_{\boldsymbol{Q}}^{\boldsymbol{T}} \hat{\boldsymbol{\omega}}_{\boldsymbol{G}}$.

From (4.14), $\dot{\mathcal{V}}_{ctr,A}$ can be written explicitely as:

$$\dot{\mathcal{V}}_{ctr,A} = -\sum_{i=1}^{n} (b_{Q,T,i} k_{Q,i}) \hat{\omega}_i^{est} \hat{\omega}_i \tag{4.15}$$

which proves that if $\hat{\omega}_i^{est}$ and $\hat{\omega}_i$ have the same sign, then $\dot{\mathcal{V}}_{ctr,A}$ is non positive, since the terms $b_{Q,T,i} k_{Q,i}$ are non negative.

**Strategy Q-LF**

Using this control strategy, the negativeness of $\dot{\mathcal{V}}_{ctr}$ cannot be guaranteed and its performance will be tested by simulation, only.

## 4.5 Results

The reactive-power control strategies presented have been tested by simulation in the modified Cigré Nordic 32A system with a 3-terminal VSC-MTDC system (see Section A.3) in the heavily loaded scenario (described in Appendix A.3.2). The operating point of the VSC-MTDC system is also reported in Section A.3. The PSS/E model reported in Chapter 2 has been used.

First of all, the following Q-control strategies will be analysed and compared with several faults:

- Q0: Constant reactive-power injection of each converter (no modulation).
- Q-LF: The reactive-power injection of each converter is controlled using the local frequency strategy.
- Q-WAF: The reactive-power injection of each converter is controlled using the weighted-average frequency of the VSC-MTDC system as the frequency set point.

The parameters used for the control strategies (Fig. 4.1) are $k_{Q,i} = 200$ p.u, $T_{f,i} = 0.1$ s, $T_{w,i} = 15$ s, $\Delta q_{max,i} = 1$ p.u and $\alpha_k = 1/3$. The gains are in nominal p.u of each converter.

### 4.5.1 Fault I

A 3-phase-to-ground short circuit has been applied to line 4031-4041a (at bus 4041) when $t = 1$ s. The fault is cleared by fully disconnecting the corridor (4031-4041 a and b) 300 ms later (Fault I, for short).

The rotor-angle difference between machines 4012 (North) and 4062 (South) is shown in Figure 4.2. Synchronism is lost with no Q modulation (Q0) and when using strategy Q-LF, while strategy Q-WAF stabilises the system.

Q injections of the VSC stations into the AC grid are shown in Figure 4.3. With strategy Q-WAF, Q injections are modulated successfully. The reactive power of converter VSC1 reaches its upper limit (+450 MVAr) during less

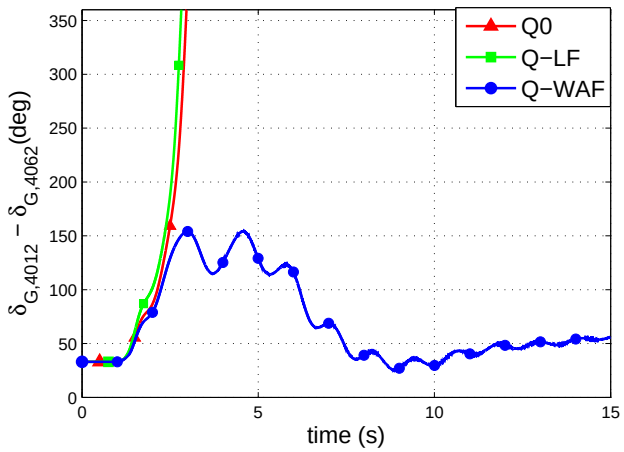


Figure 4.2: Fault I cleared after 300 ms. Generator angle difference.

than a second ($t = 2.1$ s). Meanwhile, strategies Q0 and Q-LF produce no beneficial effect and they cannot maintain stability. In the latter case, the converter reactive-power limits are reached most of the time. All Q injections with strategy Q-LF are positive initially ( Fig. 4.3) because the three frequencies measured at the VSCs increase. However, with strategy Q-WAF, VSCs only inject Q at the points with larger frequency growth (those above the average).

The critical clearing time (CCT) for this fault using strategy Q0 is 105 ms; it is 0 ms (unstable) using Q-LF and improves to 370 ms with Q-WAF. A CCT of 0 ms (when using Q-LF) means that the system loses synchronism when corridors 4031-4041 a and b are tripped, even if there is no short circuit. Therefore, increasing the electromagnetic torque in all the AC buses is not the best option (even if frequency is rising); one should only act upon those with the larger frequency growth, with the purpose of slowing them down [156].

Finally, an approximation of the derivatives in (4.11) using strategy Q-WAF are shown in Fig. 4.4 and they were found similar and negative in strategy Q-WAF, except in a limited number of points during the simulations. Although stability is not rigorously guaranteed, none of the simulated cases was found to be problematic.

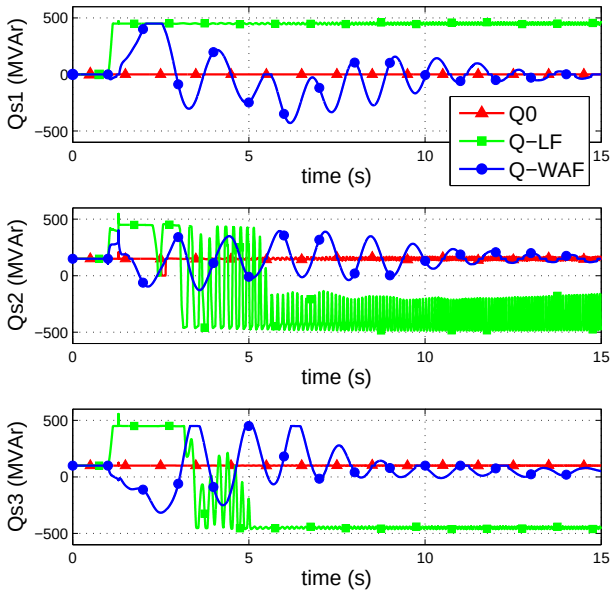


Figure 4.3: Fault I cleared after 300 ms. Q injections ($Q_{s,i}$).

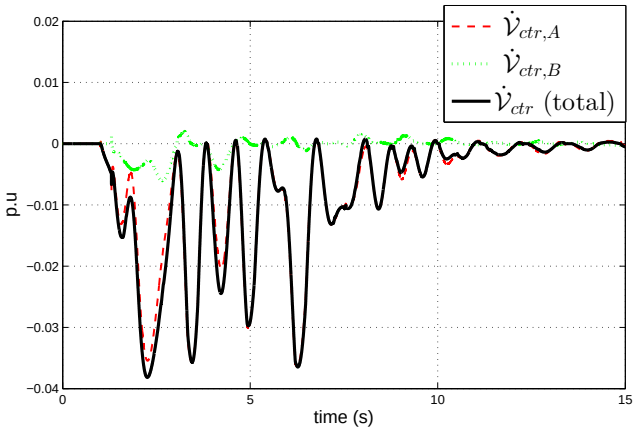


Figure 4.4: Q-WAF. Derivatives in (4.11). Base: 100MVA, 100$\pi$ rad/sec.

### 4.5.2 Critical clearing times (CCTs)

Several faults have been simulated (see Table 3.2 of Chapter 3). The CCTs of each fault have been obtained for the base case (Q0) and for control strategies Q-LF and Q-WAF (see Table 4.1). Results show strategy Q-WAF increases the CCTs significantly. Furthermore, results show that local strategy Q-LF produces very poor results. Therefore, the latter strategy is discarded for transient-stability support.

Table 4.1: CCTs for simulated faults.

| Fault | Q0 CCT (ms) | Q-LF CCT (ms) | Q-WAF CCT (ms) |
|---|---|---|---|
| Fault I | 105 | 0 | 370 |
| Fault II | 188 | 190 | 247 |
| Fault III | 237 | 225 | 253 |
| Fault IV | 390 | 344 | 564 |
| Fault V | 205 | 207 | 250 |

### 4.5.3 Impact of the control parameters

The impact of $k_{Q,i}$ and $\Delta q_{max,i}$ of strategy Q-WAF (Fig. 4.1) on the CCTs is investigated in Table 4.2. CCTs increase if gain values $k_{Q,i}$ are augmented, since gains $k_{Q,i}$ determine how much reactive power is modulated by each converter under a frequency error. Nevertheless, very large gains should not be used, because the converters may reach their reactive-power and/or current limits very often during contingencies. In this work, good results have been obtained with $k_{Q,i} = 200$ p.u. (nominal p.u's of the VSC stations). Naturally, higher values of $\Delta q_{max,i}$ will also produce higher values of the CCTs since each VSC will have a larger margin for its Q injection. However, TSOs may prefer to limit Q modulation in order to optimise other aspects of the system. The results of Table 4.2 show that reasonable improvements could be achieved with low values of the saturation parameter $\Delta q_{max,i}$. For example, if $\Delta q_{max,i} = 0.2$ p.u (nominal p.u's), the CCT of Fault I increases from 105 ms to 277 ms.

Table 4.2: Effect of parameters $k_{Q,i}$ and $\Delta q_{max,i}$ of Q-WAF.

| Q-WAF | CCT (ms) | | | | |
|---|---|---|---|---|---|
| $k_{Q,i}$ (p.u) ($\Delta q_{max,i} = 1$ p.u) | 0 | 50 | 200 | 500 | 1000 |
| Fault I | 105 | 171 | 370 | 390 | 423 |
| Fault II | 188 | 209 | 247 | 260 | 264 |
| Fault III | 237 | 242 | 253 | 263 | 268 |
| Fault IV | 390 | 483 | 564 | 554 | 550 |
| Fault V | 205 | 222 | 250 | 262 | 266 |
| $\Delta q_{max,i}$ (p.u) ($k_{Q,i} = 200$ p.u) | 0 | 0.1 | 0.2 | 0.5 | 1.0 |
| Fault I | 105 | 203 | 277 | 306 | 370 |
| Fault II | 188 | 202 | 214 | 242 | 247 |
| Fault III | 237 | 242 | 248 | 253 | 253 |
| Fault IV | 390 | 435 | 486 | 557 | 564 |
| Fault V | 205 | 216 | 226 | 247 | 250 |

### 4.5.4 Comparing with strategy Q-CLF

In [49], control strategies for the active- and reactive-power injections of a VSC-MTDC system for transient stability improvement were proposed. In that approach, the control laws were also derived using Lyapunov theory and they make use of global measurements: the speed deviation of each generator of the system with respect to the synchronous speed ($\boldsymbol{\Delta\omega_G}$). Good results were obtained in [49]. However, P or Q control strategies were evaluated simultaneously and the effect of either P and Q modulation, separately, was not studied. In this section, control strategy Q-WAF will be compared with the reactive-power control strategy proposed in [49] (Q-CLF, for short), in which reactive-power set points are computed as:

$$\boldsymbol{\Delta Q_s^{ref}} = \boldsymbol{K'_Q}(\boldsymbol{B_Q^0})^{\boldsymbol{T}}\boldsymbol{\Delta\omega_G} = \boldsymbol{K_Q}(\boldsymbol{M_Q^0})^{\boldsymbol{T}}\boldsymbol{\Delta\omega_G} \tag{4.16}$$

where $\boldsymbol{B_Q^0} = \boldsymbol{M_Q^0 B_T^0}$ is the one defined in Section 4.4.1 evaluated at the operating point. The gain matrix $\boldsymbol{K_Q} = \boldsymbol{K'_Q B_T^0}$ has been defined in order to be able to compare the results with Q-WAF, using the same gains.

The same scheme (Fig. 4.1) and parameters have been used for the comparison of Q-WAF and Q-CLF and only the input signal has been changed.

Results in Table 4.3 show that strategy Q-WAF, proposed in this chapter, produces better results than Q-CLF. Probably, the main improvement on angle stability against large disturbances in [49] was due to the active-power strategy and not to the reactive-power strategy. Besides, using 1 p.u as the frequency set point (like in Q-CLF) has clear limitations. For example, in faults that produce acceleration of all generators, the use of the weighted-average frequency of several buses of the grid makes it possible to slow down some generators, while others are accelerated, in order to reduce the transient angle separation. Last but not least, strategy Q-WAF requires frequency measurements at the VSC stations, which are always available for synchronisation purposes, while Q-CLF requires global measurements of all the machines of the system and, therefore, requires an additional measurement system.

Table 4.3: CCTs obtained with two Q-based strategies.

| Fault | Q0 CCT (ms) | Q-WAF CCT (ms) | Q-CLF CCT (ms) |
|---|---|---|---|
| I | 105 | 370 | 0 |
| II | 188 | 247 | 193 |
| III | 237 | 253 | 228 |
| IV | 390 | 564 | 344 |
| V | 205 | 250 | 211 |

## 4.6 The effect of communication latency

Since strategy Q-WAF uses global measurements, the effect of the communication latency was also investigated introducing a delay in the frequency at terminal $i$ measured by VSC $j$ ($\omega_i^j$):

$$\omega_i^j = \omega_i e^{-\tau_{ij} s},\ \tau_{ij} = \tau_{ij}^0 + \tau_{ij}^X = \tau_{ij}^0 \pm \Delta\tau, \tag{4.17}$$

where $\tau_{ij}^0$ is a constant value ($\tau_{ii}^0 = 0$ for $i = j$) and $\tau_{ij}^X$ is a stochastic random variable which follows a triangular distribution with upper/lower limits $\pm\Delta\tau$ and centred at zero. The delay was implemented in PSS/E using a second-order Padé's approximation.

The impact of the communication latency is illustrated in Fig. 4.5, where

simulation results of Fault I cleared after 150 ms are shown. As the communication latencies are greater, the rotor-angle difference of generators 4012 and 4062 are greater during the transient, leading to the loss of synchronism for latencies of $150 \pm 20$ ms. Therefore, the greater the communication latency is, the more difficult is for strategy Q-WAF to improve transient stability.

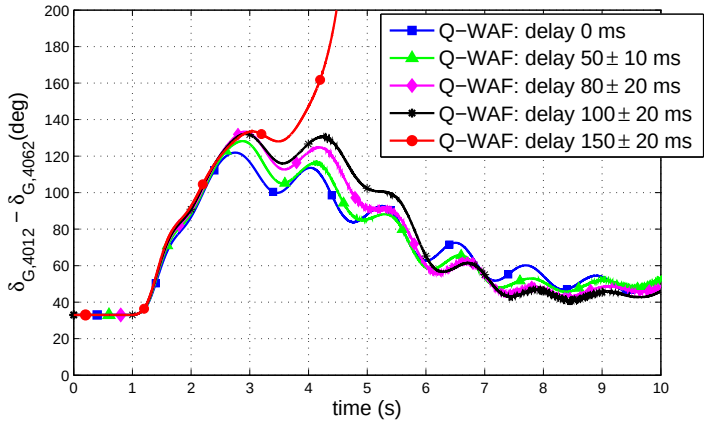


Figure 4.5: Generator angle difference: Fault I cleared after 150 ms.

The CCTs of faults I-V obtained for different latency values when using strategy Q-WAF are provided in Table 4.4. CCTs are increased significantly when using Q-WAF, although the improvement deteriorates, in most cases, as the communication delay increases. The effect of the communication delay is most noticeable in Fault I (a severe fault) although the CCT obtained in the worst case (139 ms) is still greater than the CCT in the base case Q0 ( 105 ms). CCTs in other faults are only marginally affected by communication latency. Surprisingly, the measurement delay has a different pattern in Fault IV, but this is the only case found during the simulation work carried out.

Table 4.4: CCTs for simulated faults.

| Fault | Q0 CCT (ms) | Q-WAF delay=0 CCT (ms) | with delay $50 \pm 10$ms CCT (ms) | $80 \pm 20$ms CCT (ms) | $100 \pm 20$ms CCT (ms) | $150 \pm 20$ms CCT (ms) |
|---|---|---|---|---|---|---|
| Fault I | 105 | 370 | 320 | 192 | 171 | 139 |
| Fault II | 188 | 247 | 235 | 228 | 225 | 215 |
| Fault III | 237 | 253 | 248 | 246 | 243 | 241 |
| Fault IV | 390 | 564 | 581 | 591 | 603 | 781 |
| Fault V | 205 | 250 | 240 | 233 | 231 | 224 |

## 4.7 Comparing active- and reactive-power control

The control strategy proposed in this chapter (Q-WAF) is similar to the control strategy proposed in Chapter 3 (P-WAF), but the latter modulates the P injections at the VSC stations whereas Q-WAF modulates the Q injections at the VSC stations. In both cases, the weighted-average frequency (WAF) seen by the converters was used as the frequency set point.

The CCTs of faults I-V, obtained with P-WAF and Q-WAF, are reported in Table 4.5. The same parameter values are used for P-WAF and Q-WAF control strategies (described at the beginning of Section 4.5). For example, teh same gain values are used for P and Q modulation: $k_{P,i} = k_{Q,i} = 200$ p.u.

Both control strategies increase the CCTs, although they have some differences. For example, it seems that when the fault is severe and affects generators that are close to one of the VSC-MTDC stations, the P modulation is more powerful than Q modulation (see Fault I): the excess of active power is evacuated successfully during the transient through the VSC-MTDC system. Meanwhile, strategy Q-WAF seems to perform better when the fault affects generators which are far to the VSC stations (see Fault III). Furthermore, Table 4.5 shows that strategy Q-WAF seems to deteriorate more than strategy P-WAF when communication latencies are present, although a very reasonable performance is obtained, anyway. The last column of Table 4.5 shows the CCTs obtained using strategies P-WAF and Q-WAF simultaneously (PQ-WAF, for short). Although CCTs improve with respect to the cases using only one of the strategies, this improvement is not very spectacular.

As a conclusion, either strategy P-WAF, Q-WAF or PQ-WAF could be used succesfully to improve transient stability, increasing significantly the CCTs of different faults. Whether using P modulation, Q modulation or

both would depend of the required improvements for a set of faults of interest in a particular system. Furthermore, if similar results are obtained with strategies P-WAF, Q-WAF or PQ-WAF, using strategy Q-WAF has advantages, because Q injections of the converters in a VSC-MTDC systems are independent and bidirectional and, therefore, Q coordination would be always easier than P coordination in VSC-MTDC systems.

Table 4.5: CCTs obtained with P-WAF and Q-WAF.

| Fault | CCT (ms) Q0 | delay=0 CCT (ms) P-WAF, Q-WAF | | with delay $50 \pm 10$ms CCT (ms) P-WAF, Q-WAF | | delay $100 \pm 20$ms CCT (ms) P-WAF, Q-WAF | | delay=0 CCT (ms) P,Q-WAF |
|---|---|---|---|---|---|---|---|---|
| Fault I | 105 | 390, | 370 | 390, | 320 | 388, | 171 | 404 |
| Fault II | 188 | 224, | 247 | 224, | 235 | 224, | 225 | 259 |
| Fault III | 237 | 240, | 253 | 240, | 243 | 240, | 243 | 250 |
| Fault IV | 390 | 824, | 564 | 823, | 581 | 823, | 603 | 854 |
| Fault V | 205 | 235, | 250 | 235, | 240 | 235, | 231 | 261 |

## 4.8 Conclusions

The results presented in this chapter have shown that:

- The proposed strategy Q-WAF improves transient stability significantly.
- The advantage of the proposed strategy Q-WAF with respect to previous ones for VSC-MTDC systems is that it uses global measurements which are much easier to implement: it uses the weighted-average frequency of the AC terminals of the VSC-MTDC system, while previous approaches use global mesurements of the speeds of all the generators of the system.
- In general, higher gains in strategy Q-WAF produce better results, although converter limits must be considered. A compromise must be reached. Good results were obtained with $k_{Q,i} = 200$ p.u.
- Results showed that strategy Q-WAF produces good results for realistic values of the communication delays. However, strategy Q-WAF deteriorates with communication latency more easily than strategy P-WAF (of Chapter 3).

- Most often, modulating either P injections (with P-WAF), Q injections (with Q-WAF) or both (PQ-WAF) produce comparable improvements on the CCTs.
  - For faults located in power paths which are in parallel to the VSC-MTDC system, P-WAF proved to be more effective than Q-WAF.
  - Meanwhile, strategy Q-WAF was able to increase the CCTs of some remote faults on which strategy P-WAF had little impact.
  - In general, the results are further improved when modulating P and Q injections simultaneously (PQ-WAF), although the improvements are small, in comparison with the improvements achieved either with Q-WAF or with P-WAF, independently.
  - If similar results are obtained with the three strategies, strategy Q-WAF should be implemented, because Q injections of the VSC stations, unlike P injections, can be set independently.
- Local strategy Q-LF has been dismissed due to its poor contribution to transient stability improvement.

# Chapter 5

# Communication-free reactive-power control

## 5.1 Introduction

In this chapter, a local reactive-power control strategy for transient stability improvement will be derived based on the estimation of the weighted-average frequency of the converter stations of a VSC-MTDC system through an auxiliary active-power local control strategy. Therefore, the proposed algorithm tries to mimic strategy Q-WAF (proposed in Chapter 4), but by using local measurements, only.

The actual value of the reactive power delivered by one of the converters is not useful to obtain global information because it is independent of the reactive-power injections of the rest of the converters in the VSC-MTDC system. Nevertheless, the results of Chapter 3 showed that, under certain conditions, local control strategy P-LF could behave very much as strategy P-WAF, suggesting that some global measurements could be estimated without a communication system between the converters available. This is due to the interaction between the AC side control strategy and the DC-voltage droop control used in strategy P-LF. The latter will be used as an auxiliary active-power local controller to estimate the weighted-average frequency, which will be used as set poiny for the Q control strategy.

The proposed local strategy for Q injections of the converters in VSC-MTDC system is described in Section 5.2. The results are presented in Section 5.3. Finally, the conclusions are reported in Section 5.4.

## 5.2 Proposed control algorithm (Q-LWAF)

The strategy proposed in this section will aim at controlling reactive power (Q) based on an estimation of the weighted-average frequency based on local measurements, only (strategy Q-LWAF, for short). This imitates strategy Q-WAF (proposed in the previous chapter), but by using local measurements instead of global measurements. In order to achieve this, the local active-power control strategy P-LF presented in Chapter 3 will be implemented in each converter, using a small gain ($k_{P,i}$), in order to produce a small active-power modulation. The DC-voltage will act as a carrier signal and it will allow each converter to estimate the weighted-average speed of the MTDC, using local measurements of the frequency and DC-voltage at the converter station. The (small) supplementary active-power reference will be used to compute the frequency set point for the reactive-power control strategy, using the scheme used in strategy Q-WAF.

As shown in Subsection 3.4.1, in strategy P-LF (with a frequency set point of 1 p.u), if

$$k_{P,i} = g_i k_{P,T} \quad \Big( \Leftrightarrow \frac{k_{P,i}}{\sum_{j=1}^{n} k_{P,j}} = \frac{1/k_{dc,i}}{\sum_{j=1}^{n} (1/k_{dc,j})} \Big), \tag{5.1}$$

the total active-power supplementary set-point value is:

$$\Delta p^*_{s,i} \simeq k_{P,i}(\bar{\omega} - \omega_i) \tag{5.2}$$

Therefore, each converter can estimate the weighted-average frequency (using local measurements) as:

$$\bar{\omega}_{e,i} = \omega_i + \frac{\Delta p^*_{s,i}}{k_{P,i}} \simeq \bar{\omega} \tag{5.3}$$

where, for each converter $i$, $\omega_i$ is the frequency measurement, $\Delta p^*_{s,i}$ is the total P supplementary reference and $k_{P,i}$ is the gain used in strategy P-LF.

The estimated value $\bar{\omega}_{e,i}$ can be used by each VSC as a frequency set point for reactive-power modulation as it was used in Chapter 4. For estimation purposes, $k_{P,i} = g_i k_{P,T}$ need not be a big value. The control scheme of strategy Q-LWAF is shown in Fig. 5.1.

Since in strategy Q-LWAF the frequency set point is computed using internal signals already available from strategy P-LF (5.3), no additional field measurements are required to compute the supplementary reactive-power

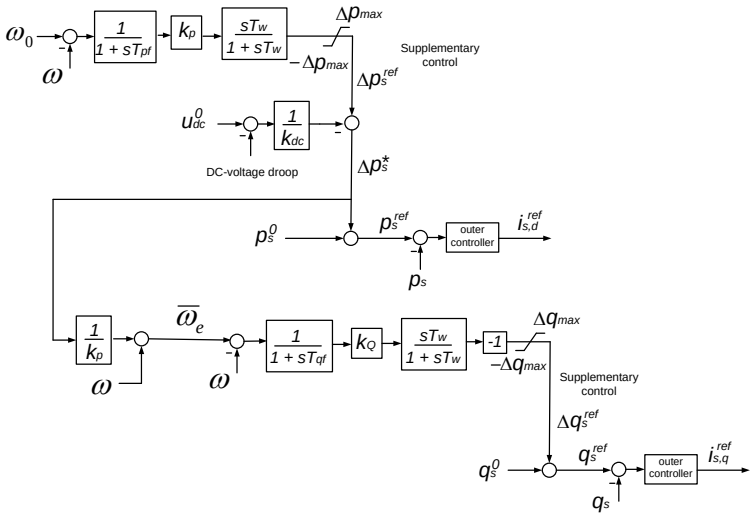


Figure 5.1: VSC control in Q-LWAF.

command. Therefore, the low-pass filter $T_{Qf}$ used for the reactive-power control scheme (Fig.5.1) could have a fast time constant ($\sim$ 10ms) or even eliminated.

## 5.3 Results

In this section, the performance of the proposed control strategy has been tested by simulation using PSS/E. The test system used is the same one used in previous Chapters: Nordic32A grid with a VSC-HVDC 3-terminal system in a heavily loaded scenario, as detailed in Section A.3.2. The operating point of the VSC-MTDC system is the same as in previous chapters and it is described in Section A.3.2. Different reactive-power (Q) control strategies will be investigated:

- Q0: Constant reactive-power injections.
- Q-WAF: Reactive-power injection based on the weighted-average frequency of the converter stations, with parameters: $k_{Q,i} = 200$ p.u, $T_{Qf,i} = 0.1$ s, $T_{w,i} = 15$ s, $\Delta q_{max,i} = 1$ p.u and $\alpha_k = 1/3$. The gains

are in nominal p.u. The frequency set point is the weighted-average frequency of the VSC-MTDC.

- Q-LWAF: Reactive-power injection based on the estimated weighted-average frequency of the converter stations using local measurements (Fig. 5.1), with parameters:
  - Q modulation: $k_{Q,i} = 200$ p.u, $T_{Qf,i} = 0.01$ s, $T_{w,i} = 15$ s, $\Delta q_{max,i} = 1$ p.u and $\alpha_k = 1/3$. The frequency set point is computed with (5.3).
  - P modulation: $k_{P,i} = 10$ p.u, $T_{Pf,i} = 0.1$ s, $T_{w,i} = 15$ s, $\Delta p_{max,i} = 1$ p.u and $k_{dc,i} = 0.1$ p.u. The frequency set point is $\omega_i^* = 1$p.u.

### 5.3.1 Fault I

A three-phase-to-ground short circuit has been applied to line 4031-4041a (close to bus 4041) at $t = 1$s and the fault was cleared after 300ms disconnecting both circuits of the corridor 4031-4041 a & b (Fault I). The results are shown in Figures 5.2-5.4.

The difference between the rotor angles of generators G4012 (North) and G4062 (South) is shown in Fig. 5.2a. Synchronism is lost for constant reactive-power control (Q0), whilst synchronism is maintained with global control strategy Q-WAF and with the local control strategy proposed in this Chapter Q-LWAF, producing both a very similar response.

The reactive-power injections of the converters are shown in Fig 5.3a. In Q-WAF and Q-LWAF, during the transient, the reactive-power injection is increased (reduced) in those terminals with frequency above (below) the weighted-average frequency of the MTDC system, slowing down (accelerating) nearby generators. Fig. 5.3a shows that the reactive-power modulation produced by strategy Q-LWAF is very similar to the one produced by strategy Q-WAF. The latter uses the weighted-average frequency as frequency set point, while the former estimates that signal by using local measurements at each converter station, thanks to the (small) active-power modulation produced by strategy P-LF, which can be seen in Fig. 5.4. The weighted-average frequency estimated by VSC1 ($\bar{\omega}_{e,1}$), using (5.3), is compared with the true weighted-average frequency of the MTDC system ($\bar{\omega}$) in Fig 5.2b, showing good agreement. Some high-frequency oscillations appear in the estimated signal $\bar{\omega}_{e,i}$ due to the DC-grid dynamics (see the inset of Fig. 5.2b).

Finally, the DC-voltages of the DC grid are shown in Fig 5.3b. In the base case (Q0) and with strategy Q-WAF, the DC-voltages remain almost

constant, while strategy Q-LWAF produce DC-voltage deviations during the transient. Therefore, gains $K_{P,i}$ of strategy P-LF (in Q-LWAF, Fig. 5.1) should be small enough to ensure admissible DC-voltage fluctuations during the transient.

The CCTs obtained for Fault I with strategies Q0, Q-WAF and Q-LWAF are 105 ms, 370 ms and 379 ms, respectively. Therefore, a significant improvement can be achieved with the proposed local strategy Q-LWAF and the improvement is comparable with the one obtained with global strategy Q-WAF. In fact, the CCT obtained with Q-LWAF is slightly longer than the one obtained with Q-WAF, due to the contribution of the auxiliary P modulation (P-LF).

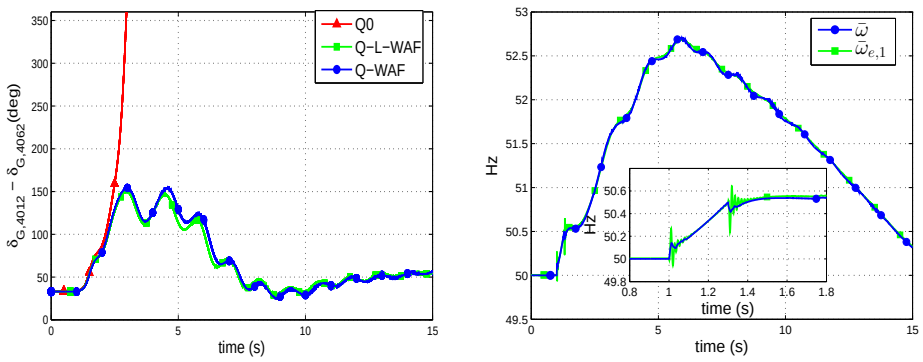


(a) (b)

Figure 5.2: Fault I cleared after 300 ms. (a) Generator angle diff. (b) Q-LWAF: weighted-average frequency: true ($\bar{\omega}$) and estimated by VSC1 ($\omega_{e,1}$).

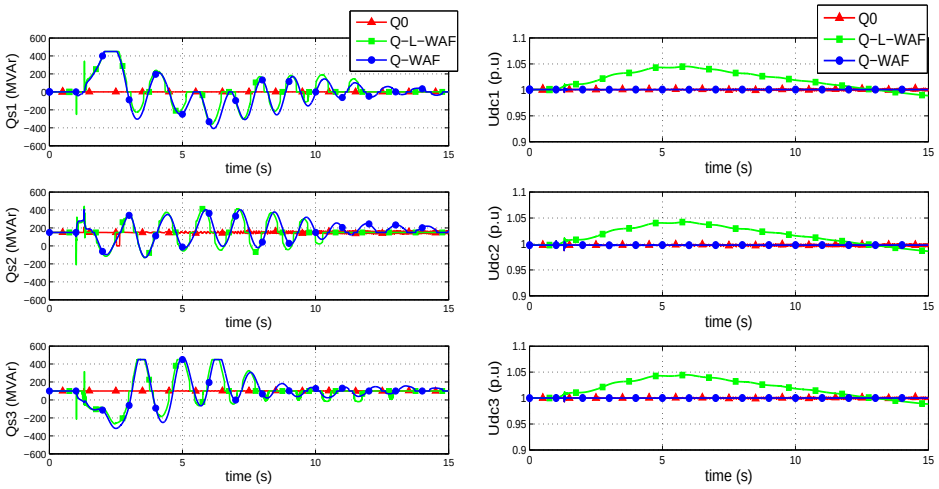


(a) Q injections ($Q_{s,i}$) (b) DC voltages ($u_{dc,i}$)

Figure 5.3: Fault I cleared after 300 ms.

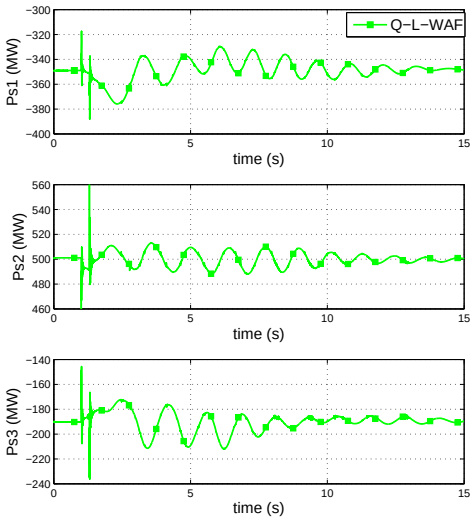


Figure 5.4: Fault I cleared after 300 ms. P injections ($P_{s,i}$) in Q-LWAF.

### 5.3.2 Fault II

Since local strategy Q-LWAF uses P modulation to estimate the weighted-average frequency, it is essential to evaluate its robustness when a converter reachs its current limit during the transient. In this situation, the auxiliary P modulation, P-LF, would change its behaviour and, therefore, the estimation of the weighted-average frequency would be affected.

A solid short circuit at bus 4012 of line 4012-4022 has been simulated (Fault II). The fault was cleared disconnecting the line after 120 ms. Notice that the short circuit occurs at the AC bus of VSC1. The results are shown in Figs. 5.5-5.7.

The rotor-angle difference between generators G4012 and G4062 is shown in Fig. 5.5a. Synchronism is maintained in all the cases. The most critical case is with no Q modulation (Q0), which presents the largest angle separation during the transient. The most favorable case is using strategy Q-WAF, which produces the smallest angle separation between the generators, although a similar response is achieved using local strategy Q-LWAF.

After the fault clearing, the reactive-power modulations produced when using Q-WAF and Q-LWAF are similar (Fig. 5.6a) and, therefore, similar effect on the rotor angles is achieved. However, Q injections when using strategies Q-WAF and Q-LWAF behave differently during the fault (from $t = 1$ s to 1.12 ), because VSC1 reachs its current limit. Since VSC1 reaches its current limit and its P injection is reduced to zero, as shown in Fig. 5.7. Hence, in strategy Q-LWAF, VSC1 is not able to use the auxiliary P modulation (strategy P-LF) during the instants when it is blocked. As a result, the weighted-average frequency cannot be estimated correctly during $t = 1 - 1.12$ s, as shown in Fig. 5.5b. Despite this inaccuracy in the estimation of the average frequency during the fault, strategy Q-LWAF still improves transient stability.

The CCTs obtained for Fault II with strategies Q0, Q-WAF and Q-LWAF are 188 ms, 247 ms and 214 ms, respectively. For the reasons already discussed (the current limiter), the improvement obtained with strategy Q-LWAF is worse than the one obtained with strategy Q-WAF (although it is useful).

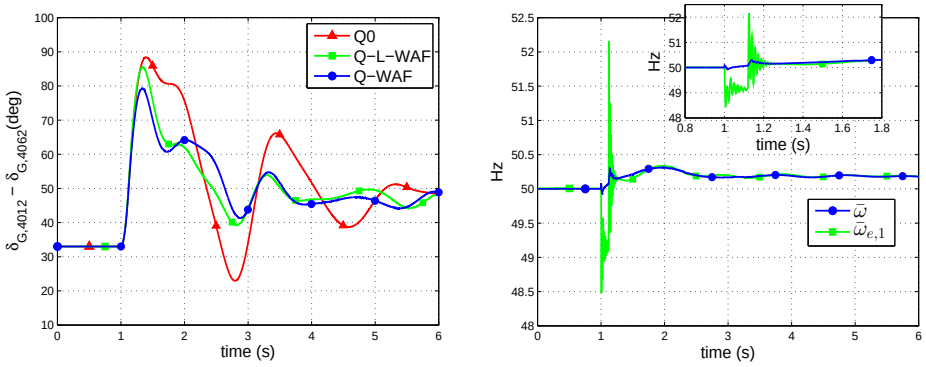


(a) (b)

Figure 5.5: Fault II cleared after 120 ms. (a) Generator angle diff. (b) Q-LWAF: weighted-average frequency: true ($\bar{\omega}$) and estimated by VSC1 ($\omega_{e,1}$).

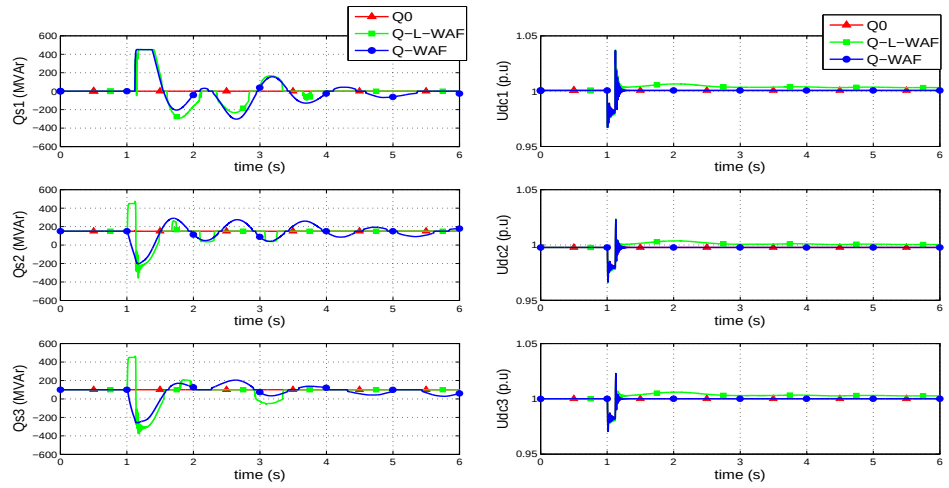


(a) Q injections ($Q_{s,i}$) (b) DC voltages ($u_{dc,i}$)

Figure 5.6: Fault II cleared after 120 ms.

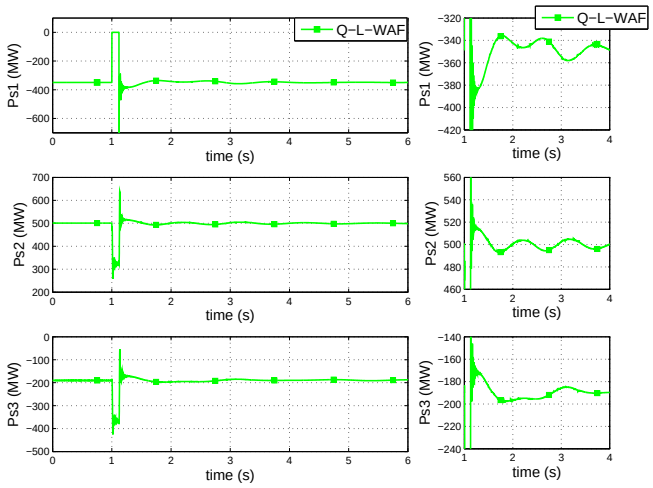


Figure 5.7: Fault II cleared after 120 ms. P injections ($P_{s,i}$) in Q-LWAF.

### 5.3.3 Critical clearing times

Several faults (described in Table 3.2 of Chapter 3) have been simulated and their CCTs have been evaluated and collected in Table 5.1. Both strategies, global Q-WAF and local Q-LWAF, increase the CCTs in comparison with the base case Q0. For some faults, the CCT is increased significantly. For example, the CCT of Fault I is increased from 105 ms to 370 ms with Q-WAF and to 379 ms with Q-LWAF (similar numbers in both strategies). As already pointed out in Section 5.3.1, a slightly longer CCT is obtained with the latter, due to the (small) help of the active-power modulation produced by the built-in strategy P-LF.

Different conclusions are drawn for Faults II and IV. The CCTs of these faults are also increased with strategies Q-WAF and Q-LWAF, but the best results are obtained with the former. These faults have in common that they are very close to the converters and the current limit of some converters are reached during the short circuit. During the time when the limits are reached, the converters do not estimate the weighted-average frequency properly with the local strategy Q-LWAF and better results are obtained using global measurements (Q-WAF). Nevertheless, local Q-LWAF proves to be robust and good results were also obtained.

Table 5.1: CCTs for simulated faults

| Fault | DC0 CCT (ms) | global Q-WAF CCT (ms) | local Q-LWAF CCT (ms) |
|---|---|---|---|
| Fault I | 105 | 370 | 379 |
| Fault II | 188 | 247 | 214 |
| Fault III | 237 | 253 | 253 |
| Fault IV | 390 | 564 | 540 |
| Fault V | 205 | 250 | 225 |

## 5.4 Conclusions

The results presented in this chapter have shown that:

- The proposed local reactive-power control strategy (Q-LWAF) improves transient stability significantly.
- Local strategy Q-LWAF behaves similar to the global strategy Q-WAF (poposed in Chapter 4).
- The advantage of strategy Q-LWAF is that, unlike Q-WAF, only local measurements at the converter stations are required.

# Chapter 6

# Modelling of VSC-MTDC systems for small-signal angle stability analysis

## 6.1 Introduction

The purpose of this chapter is to derive a linearised model of VSC-MTDC systems suitable for small-signal angle stability analysis of large power systems, which will be used in Chapter 7 to analyse control strategies for power-oscillation damping.

The rest of this chapter is organised as follows. Section 6.2 presents a review of previous work on modelling of VSC-MTDC systems for small-signal stability analysis. The proposed small-signal model is described for the whole model in Section 6.3, while the details of each component are described in Appendix D. The proposed small-signal model is validated by time-domain simulation and by eigenvalue comparison in sections 6.5 and 6.6, respectively. Small-signal analysis of the Nordic32A test system with an embedded VSC-MTDC system is carried out in Section 6.7. Finally, a summary is presented in Section 6.8.

## 6.2 Review of previous work

Due to the potential relevance of VSC-HVDC systems in future power systems, TSOs are eager to understand their possible effects on the overall system stability. This interest has motivated a good number of studies of Small Signal Analysis (SSA) of VSC-MTDC systems lately.

A small-signal model for VSC-MTDC systems was first proposed in [165] and similar approaches were proposed later in [115, 141, 166, 167]. Furthermore, SSA techniques have been applied to VSC-MTDC systems to design the parameters of the outer controllers of the VSCs [115, 166, 168] and the DC-voltage droop constants [112, 113, 117, 141, 167], to analyse the impact of DC-cable modelling on small-signal stability [112, 130, 131, 169–171], to investigate small-signal models for VSC stations with MMC technology [118, 172–175] and for angle stability analysis of hybrid HVAC/VSC-HVDC systems [72, 74–76, 176, 177]. All those models of VSC-MTDC systems for SSA have in common that the VSCs and the HVDC grids are subsystems of the main state-space system. Those subsystems must be changed, dependig of the controllers used, the VSC technology, the DC-cable modelling details or the level of detail required for different studies.

The main aspects to be taken into account for small-signal modelling of VSC-MTDC systems with the purpose of angle-stability analysis are discussed below:

- Type of models
  As in non-linear time-domain simulation, the linearised model of a hybrid HVAC/VSC-HVDC system can be of either electromagnetic type or electromechanical type. In electromagnetic models, the HVAC grids are represented with the differential equations of the lines and detailed models of the VSC-MTDC systems are used, while in electromechanical models, the dynamics of the HVACs grid are assumed instantaneous (phasors) and the VSC-MTDC systems can neglect some fast dynamics. The VSC-MTDC linearised models in [112, 113, 115, 117, 118, 167, 169–175] are of electromagnetic type and the ones in [72, 74–76, 166, 168, 176, 177] are of electromechanical type.

  Electromechanical models are suitable for small-signal angle stability analysis, in which the time-frame of interest is of the order of 10 to 20 s [31]. Naturally, electromagnetic models could also be used to study slow dynamics, but the order of the system would be unnecessarily high.

- VSC stations

In the linearised models proposed in [165–167,178] and [115] every VSC is prepresented with its inner and outer controllers. The PLL of every VSC is included in the model in [115, 165, 178], whilst it is neglected in [166, 167]. In principle, VSC stations can be modelled regardless the technology used (e.g. 2-level VSC, MMC, etc...). However, recent studies have shown that MMC technology adds new dynamics to the problem, which might be important or not, depending on the dynamics of interest of the study [118, 172–175]. Furthermore, the study of [118] showed that sometimes the dynamics of MMC stations could have an impact on the stability of VSC-MTDC systems controlled with DC-voltage droop.

In angle-stability studies of conventional power systems, the dynamics of interest are slow in comparison with the dynamics of VSC stations and these studies only make sense if the embedded VSC-MTDC system is stable. Therefore, reduced-order electromechanical models for the VSC stations can be used for small-signal angle stability analysis, neglecting some fast dynamics of the VSCs, as done in [72, 74–76, 177]. The inner current loops of the VSCs are represented in detail in [72, 74, 177], the closed-loop systems of the inner current controllers are assumed instantaneous in [75] and the details of the VSC-MTDC model used in [76] are not provided in the paper. In this thesis, the outer control loops of the VSCs have been modelled in detail, but the closed loop of the inner current control systems have been approximated by a first-order system, due to their fast dynamics in comparison with the electromechanical oscillations.

- HVDC grids
  The most simplified linearised models do not represent the HVDC grids [75], which means that the whole DC grid is seen as an aggregated capacitor and the VSCs are seen by the AC grid as power injections. In [166], the equivalent DC-side capacitor of each VSC is represented at each bus of the DC grid and the DC lines are represented as resistances, neglecting their inductances and charging capacitances. The most common approach is to model the HVDC grid with equivalent capacitors at the DC buses (including the equivalent capacitors of the VSCs and the total shunt capacitances of the DC lines connected to each bus), while each DC branch is modelled by a resistance plus an inductance [72, 74, 165, 177]. This is the approach used in this thesis.

  Recent studies have investigated higher-order models for the DC cables,

to improve the accuracy of the model [112,130,131,169–171]. According to those studies, the lumped $\pi$-section representation of the DC lines can introduce innacuracies into the SSA. The work in [169] proposed a detailed linear state-space model for the DC cables, dividing the DC cable into several sections and each section with additional parallel branches. Results showed that this model is more accurate than the lumped $\pi$-section representation. However, the dynamics neglected in the lumped $\pi$-section representation will only be relevant in very long cables and when high-frequency effects are of interest [131]. In fact, it is generally accepted that the lumped $\pi$-section model for the DC cables is suitable for angle stability studies. The SSA model developed in this thesis also admits DC cables modelled as in [169] (simply by defining additional DC branches and DC buses, to model the additional parallel branches and sections of each cable, respectively), which could be used if faster dynamics were of interest.

- Formulation
  The studies in [115, 117, 165–168] described VSC-MTDC models for SSA and they presented the guidelines to obtain the state-space representation of a hybrid HVAC/VSC-HVDC system. However, none of those publications formulated the complete state-space model of a general hybrid HVAC/VSC-HVDC system explicitly. A generalised small-signal model for an arbitrary HVAC/VSC-HVDC system will be presented in this Chapter. Details of the models of each component are presented in Appendix D.

- Simulation tools
  Since VSC-HVDC technology is relatively new and it is still evolving, SSA of hybrid HVAC/VSC-HVDC systems is not possible in all commercial tools for power-system analysis. For example, SSA of hybrid HVAC/VSC-HVDC grids can be carried out in PowerFactory (DigSilent) or EUROSTAG, but not in PSS/E. However, Refs. [176,179,180] analysed the fidelity of the SSA provided by PowerFactory (DigSilent) when considering hybrid HVAC/VSC-HVDC systems, identifying some unexplained results, which will be discussed in this Chapter of the thesis.

A generalised model for small-signal angle stability analysis for hybrid HVAC/VSC-HVDC systems has been formulated, implemented and validated in this work and will be reported in this Chapter. The model is of

electromechanical type (for angle stability studies) and the simplifications used are the same ones as in Section 2.4.1 of Chapter 2. No new contribution has been made regarding the modelling of the different components of VSC-MTDC systems (e.g. VSC stations, DC grids, etc...) which have been modelled following the guidelines proposed previously in the literature. Nevertheless, the proposed small-signal model has the following characteristics that have not been addressed before:

- The generalised formulation can address a hybrid HVAC/VSC-HVDC system with arbitrary topology. For example, the system could have several asynchronous HVAC grids. Besides, all the different VSC-MTDC systems interconnecting different HVAC grids or embedded in a meshed HVAC grid; and the different control operation modes of the VSCs have been included in the model.
- The model has been written with a modular structure, so that any subsystem can be changed without changing the main core.
- A systematic procedure to include the VSC-MTDC models in a small-signal tool for large HVAC systems already available has been made available.
- Supplementary controllers for angle stability improvement have been included in the model.

The linearised model for VSC-MTDC systems has been incorporated in Small-Signal Stability Toolbox (SSST), which is a matlab-based tool for small-signal analysis of large power systems previously developed in IIT [181]. The tool has been validated against a detailed electromagnetic simulator (Matlab + Simulink + SimPowerSystems) and the results have been compared to the results provided by PowerFactory. Finally, the flexibility of the tool has been illustrated in a modified Cigré Nordic32A test system with an embedded VSC-MTDC system.

## 6.3 Small-signal model: HVAC/VSC-HVDC grid

Hybrid HVAC/VSC-HVDC grids consist of the following main components:

- HVAC grids
  - Generators, governors and exciters.
  - Non-conventional generators, induction motors and series and shunt FACTS devices.
  - Electrical elements of the AC grid, such as lines or shunt elements (assumed to be quasi-static).
  - Loads: Typically they are assumed to be quasi-static (constant impedance, constant power or constant current), although some specific loads may be represented by dynamic models.
- VSC-MTDC systems
  - VSC stations
  - HVDC grid

The linearised model of a hybrid HVAC/VSC-HVDC system will be derived following the procedure of [181] and will include all the elements mentioned above.

Firstly, an HVAC grid without VSC-MTDC systems must considered. For the analysis, voltages and current injections at the AC buses are written in a common synchronous reference frame ($D-Q$ axes):

$$\begin{aligned} \bar{v}_i &= v_{D,i} + jv_{Q,i}, \\ \bar{i}_i &= i_{D,i} + ji_{Q,i}. \end{aligned} \tag{6.1}$$

The vectors of increments of the current injections and voltages are, therefore, written as:

$$\boldsymbol{\Delta v_{AC}} = \begin{bmatrix} \begin{bmatrix} \Delta v_{D,1} \\ \Delta v_{Q,1} \end{bmatrix} \\ \vdots \\ \begin{bmatrix} \Delta v_{D,n_{AC}} \\ \Delta v_{Q,n_{AC}} \end{bmatrix} \end{bmatrix}, \quad \boldsymbol{\Delta i_{AC}} = \begin{bmatrix} \begin{bmatrix} \Delta i_{D,1} \\ \Delta i_{Q,1} \end{bmatrix} \\ \vdots \\ \begin{bmatrix} \Delta i_{D,n_{AC}} \\ \Delta i_{Q,n_{AC}} \end{bmatrix} \end{bmatrix}, \tag{6.2}$$

where $n_{AC}$ is the number of buses of the HVAC grid.

The linearised model of an abritrary HVAC power system can be written as:

$$\begin{aligned} \boldsymbol{\Delta \dot{x}_{AC}} &= \boldsymbol{A_{AC}} \cdot \boldsymbol{\Delta x_{AC}} + \boldsymbol{B_{AC}} \cdot \boldsymbol{\Delta v_{I,AC}}, \\ \boldsymbol{\Delta i_{I,AC}} &= \boldsymbol{C_{AC}} \cdot \boldsymbol{\Delta x_{AC}} + \boldsymbol{D_{AC}} \cdot \boldsymbol{\Delta v_{I,AC}}, \end{aligned} \tag{6.3}$$

where $\boldsymbol{\Delta x_{AC}}$ is the state vector of the system, $\boldsymbol{\Delta i_{I,AC}}$ is the vector of the current injections (e.g. generators, FACTS, etc...) and $\boldsymbol{\Delta v_{I,AC}}$ is the vector of the voltages of the buses involved in the dynamic model of those devices.

Static loads of an HVAC system are typically modelled as algebraic equations:

$$\boldsymbol{\Delta i_{L,AC}} = \boldsymbol{D_{L,AC}} \cdot \boldsymbol{\Delta v_{L,AC}}, \tag{6.4}$$

where $\boldsymbol{\Delta i_{L,AC}}$ and $\boldsymbol{\Delta v_{L,AC}}$ are the current injections of the loads and the voltages applied to them, respectively. Notice that matrix $\boldsymbol{D_{L,AC}}$ depends on the load modelling. Commonly, loads are represented by constant impedance, constant current, constant power characteristics. Sometimes they are represented by a combination of those three characteristics.

If one or several VSC-MTDC systems are plugged into the HVAC system, the linearised model of all the VSC-MTDCs of the system will be written as (see Appendix D):

$$\begin{aligned} \boldsymbol{\Delta \dot{x}_{MTDC}} &= \boldsymbol{A_{MTDC}} \cdot \boldsymbol{\Delta x_{MTDC}} + \boldsymbol{B_{MTDC,A}} \cdot \boldsymbol{\Delta v_{MTDC,AC}}, \\ \boldsymbol{\Delta i_{MTDC,AC}} &= \boldsymbol{C_{MTDC,A}} \cdot \boldsymbol{\Delta x_{MTDC}} + \boldsymbol{D_{MTDC,AA}} \cdot \boldsymbol{\Delta v_{MTDC,AC}}, \end{aligned} \tag{6.5}$$

where converters, their controllers and the HVDC grids will be included.

Vector $\boldsymbol{\Delta x_{MTDC}}$ contains the states of all the VSC-MTDC systems present, $\boldsymbol{\Delta i_{MTDC,AC}}$ are the current injections of the converters of the VSC-MTDC systems into the AC side (PCC) and $\boldsymbol{\Delta v_{MTDC,AC}}$ are the voltages of the converters at the PCCs of the AC system. Notice that a subscript $A$ has been included in some state matrices of (6.5), because it will help to tell apart the AC signals of the VSCs from the DC ones during the derivation of the model, as will be explained in Appendix D.

The linearised model of the hybrid HVAC/VSC-HVDC grid will contain full models of the HVAC system (generators, FACTS, loads, etc...) and the VSC-MTDC systems. All voltages and currents injections of the HVAC grid

must verify the grid equations:

$$\boldsymbol{\Delta i_{AC}} = \boldsymbol{J_{AC}} \boldsymbol{\Delta v_{AC}}. \tag{6.6}$$

where:

$$\begin{aligned} \boldsymbol{\Delta i_{AC}} &= [\boldsymbol{\Delta i_{I,AC}},\ \boldsymbol{\Delta i_{MTDC,AC}},\ \boldsymbol{\Delta i_{L,AC}}]^T. \\ \boldsymbol{\Delta v_{AC}} &= [\boldsymbol{\Delta v_{I,AC}},\ \boldsymbol{\Delta v_{MTDC,AC}},\ \boldsymbol{\Delta v_{L,AC}}]^T, \end{aligned} \tag{6.7}$$

and

$$\boldsymbol{J_{AC}} = \begin{bmatrix} \boldsymbol{J_{II}} & \boldsymbol{J_{IM}} & \boldsymbol{J_{IL}} \\ \boldsymbol{J_{MI}} & \boldsymbol{J_{MM}} & \boldsymbol{J_{ML}} \\ \boldsymbol{J_{LI}} & \boldsymbol{J_{LM}} & \boldsymbol{J_{LL}} \end{bmatrix}, \tag{6.8}$$

In order to simplify the notation, $M$ in (6.8) will be used instead of $MTDC$.

Joining all the state and voltage vectors, following the same procedure used in SSA programs for HVAC grids [181], the linearised model of the hybrid HVAC/VSC-HVDC system can be written as:

$$\begin{bmatrix} \boldsymbol{\Delta \dot{x}_{AC}} \\ \hline \boldsymbol{\Delta \dot{x}_{MTDC}} \\ \hline \boldsymbol{0} \\ \boldsymbol{0} \\ \boldsymbol{0} \end{bmatrix} = \left[\begin{array}{cc|ccc} \boldsymbol{A_{AC}} & \boldsymbol{0} & \boldsymbol{B_{AC}} & \boldsymbol{0} & \boldsymbol{0} \\ \boldsymbol{0} & \boldsymbol{A_{MTDC}} & \boldsymbol{0} & \boldsymbol{B_{MTDC,A}} & \boldsymbol{0} \\ \hline \boldsymbol{-C_{AC}} & \boldsymbol{0} & \boldsymbol{J_{II} - D_{AC}} & \boldsymbol{J_{IM}} & \boldsymbol{J_{IL}} \\ \boldsymbol{0} & \boldsymbol{-C_{MTDC,A}} & \boldsymbol{J_{MI}} & \boldsymbol{J_{MM} - D_{MTDC,AA}} & \boldsymbol{J_{ML}} \\ \boldsymbol{0} & \boldsymbol{0} & \boldsymbol{J_{LI}} & \boldsymbol{J_{LM}} & \boldsymbol{J_{LL} - D_{L,AC}} \end{array}\right] \cdot \begin{bmatrix} \boldsymbol{\Delta x_{AC}} \\ \hline \boldsymbol{\Delta x_{MTDC}} \\ \hline \boldsymbol{\Delta v_{I,AC}} \\ \boldsymbol{\Delta v_{MTDC,AC}} \\ \boldsymbol{\Delta v_{L,AC}} \end{bmatrix}. \tag{6.9}$$

which, in a compact form, becomes:

$$\begin{bmatrix} \boldsymbol{\Delta \dot{x}} \\ \boldsymbol{0} \end{bmatrix} = \begin{bmatrix} \boldsymbol{A_{11}} & \boldsymbol{A_{12}} \\ \boldsymbol{A_{21}} & \boldsymbol{A_{22}} \end{bmatrix} \begin{bmatrix} \boldsymbol{\Delta x} \\ \boldsymbol{\Delta v_{AC}} \end{bmatrix}, \tag{6.10}$$

where $\boldsymbol{\Delta x} = [\boldsymbol{\Delta x_{AC}}, \quad \boldsymbol{\Delta x_{MTDC}}]^T$.

Finally, voltages are eliminated from (6.10) using the Schur complement:

$$\boldsymbol{\Delta \dot{x}} = \boldsymbol{A \Delta x} \quad \text{with} \quad \boldsymbol{A} = \boldsymbol{A_{11}} - \boldsymbol{A_{12}} \boldsymbol{A_{22}^{-1}} \boldsymbol{A_{21}}. \tag{6.11}$$

The modes of the hybrid HVAC/VSC-HVDC linear system will be the eigenvalues of matrix $\boldsymbol{A}$ in (6.11) and the electromechanical modes can be identified computing the participation factors [78–80].

## 6.4 Implementation in SSST under Matlab

SMAS3 is a commercial FORTRAN-based tool for small-signal stability analysis of large power systems [182]. The tool was developed by IIT (Comillas Pontifical University) and it has been used successfully in Industry, for example, in Iberdrola, Red Eléctrica de España (REE), Réseau de Transport d'Électricité (RTE) and CAMMESA. Small-Signal Stability Toolbox (SSST) is a matlab-based version of SMAS3 [181]. These tools were initially intended for HVAC grids, although new models of FACTS devices and wind turbines have been included in the last few years. No models for VSC-MTDC systems were available. In this thesis, the small-signal model for VSC-MTDC systems proposed in this chapter has been included in SSST.

The sequential AC/DC power-flow algorithm proposed in [91] and described in Chapter 2 was also implemented in SSST to obtain the initial operating point.

## 6.5 Model validation by time-domain comparison

The small test system shown in Fig. 6.1 has been used to validate the small-signal VSC-MTDC model proposed (implemented in Matlab + SSST). The purpose of using such a small test system for this validation is to assess the accuracy of the linearised model of the VSC-MTDC system, only. The results obtained with the linear model implemented in matlab + SSST will be compared with an electromagnetic model in Simulink + SimPowerSystems (including the switches of the power converters) and with electromechanical VSC-MTDC models in PSS/E and in PowerFactory (as done in Chapter 2).

The same set-point changes of Subsection 2.6 were simulated. The results are shown in Fig. 6.2 and 6.3. The simulation results obtained with the linear model in SSST show good agreement with the ones obtained with the other

non-linear models. A detailed scale (20 ms) of the time response of the DC voltages is shown in Fig. 6.4, which confirms the validity of the small-signal VSC-MTDC model proposed in this Chapter of the thesis.

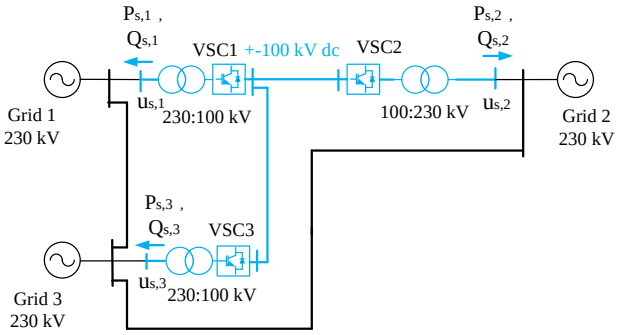


Figure 6.1: Test system for validation.

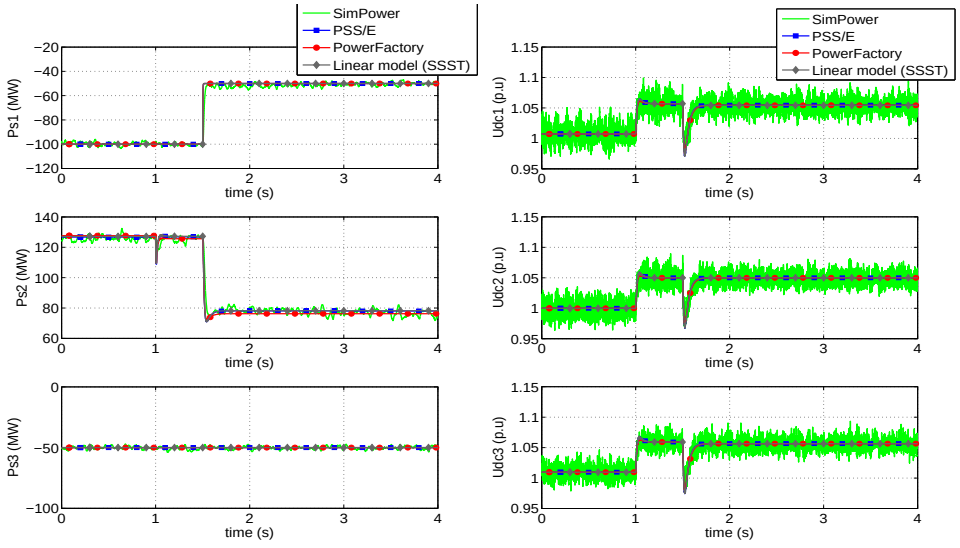


(a) Active-power injections. (b) DC voltages.

Figure 6.2: Validation of the linear model of the VSC-MTDC (in SSST).

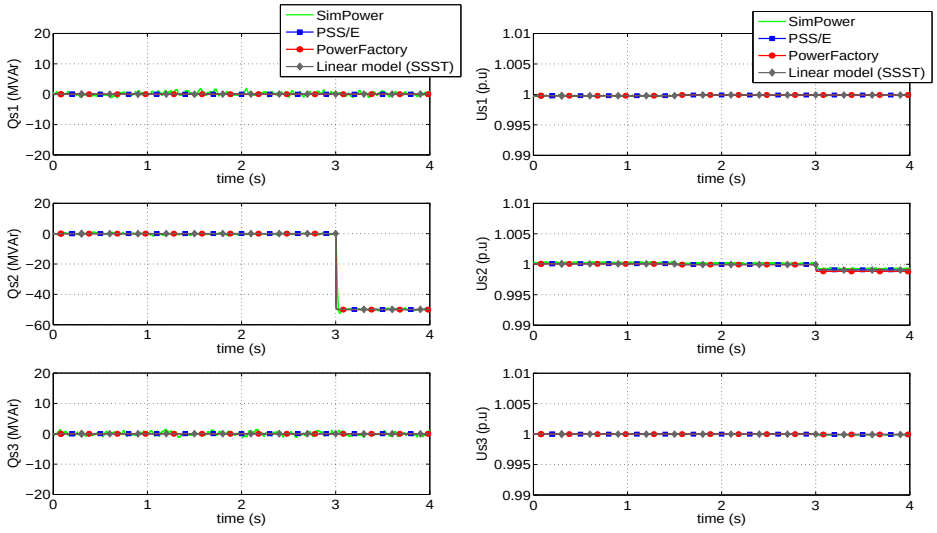


(a) Reactive-power injections. (b) AC voltages.

Figure 6.3: Validation of the linear model of the VSC-MTDC (in SSST).

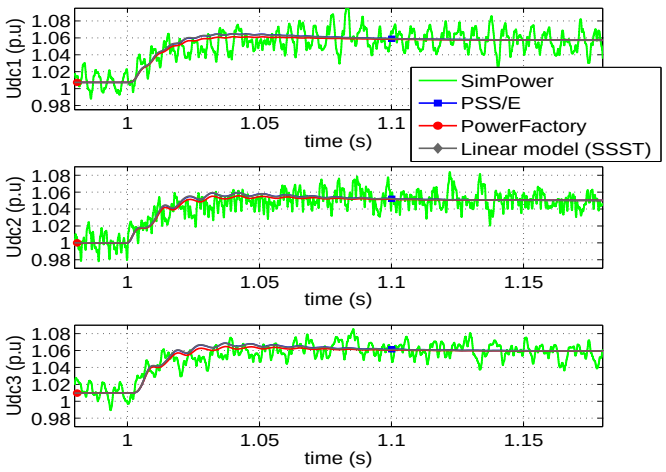


Figure 6.4: Validation of the linear model of the VSC-MTDC (in SSST). DC voltages (zoom).

## 6.6 Model validation by eigenvalue comparison

As discussed in Section 1.4 of Chapter 1, PSS/E cannot be used for SSA of hybrid HVAC/VSC-HVDC systems because it cannot deal with user-defined models (for SSA). Nevertheless, SSA of HVAC/VSC-HVDC grids can be carried out with PoweFactory (DigSILENT). Although some inconsistencies have been reported, but not explained, in the literature in [176,179,180], while other references use PowerFactory for SSA of hybrid HVAC/VSC-HVDC systems without reporting any problem [74, 183, 184].

In order to dispel these doubts, a comparison of the SSA obtained with PowerFactory and with the VSC-MTDC model developed for matlab-based SSST will be carried out in this Subsection. The test system of Fig. 6.1 has been considered.

The eigenvalues of the linear models obtained with SSST and with PowerFactory are written in Table 6.1. The dominant states for each mode were obtained from the participation factors [78–80]. The errors between the eigenvalues obtained with both tools are reported in the last column of Table 6.1. Those error values were computed as:

$$error(\lambda_i) = \frac{|\lambda_i^{SSST} - \lambda_i^{PowerFactory}|}{|\lambda_i^{SSST}|}. \tag{6.12}$$

The results of Table 6.1 show that:

- Most of the eigenvalues associated to the VSC stations and the DC grid obtained with SSST and PowerFactory match very well. These eigenvalues are 1-4 and 7-11 in Table 6.1.
- For some other eigenvalues associated also to the VSC stations and the DC grid, the errors are acceptable and the results obtained with both tools show good agreement (eigenvalues are 5-6 of Table 6.1). Notice that, although the relative error of these two eigenvalues is bigger, its has no significant impact, since modes 5 and 6 are real.
- Modes 13-15 of Table 6.1 are associated to the first-order systems for frequency measurement at the AC side of the VSCs in the VSC-MTDC model of SSST tool. These eigenvalues do not appear in PowerFactory, since those states are not included in its VSC-MTDC model.
- Modes 25-35 of Table 6.1 are associated to the states of the PLL of each VSC. The detailed model of the PLLs are only represented in PowerFactory.

- Some unexplained eigenvalues appear when using PowerFactory (modes 22-23). These eigenvalues appear only when hybrid AC/DC grids are considered and they were referred by DigSilent support team as "numerical artefacts". They have only real part (negative) and they have a large module ($\sim -10^{10}$). After a thorough anlaysis of the results obtained in the test system of Fig. 6.1 and in other AC/DC systems, it was concluded that the results provided by the SSA of PowerFactory are reliable and the dummy eigenvalues (modes 22-23 in this example) should just be excluded from the analysis.

- Finally, some zero modes appear in PowerFactory (24–39). These modes are associated to the states of some models included in PowerFactory whose gains are set to zero (e.g. $K/(1+Ts)$ with $K=0$). On the contrary, SSST excludes the dynamic models that have zero gain from the analysis using $if-else$ conditions.

Table 6.1: SSA results obtained with SSST and PowerFactory.

| Mode | SSST Eigenvalue (rad/s) | $\zeta$ (%) | Freq. (Hz) | PowerFactory Eigenvalue (rad/s) | $\zeta$ (%) | Freq. (Hz) | dominant states | error (%) |
|---|---|---|---|---|---|---|---|---|
| 1, 2 | $-34.20 \pm j1096.39$ | 3.12 | 174.50 | $-38.09 \pm j1097.81$ | 3.47 | 174.72 | $u_{dc,1}$ | 0.31 |
| 3, 4 | $-29.18 \pm j665.05$ | 4.38 | 105.85 | $-33.17 \pm j666.18$ | 4.97 | 106.03 | $u_{dc,2}$ | 0.45 |
| 5 | $-28.53$ | 100 | - | $-24.29$ | 100 | - | $n_{d,2}$ | 17.50 |
| 6 | $-82.05$ | 100 | - | $-97.94$ | 100 | - | $u_{dc,2}$ | 16.23 |
| 7 | $-340.37$ | 100 | - | $-336.09$ | 100 | - | $i_{s,d2}$ | 1.28 |
| 8 | $-499.88$ | 100 | - | $-499.88$ | 100 | - | $i_{s,d1}$ | 0.00 |
| 9 | $-499.95$ | 100 | - | $-499.95$ | 100 | - | $i_{s,d3}$ | 0.00 |
| 10 | $-500.00$ | 100 | - | $-500.00$ | 100 | - | $i_{s,q1}$ | 0.00 |
| 11 | $-500.00$ | 100 | - | $-500.00$ | 100 | - | $i_{s,q2}$ | 0.00 |
| 12 | $-500.00$ | 100 | - | $-500.00$ | 100 | - | $i_{s,q3}$ | 0.00 |
| 13 | $-1000.00$ | 100 | - | - | - | - | $\omega_{vsc,1}$ | - |
| 14 | $-1000.00$ | 100 | - | - | - | - | $\omega_{vsc,2}$ | - |
| 15 | $-1000.00$ | 100 | - | - | - | - | $\omega_{vsc,3}$ | - |
| 16 | - | - | - | $-0.38$ | 100 | - | PLL1 | - |
| 17 | - | - | - | $-2.62$ | 100 | - | PLL1 | - |
| 18 | - | - | - | $-0.38$ | 100 | - | PLL2 | - |
| 19 | - | - | - | $-2.63$ | 100 | - | PLL2 | - |
| 20 | - | - | - | $-0.38$ | 100 | - | PLL3 | - |
| 21 | - | - | - | $-2.60$ | 100 | - | PLL3 | - |
| 22 | - | - | - | $-2.6 \cdot 10^{10}$ | 100 | - | ? | - |
| 23 | - | - | - | $-2.6 \cdot 10^{10}$ | 100 | - | ? | - |
| 24 – 39 | - | - | - | 0 | - | - | - | - |

## 6.7 Nordic32A system with a VSC-MTDC

Small-signal analysis was carried out on the Nordic32A test system with a VSC-MTDC, in the heavily loaded scenario, as described in Appendix A. The operating point of the VSCs and their control mode are described also in Appendix A. In the scenario considered here, each converter has the DC-voltage droop control implemented, but they have no additional supplementary set-point value for the outer controllers, which will be the scope of Chapter 7 of this thesis.

All the eigenvalues obtained from the linearised system are shown in Fig. 6.5-(a), whilst the the eigenvalues which are close to the imaginary axis are shown in Fig. 6.5-(b). The damping ratio of each eigenvalue versus its magnitude is shown in Fig. 6.6. Plotting the damping ratio versus the magnitude of the modes helps to visualise the modes close to instability when the system has too many eigenvalues and when the time constants involved are of different order of magnitude.

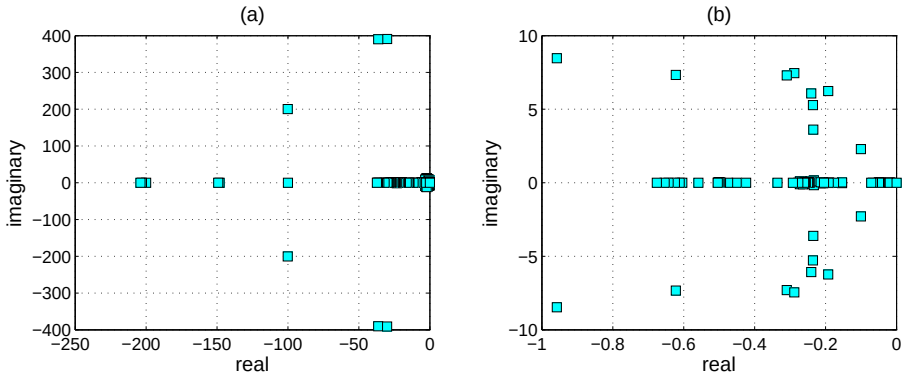


Figure 6.5: Eigenvalues.

As shown in Figs. 6.5 and 6.6, the system is stable, since all the modes have negative real parts. The modes associated to the VSC-MTDC system, i.e, the modes associated to the converters and the DC grid, are written in Table 6.2. The electromechanical modes of the system are reported in Table 6.3. Notice that the system has poorly damped local (modes 81-84) and inter-area (modes 85-88) electromechanical modes. Control strategies for damping the electromechanical modes will be studied in Chapter 7. Tables 6.2 and 6.3 also show that the dynamics associated to the state variables

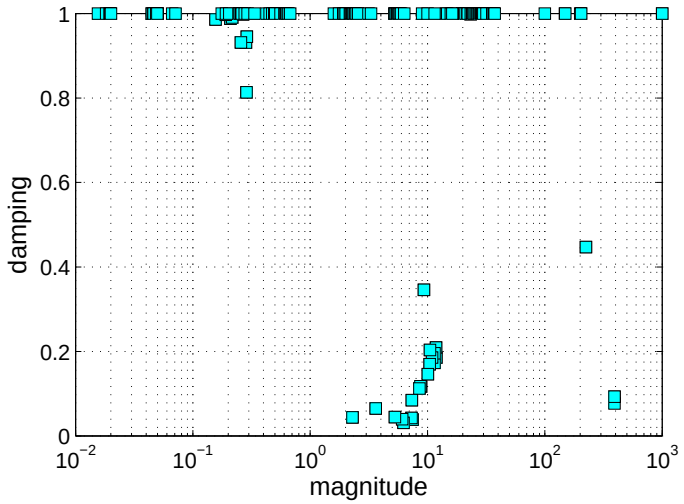


Figure 6.6: Eigenvalues. Damping versus magnitude.

of the VSC-MTDC are much faster than the dynamics associated to the electromechanical modes.

The results presented in this Subsection prove that the model proposed and included in SSST can be used succesfully for small-signal analysis of large multi-machine sistems containing embedded VSC-MTDC systems. Furthermore, the possibility of implementing supplementary control strategies for the VSCs has also been illustrated by implementing the DC-voltage droop control in the VSCs.

Table 6.2: Modes associated to the state variables of the VSC-MTDC system (obtained with SSST).

| Mode | Eigenvalue (rad/s) | $\zeta$ (%) | Freq. (Hz) | states with greatest participation |
|---|---|---|---|---|
| 66 | $-30.09 \pm j390.90$ | 7.68 | 62.21 | $u_{dc,2}$ |
| 67 | $-36.34 \pm j390.29$ | 9.27 | 62.12 | $u_{dc,1}$ |
| 68 | $-100.14 \pm j200.31$ | 44.72 | 31.88 | $u_{dc,1}$ |
| 229 | $-14.71$ | 100 | - | $i_{cc,13}$ |
| 290 | $-148.22$ | 100 | - | $i_{d,3}$ |
| 291 | $-149.08$ | 100 | - | $i_{d,2}$ |
| 292 | $-200.00$ | 100 | - | $i_{q,1}$ |
| 293 | $-203.08$ | 100 | - | $i_{q,3}$ |
| 294 | $-204.12$ | 100 | - | $i_{q,2}$ |

Table 6.3: Electromechanical modes (obtained with SSST).

| Mode | Eigenvalue (rad/s) | $\zeta$ (%) | Freq. (Hz) | states with greatest participation |
|---|---|---|---|---|
| 69 | $-2.20 \pm j11.67$ | 18.59 | 1.86 | $\delta_{G,1022}$ |
| 70 | $-2.47 \pm j11.56$ | 20.93 | 1.84 | $\delta_{G,1014}$ |
| 71 | $-1.98 \pm j11.30$ | 17.30 | 1.80 | $\delta_{G,4031}$ |
| 72 | $-2.24 \pm j11.25$ | 19.55 | 1.79 | $\delta_{G,1012}$ |
| 73 | $-2.03 \pm j10.74$ | 18.54 | 1.71 | $\delta_{G,4011}$ |
| 74 | $-1.77 \pm j10.28$ | 16.97 | 1.64 | $\delta_{G,4021}$ |
| 75 | $-2.13 \pm j10.28$ | 20.33 | 1.64 | $\delta_{G,4071}$ |
| 76 | $-1.47 \pm j9.98$ | 14.61 | 159 | $\delta_{G,4012}$ |
| 77 | $-3.22 \pm j8.75$ | 34.54 | 1.39 | $\omega_{G,4041}$ |
| 78 | $-1.03 \pm j8.74$ | 11.69 | 1.39 | $\delta_{G,4062}$ |
| 79 | $-1.03 \pm j8.74$ | 11.76 | 1.37 | $\delta_{G,1043}$ |
| 80 | $-0.96 \pm j8.47$ | 11.23 | 1.35 | $\omega_{G,4047}$ |
| 81 | $-0.29 \pm j7.46$ | 3.86 | 1.19 | $\omega_{G,2032}$ |
| 82 | $-0.62 \pm j7.33$ | 8.45 | 1.17 | $\omega_{G,4051}$ |
| 83 | $-0.31 \pm j7.29$ | 4.24 | 1.16 | $\omega_{G,1021}$ |
| 84 | $-0.19 \pm j6.23$ | 3.09 | 0.99 | $\omega_{G,1021}$ |
| 85 | $-0.24 \pm j6.07$ | 3.95 | 0.97 | $\omega_{G,1042}$ |
| 86 | $-0.24 \pm j5.28$ | 4.46 | 0.84 | $\delta_{G,4063}$ |
| 87 | $-0.24 \pm j3.61$ | 6.50 | 0.57 | $\omega_{G,4072}$ |
| 88 | $-0.10 \pm j2.29$ | 4.37 | 0.36 | $\omega_{G,4042}$ |

## 6.8 Summary

This chapter can be summarised as follows:

- A systematic methodology has been presented to add the linearised models of VSC-MTDC systems into the linearised model of a given HVAC system (the details are presented in Appendix D). In comparison with previous approaches, the contribution of this work is to provide a generalised modelling framework valid for hybrid HVAC/VSC-HVDC system with arbitrary topology. Although the guidelines to build linerised models of HVAC/VSC-HVDC systems can be found in the literature, such generalised approach has not been presented before.
- The linearised model (in SSST) has been validated by time-domain simulation against the different models studied in Chapter 2: a detailed electromagnetic simulation model in SimPowerSystems, and electromechanical models in PSS/E and PowerFactory.
- The linearised model (in SSST) has been validated by eigenvalue comparison against PowerFactory.
- Although some details of the SSA of PowerFactory are not accesible by the users, it has been concluded that the results of the SSA provided by that tool are consistent.
- SSA of the Nordic32A test system with an embedded VSC-MTDC has been carried out, to illustrate the use of the proposed tool for SSA of large HVAC/VSC-HVDC systems.

# Chapter 7

# Control strategies for power-oscillation damping

## 7.1 Introduction

The small-signal model for VSC-MTDC systems proposed in Chapter 6 has been used for two purposes:

1. To analyse the impact of the control strategies proposed to improve transient stability in Chapters 3-5 (P-WAF, Q-WAF, Q-LWAF and PQ-WAF) on the eigenvalues of the system. More precisely, their capability to damp electromechanical oscillations has been analysed.

2. To design controllers in VSC-MTDC systems for power-oscillation damping (POD).

The rest of this chapter is organised as follows. Section 7.2 presents a review of the state of the art on control strategies in VSC-MTDC systems for power-oscillation damping. Section 7.3 presents the results of the small-signal analysis of the transient-stability controllers, analysing their impact on electromechanical modes. Section 7.4 describes the proposed control strategies for power-oscillation damping and analyses the residues of the controllers numerically. Section 7.5 presents the coordinated-design algorithm (based on eigenvalue sensitivities) for POD controllers in VSC-MTDC systems. The results of the POD controllers are presented in Section 7.6. The proposed POD controllers are tested by time-domain simulation in Section 7.7. Finally, the conclusions are presented in Section 7.8.

## 7.2 Review of previous work

Traditionally, Power System Stabilisers (PSSs) in synchronous machines have been the most effective way to damp electromechanical oscillations [62]. Nevertheless, the development of power electronics has also made FACTS devices [64–66, 185–187], wind turbines [68, 69, 188] and point-to-point VSC-HVDC links [70, 189] attractive alternatives to help damping power oscillations, due to the fast control of power converters. Meanwhile, several publications have showed the potential of VSC-MTDC systems to damp power oscillations [71–77, 190].

The work in [71] proposed a POD controller for the P injection of one of the converter stations in a VSC-MTDC system (integrating offshore wind farms). The input signal of the POD controller is the active-power flow through an AC line. Ref. [72] proposed P controllers to damp power oscillations (in the onshore VSC stations of a VSC-MTDC incorporating offshore wind energy), using the frequency deviation as input signal. POD controllers at the VSC stations of a VSC-MTDC system are proposed in [73]. Those controllers use the P injections of the converters as outputs and wide-area measurements of the speed of one or more generators as input signals.

Reference [74] proposed local POD controllers for the converter stations of a VSC-MTDC system embedded in an HVAC grid. In the proposed control strategy, one VSC station changes its DC-voltage set point (for the DC-voltage droop) using the frequency deviation measured at its AC side (local measurement) as input signal. An additional controller is added to the DC-droop controller of each VSC station (DC-voltage loop shaping) to maximise the controllability.

The work in [75] proposed P-controllers for power-oscillation damping by using widea-area measurements of the active-power flows through a set of AC tie lines. A modal linear quadratic Gaussian (MLDG) method is used to damp a required set of electromechanical modes. Ref. [77] also proposed a WAMS-based POD controller for P injections of the VSC stations of a MTDC system. The controllers are also designed using MLDG method and the location of the controllers are selected using eigenvalue-sensitivity techniques.

The work in [190] proposed POD controllers for P and Q injections in VSC-MTDC systems, by using local and global measurements of the voltage angles. An heuristic algorithm is used to design the POD controllers.

The study in [76] proposed POD controllers for the active-power through different point-to-point VSC-HVDC links in a meshed HVAC system, using the frequency differences of the AC terminals of the different links. The

authors state that the approach can be extended to multi-terminal systems, but this possibility was not investigated in the paper.

In this work, controllers for power-oscillation damping in VSC-MTDC systems, using P and Q injections as output signals and the weighted-average frequency error as input, will be investigated. Coordinated design of the damping controllers will be done, using the algorithm based on eigenvalue sensitivities proposed in [64].

The contributions of the POD controllers proposed in this thesis, in comparison with previous approaches, are as follows:

1. The POD controllers proposed in [71–77] are restricted to P injections at the VSC stations, while the POD controllers proposed here will have flexibility to use P and/or Q injections of the VSCs as output signals. Using Q injections has the advantage that they do not interfere with the active-power and DC-voltage control of the VSC-MTDC system.

2. Global signals used in the proposed POD controllers (frequency measurementes at the converter stations of a VSC-MTDC system) are easier to implement than a WAMS (as in [71, 73, 75, 77]).

3. The proposal of [74] has the advantage that it uses local measurements. However, it is based on a DC-voltage loop shaping, which modifies the DC-voltage droop control. The impact of the POD controllers on the DC voltages was not analysed in [74]. Since voltage control in the DC grid is a critical aspect in a VSC-MTDC system, the POD controllers proposed here avoid any interaction with the DC-voltage droop control.

4. The POD controllers proposed in [190] modulate P and Q injections of the VSC stations using local and global measurements of voltage angles. This work investigates the modulation of P and Q injections using frequency measurements at the converter stations of a VSC-MTDC system. Furthermore, the work in [190] uses a non-linear heuristic optimisation algorithm to design the POD controllers, while a linear optimisation problem is solved to design the POD controllers in this work.

5. The coordinated-design algorithm proposed makes it possible a systematic design of the controllers to obtain the required damping ratio of a set of electromechanical modes, as it was also done in [72, 75, 190].

## 7.3 Impact of transient-stability controllers on power-oscillation damping

In general, small- and large-signal angle stability are related and controllers that improve one type of stability also improve the other one, but this is not a always the case (as seen in [191]). Therefore, this section has been tailored to analyse the capability of control strategies P-WAF, Q-WAF and Q-LWAF (chapters 3-5) to damp power oscillations.

As in the previous chapters, the Noridc32A test system with an embedded VSC-MTDC system in a heavily loaded scenario, as described in section A.3.2, is considered.

The electromechanical modes obtained from the small-signal analysis were shown in Table 6.7 of Chapter 6. The impact of the control strategies on the electromechanical modes with low damping will be analysed now. Special attention will be given to inter-area modes. For the sake of clarity, the electromechanical modes with low damping are named as A-H and they are reported in Table 7.1.

The shapes of the inter-area modes A, B and C are shown in Figs. 7.1, 7.2 and 7.3, respectively. Modes A and B describe the oscillation of the machines of the North area against the machines of the Centre and South areas, while mode C describes the oscillation of the North and South against the Central area (see the single-line diagram of the Nordic32A test system in Fig. A.3 of section A.3 ).

The analysis will study how strategies P-WAF, Q-WAF and Q-LWAF (chapters 3-5) affect the electromechanical modes of Table 7.1.

### 7.3.1 Small-signal analysis

The electromechanical modes of interest (A-H of Table 7.1) obtained with strategies P-WAF, Q-WAF, Q-LWAF and with strategies P-WAF and Q-WAF simultaneously (PQ-WAF) are shown in tables 7.2 and 7.3. The designs used for transient stability improvement in chapters 3-5 have been considered: $k_{P,i} = 200$ p.u in P-WAF; $k_{Q,i} = 200$ p.u in Q-WAF and Q-LWAF; and $k_{P,i} = k_{Q,i} = 200$ p.u in PQ-WAF. The results obtained with no P/Q modulation (DC0) are also included in tables 7.2 and 7.3, for comparison.

Results of tables 7.2 and 7.3 show that, in general, P and Q modulation in the VSCs improve the damping ratio of electromechanical oscillations, specially inter-area modes B and C. The impact of the control strategies on the inter-area oscillations on the damping ratios of inter-area modes (A, B

Table 7.1: Nordic32A system with a VSC-MTDC (with no supplementary controllers). Electromechanical modes of interest.

| Mode | Eigenvalue (rad/s) | $\zeta$ (%) | Freq. (Hz) | machines with greatest participation | description |
|---|---|---|---|---|---|
| A | $-0.1006 \pm j2.2873$ | 4.37 | 0.36 | G4042, G4072 | Inter-area North - Centre, South |
| B | $-0.2348 \pm j3.6088$ | 6.50 | 0.57 | G4072, G4042, G4063 | Inter-area North - Centre, South |
| C | $-0.2356 \pm j5.2768$ | 4.46 | 0.84 | G4063, G1042, G4062, G4072 | Inter-area North, South - Centre |
| D | $-0.2403 \pm j6.0733$ | 3.95 | 0.97 | G1042, G4072, G1021 | local North |
| E | $-0.1925 \pm j6.2343$ | 3.09 | 0.99 | G1021, G4072, G1042, G2032 | local North |
| F | $-0.3094 \pm j7.2948$ | 4.24 | 1.16 | G1021, G2032 | local North |
| G | $-0.6223 \pm j7.3340$ | 8.45 | 1.17 | G4051, G4047 G1043 | local Centre |
| H | $-0.2882 \pm j7.4570$ | 3.86 | 1.19 | G2032, G1014, G1013, G4072, G1012, G4012, G4011, G1021 | local Centre |

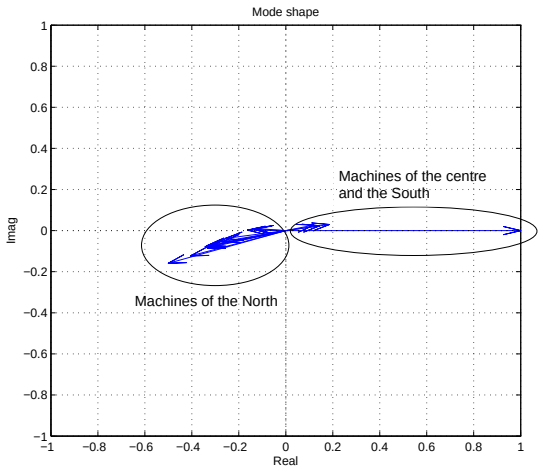


Figure 7.1: Nordic32A + VSC-MTDC (no supplementary controllers). Shape of inter-area mode A.

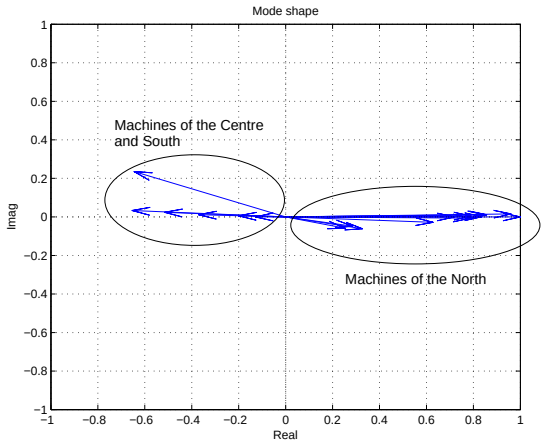


Figure 7.2: Nordic32A + VSC-MTDC (no supplementary controllers). Shape of inter-area mode B.

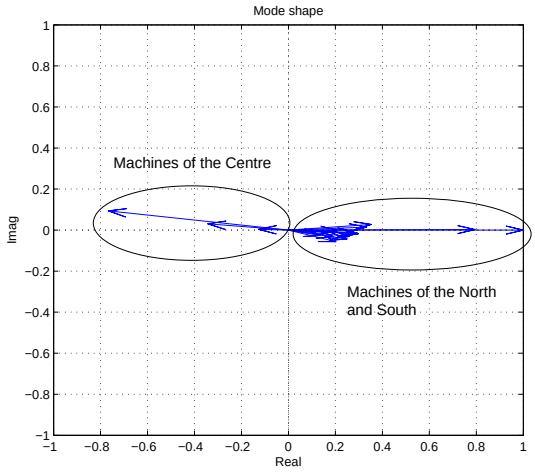


Figure 7.3: Nordic32A + VSC-MTDC (no supplementary controllers). Shape of inter-area mode C.

Table 7.2: Electromechanical modes of interest (P-WAF and PQ-WAF).

| Mode | DC0 | P-WAF $k_{P,i} = 200$ p.u | PQ-WAF $k_{P,i} = k_{Q,i} = 200$ p.u |
|---|---|---|---|
| A | $-0.1006 \pm j2.2873$<br>4.37 %, 0.36 Hz | $-0.0542 \pm j1.9603$<br>2.77 %, 0.31 Hz | $-0.1504 \pm j1.9994$<br>7.50 %, 0.32 Hz |
| B | $-0.2348 \pm j3.6088$<br>6.50 %, 0.57 Hz | $-0.6403 \pm j4.6678$<br>13.59 %, 0.74 Hz | $-0.5606 \pm j4.8909$<br>11.39 %, 0.78 Hz |
| C | $-0.2356 \pm j5.2768$<br>4.46 %, 0.84 Hz | $-0.6491 \pm j5.5970$<br>11.52 %, 0.89 Hz | $-0.6319 \pm j5.9672$<br>10.53 %, 0.95 Hz |
| D | $-0.2403 \pm j6.0733$<br>3.95 %, 0.97 Hz | $-0.3214 \pm j6.0152$<br>5.33 %, 0.96 Hz | $-0.4260 \pm j6.3755$<br>6.67 %, 1.01 Hz |
| E | $-0.1925 \pm j6.2343$<br>3.09 %, 0.99 Hz | $-0.3864 \pm j6.3752$<br>6.05 %, 1.01 Hz | $-0.3942 \pm j5.9685$<br>6.59 %, 0.95 Hz |
| F | $-0.3094 \pm j7.2948$<br>4.24 %, 1.16 Hz | $-0.3269 \pm j7.3402$<br>4.45 %, 1.17 Hz | $-0.3221 \pm j7.3339$<br>4.38 %, 1.17 Hz |
| G | $-0.6223 \pm j7.3340$<br>8.45 %, 1.17 Hz | $-0.6267 \pm j7.3361$<br>8.51 %, 1.17 Hz | $-0.6267 \pm j7.3368$<br>8.51 %, 1.17 Hz |
| H | $-0.2882 \pm j7.4570$<br>3.86 %, 1.19 Hz | $-0.4359 \pm j7.5110$<br>5.74 %, 1.20 Hz | $-0.4522 \pm j7.5523$<br>5.98 %, 1.20 Hz |

Table 7.3: Electromechanical modes of interest (Q-WAF and Q-LWAF).

| Mode | Base case (DC0) | Q-WAF $k_{Q,i} = 200$ p.u | Q-LWAF $k_{Q,i} = 200$ p.u |
|---|---|---|---|
| A | $-0.1006 \pm j2.2873$<br>4.37 %, 0.36 Hz | $-0.1988 \pm j2.2533$<br>8.79 %, 0.36 Hz | $-0.1938 \pm j2.2358$<br>8.6343 %, 0.36 Hz |
| B | $-0.2348 \pm j3.6088$<br>6.50 %, 0.57 Hz | $-0.5558 \pm j3.9280$<br>14.01 %, 0.63 Hz | $-0.5910 \pm j3.9865$<br>14.66 %, 0.63 Hz |
| C | $-0.2356 \pm j5.2768$<br>4.46 %, 0.84 Hz | $-0.4929 \pm j5.4413$<br>9.02 %, 0.87 Hz | $-0.4981 \pm j5.4614$<br>9.08 %, 0.87 Hz |
| D | $-0.2403 \pm j6.0733$<br>3.95 %, 0.97 Hz | $-0.3900 \pm j6.1826$<br>6.30 %, 0.98 Hz | $-0.3925 \pm j6.2021$<br>6.14 %, 0.99 Hz |
| E | $-0.1925 \pm j6.2343$<br>3.09 %, 0.99 Hz | $-0.1253 \pm j6.1469$<br>2.04 %, 0.98 Hz | $-0.1335 \pm j6.1361$<br>2.18 %, 0.98 Hz |
| F | $-0.3094 \pm j7.2948$<br>4.24 %, 1.16 Hz | $-0.3101 \pm j7.2911$<br>4.25 %, 1.16 Hz | $-0.3127 \pm j7.2931$<br>4.28 %, 1.16 Hz |
| G | $-0.6223 \pm j7.3340$<br>8.45 %, 1.17 Hz | $-0.6229 \pm j7.3345$<br>8.46 %, 1.17 Hz | $-0.6229 \pm j7.3347$<br>8.46 %, 1.17 Hz |
| H | $-0.2882 \pm j7.4570$<br>3.86 %, 1.19 Hz | $-0.3167 \pm j4740$<br>4.25 %, 1.16 Hz | $-0.3210 \pm j7.4777$<br>4.29 %, 1.19 Hz |

and C) is summarised in Table 7.4. Notice that Q modulation (with Q-WAF and Q-LWAF) damps successfully all the inter-area modes A, B and C.

Nevertheless, the control strategies might reduce the damping ratio of some other electromechanical modes. For example, the damping ratio of inter-area mode A deteriorates with strategy P-WAF (from 4.37 % to 2.77 %). The design of gain $k_{P,i}$ could be updated to obtain a larger damping ratio that mode, if required. Strategies Q-WAF and Q-LWAF (with $k_{Q,i} = 200$ p.u) reduce (slightly too) the damping ratio of local mode E (from 3.09 % to 2.18 %). That local mode could be damped with a PSS of a generator, if required. Strategy PQ-WAF does not reduce the damping of any electromechanical mode.

In general, the control strategies have a small impact on the damping ratio of local modes D-H.

Notice that results of Table 7.3 show that the effect of local strategy Q-LWAF on the electromechanical modes is remarkably similar to the effect of global strategy Q-WAF, as could be expected from the results of Chapter 5.

Finally, a more detailed small-signal analysis of the control strategies can be found in Appendix F.

Table 7.4: Impact of the control strategies on the electromechanical modes.

| Strategy | $k_{P,i}$ (p.u) | $k_{Q,i}$ (p.u) | Damping (%) Iner-area modes: A, B, C |
|---|---|---|---|
| Base case (DC0) | - | - | 4.37, 6.50, 4.46 |
| P-WAF | 200 | - | 2.77, 13.59, 11.39 |
| Q-WAF | - | 200 | 8.79, 14.01, 9.02 |
| Q-LWAF | 10 (in P-LF) | 200 | 8.63, 14.66, 9.08 |
| PQ-WAF | 200 | 200 | 7.50, 11.39, 10.53 |

### 7.3.2 Time-domain simulation

The disconnection of line 4012-4022 of a heavily loaded Nordic32A system (see Section A.3.2) has been simulated using the PSS/E electromechanical model described in Chapter 2. The base case (DC0) will be compared with strategies P-WAF, Q-WAF, Q-LWAF and PQ-WAF, using the designs proposed in Table 7.4. The angle difference between generators G4072 and G4063 and the active-power flow through corridor 4031-4041 a&b are shown in Fig. 7.4, while P and Q injections of the VSCs are shown in Fig. 7.5.

Results show that the proposed strategies are capable of damping the angle and power electromechanical oscillations. Notice that local strategy Q-LWAF produce very similar results as those of global strategy Q-WAF, which is consistent with the results of Chapter 5 and with the results of Table 7.3.

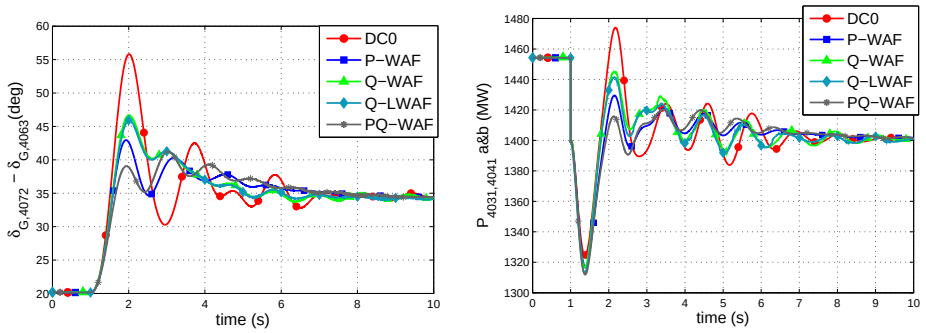


(a) (b)

Figure 7.4: Line 4012-4022 disconnected. (a) Angle difference of generators G4072 and G4063. (b) Power flow through corridor 4031-4041 a&b.

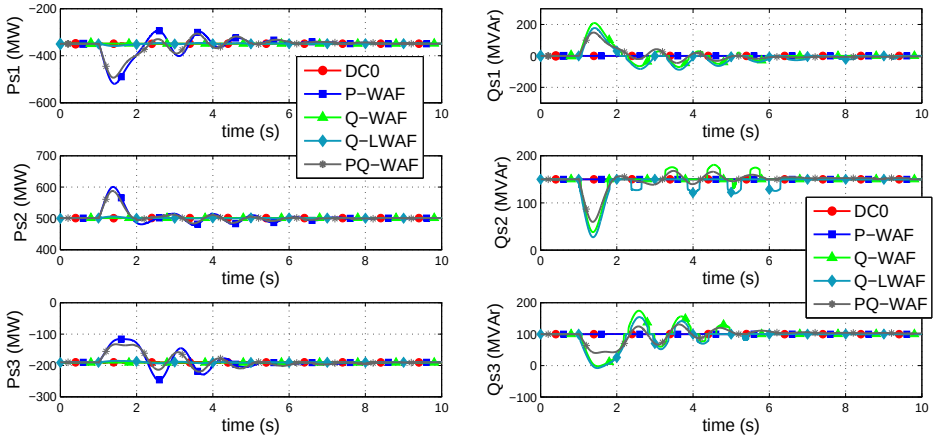


(a) (b)

Figure 7.5: Line 4012-4022 disconnected. (a) P injections ($P_{s,i}$). (b) Q injections ($Q_{s,i}$).

## 7.4 POD controllers and eigenvalue sensitivities

While the main purpose of transient stability controllers is to help to maintain synchronism when large disturbances occur, controllers for power-oscillation damping (POD) are aimed to improve angle stability during those small disturbances that continuously occur in the system (changes in the set points of generators or in other devices, changes on the loads or line disconnections, among others). These controllers are commonly known as POD controllers or Power System Stabilisers (PSSs). In this thesis, the design of POD controllers in VSC-MTDC systems using the eigenvalue sensitivities will be studied, following the guidelines in [64, 68, 186, 192, 193].

A powerful way of analysis the sensitivities of the system eigenvalues with respect to the parameters of a POD controller is to use the hybrid representation of the linearised system, shown in Fig. 7.6 [192], [1] where the system without the supplementary POD controllers installed is represented as:

$$\boldsymbol{\Delta \dot{x}} = \boldsymbol{A \Delta x} + \boldsymbol{b} \Delta u, \tag{7.1}$$

$$\Delta y = \boldsymbol{c^T \Delta x} + d \Delta u, \tag{7.2}$$

$F(s,q) = \Delta u / \Delta y$ is the transfer function of the POD controller of a device and $q$ is the parameter to design (typically gains).

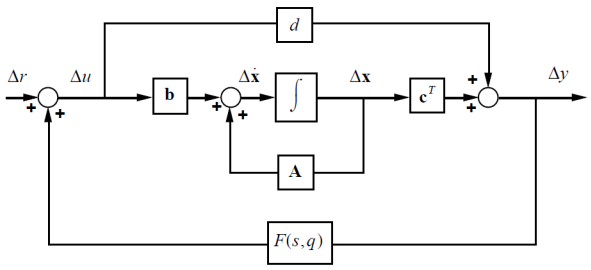


Figure 7.6: Hybrid representation of a linear system).

The sensitivity of mode $i$ to changes in the gain controller $j$ is given by [193]:

$$S_{ij} = R_{ij} \cdot \frac{\partial F_j(s)}{\partial K_{S,j}} \tag{7.3}$$

[1] Fig. 7.6 was obtained from [181].

where $K_{S,j}$ is the gain of controller $j$ and $R_{ij}$ is the residue of the transfer function of controller $j$, associated to mode $i$, which is given by [193]:

$$R_{ij} = \boldsymbol{w_i^T b_j} \frac{1}{(1 - F_j(\lambda_i) d_j)^2} \boldsymbol{c_j^T v_i} \tag{7.4}$$

where:

- $\boldsymbol{v_i}$ and $\boldsymbol{w_i}$ are the right and left eigenvectors associated to mode $\lambda_i$, respectively.
- $\boldsymbol{b_j}$ and $\boldsymbol{c_j}$ are controllability and observability vectors of the output and the input signals of controller $j$, respectively.

The terms $\boldsymbol{w_i^T b_j}$ and $\boldsymbol{c_j^T v_i}$ are known as the modal controllability and observability factors, respectively.

An effective POD controller will seek moving the modes of interest to the left hand side of the complex plane, with the smallest possible change on its imaginary part, as illustrated in Fig. 7.7. [2] Hence the sensitivities of a good candidate for a POD controller should have a large absolute value and a phase as close to 180° as possible. Lead/lag filters are commonly used to obtain the desirable phase of the sensitivities.

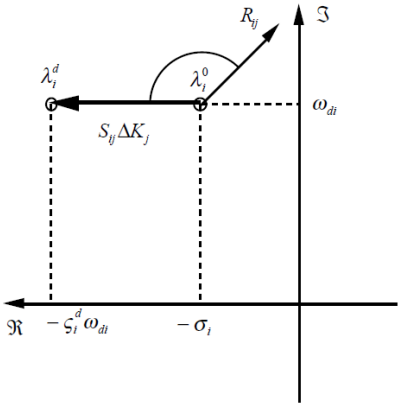


Figure 7.7: Interpretation of the eigenvalue sensitivities.

In VSC-MTDC systems, different input/output signals could be used in POD controllers [69]. A general structure of a POD controller in a VSC

[2] Fig. 7.7 was obtained from [181].

station of a VSC-MTDC system is shown in Fig. 7.8, giving a general POD transfer function as:

$$F(s) \quad = \quad K_S \cdot \frac{sT_w}{1+sT_w}\Big(\frac{1+sT_{S1}}{1+saT_{S1}}\Big)^{N_S} \tag{7.5}$$

where $K_S$ is the gain, $T_w$ is the parameter of the washout filter and $(T_{S1}, a, N_S)$ are the parameters of the lead/lag filter, which is used to compensate the phase of the eigenvalue sensitivity.

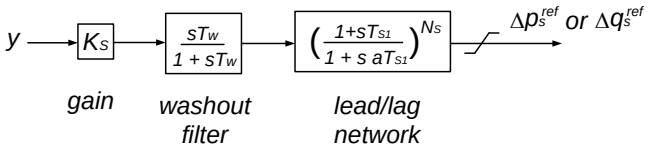


Figure 7.8: POD controller.

Motivated by the good results obtained modulating P and Q injections of the VSCs using the weighted-average frequency error as input signal, POD controllers using that signals will be investigated in this thesis. The proposed POD controllers for P and Q injections of the VSCs, which will be called P-WAF-POD and Q-WAF-POD, are shown in Fig. 7.9, where the frequency set point is the weighted-average frequency:

$$\omega_i^* = \bar{\omega} = \sum_{k=1}^{n} \alpha_k \omega_k, \quad \text{with} \quad \alpha_k \in [0,1] \text{ and } \sum_{k=1}^{n} \alpha_k = 1. \tag{7.6}$$

The controllers of Fig. 7.9 have the following characteristics:

- P-WAF-POD (Fig. 7.9a): Gains $k_{P,j}$ of the supplementary controllers will verify:

$$k_{P,i} = \alpha_i k_{P,T}, \;\; k_{P,T} = \sum_{j=1}^{n} k_{P,j}, \tag{7.7}$$

  where $\alpha_i$ is the weighting factor used to compute the weighted-average frequency.

  Therefore, $\sum_{j=1}^{n} \Delta p_{s,j}^{ref} \simeq 0$ will be ensured during transients, avoiding undesirable interactions with the power and DC-voltage control of the DC grid, which is the most important aspect in the control of VSC-MTDC systems.

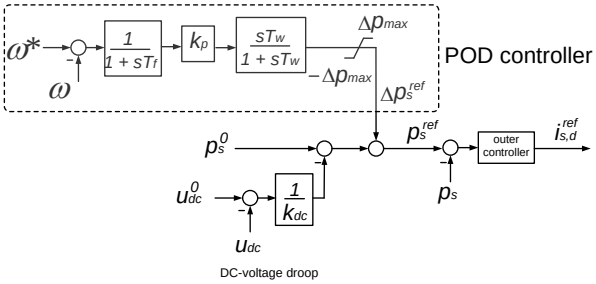


(a) P-WAF-POD

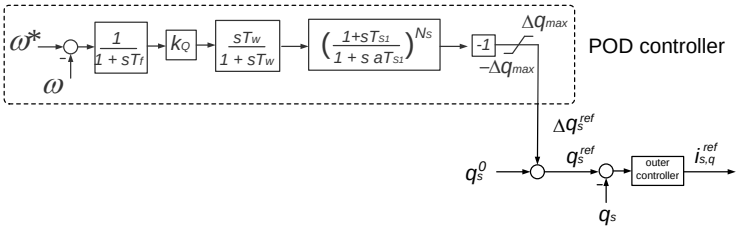


(b) Q-WAF-POD

Figure 7.9: Proposed POD controllers.

Furthermore, the supplementary controllers for P injections will not have lead/lag filters, as in [69, 71].

Notice that these assumptions imply that the controllers will have less flexibility to damp electromechanical oscillations. Nevertheless, the efectiveness of this controller to damp electromechanical oscillations has been already showed by numerical simulation in Subsection 7.3 ( and a detailed analysis can be found in Appendix F.1).

- Q-WAF-POD (Fig. 7.9b): Since the control of the Q injection of each VSC in a VSC-MTDC is independent from the others, no constraints in the gains $k_{Q,j}$ are added and a lead/lag filter is included for each controller, looking for the most effective control action.

The transfer function of P and Q controllers in the hybrid representation (see Fig. 7.6) is given by:

$$F_{P,j}(s) = k_{P,j} \cdot \frac{1}{1+sT_f} \cdot \frac{sT_w}{1+sT_w}, \tag{7.8}$$

$$F_{Q,j}(s) = (-1) \cdot k_{Q,j} \cdot \frac{1}{1+sT_{f,j}} \cdot \frac{sT_{w,j}}{1+sT_{w,j}} \cdot \left(\frac{1+sT_{S1,j}}{1+sa_jT_{S1,j}}\right)^{N_{S,j}}, \tag{7.9}$$

Notice that in Fig. 7.6 the open-loop system is the complete linearised model of the hybrid AC/DC system derived in Chapter 6. The observability factor of the weighted-average frequency error and the controlability factors of the P and Q injections of the VSCs are described in Section E.2.

### 7.4.1 Residues and eigenvalue sensitivities in the Nordic32A test system with a VSC-MTDC system

The purpose of this subsection is to evaluate the residues of the POD controllers proposed in Fig. 7.9 in the Nordic32A system with a VSC-MTDC system (Section A.3.2). The magnitude of the residues will determine whether the proposed controllers are suitable to damp the electromechanical modes and the phase of the residues will dertermine the angle compensation required in the controllers to be able to damp each electromechanical mode.

As explained in Fig. 7.7, the ideal POD controller will have an eigenvalue sensitivity of 180°. The closer the sensitivity phase is to 180° ($\varphi_S$), the more efficient the POD controller will be. It is not always possible to obtain $\varphi_S = 180°$ exactly, but the POD controller wil still be able to damp a mode,

Table 7.5: Nordic32A system with a VSC-MTDC. Electromechanical modes of interest written in polar form.

| Mode | magnitude (rad/s) | phase (deg) |
|---|---|---|
| A | 2.2896 | 92.52 |
| B | 3.6164 | 93.72 |
| C | 5.2821 | 92.56 |
| D | 6.0780 | 92.27 |
| E | 6.2373 | 91.77 |
| F | 7.3013 | 92.43 |
| G | 7.3604 | 94.85 |
| H | 7.4625 | 92.21 |

satisfactory, if the angle of the mode sensitivityverifies:

$$\varphi_z - 180^\circ < \varphi_S < \varphi_z \tag{7.10}$$

where $\varphi_z$ is the phase of the mode.

This is illustrated in Fig. 7.10, [3] where the geometric interpretation of eigenvalue sensitivities with different phases are showed. Sensitivity $S_1$ is the best option, since its phase is 180° and the controllers pushes the eigenvalue to the left hand side. The phases of $S_2$ and $S_3$ are not $\varphi_S = 180^\circ$, but they verify (7.10) and, therefore, the controller will increase the damping ratio of the mode. If the phase of the sensitivity is equal to the phase of the eigenvalue (as with $S_4$), the damping ratio of the mode will do not change. Controllers with sensitivity $S_5$ will decrease the damping ratio, since they do not verify (7.10). Finally, damping will not deteriorate with controllers with sensitivity $S_6$, but the latter is not recommended, since the mode will be moved to the right hand side of the complex plane.

The magnitude and phases of the electromechanical modes of Table 7.1 are given in Table 7.5. The phase of the electromechanical modes A-E are slightly greater than 90°. therefore, it can be stated that POD controllers with sensitivities to those modes within the range $(-90^\circ, 90^\circ)$ will improve their damping ratio.

The residues of the proposed controllers P-WAF-POD and Q-WAF-POD

[3] Fig. 7.10 was obtained and modified from [181].

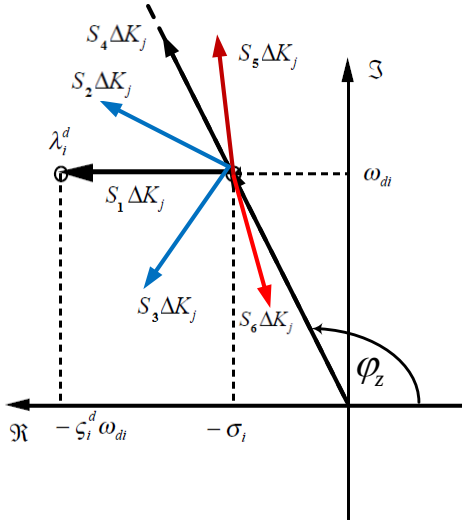


Figure 7.10: Eigenvalue sensitivities.

(of Fig. 7.9) for each VSC are shown in Fig. 7.11. The phase of the residues are represented in the range $[0, 360°]$, for the sake of clarity. This means that the residues with phases within $(90°, 270°)$ will contribute to damp the corresponding mode. For example, the residue of VSC1 to inter-area mode B when using P-WAF-POD presents a high sensitivity. On the other hand the phase of sensitivity to inter-area mode A when using strategy P-WAF-POD (at VSC1) is 330°, and will contribute to reduce the damping ratio.

The sum of the residues obtained for all the converters of the VSC-MTDC system when (a) modulating the P injections with P-WAF-POD, (b) modulating the Q injections with Q-WAF-POD (c) modulating simultaneously the P and Q injections are shown in Fig. 7.12. The sum of the residues gives useful insight into the effect of POD controllers in the VSC-MTDC system on the modes of interest.

P modulation (Fig. 7.9a) could be used to damp inter-are modes B and C, since they have a high value of total residue and the phase is close to 180°. On the contrary, the total effect of P modulation on mode A is negative, since the phase of the residue is close to 330°. The total effect of P modulation in the VSC-MTDC system on eigenvalues D-H is low, since the magnitudes of their total residue are low.

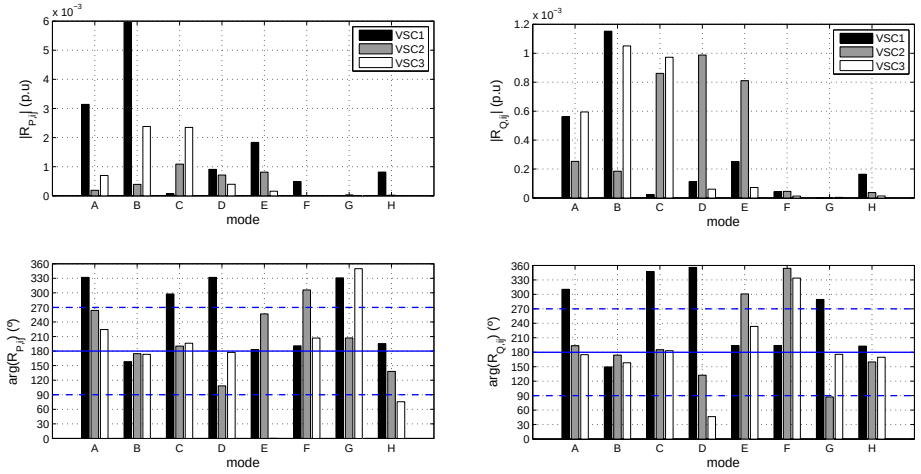


Figure 7.11: Residues (p.u-nom). (a) P-WAF-POD. (b) Q-WAF-POD.

Q modulation (Fig. 7.9b) would have a positive impact on inter-area modes A, B and C, because the phase of the residues of those modes are within the range $(90°, 270°)$ and they are close to 180°. Nevertheless, the magnitudes of the residues of those modes controlling Q injections are lower than the ones obtained when controlling P injections. Low impact of POD controllers for Q injections on modes D-H is expected, since the magnitude of the residues of those modes are small. The proposed POD controller for Q injections (Fig. 7.9b) has a lead/lag filter. Therefore, the phase of the residues can be compensated to obtain a phase of the sensitivities close to 180°.

The main conclusion obtained from the results of Fig. 7.12 is that inter-area modes B and C are the ones that can be better damped by the controllers of the converter sations of the VSC-MTDC system.

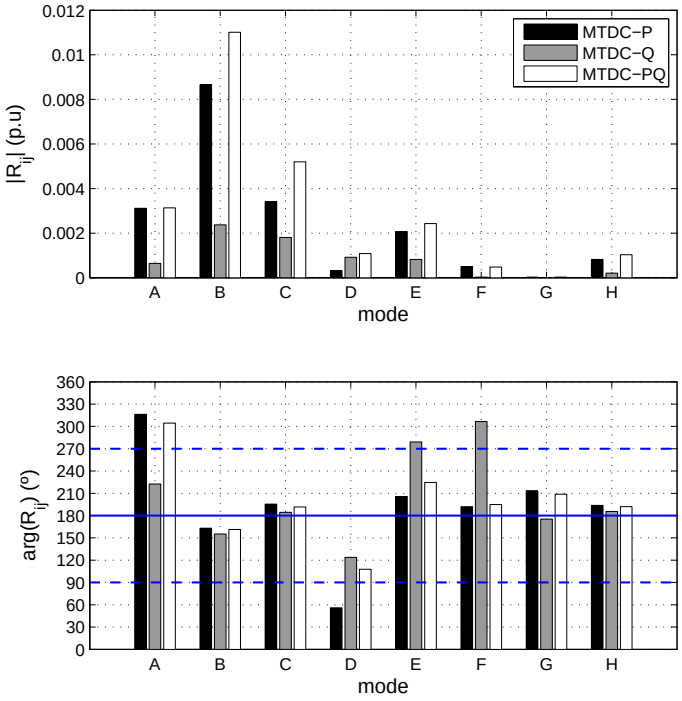


Figure 7.12: Total residues (p.u-nom). (sum of the residues of all the VSCs)

## 7.5 Coordinated design of control strategies for power-oscillation damping

The algorithm for coordinated design of multiple controllers proposed in [64] has been applied to VSC-MTDC systems in this thesis. The problem consists in trying to damp a set of modes of interest $i = 1, \dots N_E$ using P and Q damping controllers on a set of VSCs $i = 1, \dots N_C$. The algorithm of [64] is based on eigenvalue sensitivities and it consists of two steps, which applied to VSC-MTDC systems are:

1. Design of the lead/lag filters of the Q controllers, only.

2. Computation of the gains of the P and Q controllers.

### 7.5.1 Design of the lead/lag filters

The first step consist in determining the time constant $T_{S1,j}$ of each lead/lag filter of Q controllers to have the phase of the eigenvalue sentitivities as close as possible to 180°. This requires the solution of the following optimisation problem for $T_{S1,j}$ [64]:

$$\min_{T_{S1,j}} G(T_{S1,j}) = \min_{T_{S1,j}} \sum_{i=1}^{N_E} \beta_{ij} \cos\{\arg[S_{ij}(T_{S1,j})]\}, \tag{7.11}$$

$$\beta_{ij} = \frac{R_{ij}}{\sum_{k=1}^{N_E} |R_{kj}|}, \quad S_{ij}(T_{S1,j}) = R_{ij} \frac{\partial F_{Q,j}(s)}{\partial k_{Q,j}}\Big|_{s=\lambda_i}. \tag{7.12}$$

The lead/lag filters are only present in the Q controllers to avoid interactions of the P controllers with the DC-voltage droop controllers.

### 7.5.2 Computation of the controller gains

The electromechanical modes to be damped, at the initial operating point, are defined as:

$$\lambda_i^0 = \sigma_i^0 \pm j\omega_{d,i}^0, \ \forall i = 1, \dots, N_E \tag{7.13}$$

If a damping ratio of $\zeta_i^d$ is required for each mode of (7.13), the target eigenvalues will take the form of:

$$\lambda_i^d = -\zeta_i^d \omega_{d,i}^0 \pm j\omega_{d,i}^0, \ \forall i = 1, \dots, N_E \tag{7.14}$$

Equation (7.14) assumes that the controllers are capable of producing 180° in the eigenvalue sensitivities, since the imaginary parts of the original and required modes remain unchanged.

The gains of the controllers are obtained by solving an optimisation problem to minimise the total control effort of the controllers [64]:

$$\min_{\Delta k_{P,j},\Delta k_{Q,j}} \sum_{j=1}^{N_C} \{\gamma_{P,j}\Delta k_{P,j}^2 + \gamma_{Q,j}\Delta k_{Q,j}^2\} \tag{7.15}$$

where $N_C$ is the number of VSCs that participate with the POD controllers, $\Delta k_{P,j} = k_{P,j} - k_{P,j}^0$, $\Delta k_{Q,j} = k_{Q,j} - k_{Q,j}^0$ and $\gamma_{P,j}$ and $\gamma_{Q,j}$ are weighting factors for the gains, to quantify the control effort of the controllers. Different criteria can be used to choose the weighting factors. For example, in [64] the weight for each controller $j$ is chosen as the sum of the absolute values of the sentitivities of each mode with respect to the gain of each controller. In this thesis, the control effort will be distributed by taking into account the size of each converter and equal weights for P and Q controllers will be used. Hence:

$$\gamma_{P,j} = \gamma_{Q,j} = \gamma_j = \frac{1/S_{N,j}}{\sum_{k=1}^{N_C} 1/S_{N,k}} \quad \forall j = 1,\ldots,N_C \tag{7.16}$$

where $S_{N,j}$ is the nominal apparent power of VSC$j$. Since in the test system used in this thesis the converters have the same rating, equal weight for each converter will be given in (7.15).

The constraints of the optimisation problem (7.15) are:

$$\sum_{j=1}^{N_C} \Big\{ Re\Big(\frac{\partial \lambda_i}{\partial k_{P,j}}\Big)\Delta k_{P,j} + Re\Big(\frac{\partial \lambda_i}{\partial k_{Q,j}}\Big)\Delta k_{Q,j} \Big\} \leq Re(\lambda_i^d - \lambda_i^0), \tag{7.17}$$

$$\forall i = 1,\ldots,N_E$$

$$k_{P,j}^{min} \leq k_{P,j} \leq k_{P,j}^{max}, \quad \forall j = 1,\ldots,N_C \tag{7.18}$$

$$k_{Q,j}^{min} \leq k_{Q,j} \leq k_{Q,j}^{max}, \quad \forall j = 1,\ldots,N_C \tag{7.19}$$

$$k_{P,j} = \alpha_j \sum_{k=1}^{N_C} k_{P,k} = \alpha_j k_{P,T}, \quad \forall j = 1,\ldots,N_C \tag{7.20}$$

where constraint (7.17) ensures that the estimated eigenvalues achive the desired damping, constraints (7.18) and (7.19) determine the range allowed

for the gains of P and Q controllers, respectively, and constraint (7.20) is used to guarranty the power balance in the active-power set points of the P controller. Notice that constraint (7.20) is condition (7.7), only imposed for the P controllers, and $\alpha_j$ is the weight of the frequency of VSC$j$ when computing the weighted-average frequency.

Finally, the estimated eigenvalues can be computed as:

$$\lambda_i^e = \lambda_i^0 + \sum_{j=1}^{N_C} \Big[ \Big( \frac{\partial \lambda_i}{\partial k_{P,j}} \Big) \Delta k_{P,j} + \Big( \frac{\partial \lambda_i}{\partial k_{Q,j}} \Big) \Delta k_{Q,j} \Big], \quad \forall i = 1, \ldots, N_E \tag{7.21}$$

The accuracy of the algorithm will be reasonably good if the eigenvalue sensitivities are almost linear within the range of change in the controller gains and if the angles of the eigenvalue sensitivities are close to 180°. If any of these two conditions is not satisfied, the algorithm will not be able to predict accurately the resulting dampings. However, even without much accuracy, the design provided by the algorithm should be able to improve the initial damping ratios of the electromechanical modes of interest.

## 7.6 Results

Again, the Nordic32A system with a VSC-MTDC in the heavily loaded scenario (Section A.3.2) has been used as a case study. The algorithm described in Section 7.5 has been used to design power-oscillation controllers in the VSCs, using the weighted-average frequency error as input signal and using the P and Q injections as input signals, following the schemes of Fig. 7.9. The algorithm will provide the gains of the POD controllers ($k_{P,i}$ and $k_{Q,i}$) and the parameters of the lead/lag network of the Q controller. The measurement filter and the washout time constants are set to $T_f = 0.1$ s and $T_w = 15$ s (see Fig. 7.9). The weights used to compute the average frequency are $\alpha_i = 1/3$. The capability of damping the electromechanical modes of Table 7.1 will be analysed.

### 7.6.1 Design 1: damping inter-area mode B

First of all, the algorithm of Section 7.5 is used to damp the inter-area mode B of Table 7.1. The required damping ratio for mode B was set to 12%.

The gains provided by the algorithm are provided in Table 7.6 and the original, estimated and final modes are compared in Table 7.7. Notice that equal gains are selected for the P controller of each converter ($k_{P,i}$), according

to constraint (7.20). On the other hand, the gains of the Q controllers are free and they do not have any additional constraint ($k_{Q,i}$). The real part of mode B is moved to the left hand side of the complex plane due to the effect of the controllers, increasing the damping from 6.50 % to 11.09 %.

The effect of the controllers on the rest of electromechanical modes A-H is analysed in Table 7.8. With the design of Table 7.6, the damping of mode C increases slightly from 4.46 % to 6.06 %, but the damping of mode A decreases slightly from 4.37 % to 3.37 %. The impact on the rest of the modes is very small.

Table 7.6: POD controller parameters.

| Converter | P | | | | Q | | | |
|---|---|---|---|---|---|---|---|---|
| | $k_{P,i}$ (p.u) | $T_{S1,i}$ (s) | $a_i$ | $N_{S,i}$ | $k_{Q,i}$ (p.u) | $T_{S1,i}$ (s) | $a_i$ | $N_{S,i}$ |
| VSC1 | 29.63 | - | - | - | 18.82 | 0.4848 | 0.135 | 1 |
| VSC2 | 29.63 | - | - | - | 2.88 | 0.6317 | 0.402 | 1 |
| VSC3 | 29.63 | - | - | - | 14.83 | 0.4046 | 0.207 | 1 |

Table 7.7: Results on the mode of interest.

| Mode | Original | Estimated | New |
|---|---|---|---|
| B | $-0.2348 \pm j3.6088$ | $-0.4331 \pm j3.7053$ | $-0.4144 \pm j3.7131$ |
| | 6.50 %, 0.57 Hz | 11.61 %, 0.59 Hz | 11.09 %, 0.59 Hz |

Table 7.8: Modes

| Mode | Original | New |
|---|---|---|
| A | $-0.1006 \pm j2.2873$<br>4.37 %, 0.36 Hz | $-0.0753 \pm j2.2313$<br>3.37 %, 0.36 Hz |
| B | $-0.2348 \pm j3.6088$<br>6.50 %, 0.57 Hz | $-0.4144 \pm j3.7131$<br>11.09 %, 0.59 Hz |
| C | $-0.2356 \pm j5.2768$<br>4.46 %, 0.84 Hz | $-0.3208 \pm j5.2860$<br>6.06 %, 0.84 Hz |
| D | $-0.2403 \pm j6.0733$<br>3.95 %, 0.97 Hz | $-0.2302 \pm j6.0770$<br>3.78 %, 0.97 Hz |
| E | $-0.1925 \pm j6.2343$<br>3.09 %, 0.99 Hz | $-0.2379 \pm j6.2328$<br>3.81 %, 0.99 Hz |
| F | $-0.3094 \pm j7.2948$<br>4.24 %, 1.16 Hz | $-0.3172 \pm j7.2979$<br>4.34 %, 1.16 Hz |
| G | $-0.6223 \pm j7.3340$<br>8.45 %, 1.17 Hz | $-0.6229 \pm j7.3341$<br>8.46 %, 1.17 Hz |
| H | $-0.2882 \pm j7.4570$<br>3.86 %, 1.19 Hz | $-0.3081 \pm j7.4584$<br>4.12 %, 1.19 Hz |

### 7.6.2 Design 2: damping of several modes

According to the studies of Sections 7.3 and 7.4, inter-area modes B and C can be damped relatively easily with P and Q modulation in the VSC stations of the VSC-MTDC system. Different is the case of inter-area mode A and local mode E. The modulation of P injections tend to reduce the damping ratio of mode A for low value of the gains (see Table 7.2), while Q modulation slightly reduces the damping ratio of mode E (see Table 7.3)).

An attempt has been made to damp modes B and C, while ensuring that the damping ratios of modes A and E do not deteriorate. The target damping ratios for modes A, B, C and E are described in Table 7.9.

The design obtained from the algorithm described in Section 7.5 is shown in Table 7.10 and the old, estimated and new eigenvalues are compared in Table 7.11. Results show that significant improvements in the damping ratio of inter-area modes B and C could be obtained, without damaging the damping ratio of the rest of electromechanical modes. The damping ratio of mode B was improved from 6.50 % to 18.93 % and the damping of mode C was improved from 4.46 % to 11.65 %.

Table 7.9: Required damping ratios.

| Mode | required damping |
|---|---|
| A | 5 % |
| B | 12 % |
| C | 12 % |
| E | 5 % |

Table 7.10: POD controller parameters.

| Converter | P | | | | Q | | | |
|---|---|---|---|---|---|---|---|---|
| | $k_{P,i}$ (p.u) | $T_{S,i}$ (s) | $a_i$ | $N_{S,i}$ | $k_{Q,i}$ (p.u) | $T_{S1,i}$ (s) | $a_i$ | $N_{S,i}$ |
| VSC1 | 52.05 | - | - | - | 14.24 | 0.2578 | 0.295 | 1 |
| VSC2 | 52.05 | - | - | - | 69.09 | 0.0699 | 1.783 | 1 |
| VSC3 | 52.05 | - | - | - | 124.07 | 0.4475 | 0.357 | 1 |

Table 7.11: Results on system modes.

A:

| Mode | Original | Estimated | New |
|---|---|---|---|
| A | $\mathbf{-0.1006 \pm j2.2873}$ | $\mathbf{-0.1144 \pm j2.1352}$ | $\mathbf{-0.1483 \pm j2.1832}$ |
| | 4.37 %, 0.36 Hz | 5.35 %, 0.34 Hz | 6.78 %, 0.35 Hz |
| B | $\mathbf{-0.2348 \pm j3.6088}$ | $\mathbf{-0.8154 \pm j3.9181}$ | $\mathbf{-0.7702 \pm j3.9958}$ |
| | 6.50 %, 0.57 Hz | 20.38 %, 0.62 Hz | 18.93 %, 0.64 Hz |
| C | $\mathbf{-0.2356 \pm j5.2768}$ | $\mathbf{-0.6446 \pm j5.3260}$ | $\mathbf{-0.6257 \pm j5.3342}$ |
| | 4.46 %, 0.84 Hz | 12.02 %, 0.85 Hz | 11.65 %, 0.85 Hz |
| D | $-0.2403 \pm j6.0733$ | - | $-0.2097 \pm j6.0797$ |
| | 3.95 %, 0.97 Hz | - | 3.45 %, 0.97 Hz |
| E | $\mathbf{-0.1925 \pm j6.2343}$ | $\mathbf{-0.3117 \pm j6.1906}$ | $\mathbf{-0.3157 \pm j6.2423}$ |
| | 3.09 %, 0.99 Hz | 5.03 %, 0.99 Hz | 5.05 %, 0.99 Hz |
| F | $-0.3094 \pm j7.2948$ | - | $-0.3224 \pm j7.3026$ |
| | 4.24 %, 1.16 Hz | - | 4.41 %, 1.16 Hz |
| G | $-0.6223 \pm j7.3340$ | - | $-0.6244 \pm j7.3344$ |
| | 8.45 %, 1.17 Hz | - | 8.48 %, 1.17 Hz |
| H | $-0.2882 \pm j7.4570$ | - | $-0.3272 \pm j7.4705$ |
| | 3.86 %, 1.19 Hz | - | 4.38 %, 1.19 Hz |

### 7.6.3 Discussion

The results presented in subsections 7.6.1 and 7.6.2 have shown the effectiveness of using the algorithm for de coordinated deisgn of damping controllers in VSC-MTDC systems, described in Section 7.5. Furthermore, the algorithm showed to be very flexible, allowing to damp different inter-area modes guaranteeing a minimum damping ratio of the rest of the electromechanical modes.

Nevertheless, the algorithm described in Section 7.5 could present inaccuracies if too many eigenvalues are tackled, or if the eigenvalue sensitivities with respect to the controller gains are not big enough. Besides, if too high gains are required, the eigenvalue sensitivities would not be linear any more and, therefore, less accuracy would be obtained in the design. Hence, the set of modes to be damped should have high eigenvalue sensitivities to obtain a good design.

## 7.7 Time-domain simulation

The proposed POD controllers with the designs of Tables 7.6 and 7.10 have been tested by non-linear time-domain simulation in PSS/E. The test system is again the heavily loaded Nordic32A grid (see Section A.3.2) and all the parameters have the same values as in Subsection 7.6. Usually the POD controllers should saturate when large disturbances occur, since they are aimed to act only under small perturbations. The saturation parameter values of Fig. 7.9 are set to $\Delta p_{max,i} = \Delta q_{max,i} = 0.2$ p.u, in these simulation studies. The time constants of the measurement and the washout filters were set to $T_{f,i} = 0.1$ s and $T_{w,i} = 15$ s, respectivelly ( Fig. 7.9). Finally, the weights used to compute the average frequency were set to $\alpha_i = 1/3$, again.

Line 4012-4022 is disconnected at $t = 1$ s (see Fig. A.3 of Section A.3) and the behaviour of the following strategies has been compared:

- Base case: with no control modulation (DC0)
- Proposed POD controller (Fig. 7.9) using the design 1 (Table 7.6)
- Proposed POD controller (Fig. 7.9) using the design 2 (Table 7.10)

The angle difference between machines G4072 and G4063 and the total active-power flow through corridor 4031-4041 (circuits a and b) are shown in Fig. 7.13. P and Q injections of the VSC stations are shown in Fig. 7.14.

The responses of the rotor-angle difference (Fig. 7.13a) and the active-power flow through the corridors (Fig. 7.13b) clearly show that the POD controllers with both designs damp electromechanical oscillations succesfully, in comparison to the base case (DC0). The best response is obtained with design 2 of the proposed POD controller (Table 7.10), as expected, since it uses higher gain values. Therefore, P and Q changes with the POD controller with the design 2 are larger (Fig. 7.14). Fig. 7.14 also shows that large changes in P and Q injections are not required by the POD controllers, and they never saturate.

Therefore, the results presented in this subsection confirm by non-linear time-domain simulation that the proposed POD controllers (Tables 7.6 and 7.10) designed using the algorithm presented in Section 7.5 can damp efficiently the inter-area oscillations. Design 2 produces the best results.

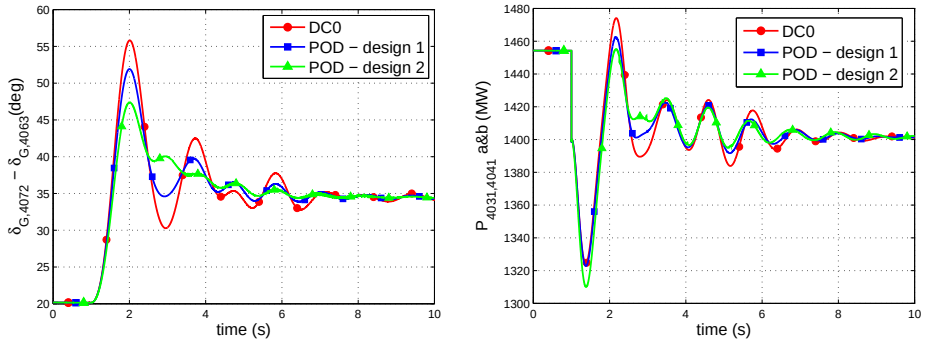


(a) (b)

Figure 7.13: Line 4012-4022 disconnected. (a) Angle difference of generators G4072 and G4063. (b) Power flow through corridor 4031-4041 a&b.

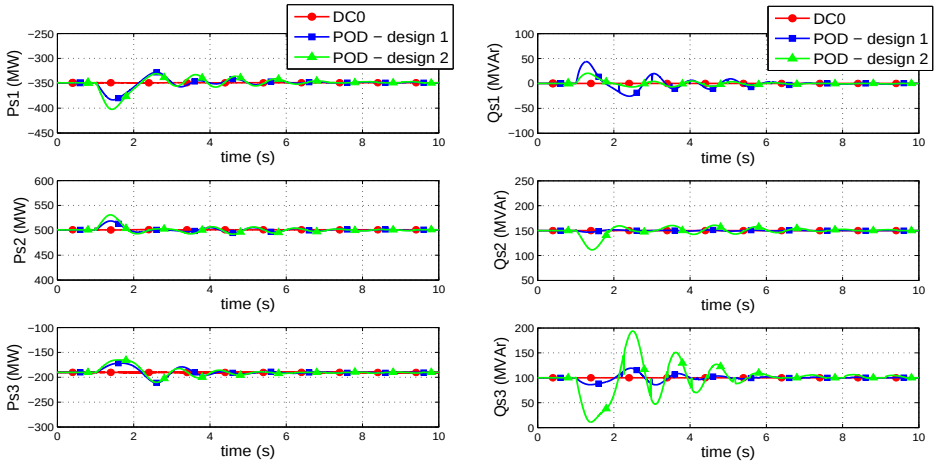


(a) P injections ($P_{s,i}$). (b) Q injections ($Q_{s,i}$).

Figure 7.14: Line 4012-4022 disconnected.

## 7.8 Conclusions

The results presented in this chapter have shown that:

- Transient-stability controllers:
  - In general, strategies P-WAF, Q-WAF, Q-LWAF and simultaneous modulation of P and Q injections of the VSCs (PQ-WAF) can help to damp electromechanical oscillations, specially inter-area oscillations.
  - Strategies P-WAF, Q-WAF, Q-LWAF and PQ-WAF increase the damping ratio of inter-area modes B and C (of the case study) significantly.
  - The damping ratio of inter-area mode A (of the case study) deteriorates slightly with strategy P-WAF. This problem can be tackled re-designing the controller gains.
  - Strategies Q-WAF and Q-LWAF reduce slightly the damping ratio of local mode E. This local mode could be damped by a PSS in a generator.

  - Strategy PQ-WAF is either neutral or improves the damping ratio of the electromechanical modes.

- POD controllers:
  - The proposed POD controllers proved to be capable of damping a required set of modes, obtaining the required damping ratios.
  - The coordinated-design algorithm for the design of POD controllers proved to be extremely flexible. This allows, for example, to give priority to P or Q modulation, if desired. As rule of thumb, if similar results can be obtained, Q modulation will be always preferred to P modulation.
- Whether a converter in a VSC-MTDC system should have a transient-stability or a POD controller will depend on the phenomenon of interest in each particular scenario. Further research would be needed to analyse the implementation of both types simultaneously.

# Chapter 8

# Conclusions and contributions

The aim of this thesis was to investigate control strategies in VSC-MTDC systems to improve angle stability in hybrid HVAC/HVDC grids (under large and small disturbances). This chaper summarises the conclusions and contributions of this PhD thesis and proposes research lines for future work.

## 8.1 Conclusions

The main conclusions and findings obtained in this thesis are classified and summarised below.

### 8.1.1 Control strategies for transient stability improvement

**Active-power control strategies**

- P-WAF (global):
  - Strategy P-WAF improves transient stability significantly.
  - The advantage of strategy P-WAF in comparison with previous ones for VSC-MTDC systems is that it uses easy-to-implement global measurements: it uses the weighted-average frequency of the AC terminals of the VSC stations, while previous approaches use global mesurements of the speeds of all the generators of the system.
  - In general, higher gains in strategy P-WAF produce better results, although converter limits must be considered. A compromise must be reached. Good results were obtained with $k_{P,i} = 200$ p.u.

  - The impact of the communication latency on strategy P-WAF is very small.

- P-LF (local):

  - The improvements on transient stability produced by local strategy P-LF are very limited, since the DC-voltage fluctuations jeopardise the performance of this control strategy.

**Reactive-power control strategies**

- Q-WAF (global):

  - Strategy Q-WAF improves transient stability significantly.
  - Again, the advantage of the proposed strategy Q-WAF in comparison to previous ones for VSC-MTDC systems is that it uses easy-to-implement global measurements: it uses the weighted-average frequency of the AC terminals of the VSC stations, while previous approaches use global mesurements of the speeds of all the generators of the system.
  - In general, higher gains in strategy Q-WAF produce better results, although converter limits must be considered. A compromise must be reached. Good results were obtained with $k_{Q,i} = 200$ p.u.
  - Results showed that strategy Q-WAF produces good results for realistic values of the communication delays. However, Q-WAF deteriorates more than P-WAF with communication latency.

- Q-LWAF (local):

  - Local strategy Q-LWAF improves transient stability significantly.
  - Local strategy Q-LWAF behaves very much like the global strategy Q-WAF, with the advantage that no communications between the VSC stations is required.

**Simultaneous active- and reactive-power modulation (PQ-WAF)**

- Simultaneous P and Q modulation in the VSC stations using strategies P-WAF and Q-WAF was also tested. Better results are obtained than those when modulating either only P or only Q, but the differences are small.

- When comparing the achievements of PQ-WAF, with P-WAF and Q-WAF, respectively, it was found that, in severe faults involving corridors in parallel with the VSC-MTDC system, P modulation is more effective than Q modulation. Nevertheless, with Q modulation the active-power injections are maintained constant, avoiding any risk of interaction with the power balance of the DC grid, which is always an advantage.

### 8.1.2 Control strategies for power-oscillation damping (POD)

Small-signal stability techniques have been used for two purposes in hybrid HVAC/VSC-HVDC systems : (1) to analyse the capability of the proposed transient stability control strategies to damp power oscillations and (2) to design specific controllers for power-oscillation damping.

1. Transient-stability controllers:

   - In general, strategies P-WAF, Q-WAF, Q-LWAF and simultaneous modulation of P and Q injections of the VSCs (PQ-WAF) can help to damp power oscillations, specially inter-area oscillations.
   - It was found that the damping ratio of a few electromechanical modes could be reduced slightly when using strategies P-WAF, Q-WAF or Q-LWAF. Nevertheless, this problem can be easily tackled by re-designing the controller gains or using strategy PQ-WAF.
   - Strategy PQ-WAF (both P and Q modulation) proved to be the best option to improve transient stability while damping power oscillations.

2. POD controllers:

   - The proposed POD controllers (designed using the coordinated-design method) proved to be capable of damping a required set of modes, obtaining the required damping ratios.
   - The coordinated-design algorithm for the design of POD controllers proved to be extremely flexible, prioritising P or Q modulation. As a general rule, if similar results can be obtained, Q modulation will be always preferred to P modulation.

## 8.2 Contributions of the thesis

The scientific contributions of this thesis can be summarised as follows.

### 8.2.1 Control strategies for transient stability improvement

**Active-power control strategies**

- Proposal of a P-control strategy for VSC-MTDC systems using global-but-practical measurements to improve transient stability (P-WAF).
- Proposal of a P-control strategy for VSC-MTDC systems using local measurements to improve transient stability (P-LF).
- Theoretical analysis of the proposed P-control strategies for VSC-MTDC systems applying Lyapunov's theory.
- Numerical analysis of the proposed P-control strategies for VSC-MTDC systems.
- Discussion and comparison of the use of local and global measurements in P-control strategies.

**Reactive-power control strategies**

- Proposal of a Q-control strategy for VSC-MTDC systems using global-but-practical measurements to improve transient stability (Q-WAF).
- Proposal of a Q-control strategy for VSC-MTDC systems using local measurements to improve transient stability (Q-LWAF).
- Theoretical analysis of the proposed Q-control strategies for VSC-MTDC systems applying Lyapunov's theory.
- Numerical analysis of the proposed Q-control strategies for VSC-MTDC systems.
- Discussion and comparison of the use of local and global measurements in Q-control strategies.

**Active- and reactive-power simultaneous modulation (PQ-WAF)**

- Simultaneous P and Q modulation (P-WAF + Q-WAF) has also been investigated and its advantages have been unveiled.

### 8.2.2 Small-signal analysis and control strategies for power-oscillation damping

- Modelling of VSC-MTDC systems for small-signal stability analysis using a modular form and a systematic procedure.
- Small-signal analysis of the control strategies proposed to improve transient stability.
- Design of controllers for power-oscillation damping (POD) in VSC-MTDC systems, using a coordinated-design algorithm.

### 8.2.3 Software production

- A tool for power-flow calculations with VSC-MTDC systems built into a conventional HVAC transmission system has been developed in PSS/E.

  It uses a sequential AC/DC power-flow algorithm proposed previously in the literature. The main subroutine has been coded in Pyhton and it calls PSS/E to solve the AC power flow. The rest of the subroutines required were also coded in Python.
- A tool for electromechanical simulation of VSC-MTDC systems in PSS/E has been developed.

  The VSC stations and the DC grids were coded in Fortran as PSS/E user-defined models.
- A model for VSC-MTDC systems has been coded for SSST, which is a Matlab-based tool for small-signal analysis of large power systems developed by the Institute for Research in Technology (IIT).
- Validation of all the tools developed.

### 8.2.4 Publications

#### Journal papers

- J. Renedo, A. García-Cerrada, and L. Rouco, *"Active Power Control Strategies for Transient Stability Enhancement of AC/DC Grids With VSC-HVDC Multi-Terminal Systems,"* IEEE Transactions on Power Systems, vol. 31, no. 6, pp. 4595-4604, 2016.

- J. Renedo, A. García-Cerrada and L. Rouco, *"Reactive-Power Coordination in VSC-HVDC Multi- Terminal Systems for Transient Stability Improvement,"* IEEE Transactions on Power Systems,vol. 32, no. 5, pp. 3758-3767, 2017.

**Conference papers and presentations**

- J. Renedo, A. García-Cerrada, L. Rouco,*"VSC-based AC/DC systems: Modelling, simulation and applications,"* 9th Seminar for Next Generation of Researchers in Power Systems. Beijing, China, 20-22 April 2017.

- J. Renedo, A. García-Cerrada, L. Rouco, L. Sigrist, I. Egido, S. Sanz Verdugo, *"Development of a PSS/E tool for power-flow calculation and dynamic simulation of VSC-HVDC multi-terminal systems,"* 13th IET international conference on AC and DC Power Transmission - ACDC 2017. Paper presented in the poster session. Manchester, United Kingdom, 14-16 February 2017.

- J. Renedo, A. García-Cerrada and L. Rouco, *"Mejora de la estabilidad transitoria de redes CA/CC con sistemas multiterminales de CC con convertidores fuente de tensión,"* Jornadas Técnicas del Comité Nacional de Cigre. Madrid, Spain, 22-23 November 2016.

- J. Renedo, A. García-Cerrada and L. Rouco, *"Transient stability enhancement of HV-AC/DC grids with VSC-HVDC multi-terminal systems,"* 46 CIGRE Session, Paris, France, 21-26 August 2016.

**Working papers**

- J. Renedo, L. Rouco, A. García-Cerrada and L. Sigrist, *"Improving transient stability using a communication-free control strategy in VSC-HVDC multi-terminal systems",* Working paper, Internal number: IIT-17-005A. Available online: www.iit.comillas.edu/people/jrenedo (accessed 25-07-2017), pp.1-8, 2017.

## 8.3 Proposals for further research

The results obtained in this thesis open the following research lines:

1. Further research on cotrol algorithms to improve transient stability using the weighted-average frequency (WAF) in VSC-MTDC systems.

   The control strategies proposed for transient stability (P-WAF and Q-WAF) used a proportional controller and gave good results. Nevertheless, more complex control algorithms (PD, PID or model predictive controllers) could now be investigated (as in [48]) using the WAF.

2. A thorough study on the design of the averaging weights $\alpha_i$ when calculating the WAF.

   In most of the results of this thesis, the averaging weights to compute the WAF have been made equal to the relative gain of the supplementary controllers of the converter stations of the VSC-MTDC system. This ensures zero net supplentary power injection. However, an optimisation problem could be formulated to design the averaging weights in such a way that the improvement of the angle stability is maximised.

3. Further research on POD controllers.

   As shown in Section 7.6 of Chapter 7, the coordinated-design algorithm for POD controllers in VSC-MTDC systems proved to be accurate when damping some specific electromechanical modes. The study on POD controllers carried out in this thesis was limited to the investigation of P and Q controllers using the WAF error as input signal. A more comprehensive study using different input signals (as done in [69]) should be carried out to assess the benefits of using the WAF in comparison with other input signals.

4. Further research on local active-power control stategies.

   Local strategy P-LF was dismissed to improve transient stability, although it was proved useful to estimate the WAF using local measurements. That estimation was used in local strategy Q-LWAF, for the Q injections. Therefore, no effective local control strategies for the P injections of the VSC stations have been proposed in this thesis. The same idea of Q-LWAF could be used for P modulation using local measurements: P-LF can be used to estimate the WAF, and the estimation could be used as frequency set point of a P controller, trying

to mimic strategy P-WAF. Since P-WAF produces $\sum_{i=1}^{n} \Delta p_{s,i}^{ref} \simeq 0$ (see the analysis of Subsection 3.4.1 of Chapter 3), low interaction of the AC-side control strategy and the DC-voltage droop control should be expected. However, active-power control in VSC-MTDC systems is much more delicate than reactive-power control and this idea requires further investigation and testing.

5. Testing the control strategies proposed for angle stability improvement using detailed models of MMC converters.

   In this thesis, simplified electromechanical models of the converter stations in VSC-MTDC systems have been used for time-domain simulation, although they have been validated using eletromagnetic models of 3-level VSC stations. It is reasonable to use electromechanical models for angle stability analysis, since the time constants of interest (the electromechanical oscillations of the synchronous machines) are relatively slow. Nevertheless, due to the ever-growing interest on Modular Multilever Converters (MMCs), it would be interesting to test the proposed control strategies for angle stability improvement using electromagnetic models of MMC stations.

6. Analysis of transient-stability-constrained optimal power flow of hybrid HVAC/VSC-HVDC, taking into account, not only the operating point, but also supplementary control strategies and corrective actions on the VSC-MTDC system.

7. An economical evaluation of the proposed control strategies for the VSC-MTDC system.

# Bibliography


[1] European Commission, "Energy Roadmap 2050," Publication Office of the European Union, Tech. Rep., 2011.

[2] ——, "Energy 2020 - A strategy for competitive, sustainable and secure energy," Publication Office of the European Union, Tech. Rep., 2011.

[3] ——, "Energy Efficiency and its contribution to energy security and the 2030 Framework for climate and energy policy," Communication from the Commision to the European Parliament and the Council, Tech. Rep., 2014.

[4] J. Blau, "Europe plans a North Sea grid," *IEEE Spectrum*, vol. 47, no. 3, pp. 12–13, 2010.

[5] D. Van Hertem and M. Ghandhari, "Multi-terminal VSC HVDC for the European supergrid: Obstacles," *Renewable and Sustainable Energy Reviews*, vol. 14, no. 9, pp. 3156–3163, 2010.

[6] D. Van Hertem, O. Gomis-Bellmunt, and J. Liang (Editors), *HVDC Grids: For Offshore and Supergrid of the Future*. IEEE Press, Wiley, 2016.

[7] E. Pierri, O. Binder, N. G. A. Hemdan, and M. Kurrat, "Challenges and opportunities for a European HVDC grid," *Renewable and Sustainable Energy Reviews*, vol. 70, no. 9, pp. 427–456, 2017.

[8] S. Gordon, "Supergrid to the rescue," *IET Power Engineer*, vol. 20, no. 5, pp. 30–33, 2006.

[9] S. Chatzivasileiadis, D. Ernst, and G. Andersson, "The Global Grid," *Renewable Energy*, vol. 57, pp. 372–383, 2013.

[10] J. Liang, T. Jing, O. Gomis-Bellmunt, J. Ekanayake, and N. Jenkins, "Operation and Control of Multiterminal HVDC Transmission for Offshore Wind Farms," *IEEE Transactions on Power Delivery*, vol. 26, no. 4, pp. 2596–2604, 2011.

[11] O. Gomis-Bellmunt, J. Liang, J. Ekanayake, R. King, and N. Jenkins, "Topologies of multiterminal HVDC-VSC transmission for large offshore wind farms," *Electric Power Systems Research*, vol. 81, no. 2, pp. 271–281, 2011.

[12] Cigré Working Group B4.52, "HVDC Grid Feasibility Study," Cigré, Tech. Rep. April, 2013.

[13] E. Bompard, G. Fulli, M. Ardelean, and M. Masera, "It's a Bird, It's a Plane, It's a... Supergrid," *IEEE power & energy magazine*, vol. 12, no. 2, pp. 41–50, 2014.

[14] FOSG, "www.friendsofthesupergrid.eu," accessed: 18-06-2017.

[15] Desertec, "Clean Power from Deserts," *White Book*, vol. 4th Edition, 2009.

[16] A. Yazdani and R. Iravani, *Voltage-sourced converters in power systems: modeling, control and applications.* Wiley IEEE Press, 2010.

[17] J. Arrillaga, Y. H. Liu, and N. R. Watson, *Flexible power transmission: the HVDC options.* John Wiley, 2007.

[18] M. Davies, M. Dommaschk, J. Dorn, J. Lang, D. Retzmann, and D. Soerangr, "HVDC PLUS - Basics and Principle of Operation," *Siemens*, 2008.

[19] N. Flourentzou, V. G. Agelidis, and G. D. Demetriades, "VSC-Based HVDC Power Transmission Systems : An Overview," *IEEE Transactions on Power Electronics*, vol. 24, no. 3, pp. 592–602, 2009.

[20] ABB, "It's time to connect with offshore wind supplement," *ABB company technical report*, 2010.

[21] Alstom Grid, "HVDC-VSC: transmission technology of the future," *Think Grid*, vol. 8, pp. 13–17, 2011.

[22] M. Barnes and A. Beddard, "Voltage Source Converter HVDC Links - The State of the Art and Issues Going Forward," *Energy Procedia*, vol. 24, no. January, pp. 108–122, Jan. 2012.

[23] J. Beerten, O. Gomis-Bellmunt, X. Guillaud, J. Rimez, A. van der Meer, and D. Van Hertem, "Modeling and control of HVDC grids: a key challenge for the future power system," in *Proc. 18th Power Systems Computation Conference (PSCC), Wroclaw, Poland*, 2014, pp. 1–21.

[24] N. R. Chaudhuri, B. Chaudhuri, R. Majumder, and A. Yazdani, *Voltage-sourced converters in power systems: modeling, control and applications*. IEEE Press, Wiley, 2014.

[25] D. Jovcic and K. Ahmed, *High Voltage Direct Current Transmission: Converters, Systems and DC Grids*. John Wiley & Sons, Ltd, 2015.

[26] A. Lesnicar and R. Marquardt, "An innovative modular multilevel converter topology suitable for a wide power range," in *Proc. IEEE/PES PowerTech Conference, Bologna, Italy*, 2003, pp. 1–6.

[27] S. Kouro, M. Malinowski, K. Gopakumar, J. Pou, L. G. Franquelo, B. Wu, J. Rodriguez, M. A. Pérez, and J. I. Leon, "Recent Advances and Industrial Applications of Multilevel Converters," *IEEE Transactions on Industrial Electronics*, vol. 57, no. 8, pp. 2553–2580, 2010.

[28] N. G. Hingorani and L. Gyugyi, *Understanding FACTS: Concepts and Technology of Flexible AC Transmission Systems*. John Wiley & Sons, 2000.

[29] E. Acha, C. R. Fuerte-Esquivel, Ambriz-Pérez, and C. Angeles-Camacho, *FACTS: modelling and simulation in power networks*. John Wiley & Sons, 2004.

[30] J. M. Maza-Ortega, E. Acha, S. García, and A. Gómez-Expósito, "Overview of power electronics technology and applications in power generation transmission and distribution," *Journal of Modern Power Systems and Clean Energy*, vol. 5, no. 4, pp. 499–514, 2017.

[31] P. Kundur, J. Paserba, V. Ajjarapu, G. Andersson, A. Bose, C. Canizares, N. Hatziargyriou, D. Hill, A. Stankovic, C. Taylor, T. Van Cutsem, and V. Vittal, "Definition and classification of power system

stability IEEE/CIGRE joint task force on stability terms and definitions," *IEEE Transactions on Power Systems*, vol. 19, no. 3, pp. 1387–1401, 2004.

[32] European Comission, "Comission Regulation (EU) 2016/1447 of 26 August 2016. Establishing a network code on requirements for grid connection of high voltage direct current systems and direct current-connected power park modules," Official Journal of the European Union, Tech. Rep., 2016.

[33] P. Kundur, *Power System Stability and Control.* McGraw Hill Education, 1993.

[34] M. A. Pai, *Energy Function Analysis for Power System Stability.* Kluwer Academic Publishers, Boston, 1989.

[35] M. Pavella, D. Ernst, and D. Ruiz-Vega, *Transient Stability of Power Systems: A Unified Approach to Assessment and Control.* Kluwer Academic Publishers, 2012.

[36] F. Milano, *Power System Modelling and Scripting.* Springer, 2010.

[37] TEIAS, "Report on Blackout in Turkey on 31 March 2015." ENTSO-E, Tech. Rep., 2015.

[38] R. J. Newell and D. Osborne, "Dynamic performance characteristics of Nowth American HVDC systems for transient and dynamic stability evaluations," *IEEE Transactions on Apparatus and Systems*, vol. PAS-100, no. 7, pp. 3356–3364, 1981.

[39] C. W. Taylor and S. Lefebvre, "HVDC Controls for System Dynamic Performance," *IEEE Transactions on Power Systems*, vol. 6, no. 2, pp. 743–752, 1991.

[40] J. Hazra, Y. Phulpin, and D. Ernst, "HVDC Control Strategies to Improve Transient Stability in Interconnected Power Systems," in *Proc. IEEE/PES Power Tech Conference, Bucharest, Romania*, 2009, pp. 1–6.

[41] R. Eriksson and L. Söder, "On the coordinated control of multiple HVDC links using input-output exact linearization in large power systems," *International Journal of Electrical Power & Energy Systems*, vol. 43, no. 1, pp. 118–125, Dec. 2012.

[42] R. Eriksson, "On the Centralized Nonlinear Control of HVDC Systems Using Lyapunov Theory," *IEEE Transactions on Power Delivery*, vol. 28, no. 2, pp. 1156–1163, 2013.

[43] L. Sigrist, F. Echavarren, L. Rouco, and P. Panciatici, "A fundamental study on the impact of HVDC lines on transient stability of power systems," in *Proc. IEEE/PES PowerTech Conference, Eindhoven, Netherlands*, 2015, pp. 1–6.

[44] Z. Jun, L. Chong, and Z. Jianjun, "Transient and dynamic stability enhancement by coordination control of hvdc links of northwest acdc grid," in *2016 China International Conference on Electricity Distribution (CICED)*, 2016, pp. 1–5.

[45] S. G. Johansson, G. Asplund, E. Jansson, and R. Rudervall, "Power system stability benefits with VSC DC-transmission systems," in *Proc. CIGRE Session, Paris, France*, 2004, pp. 1–8.

[46] L. Zhang, "Power System Reliability and Transfer Capability Improvement by VSC-HVDC (HVDC Light)," in *Proc. CIGRE Regional Meeting, Tallinn,Estonia*, 2007, pp. 1–7.

[47] H. Latorre, M. Ghandhari, and L. Söder, "Active and reactive power control of a VSC-HVdc," *Electric Power Systems Research*, vol. 78, no. 10, pp. 1756–1763, 2008.

[48] A. Fuchs, M. Imhof, T. Demiray, and M. Morari, "Stabilization of Large Power Systems Using VSC-HVDC and Model Predictive Control," *IEEE Transactions on Power Delivery*, vol. 29, no. 1, pp. 480–488, 2014.

[49] J. Machowski, P. Kacejko, L. Nogal, and M. Wancerz, "Power system stability enhancement by WAMS-based supplementary control of multi-terminal HVDC networks," *Control Engineering Practice*, vol. 21, no. 5, pp. 583–592, 2013.

[50] R. Eriksson, "Coordinated Control of Multiterminal DC Grid Power Injections for Improved Rotor-Angle Stability Based on Lyapunov Theory," *IEEE Transactions on Power Delivery*, vol. 29, no. 4, pp. 1789–1797, 2014.

[51] G. Tang, Z. Xu, H. Dong, and Q. Xu, "Sliding Mode Robust Control Based Active-Power Modulation of Multi-Terminal HVDC Transmissions," *IEEE Transactions on Power Systems*, vol. 31, no. 2, pp. 1614–1623, 2016.

[52] M. H. Haque and P. Kumkratug, "Application of Lyapunov stability criterion to determine the control strategy of a STATCOM," *IEE Proc. Gener. Transm. Distrib.*, vol. 151, no. 3, pp. 415–420, 2004.

[53] M. H. Haque, "Improvement of First Swing Stability Limit by Utilizing Full Benefit of Shunt FACTS Devices," *IEEE Transactions on Power Systems*, vol. 19, no. 4, pp. 1894–1902, 2004.

[54] M. Ghandhari, G. Andersson, and I. A. Hiskens, "Control Lyapunov Functions for Controllable Series Devices," *IEEE Transactions on Power Systems*, vol. 16, no. 4, pp. 689–694, 2001.

[55] A. Gomez-Exposito, A. J. Conejo, and C. Canizares (Editors), *Electric Energy Systems: Analysis and Operation.* CRC Press, Taylor & Francis group, 2016.

[56] L. Diez-Maroto, L. Rouco, and F. Fernandez-Bernal, "Fault ride through capability of round rotor synchronous generators: Review, analysis and discussion of European grid code requirements," *Electric Power Systems Research*, vol. 140, pp. 27–36, 2016.

[57] ENTSO-E, "Network code for requirements for grid connection applicable to all generators. Requirements in the context of present practices," Tech. Rep., 2012.

[58] KEMA, "Technical Report on ENTSO-E Network Code: Requirements for Generators," European Commission DG TREN, Tech. Rep., 2013.

[59] ENTSO-E, "Determining generator fault clearing time for the synchronous zone of Continental Europe," RG-CE System Protection & Dynamics Sub Group, Tech. Rep., 2017.

[60] J. Chow (Editor), *Coherency and Model Reduction of Large Power Systems.* Springer, 2013.

[61] ENTSO-E, "Analysis of CE inter-area oscillations of 1st December 2016," Tech. Rep., 2017.

[62] M. Klein, G. J. Rogers, S. Moorty, and P. Kundur, "Analytical Investigation of Factors Influencing Power System Stabilizers Performance," *IEEE Transactions on Energy Conversion*, vol. 7, no. 3, pp. 382–391, 1992.

[63] P. Kundur, G. R. Berube, L. M. Hajagos, and R. Beaulieu, "Practical Utility Experience with and Effective Use of Power System Stabilizers," in *Proc. IEEE/PES General Meeting, Toronto, Ontario, Canada*, 2003, pp. 1–9.

[64] L. Rouco, "Coordinated design of multiple controllers for damping power system oscillations," *Electric Power and Energy Systems*, vol. 23, pp. 517–530, 2001.

[65] N. Mithulananthan, C. A. Canizares, J. Reeve, and G. J. Rogers, "Comparison of PSS, SVC and STATCOM controllers for damping power system oscillations," *IEEE Transactions on Power Systems*, vol. 18, no. 2, pp. 786–792, 2003.

[66] A. R. Messina, O. Begovich, López, and E. N. Reyes, "Coordinated design of multiple controllers for damping power system oscillations," *Electric Power and Energy Systems*, vol. 26, pp. 19–29, 2004.

[67] K. Uhlen, L. Vanfretti, M. M. de Oliveira, A. B. Leirbukt, V. H. Aarstrand, and J. O. Gjerde, "Wide-Area Power Oscillation Damper Implementation and Testing in the Norwegian Transmission Network," *Proc. IEEE/PES General Meeting, San Diego, California, United States of America*, pp. 1–7, 2012.

[68] L. Sigrist and L. Rouco, "Design of damping controllers for doubly fed induction generators using eigenvalue sensitivities," in *Proc. IEEE/PES Power Systems Conference and Exposition, Seattle, United States of America*, 2009, pp. 316–321.

[69] J. L. Domínguez-García, O. Gomis-Bellmunt, F. Bianchi, and A. Sumper, "Power oscillation damping supported by wind power: A review," *Renewable and Sustainable Energy Reviews*, vol. 16, pp. 4994–5006, 2012.

[70] A. M. Vural, "Contribution of high voltage direct current transmission systems to inter-area oscillation damping: A review," *Renewable and Sustainable Energy Reviews*, vol. 57, pp. 892–915, 2016.

[71] M. Ndreko, A. Van der Meer, B. Rawn, and M. Gibescu, "Damping of power system oscillations by VSC-HVDC multi-terminal transmission networks," WP 6.1. NSTG Project Technical Report, Part I, Delft University of Technology, Tech. Rep., 2013.

[72] F. O. Resende, M. H. Vasconcelos, and J. A. Peças Lopes, "Simultaneous Tuning of Power System Stabilizers Installed in the VSC-based MTDC Networks of Large Offshore Wind Farms," in *Proc. Power Systems Computation Conference (PSCC), Wroclaw, Poland*, 2014, pp. 1–7.

[73] L. Harnefors, N. Johansson, L. Zhang, and B. Berggren, "Tuning of a Damping Controller for Multiterminal VSC-HVDC Grids Using the Probabilistic Collocation Method," *IEEE Transactions on Power Systems*, vol. 29, no. 5, pp. 2529–2539, 2014.

[74] R. Eriksson, "A New Control Structure for Multi-Terminal dc Grids to Damp Inter-Area Oscillations," *IEEE Transactions on Power Delivery*, vol. 31, no. 3, pp. 990–998, 2016.

[75] R. Preece and J. V. Milanovic, "Tuning of a Damping Controller for Multiterminal VSC-HVDC Grids Using the Probabilistic Collocation Method," *IEEE Transactions on Power Delivery*, vol. 29, no. 1, pp. 318–326, 2014.

[76] P. Agnihotri, A. Kulkarni, A. Gole, B. Archer, and T. Weekes, "Robust Wide-Area Measurement Based Damping Controller for Networks with Embedded Multi-Terminal and Multi-Infeed HVDC Links," *IEEE Transactions on Power Systems*, vol. 32, no. 5, pp. 3884–3892, 2017.

[77] O. Kobt, M. Ghandhari, J. Renedo, L. Rouco, and R. Eriksson, "On the Design and Placement of a Supplementary Damping Controller in an Embedded VSC-MTDC Network," in *Proc. IEEE/PES International Conference on Innovative Smart Grid Technologies Europe (ISGT), Torino, Italy*, 2017, pp. 1–6.

[78] I. J. Pérez-Arriaga, G. C. Verghese, and F. C. Schweppe, "Selective Modal Analysis With Applications to Electric Power Systems, Part I: Heuristic introduction," *IEEE Transactions on Power Apparatus and Systems*, vol. PAS-101, no. 9, pp. 3117–3125, 1982.

[79] G. C. Verghese, I. J. Pérez-Arriaga, and F. C. Schweppe, "Selective Modal Analysis With Applications to Electric Power Systems, Part II: The Dynamic Stability Problem," *IEEE Transactions on Power Apparatus and Systems*, vol. PAS-101, no. 9, pp. 3126–3125, 1982.

[80] F. L. Pagola, I. J. Pérez-Arriaga, and G. C. Verghese, "On Sensivities, Residues and Participations: Applications to Oscillatory Stability Analysis and Control," *IEEE Transactions on Power Systems*, vol. 4, no. 1, pp. 278–285, 1989.

[81] N. Watson and J. Arrillaga, *Power systems electromagnetic transient simulation*. The Institution of Electrical Engineers, 2003.

[82] J. A. Martinez-Velasco, *Power system transients: parameter determination*. Boca Raton: Taylor & Francis, 2010.

[83] Siemens PTI, *PSS/E 32.0.5 Users Manual*, 2010.

[84] X.-P. Zhang, "Multiterminal Voltage-Sourced Converter-Based HVDC Models for Power Flow Analysis," *IEEE Transactions on Power Systems*, vol. 19, no. 4, pp. 1877–1884, 2004.

[85] T. M. Haileselassie and K. Uhlen, "Power Flow Analysis of Multiterminal HVDC Networks," in *Proc. IEEE/PES PowerTech Conference, Trondheim, Norway*, 2011, pp. 1–6.

[86] M. Baradar and M. Ghandhari, "A Multi-Option Unified Power Flow Approach for Hybrid AC / DC Grids Incorporating Multi-Terminal VSC-HVDC," *IEEE Transactions on Power Systems*, vol. 28, no. 3, pp. 2376–2383, 2013.

[87] R. Chai, B. Zhang, J. Dou, Z. Hao, and T. Zheng, "Unified Power Flow Algorithm Based on the NR Method for Hybrid AC/DC Grids Incorporating VSCs," *IEEE Transactions on Power Systems*, vol. 31, no. 6, pp. 4310–4318, 2016.

[88] E. Acha and L. M. Castro, "A generalized frame of reference for the incorporation of multi-terminal VSC-HVDC systems in power flow solutions," *Electric Power Systems Research*, vol. 136, pp. 415–424, 2016.

[89] L. Gengyin, Z. Ming, H. Jie, L. Guangkai, and L. Haifeng, "Power flow calculation of power systems incorporating vsc-hvdc," in *Proc. In-*

*ternational Conference on Power System Technology (POWERCON), Singapore,*, vol. 2, Nov 2004, pp. 1562–1566.

[90] Q. Chen, T. Q. Tang, and W. Xu, "AC-DC power flow algorithm for multi-terminal VSC-HVDC systems," *Electric Power Automation Equipment*, vol. 25, no. 6, pp. 2602–2612, 2005.

[91] J. Beerten, S. Cole, and R. Belmans, "Generalized Steady-State VSC MTDC Model for Sequential AC/DC Power Flow Algorithms," *IEEE Transactions on Power Systems*, vol. 27, no. 2, pp. 821–829, 2012.

[92] F. Gonzalez-Longatt, J. M. Roldan, and C. A. Charalambous, "Solution of AC/DC Power Flow on a Multi- Terminal HVDC System: Illustrative Case Supergrid Phase I," in *Proc. Universities Power Engineering Conference (UPEC)*, 2012, pp. 1–6.

[93] W. Wang and M. Barnes, "Power Flow Algorithms for Multi-Terminal VSC-HVDC With Droop Control," *IEEE Transactions on Power Systems*, vol. 29, no. 4, pp. 1721–1730, 2014.

[94] R. Teixeira Pinto, C. Leon-Ramirez, M. Aragues-Penalba, A. Sumper, and E. Sorrentino, "A fast methodology for solving power flows in hybrid ac/dc networks: The European North Sea Supergrid case study," in *Proc. International Exhibition and Conference for Power Electronics, Intelligent Motion, Renewable Energy and Energy Management (PCIM Europe), Nuremberg, Germany*, 2016, pp. 1–8.

[95] J. C. Fernández-Pérez, F. M. Echavarren, and L. Rouco, "On the convergence of the sequential power flow for multiterminal VSC AC/DC systems," *IEEE Transactions on Power Systems*, vol. Available on line: http://dx.doi.org/10.1109/TPWRS.2017.2720740, pp. 1–9, 2017.

[96] R. D. Zimmerman, C. E. Murillo-Sánchez, and R. J. Thomas, "MATPOWER: Steady-State Operations, Systems Research and Education," *IEEE Transactions on Power Systems*, vol. 26, no. 1, pp. 12–19, 2011.

[97] J. Beerten and R. Belmans, "Development of an open source power flow software for high voltage direct current grids and hybrid AC/DC systems: MATACDC," *IET Generation, Transmission & Distribution*, vol. 9, no. 10, pp. 966–974, 2015.

[98] S. Cole and R. Belmans, "MatDyn, A New Matlab-Based Toolbox for Power System Dynamic Simulation," *IEEE Transactions on Power Systems*, vol. 26, no. 3, pp. 1129–1136, 2011.

[99] S. Cole, J. Beerten, and R. Belmans, "Generalized Dynamic VSC MTDC Model for Power System Stability Studies," *IEEE Transactions on Power Systems*, vol. 25, no. 3, pp. 1655–1662, 2010.

[100] J. Beerten, S. Cole, and R. Belmans, "Modeling of Multi-Terminal VSC HVDC Systems With Distributed DC Voltage Control," *IEEE Transactions on Power Systems*, vol. 29, no. 1, pp. 34–42, 2014.

[101] R. Eriksson, J. Beerten, and M. Ghandhari, "Optimizing DC Voltage Droop Settings for AC / DC System Interactions," *IEEE Transactions on Power Delivery*, vol. 29, no. 1, pp. 362–369, 2014.

[102] F. Milano, "An Open Source Power System Analysis Toolbox," *IEEE Transactions on Power Systems*, vol. 20, no. 3, pp. 1199–1206, 2005.

[103] F. M. Gonzalez-Longatt and J. L. Rueda (Editors), *PowerFactory Applications for Power System Analysis*. Springer, 2014.

[104] F. Gonzalez-Longatt, A.-G. S, and J. Rodriguez-Amenedo, " Dynamic behaviour of multi-terminal VSC-based HVDC after a converter outage: DC control strategy. Article no.266," *Renewable Energy and Power Quality Journal (RE&PQJ)*, vol. 14, pp. 1–6, 2016.

[105] DigSILENT, *PowerFactory 15 User Manual*, 2013.

[106] L. M. Castro and E. Acha, "A Unified Modeling Approach of Multi-Terminal VSC-HVDC Links for Dynamic Simulations of Large-Scale Power Systems," *IEEE Transactions on Power Systems*, vol. 31, no. 6, pp. 5051–5060, 2016.

[107] P. J. D. Chainho, "General Modeling of Multi-Terminal VSC-HVDC Systems for Transient Stability Analysis," Master thesis, Universidade Técnica de Lisboa, 2012.

[108] M. Ndreko, "Offshore Wind Power Connected to the Dutch Transmission System by VSC-HVDC Networks: Modeling and Stability Analysis," Master's thesis, Delft University of Technology, 2012.

[109] S. Liu, Z. Xu, W. Hua, G. Tang, and Y. Xue, "Electromechanical Transient Modeling of Modular Multilevel Converter Based Multi-Terminal HVDC Systems," *IEEE Transactions on Power Systems*, vol. 29, no. 1, pp. 72–83, 2014.

[110] N. T. Trinh, M. Zeller, K. Wuerflinger, and I. Erlich, "Generic Model of MMC-VSC-HVDC for Interaction Study With AC Power System," *IEEE Transactions on Power Systems*, vol. 31, no. 1, pp. 27–34, 2016.

[111] J. Freytes, L. Papangelis, H. Saad, P. Rault, T. Van Cutsem, and X. Guillaud, "On the modeling of MMC for use in large scale dynamic simulations," in *Proc. Power Systems Computation Conference (PSCC), Genoa, Italy*, 2016, pp. 1–7.

[112] N. R. Chaudhuri, R. Majumder, B. Chaudhuri, and J. Pan, "Stability Analysis of VSC MTDC Grids Connected to Multimachine AC Systems," *IEEE Transactions on Power Delivery*, vol. 26, no. 4, pp. 2774–2784, Oct. 2011.

[113] E. Prieto-Araujo, F. D. Bianchi, A. Junyent-Ferré, and O. Gomis-Bellmunt, "Methodology for Droop Control Dynamic Analysis of Multiterminal VSC-HVDC Grids for Offshore Wind Farms," *IEEE Transactions on Power Delivery*, vol. 26, no. 4, pp. 2476–2485, 2011.

[114] G. P. Adam, K. H. Ahmed, S. J. Finney, and B. W. Williams, "Generalized modeling of DC grid for stability studies," *Proc. 4th International Conference on Power Engineering, Energy and Electrical Drives (POWERENG), Istanbul, Turkey*, pp. 1168–1174, 2013.

[115] G. Pinares, L. B. Tjernberg, L. A. Tuan, C. Breitholtz, and A.-A. Edris, "On the analysis of the dc dynamics of multi-terminal VSC-HVDC systems using small signal modeling," *Proc. IEEE/PES PowerTech Conference, Grenoble, France*, pp. 1–6, Jun. 2013.

[116] A. Egea-Alvarez, F. Bianchi, A. Junyent-Ferré, G. Gross, and O. Gomis-Bellmunt, "Voltage Control of Multiterminal VSC-HVDC Transmission Systems for Offshore Wind Power Plants : Design and Implementation in a Scaled Platform," *IEEE Transactions on Industrial Electronics*, vol. 60, no. 6, pp. 2381–2391, 2013.

[117] E. Prieto-Araujo, A. Egea-Alvarez, S. Fekriasl, and O. Gomis-Bellmunt, "DC Voltage Droop Control Design for Multiterminal HVDC

Systems Considering AC and DC Grid Dynamics," *IEEE Transactions on Power Delivery*, vol. 31, no. 2, pp. 575–585, 2016.

[118] E. Sanchez-Sanchez, E. Prieto-Araujo, and O. Gomis-Bellmunt, "Multi-terminal HVDC voltage droop control design considering DC grid, AC grid and MMC dynamics," in *Proc. 13th IET International Conference on AC and DC Power Transmission, Manchester, UK*, 2017, pp. 1–6.

[119] C. E. Ugalde-Loo, O. D. Adeuyi, S. Eang, N. Jenkins, S. Ceballos, M. Santos, I. Vidaurrazaga, S. D'Arco, G. Bergna, M. Barenys, M. Parker, S. Finney, A. Gatti, A. Pitto, M. Rapizza, D. Cirio, P. Lund, A. Castro, and I. Azpiri, "Open access simulation toolbox for the grid connection of offshore wind farms using multi-terminal HVDC networks," in *Proc. 13th IET International Conference on AC and DC Power Transmission, Manchester, UK*, 2017, pp. 1–6.

[120] A. A. van der Meer, M. Gibescu, M. A. M. M. van der Meijden, W. L. Kling, and J. A. Ferreira, "Advanced Hybrid Transient Stability and EMT Simulation for VSC-HVDC Systems," *IEEE Transactions on Power Delivery*, vol. 30, no. 3, pp. 1057–1066, 2015.

[121] H. Saad, J. Peralta, S. Dennetière, J. Mahseredjian, J. Jatskevich, J. A. Martinez, A. Davoudi, M. Saeedifard, V. Sood, X. Wang, J. Cano, and A. Mehrizi-Sani, "Dynamic Averaged and Simplified Models for MMC-Based HVDC Transmission Systems," *IEEE Transactions on Power Delivery*, vol. 28, no. 3, pp. 1723–1730, 2013.

[122] Cigré WG B4.57, "Guide for the Development of Models for HVDC Converters in a HVDC Grid," TB 604, Tech. Rep., 2014.

[123] Hydro-Québec, *SimPowerSystems For Use with Simulink. User's Guide-*. The MathWorks, 2003.

[124] G. Daelemans, "VSC HVDC in meshed networks," Master thesis, Katholieke Universiteit Leuven, 2008.

[125] G. Daelemans, K. Srivastava, M. Reza, S. Cole, and R. Belmans, " Minimization of steady-state losses in meshed networks using VSC HVDC," in *IEEE Power & Energy Society General Meeting.* IEEE, 2009, pp. 1–5.

[126] Manitoba HVDC Research Centre, *EMTDC: Transient Analysis for PSCAD Power System Simulation. User's manual.*, 2005.

[127] S. Cole, "Steady-State and Dynamic Modelling of VSC HVDC Systems for Power System Simulation," PhD thesis, Katholieke Universiteit Leuven, 2010.

[128] M. Mohaddes, "Introduction to HVDC," *SC B4, Tutorial, CIGRE Session, Paris*, pp. 1–25, 2016.

[129] S. Cole and R. Belmans, "A proposal for standard VSC HVDC dynamic models in power system stability studies," *Electric Power Systems Research*, vol. 81, no. 4, pp. 967–973, 2011.

[130] J. Beerten, S. D'Arco, and J. A. Suul, "Cable Model Order Reduction for HVDC Systems Interoperability Analysis," in *Proc. International Conference on AC and DC Power Transmission, Birmingham, UK*, 2015, pp. 1–10.

[131] S. D'Arco, J. A. Suul, and J. Beerten, "Analysis of accuracy versus model order for frequency-dependent Pi-model of HVDC cables," in *Proc. IEEE 17th Workshop on Control and Modeling for Power Electronics (COMPEL)*, 2016, pp. 1–8.

[132] L. Zhang, L. Harnefors, and N. Hans-Peter, "Interconnection of Two Very Weak AC Systems by VSC-HVDC Links Using Power-Synchronization Control," *IEEE Transactions on Power Systems*, vol. 26, no. 1, pp. 344–355, 2012.

[133] J. Z. Zhou, H. Ding, S. Fan, Y. Zhang, and A. M. Gole, "Impact of Short-Circuit Ratio and Phase-Locked-Loop Parameters on the Small-Signal Behavior of a VSC-HVDC Converter," *IEEE Transactions on Power Delivery*, vol. 29, no. 5, pp. 2287–2296, 2014.

[134] A. Egea-Alvarez, S. Fekriasl, H. Fainan, and O. Gomis-Bellmunt, "Advanced Vector Control for Voltage Source Converters Connected to Weak Grids," *IEEE Transactions on Power Systems*, vol. 30, no. 6, pp. 3072–3081, 2015.

[135] S. Arunprasanth, U. D. Annakkage, C. Karawita, and R. Kuffel, "Generalized Frequency-Domain Controller Tuning Procedure for VSC Systems," *IEEE Transactions on Power Delivery*, vol. 31, no. 2, pp. 2287–2296, 2016.

[136] Cigré WG B4.62, "Connection of wind farms to weak AC networks," TB 671, Tech. Rep., 2016.

[137] R. Irnawan, F. F. da Silva, C. L. Bak, and T. C. Bregnhoj, " Evaluation of half-bridge modular multilevel converter model for VSC-HVDC transient stability studies," in *Proc. 13th IET International Conference on AC and DC Power Transmission, Manchester, UK*, 2017, pp. 1–6.

[138] T. K. Vrana, J. Beerten, R. Belmans, and O. B. Fosso, "A classification of DC node voltage control methods for HVDC grids," *Electric Power Systems Research*, vol. 103, pp. 137–144, 2013.

[139] F. D. Bianchi, J. L. Domínguez-García, and O. Gomis-Bellmunt, "Control of multi-terminal HVDC networks towards wind power integration: A review," *Renewable and Sustainable Energy Reviews*, vol. 55, pp. 1055–1068, 2016.

[140] N. R. Chaudhuri, R. Majumder, B. Chaudhuri, and J. Pan, "Adaptive Droop Control for Effective Power Sharing in Multi-Terminal DC (MTDC) Grids," *IEEE Transactions on Power Systems*, vol. 28, no. 1, pp. 21–29, 2013.

[141] W. Wang, "Operation, Control and Stability Analysis of Multi-Terminal VSC-HVDC Systems," PhD thesis, School of Electrical and Electronic Engineering, The University of Manchester, 2015.

[142] Mathworks, "Matlab2016b on-line documentation for `power_hvdc_vsc`," http://www.mathworks.com, accessed: 2016-12-01.

[143] M. Stubbe (Convener), "Long Term Dynamics Phase II," Cigré Task Force 38.02.08 - TB 102, Tech. Rep., 1995.

[144] O. Kotb, M. Ghandhari, R. Eriksson, R. Leelarujic, and V. K. Sood, "Stability enhancement of an interconnected AC/DC power system through VSC-MTDC operating point adjustement," *Electric Power Systems Research*, vol. 151, pp. 308–318, 2017.

[145] J. Bola, R. Rivas, R. Fernández-Alonso, G. Pérez, J. Hidalgo, L. M. Coronado, C. Longás, S. Sanz, G. Lemerchand, J. Roguin, and D. Glaise, "Operational experience of new Spain-France HVDC interconnection," in *Proc. CIGRE Session, Paris, France*, 2016, pp. 1–13.

[146] T. M. Haileselassie and K. Uhlen, "Primary frequency control of remote grids connected by multi-terminal HVDC," in *Proc. IEEE/PES General Meeting, Providence, RI, USA*, 2010, pp. 1–6.

[147] N. R. Chaudhuri, R. Majumder, and B. Chaudhuri, "System Frequency Support Through Multi-Terminal DC (MTDC) Grids," *IEEE Transactions on Power Systems*, vol. 28, no. 1, pp. 347–356, 2013.

[148] B. Silva, C. L. Moreira, L. Seca, Y. Phulpin, and J. A. Peças Lopes, "Provision of Inertial and Primary Frequency Control Services Using Offshore Multiterminal HVDC Networks," *IEEE Transactions on Sustainable Energy*, vol. 3, no. 4, pp. 800–808, Oct. 2012.

[149] A. Sarlette, J. Dai, Y. Phulpin, and D. Ernst, "Cooperative frequency control with a multi-terminal high-voltage DC network," *Automatica*, vol. 48, no. 12, pp. 3128–3134, 2012.

[150] L. Papangelis, X. Guillaud, and T. Van Cutsem, "Frequency support among asynchronous AC systems through VSCs emulating power plants," in *Proc. 11th IET Conference on AC and DC Power Transmission, Birmingham, UK*, Feb. 2015, pp. 1–6.

[151] S. Akkari, J. Dai, M. Petit, and X. Guillaud, "Interaction between the voltage-droop and the frequency-droop control for multi-terminal HVDC systems," in *Proc. 11th IET Conference on AC and DC Power Transmission*, Feb. 2015, pp. 1–6.

[152] L. M. Castro and E. Acha, "On the Provision of Frequency Regulation in Low Inertia AC Grids Using HVDC Systems," *IEEE Transactions on Smart Grid*, vol. 7, no. 6, pp. 2680–2690, 2016.

[153] Y. Wang, G. Delille, H. Bayem, X. Guillaud, and B. Francois, "High Wind Power Penetration in Isolated Power Systems - Assessment of Wind Inertial and Primary Frequency Responses," *IEEE Transactions on Power Systems*, vol. 28, no. 3, pp. 2412–2420, 2013.

[154] L. Díez-Maroto, "Improvement of Voltage Ride Through Capability of Synchronous Generators with Supplementary Excitation Controllers," Master thesis, Universidad Pontificia Comillas, 2013.

[155] L. Diez-Maroto, L. Vanfretti, M. S. Almas, G. M. Jónsdóttir, and L. Rouco, "A WACS exploiting generator Excitation Boosters for power system transient stability enhancement," *Electric Power Systems Research*, vol. 148, pp. 245–253, 2017.

[156] L. Díez Maroto, "Ultracapacitor Based Supplementary Excitation Module for the Improvement of Synchronous Generator Transient Stability," PhD thesis, Universidad Pontificia Comillas de Madrid, 2017.

[157] A. A. Fouad and V. Vittal, "The transient energy function method," *Electrical Power & Energy Systems*, vol. 10, no. 4, pp. 233–246, 1988.

[158] J. Machowski, J. W. Bialek, S. Robak, and J. R. Bumby, "Excitation control system for use with synchronous generators," *IEE Proceedings - Generation, Transmission and Distribution*, vol. 145, no. 5, pp. 537–546, 1998.

[159] T. Van Cutsem and L. Papangelis, "Description, Modeling and Simulation Results of a Test System for Voltage Stability Analysis," Université de Liège, Tech. Rep., 2014.

[160] F. R. P. Safaei, S. G. Ghiocel, J. P. Hespanha, and J. H. Chow, "Stability of an adaptive switched controller for power system oscillation damping using remote synchrophasor signals," in *Proc. 53rd IEEE Conference on Decision and Control, Los Angeles, CA, USA*, 2014, pp. 1695–1700.

[161] M. A. Abido, "Power system enhancement using FACTS controllers: A review," *The Arabian Journal for Science and Engineering*, vol. 34, no. 1B, pp. 153–172, 2009.

[162] I. Martínez Sanz, B. Chaudhuri, and G. Strbac, "Coordinated Corrective Control for Transient Stability Enhancement in Future Great Britain Transmission System," in *Proc. 19th Power Systems Computation Conference (PSCC), Genoa, Italy*, 2016, pp. 1–7.

[163] N. R. Trinh, I. Erlich, M. Zeller, and K. Wuerflinger, "Enhancement of grid transient stability using MMC-VSCH-VDC control," in *Proc. 11th IET Conference on AC and DC Power Transmission, Birmingham, UK*, Feb. 2015, pp. 1–6.

[164] M. Ghandhari, "Control Lyapunov Functions: A Control Strategy for Damping of Power Oscillations in Large Power Systems," PhD thesis, KTH Royal Institute of Technology, Dept. of Electric Power Engineering Electric Power Systems, 2000.

[165] M. A. Aleisawee, D. Jovcic, and A. Starkey, "Small signal modelling and stability analysis of multiterminal VSC-HVDC," in *Proc. 14th European Conference on Power Electronics and Applications*, 2011, pp. 1–10.

[166] G. O. Kalcon, G. P. Adam, O. Anaya-Lara, S. Lo, and K. Uhlen, "Small-Signal Stability Analysis of Multi-Terminal VSC-Based DC Transmission Systems," *IEEE Transactions on Power Systems*, vol. 27, no. 4, pp. 1818–1830, Nov. 2012.

[167] P. Rault, F. Colas, X. Guillaud, and S. Nguefeu, "Method for Small Signal Stability Analysis of VSC-MTDC grids," in *IEEE/PES General Meeting, San Diego, CA, USA*, 2012, pp. 1–7.

[168] O. Kotb, M. Ghandhari, R. Eriksson, and V. K. Sood, "On small signal stability of an AC/DC power system with a hybrid MTDC network," *Electric Power Systems Research*, vol. 136, pp. 79–88, 2016.

[169] J. Beerten, S. D'Arco, and J. Suul, "Identification and Small-Signal Analysis of Interaction Modes in VSC MTDC Systems," *IEEE Transactions on Power Delivery*, vol. 31, no. 2, pp. 888–897, 2016.

[170] G. Pinares and M. Bongiorno, "Modeling and Analysis of VSC-based HVDC Systems for DC Network Stability Studies," *IEEE Transactions on Power Delivery*, vol. 31, no. 2, pp. 848–856, 2016.

[171] S. Akkari, E. Prieto-Araujo, J. Dai, O. Gomis-Bellmunt, and X. Guillaud, "Impact of the DC cable models on the SVD analysis of a Multi-Terminal HVDC system," in *Proc. Power System Computation Conference (PSCC), Genoa, Italy*, 2016, pp. 1–7.

[172] G. Bergna-Diaz, J. A. Suul, and S. D'Arco, "Small-signal state-space modeling of modular multilevel converters for system stability analysis," in *Proc. IEEE Energy Conversion Congress and Exposition (ECCE)*, 2015, pp. 1–6.

[173] J. Freytes, S. Akkari, J. Dai, F. Gruson, P. Rault, and X. Guillaud, "Small-signal state-space modeling of an HVDC link with modular multilevel converters," in *Proc. IEEE 17th Workshop on Control and Modeling for Power Electronics (COMPEL)*, 2016, pp. 1–8.

[174] J. Beerten, G. Bergna-Diaz, S. D'Arco, and J. A. Suul, "Comparison of small-signal dynamics in MMC and two-level VSC HVDC transmission schemes," in *Proc. IEEE International Energy Conference (ENERGYCON)*, 2016, pp. 1–6.

[175] A. Jamshidifar and D. Jovcic, "Small-Signal Dynamic DQ Model of Modular Multilevel Converter for System Studies," *IEEE Transactions on Power Delivery*, vol. 31, no. 1, pp. 191–199, 2016.

[176] Y. Pipelzadeh, N. Chaudhuri, B. Chaudhuri, and T. Green, "System stability improvement through optimal control allocation in voltage source converter-based high-voltage direct current links," *IET Generation, Transmission & Distribution*, vol. 6, no. 9, pp. 811–821, 2012.

[177] L. Shen, M. Barnes, R. Preece, J. V. Milanovic, K. Bell, and M. Belivanis, "The Effect of VSC-HVDC Control on AC System Electromechanical Oscillations and DC System Dynamics," *IEEE Transactions on Power Delivery*, vol. 31, no. 3, pp. 1085–1095, 2016.

[178] D. Jovcic, L. A. Lamont, and L. Xu, "Advanced Vector Control for Voltage Source Converters Connected to Weak Grids," *Proc. IEEE/PES General Meeting, Toronto, Canadá*, pp. 1–6, 2003.

[179] B. Berggren, R. Majumder, and N. Johansson, "A Generic VSC HVDC Primary Control Structure Suitable for Stability Studies," in *Proc. EPRI HVDC/FACTS Conference, Palo Alto, USA*, 2013, pp. 1–8.

[180] M. Amin, J. A. Suul, S. D'Arco, E. Tedeschi, and M. Molinas, "Impact of state-space modelling fidelity on the small-signal dynamics of VSC-HVDC systems," in *11th IET International Conference on AC and DC Power Transmission*, 2015, pp. 1–11.

[181] L. Rouco, "Small Signal Stability Toolbox (SSST): Reference Manual," *IIT, Universidad Pontificia Comillas*, 2002.

[182] L. Rouco, I. Pérez-Arriaga, R. Criado-Calero, and J. Soto, "A computer package for analysis of small signal stability in large electric power systems," in *Proc. Power System Computation Conference (PSCC), Aviñón, France*, 1993.

[183] M. Amin, M. Zadeh, J. A. Suul, E. Tedeschi, M. Molinas, and O. B. Fosso, "Stability analysis of interconnected AC power systems with

multi- terminal DC grids based on the Cigré DC grid test system," in *Proc. Renewable Power Generation Conference (RPG), Naples, Italy*, 2014, pp. 1–6.

[184] M. K. Zadeh, M. Amin, J. A. Suul, M. Molinas, and O. B. Fosso, "Small-Signal Stability Study of the Cigré DC Grid Test System with Analysis of Participation Factors and Parameter Sensitivity of Oscillatory Modes," in *Proc. 18th Power Systems Computation Conference (PSCC), Wroclaw, Poland*, 2014, pp. 1–8.

[185] L. Rouco and F. L. Pagola, "Damping of Electromechanical Oscillations in Power Systems with Controllable Phase Angle Regulators: Location and Controller Design," in *Proc. 28th North American Power Symposium, MIT, Cambridge, Massachusetts, United States of America*, 1996, pp. 249–256.

[186] L. Sigrist and L. Rouco, "Damping electromechanical oscillations with both ratio and phase modulation of static synchronous series sources: Controller design," in *Proc. IEEE Lausanne PowerTech, Lausanne, Switzerland*, 2007, pp. 1–7.

[187] C. Li, D. Kong, Y. Xue, R. Guan, A. Taylor, R. Zhang, X.-P. Zhang, and D. Jayaweera, " Enhancement of power system small-signal stability by coordinated damping control of multiple FACTS devices," in *Proc. 13th IET International Conference on AC and DC Power Transmission, Manchester, UK*, 2017, pp. 1–6.

[188] J. L. Domínguez-García, C. E. Ugalde-Loo, F. Bianchi, and O. Gomis-Bellmunt, "Input-output signal selection for damping of power system oscillations using wind power plants," *International Journal of Electrical Power & Energy Systems*, vol. 58, pp. 75–84, 2014.

[189] R. Preece, J. V. Milanovic, M. A. Almutairi, and O. Marjanovic, "Damping of inter-area oscillations in mixed AC/DC networks using WAMS based supplementary controller," *IEEE Transactions on Power Systems*, vol. 28, no. 2, pp. 1160–1169, 2013.

[190] N.-T. Trinh, "Enhancement of Grid Dynamic Performance using VSC-based Multi-terminal HVDC Systems in Multilevel Modular Converter Topology," PhD thesis, Institute of Electrical Power Systems (EAN), University Duisburg-Essen, Germany, 2016.

[191] P. Kundur, M. Klein, G. J. Rogers, and M. S. Zywno, "Application of Power System Stabilizers for Enhancement of Overall System Stability," *IEEE Transactions on Power Systems*, vol. 4, no. 2, pp. 614–627, 1989.

[192] L. Rouco, F. L. Pagola, A. Garcia-Cerrada, J. M. Rodríguez-García, and R. M. Sanz, "Damping of electromechanical oscillations in power systems with superconducting magnetic energy storage systems: location and controller design," in *Proc. Power System Computation Conference (PSCC), Dresde, Germany*, 1996, pp. 1–8.

[193] L. Rouco and F. L. Pagola, "An Eigenvalue Sensitivity Approach to Location and Controller Design of Controllable Series Capacitors for Damping Power System Oscillations," *IEEE Transactions on Power Systems*, vol. 4, no. 12, pp. 1660–1667, 1997.

[194] G. W. Stagg and A. H. El-Abiad, *Computer Methods in Power System Analysis*. McGraw-Hill, 1968.

[195] J. Beerten, S. Cole, and R. Belmans, "A sequential AC/DC power flow algorithm for networks containing Multi-terminal VSC HVDC systems," in *Proc. IEEE/PES General Meeting, Providence, RI, USA*, 2010, pp. 1–7.

[196] J. Beerten, "MatACDC 1.0 User's Manual," *ESAT-ELECTA, Katholieke Universiteit Leuven*, pp. 1–36, 2012.

[197] B. Karlsson, "Comparison of PSSE & PowerFactory." Degree Project, Uppsala Universitet., 2013.

[198] J. Beerten, "Modeling and Control of DC Grids," PhD thesis, Katholieke Universiteit Leuven, 2013.

# Appendix A

# Test systems

## A.1 Stagg 5-bus test system with a VSC-MTDC system

The test system in Fig. A.1 has been used for the validation of the proposed AC/DC power-flow algorithm in PSS/E against MatACDC [97], carried out in Section 2.5 of Chapter 2. It consists of an AC grid (described in [194]) with an embedded VSC-MTDC system. This AC/DC test system was first proposed in [195].

The data of the system can be found in cases `case5_stagg` (AC grid) and `case5_stagg_MTDCslack` (DC grid) of MatACDC [196].

The variables of the AC system specified for power-flow calculation are provided in Table A.1. The variables of the VSC stations specified for power-flow calculation are:

- VSC1: Mode $P_s - Q_s$, with $P^0_{s,1} = -60$ MW and $Q^0_{s,1} = -40$ MVAr.
- VSC2: Mode $U_{dc} - U_s$, with $u^0_{dc,2} = 1$ p.u and $u^0_{s,2} = 1$ p.u.
- VSC3: Mode $P_s - Q_s$, with $P^0_{s,3} = 35$ MW and $Q^0_{s,3} = 5$ MVAr.

The data of the system can be found in Tables A.1-A.5. The base values for the AC/DC p.u. system are: $U_{ac,B} = U_{dc,B} = 345$ kV are $S_B = 100$ MVA.

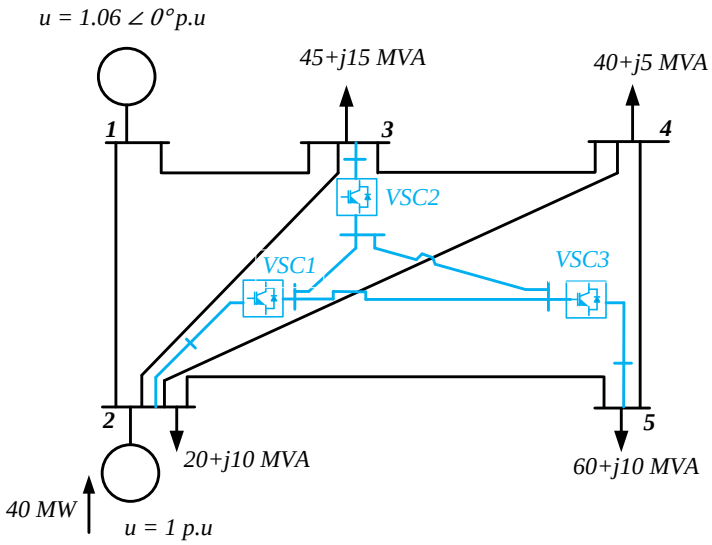


Figure A.1: 5-bus test system with a VSC-MTDC system.

Table A.1: AC system: variables specified for the power flow.

| bus | type | $u$ (p.u) | $\delta$ (deg) | $P_G$ (MW) | $Q_G$ (MVAr) | $P_D$ (MW) | $Q_D$ (MVAr) |
|---|---|---|---|---|---|---|---|
| 1 | slack | 1.060 | 0.00 | - | - | 0.00 | 0.00 |
| 2 | PV | 1.000 | - | 40.00 | - | 20.00 | 10.00 |
| 3 | PQ | - | - | - | - | 45.00 | 15.00 |
| 4 | PQ | - | - | - | - | 40.00 | 5.00 |
| 5 | PQ | - | - | - | - | 60.00 | 10.00 |

Table A.2: AC-line data.

| Línea | $r$ (p.u) | $x$ (p.u) | $b$ (p.u) | $S_N$ (MVA) |
|---|---|---|---|---|
| 1-2 | 0.02 | 0.06 | 0.06 | 100 |
| 1-3 | 0.08 | 0.24 | 0.05 | 100 |
| 2-3 | 0.06 | 0.18 | 0.04 | 100 |
| 2-4 | 0.06 | 0.18 | 0.04 | 100 |
| 2-5 | 0.04 | 0.12 | 0.03 | 100 |
| 3-4 | 0.01 | 0.03 | 0.02 | 100 |
| 4-5 | 0.08 | 0.24 | 0.05 | 100 |

Table A.3: VSC-station data. Converter rating are base values for p.u.

| VSC | $S_N(MVA)$ | $r_{tf}$ | $x_{tf}$ | $b_f$ | $r_c$ | $x_c$ |
|---|---|---|---|---|---|---|
| 1 | 100 | 0.0015 | 0.1121 | 0.0887 | 0.0001 | 0.1643 |
| 2 | 100 | 0.0015 | 0.1121 | 0.0887 | 0.0001 | 0.1643 |
| 3 | 100 | 0.0015 | 0.1121 | 0.0887 | 0.0001 | 0.1643 |

Table A.4: VSC-station data. Parameters of the converter losses. Converter rating are base values for p.u.

| VSC | $a$ | $b$ | $c_{rect}$ | $c_{inv}$ | |
|---|---|---|---|---|---|
| 1 | 11.03 | 1.60 | 2.817 | 4.269 | $\times 10^{-3}$ |
| 2 | 11.03 | 1.60 | 2.817 | 4.269 | |
| 3 | 11.03 | 1.60 | 2.817 | 4.269 | |

Table A.5: DC-line data.

| Línea DC | $r_{dc,ij}$ (p.u) | $U_{dc,N}$ (kV) | $P_{dc,N}$ (MW) |
|---|---|---|---|
| 1-2 | 0.0260 | 345 | 100 |
| 1-3 | 0.0365 | 345 | 100 |
| 2-3 | 0.0260 | 345 | 100 |

## A.2 3-bus test system for validation

The test system in Fig. A.2 was used for validation of the different dynamic models proposed for VSC-MTDC systems (Section 2.6 of Chapter 2 and sections 6.5 and 6.6 of Chapter 6).

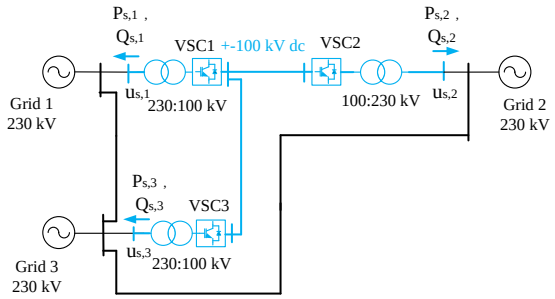


Figure A.2: Test system for validation.

The data of the AC system are as follows:

- External grids 1, 2 and 3: They are modelled as voltage sources with data: 230 kV, 500 MVA, $S_{cc} = 40687$ MVA and $X/R = 7.05$.
- Lines 1-3 and 2-3: $z = 0.0033 + j0.0331$ p.u (p.u. base values: 100 MVA and 230 kV).

The data of the VSC stations, including controller parameters, and the DC grid are provided in Table A.6.

Table A.6: 3-bus test system. Converter and DC grid parameters

| Parameters<br>Converter rating are base values for p.u. | Values |
|---|---|
| Rating VSC, DC voltage | 200 MVA, ±100 kV |
| Configuration | Symmetrical monopole |
| Max. active (reactive) power | ±200 MW (±200 MVAr) |
| Max. current | 1 p.u (d-priority) |
| Max. DC voltage | ±10 % |
| Max. modulation index | 1.23 p.u |
| Current-controller time constant ($\tau$) | 2 ms |
| Connection resistance ($r_s$)/reactance ($x_s$) | 0.008 p.u / 0.30 p.u |
| P proportional/integral control ($K_{d,p1}/K_{d,i1}$) | 0/0 |
| Vdc proportional/integral control ($K_{d,p2}/K_{d,i2}$) | 2.45 p.u/49 p.u/s |
| Q proportional/integral control: ($K_{q,p1}/K_{q,i1}$) | 0/0 |
| Vac proportional/integral control ($K_{q,p2}/K_{q,i2}$) | 10 p.u/100 p.u/s |
| VSCs' loss coefficients ($a/b$) in p.u. | 0.035/0 |
| VSCs' loss coefficients ($c_{rec}/c_{inv}$) in p.u. | 0/0 |
| DC-bus capacitance ($C_{dc,i}$) | 90.6625 $\mu$F |
| DC-bus shunt conductance ($G_{dc,i}$) | 0 |
| DC-line series parameters ($R_{dc,ij}/L_{dc,ij}$) | 1.0925 Ω/27.925 mH |

## A.3 Cigré Nordic32A test system

The Cigré Nordic 32A system is a 32-bus equivalent system of the Swedish grid and it was proposed in [143] for transient-stability and long-term simulations. A description and the data of the Nordic32A system (including full generator+control models) can be found in [143] and in [197]. A comprehensive description of the test system and the evaluation of different operating points can be found in [159].

The Cigré Nordic 32A system with a VSC-MTDC system of 3 terminals is shown in Figure A.3. This hybrid AC/DC system is similar to the one used in [50] and it has been used in this thesis for angle stability studies (non-linear time-domain simulation and small-signal analysis).

The demand in the Nordic32A system is concentrated in the central area, while North and South areas concentrate the generation units (see [143] and [50]). Therefore, an initial operating point in which the active power is transmitted from North and South areas to the central area has been used. The variables specified for power-flow calculation of the initial operating point are:

- VSC1: bus 4012 (s,1): $P^0_{s,1} = -350$ MW and $Q^0_{s,1} = 0$ MVAr.
- VSC2: bus 4044 (s,2): $P^0_{s,2} = 500$ MW and $Q^0_{s,2} = 150$ MVAr.
- VSC3: bus 4062 (s,3): $u^0_{dc,3} = 1$ p.u and $Q^0_{s,3} = 100$ MVAr (VSC3 is used as the a DC-slack converter for power-flow calculation of the initial operating point but DC-voltage droop has been used for dynamic simulation).

Two different scenarios have been used (operating points A and B).

### A.3.1 Operating point A

This operating point is reported in [143].

### A.3.2 Operating point B: heavily loaded scenario

A heavily loaded scenario has been considered with a 580 MW load increase (in the central area) with respect to the base case in [143]. The modifications made are reported in Table A.7.

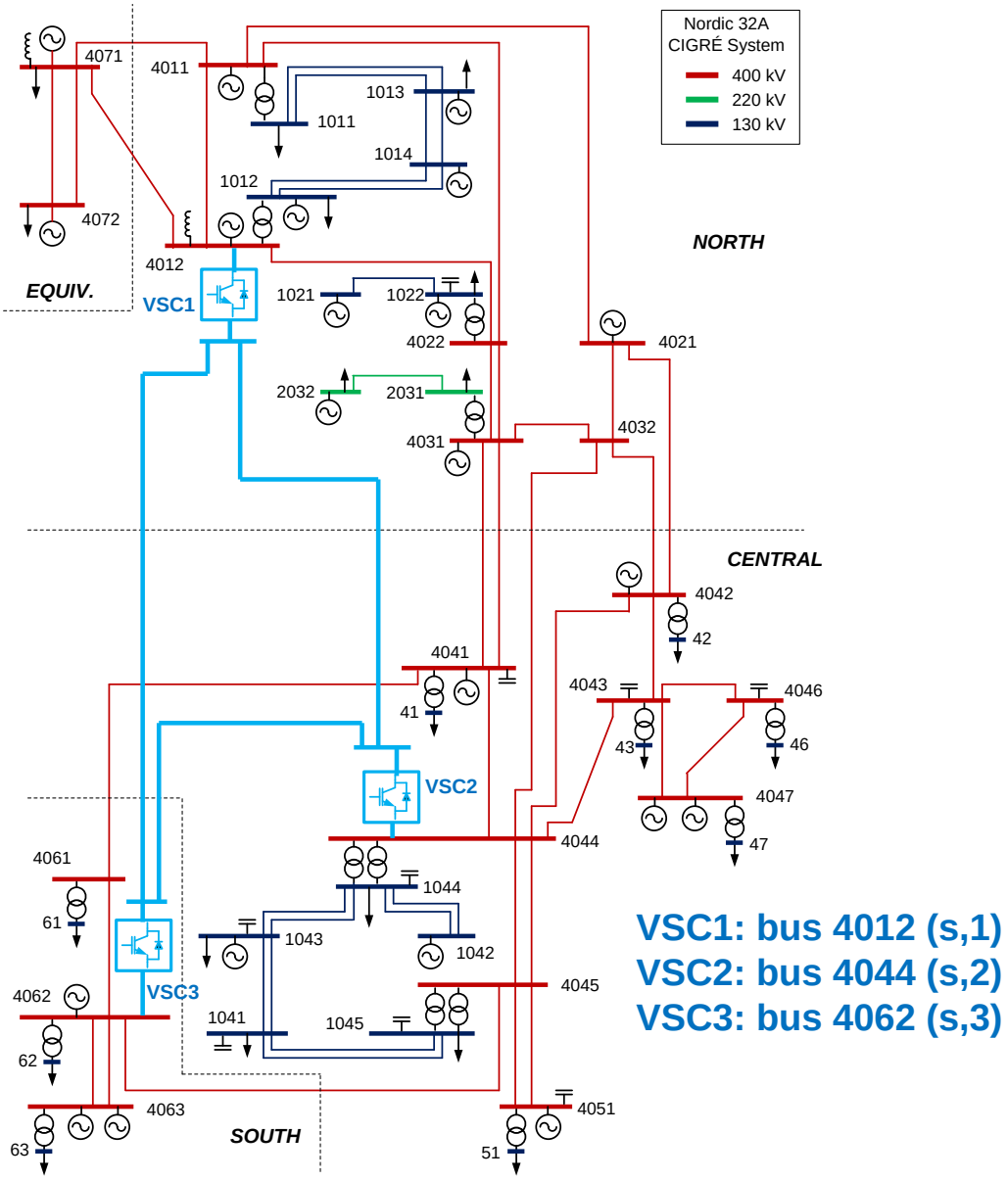


Figure A.3: Nordic 32A system + a VSC-MTDC system.

Table A.8: Nordic 32A system + a VSC-MTDC system. Converter and DC grid parameters

| Parameters<br>Converter rating are base values for p.u. | Values |
|---|---|
| Rating VSC, DC voltage | 1000 MVA, ±320 kV |
| Configuration | Symmetrical monopole |
| Max. active (reactive) power | ±1 GW (±450 MVAr) |
| Max. current | 1 p.u (d-priority) |
| Max. DC voltage | ±10 % |
| Max. modulation index | 1.25 p.u |
| Current-controller time constant ($\tau$) | 5 ms |
| Connection resistance ($r_s$)/reactance ($x_s$) | 0.002 p.u / 0.17 p.u |
| P proportional/integral control ($K_{d,p1}/K_{d,i1}$) | 0/0 |
| Vdc proportional/integral control ($K_{d,p2}/K_{d,i2}$) | 2 p.u/0.12 p.u/s |
| Q proportional/integral control: ($K_{q,p1}/K_{q,i1}$) | 0/0 |
| Vac proportional/integral control ($K_{q,p2}/K_{q,i2}$) | 15 p.u/300 p.u/s |
| DC-voltage droop constant ($k_{dc,i}$) | 0.1 p.u |
| VSCs' loss coefficients ($a/b$) in p.u. | 11.033/3.464 $\times 10^{-3}$ |
| VSCs' loss coefficients ($c_{rec}/c_{inv}$) in p.u. | 4.40/6.67 $\times 10^{-3}$ |
| DC-bus capacitance ($C_{dc,i}$) | 195 $\mu$F |
| DC-bus shunt conductance ($G_{dc,i}$) | 0 |
| DC-line series parameters ($R_{dc,ij}/L_{dc,ij}$) | 2.05 Ω/140.1 mH |

Table A.7: Modifications of NORDIC32A case for operating point B.

| | | Original value | New value |
|---|---|---|---|
| **Loads** | bus 1044 | 800 MW | 1300 MW |
| | bus 41 | 540 MW | 620 MW |
| | bus 4071 (equiv.) | 300 MW | 0 MW |
| | bus 4072 (equiv.) | 2000 MW | 1840 MW |
| | bus 62 | 300 MW | 200 MW |
| **Shunts** | buses 1044 and 4041 | 200 MVAr | 300 MVAr |

# Appendix B

# AC/DC per-unit system used

The per-unit (p.u) system for AC/DC grids is explained in this appendix, following the guidelines presented in [198]. The AC/DC p.u system uses an AC-voltage base value, a DC-voltage base value and an abritary common power base value, which is explained in detail below.

The AC systems use the traditional three-phase per-unit system:

- $S_{ac,B}$ is the power base value.
- $U_{ac,B}$ is the AC-voltage base value (phase to phase).
- The current ($I_{ac,B}$) and impedance ($Z_{ac,B}$) base values are defined as:

$$I_{ac,B} = \frac{S_{ac,B}}{\sqrt{3}U_{ac,B}},\ Z_{ac,B} = \frac{U_{ac,B}^2}{S_{ac,B}}. \tag{B.1}$$

The DC p.u. base values are defined as:

- $S_{dc,B} = S_{ac,B}$ is the power base value.
- $U_{dc,B}$ is the DC-voltage base value (pole to ground).
- The current ($I_{dc,B}$) and impedance ($Z_{dc,B}$) base values are defined as:

$$I_{dc,B} = \frac{S_{dc,B}}{n_{poles}U_{dc,B}},\ \ Z_{dc,B} = \frac{n_{poles}U_{dc,B}^2}{S_{dc,B}}. \tag{B.2}$$

- $n_{poles}$ is the number of poles of the HVDC link: $n_{poles} = 1$ for asymmetrical monopolar configuration and $n_{poles} = 2$ for symmetrically

grounded monopolar or bipolar configurations. All HVDC systems used in this thesis have symmetrical monopolar configuration.

Using this p.u. system, the steady-state equations of a symmetrical monopolar HVDC link, as the one shown in Fig. B.1, are:

$$U_{dc,1} - U_{dc,2} = R_{dc,12} I_{cc,12} \text{ (real)} \Leftrightarrow u_{dc,1} - u_{dc,2} = r_{dc,12} i_{cc,12} \text{ (p.u)} \tag{B.3}$$

$$P_{cc,12} = 2 U_{dc,1} I_{cc,12} \text{ (real)} \Leftrightarrow p_{cc,12} = u_{dc,1} i_{cc,12} \text{ (p.u)} \tag{B.4}$$

where $U_{dc,i}$ is the DC voltage at DC bus $i$ (pole to ground), $P_{cc,ij}$ is the total power leaving DC line $ij$ (through both poles), $I_{cc,ij}$ is the DC current through DC line $ij$ (through each pole) and $R_{dc,ij}$ is the resistance of DC line $ij$ (of each pole).

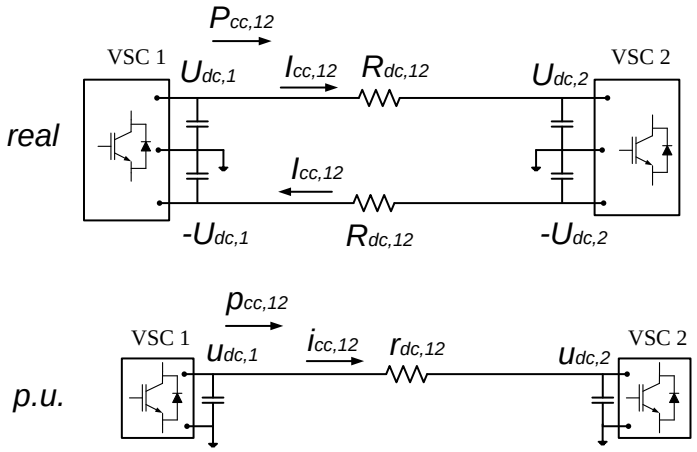


Figure B.1: Equivalent circuit of a DC line (in steady-state).

# Appendix C

# Power system models and Lyapunov's functions

The control strategies for VSC-MTDC systems proposed in this thesis have been analysed by nonlinear time-domain simulation using full-detailed electromechanical models of the power system. Nevertheless, simpler models were used in some cases for theoretical analysis. This appendix describes the models of the power systems and Lyapunov's functions used for Lyapunov-based stability analysis of the control strategies proposed in this thesis.

## C.1 Control Lyapunov's Function

An uncontrolled dynamic system: $\dot{\boldsymbol{x}} = \boldsymbol{f}(\boldsymbol{x})$ will have a stable operating point $\boldsymbol{x}_0$, if there exist a function $\mathcal{V}(\boldsymbol{x})$ such that $\mathcal{V}(\boldsymbol{x}) > 0$ if $\boldsymbol{x} \neq \boldsymbol{x}_0$, $\mathcal{V}(\boldsymbol{x}_0) = 0$, and $\dot{\mathcal{V}}(\boldsymbol{x}) \leq 0$ in the neighbourhood of $\boldsymbol{x}_0$ [157, 158]. A function that verifies these conditions is known as Lyapunov's function. The same system but controlled with an input vector $\boldsymbol{u}$, is [54]:

$$\dot{\boldsymbol{x}} = \boldsymbol{f}(\boldsymbol{x}) + \boldsymbol{g}(\boldsymbol{x})\boldsymbol{u} \tag{C.1}$$

Assuming that the uncontrolled system is stable with a Lyapunov's function $\mathcal{V}$ and that the same function is used as Lyapunov's function candidate for the controlled system:

$$\dot{\mathcal{V}} = \nabla\mathcal{V} \cdot \dot{\boldsymbol{x}} = \overbrace{\nabla\mathcal{V} \cdot \boldsymbol{f}(\boldsymbol{x})}^{\dot{\mathcal{V}}_{unctr}} + \overbrace{\nabla\mathcal{V} \cdot \boldsymbol{g}(\boldsymbol{x})\boldsymbol{u}}^{\dot{\mathcal{V}}_{ctr}} \tag{C.2}$$

where $\dot{\mathcal{V}}_{unctr}$ is the derivative when there was no control ($\dot{\mathcal{V}}_{unctr} \leq 0$) and $\dot{\mathcal{V}}_{ctr}$ is the contribution of the control law. Clearly, if $\dot{\mathcal{V}}_{ctr} \leq 0$, the controlled system (3.14) will also be stable at $\boldsymbol{x}_0$ [54].

This methodology has been used to derive suitable control strategies for transient stability improvement in the context of excitation control systems [158], series [54] and shunt [52] FACTS devices, HVDC point-to-point links [42, 47] and VSC-MTDC systems [49, 50].

## C.2 Classical multi-machine reduced-network model

In this model, generators are described using a simplified model for synchronous machines, losses in the lines are neglected and the loads are represented as constant-impedance loads. The latter assumption makes it possible to reduce the system to the buses of the generators, only. P and Q modulation of the VSC stations are modelled as power injections into the AC grid [50].

This model was used for the theoretical analysis of Q control strategies in Chapter 4. The choice of this simplified model for that analysis was due to the lack of suitable energy functions of detailed models where Q injections are controlled as a function of the frequency. Hence, the purpose of using the reduced network model is to provide useful insight into the effect of Q modulation of the VSC stations on transient stability.

The dynamic model of the power system consists of a set of differential equations, which will be written in a reference frame rotating synchronously with the centre of inertia (COI). The angle and speed of the COI ($\delta_{COI}$ and $\omega_{COI}$, respectively) are defined as:

$$\delta_{COI} = \sum_{k=1}^{n_G} \frac{M_k}{M_T} \delta_{G,k}, \quad \omega_{COI} = \sum_{k=1}^{n_G} \frac{M_k}{M_T} \omega_{G,k} \tag{C.3}$$

$$\text{with:} \quad M_T = \sum_{k=1}^{n_G} M_k$$

where $n_G$ is the number of generators and $\delta_{G,k}$, $\omega_{G,k}$ and $M_k$ are the rotor angle, the speed and the moment of intertia of machine $k$.

Hence, the dynamic model of the power system is [164]:

$$\dot{\tilde{\delta}}_{G,k} = \tilde{\omega}_{G,k} \tag{C.4}$$

$$\dot{\tilde{\omega}}_{G,k} = \frac{1}{M_k}(p_k - p_{e,k} + \frac{M_k}{M_T}P_{COI}) \tag{C.5}$$

$$\forall k = 1, \ldots, n_G$$

where:

$$\tilde{\delta}_{G,k} = \delta_{G,k} - \delta_{COI}, \quad \tilde{\omega}_{G,k} = \omega_{G,k} - \omega_{COI}, \tag{C.6}$$

and

- $p_k = p_{m,k} - g_{kk}e_k^2$ is the net active power of machine $k$ ($p_{m,k}$ is the mechanical power, $e_k$ is the internal voltage and $g_{kk}$ is the bus conductance)
- $p_{e,k}$ is the electrical power of machine $k$
- $P_{COI} = \sum_{k=1}^{n_G}(p_k - p_{e,k})$

Using this model, if there is no modulation in the VSC stations, the converters are seen by the AC grid in the same way as static loads (as constant impedance) and they are included in the admittance matrix. Therefore, the electrical power of machine $k$ with no modulation in the VSCs ($p_{e,k}^{nc}$) is given by:

$$p_{e,k}^{nc} = \sum_{l \neq k} e_k e_l b_{kl} \cos(\tilde{\delta}_{G,k} - \tilde{\delta}_{G,l}) \tag{C.7}$$

where $b_{kl}$ is the transfer susceptance between generators $k$ and $l$.

The effect of the modulation of P and Q injections of the converters on the states of the system are implicit in the electrical power [42,50]:

$$p_{e,k} = p_{e,k}^{nc} + \sum_{j=1}^{n}(b_{P,kj}\Delta p_{s,j} + b_{Q,kj}\Delta q_{s,j}) \tag{C.8}$$

where:

- $b_{P,kj}$ accounts for the effect of the P modulation of VSC$j$ ($\Delta p_{s,j}$) on the electrical power of machine $k$.
- $b_{Q,kj}$ accounts for the effect of the Q modulation of VSC$j$ ($\Delta q_{s,j}$) on the electrical power of machine $k$.

- $n$ is the number of VSC stations.

References [34, 164] showed that the uncontrolled system (system (C.4)-(C.5) with $\Delta p_{s,j} = \Delta q_{s,j} = 0$) is stable and the following energy function of the system is a Lyapunov's function [34, 50, 164]:

$$\mathcal{V} = \frac{1}{2}\sum_{k=1}^{n_G} M_k \tilde{\omega}_{G,k}^2 - \sum_{k=1}^{n_G} p_k \tilde{\delta}_{G,k} - \sum_{k=1}^{n_G-1}\sum_{l=k+1}^{n_G} e_k e_l b_{kl} \cos(\tilde{\delta}_{G,k} - \tilde{\delta}_{G,l}) + C_0 \tag{C.9}$$

where $C_0$ is a constant used to make $\mathcal{V} = 0$ at the equilibrium point.

If $\mathcal{V}$ of (C.9) is used as Lyapunov's function candidate of the controlled system (system (C.4)-(C.5) with $\Delta p_{s,j} \neq 0$ and $\Delta q_{s,j} \neq 0$), the contribution of P and Q modulation in the VSCs to the derivative of the Lyapunov's function candidate ($\dot{\mathcal{V}}_{ctr}$ in (C.2)) is given by:

$$\dot{\mathcal{V}}_{ctr} = -\sum_{k=1}^{n_G}\sum_{j=1}^{n} \tilde{\omega}_{G,k} b_{P,kj} \Delta p_{s,j} - \sum_{k=1}^{n_G}\sum_{j=1}^{n} \tilde{\omega}_{G,k} b_{Q,kj} \Delta q_{s,j} \tag{C.10}$$

Therefore, control laws for the P and Q injections of the VSCs ($\Delta p_{s,j}$ and $\Delta p_{s,j}$) that make $\dot{\mathcal{V}}_{ctr} \leq 0$ will make $\mathcal{V}$ a Lyapunov's function.

## C.3 Multi-machine structure-preserving model

This model includes detailed representations of the generators and it includes explicitely the buses of the AC system, giving more flexibility in the models of the VSC stations and the loads. A detailed description of the structure-preserving model and its energy functions can be found in [34], [164] and [54]. The work in [47] used structure-preserving models for power systems with point-to-point VSC-HVDC links. Furthermore, the energy function of the system was used for stability analysis of control strategies in the VSC stations. The work in [47] has been extended to VSC-MTDC systems in this subsection, considering $n$ VSC stations instead of two.

Since the energy function of the structure-preserving model can handle frequency-dependent active-power injections, it was used for theoretical stability analysis of active-power control strategies for VSC-MTDC systems in Chapter 3.

The multi-machine structure-preserving model consists of a set of differential-

algebraic equations. A system with $n_G$ generators, $N$ AC-buses and a multi-terminal HVDC system with $n$ VSC stations is now considered.

The set of differential equations is given by [164]:

$$\dot{\tilde{\delta}}_{G,k} = \tilde{\omega}_{G,k} \tag{C.11}$$

$$\dot{\tilde{\omega}}_{G,k} = \frac{1}{M_k}(p_{m,k} - p_{e,k} + \frac{M_k}{M_T}P_{COI}) \tag{C.12}$$

$$\dot{e}'_{q,k} = \frac{1}{T'_{do,k}}\Big[\frac{x_{d,k} - x'_{d,k}}{x'_{d,k}}u_{n_G+k}\cos(\tilde{\delta}_{G,k} - \tilde{\theta}_{n_G+k}) + e_{fd,k} - \frac{x_{d,k}}{x'_{d,k}}e'_{q,k}\Big] \tag{C.13}$$

$$\forall k = 1, \ldots, n_G \tag{C.14}$$

The algebraic equations are the P and Q conservation conditions at every bus (see Chapter 3 of [164] for further details). The VSC stations are represented as P and Q injections into the AC buses [47].

The following energy function was proposed for a multi-machine structure-preserving model with VSC stations (modelled as power injections) [47, 54, 164]:

$$\mathcal{V} = \sum_{k=1}^{10}\mathcal{V}_k + C_0 \tag{C.15}$$

where:

$$\mathcal{V}_1 = \frac{1}{2}\sum_{k=1}^{n_G}M_k\tilde{\omega}^2_{G,k}, \quad \mathcal{V}_2 = -\sum_{k=1}^{n_G}p_{m,k}\tilde{\delta}_{G,k} \tag{C.16}$$

$$\mathcal{V}_3 = \sum_{k=n_G+1}^{n_G+N}\int p_{L,k}d\tilde{\theta}_k, \quad \mathcal{V}_4 = \sum_{k=n_G+1}^{n_G+N}\int \frac{q_{L,k}}{u_k}du_k, \tag{C.17}$$

$$\mathcal{V}_5 = \sum_{k=n_G+1}^{2n_G}\frac{1}{2x_{d,k-n_G}}[e'^2_{q,k-n_G} + u_k^2 - 2e'_{q,k-n_G}u_k\cos(\tilde{\delta}_{G,k-n} - \tilde{\theta}_k)], \tag{C.18}$$

$$\mathcal{V}_6 = -\frac{1}{2}\sum_{k=n_G+1}^{n_G+N}\sum_{l=n_G+1}^{n_G+N} b_{kl}u_k u_l \cos(\tilde{\theta}_k - \tilde{\theta}_l), \tag{C.19}$$

$$\mathcal{V}_7 = \sum_{k=n_G+1}^{2n_G} \frac{x'_{d,k-n_G} - x_{q,k-n_G}}{4x'_{d,k-n_G}x_{q,k-n_G}}[u_k^2 - u_k^2\cos(2(\tilde{\delta}_{G,k-n_G} - \tilde{\theta}_k))], \tag{C.20}$$

$$\mathcal{V}_8 = -\sum_{k=1}^{n_G}\frac{e_{fd,k}e'_{q,k}}{x_{d,k} - x'_{d,k}}, \quad \mathcal{V}_9 = \sum_{k=1}^{n_G}\frac{e'^2_{q,k}}{2(x_{d,k} - x'_{d,k})}, \tag{C.21}$$

$$\mathcal{V}_{10} = -\sum_{k=1}^{n}\int p_{s,k}d\tilde{\delta}_{s,k}. \tag{C.22}$$

The term $\mathcal{V}_{10}$ is associated to P modulation of the VSC stations of the multi-terminal system, where $p_{s,k}$ is the P injection of VSC $k$ and $\tilde{\delta}_{s,k}$ is the angle of the voltage at its PCC.

The work in [34, 47, 54] showed that the energy function in (C.15) is a Lyapunov's function of the uncontrolled system ($p_{s,k} = p^0_{s,k}$).

If $\mathcal{V}$ of (C.15) is used as Lyapunov's function candidate for the controlled system ($p_{s,k} = p^0_{s,k} + \Delta p_{s,k}$), then the derivative $\dot{\mathcal{V}}_{ctr}$ of (C.2) is given by [47]:

$$\dot{\mathcal{V}}_{ctr} = \sum_{i=1}^{n}\Delta p_{s,i}(\omega_i - \omega_{COI}) \tag{C.23}$$

Therefore, control laws for the P injections of the VSC stations, $\Delta p_{s,k}$, such that $\dot{\mathcal{V}}_{ctr} \leq 0$ will make $\mathcal{V}$ a Lyapunov's function.

# Appendix D

# Small-signal model

This appendix spells out how the linearised model of a VSC-MTDC system like the one mentioned in Chapter 6 has been derived. First of all, each one of the subsystem (converters, controllers, HVDC,...) will be tackled. Secondly, all subsystems will be put together in a single linear model. Finally, the way in which several VSC-MTDC systems can be gathered in a single model will be described.

## D.1 VSC station

A VSC is depicted in Fig. D.1. The converter is controlled using vector control, with the converter $d-q$ axes (synchronous to the frequency at the PCC of each VSC station) aligned with the AC voltage: $\bar{u}_{s,i} = u_{s,d,i} + ju_{s,q,i}$ with $u_{s,d,i} = u_{s,i}$ and $u_{s,q,i} = 0$). Therefore, the VSC converter consists of the following subsystems:

- The inner current control loop.
- The outer controllers.
- AC/DC coupling.

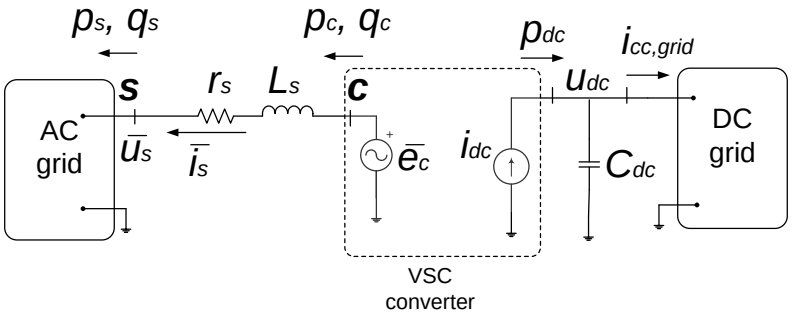


Figure D.1: VSC converter modelling.

The model of each VSC converter $i$ will have the form: [1], [2]

$$\begin{aligned}
\boldsymbol{\Delta \dot{x}_{conv,i}} &= \boldsymbol{A_{conv,i}} \cdot \boldsymbol{\Delta x_{conv,i}} + \boldsymbol{B_{conv,R,i}} \cdot \boldsymbol{\Delta r_{conv,i}} \\
&\quad + \boldsymbol{B_{conv,A,i}} \cdot \boldsymbol{\Delta v_{AC,i}} + \boldsymbol{B_{conv,D,i}} \cdot \Delta u_{dc,i}, \\
\boldsymbol{\Delta i_{conv,AC,i}} &= \boldsymbol{C_{conv,A,i}} \cdot \boldsymbol{\Delta x_{conv,i}} + \boldsymbol{D_{conv,AR,i}} \cdot \boldsymbol{\Delta r_{conv,i}} \\
&\quad + \boldsymbol{D_{conv,AA,i}} \cdot \boldsymbol{\Delta v_{AC,i}} + \boldsymbol{D_{conv,AD,i}} \cdot \Delta u_{dc,i} \\
\Delta i_{dc,i} &= \boldsymbol{C_{conv,D,i}} \cdot \boldsymbol{\Delta x_{conv,i}} + \boldsymbol{D_{conv,DR,i}} \cdot \boldsymbol{\Delta r_{conv,i}} \\
&\quad + \boldsymbol{D_{conv,DA,i}} \cdot \boldsymbol{\Delta v_{AC,i}} + \boldsymbol{D_{conv,DD,i}} \cdot \Delta u_{dc,i}. \quad \text{(D.1)}
\end{aligned}$$

with input signals:

- References of the outer controllers: [3] $\boldsymbol{\Delta r_{conv,i}} = [\Delta p_{s,i}^{Ref}, \Delta u_{dc,i}^{Ref}, \Delta q_{s,i}^{Ref}, \Delta u_{s,i}^{Ref}]^T$.
- AC voltage at the PCC: $\boldsymbol{\Delta v_{AC,i}} = [\Delta u_{s,Di}, \Delta u_{s,Qi}]^T$, written in the system synchronous frame ($D-Q$ axes).
- DC voltage: $\Delta u_{dc,i}$.

The output signals are the currents injected into the AC and DC grids:

[1] *conv* refers to converter (VSC station).

[2] $A$ and $D$ have been used to denote $AC$ and $DC$, respectively, for the sake of clarity. For example, in matrix $\boldsymbol{D_{conv,DA,i}}$.

[3] Superscript "Ref" is used instead of "ref", to distinguish the increment of the P set-point value of the outer controller in the SSA ($\Delta p_{s,i}^{Ref}$) and the supplementary P set-point value for transient stability improvement described in Chapter 3 ($\Delta p_{s,i}^{ref}$).

- AC current: $\boldsymbol{\Delta i_{conv,AC,i}} = [\Delta i_{D,i}, \Delta i_{Q,i}]^T$.
- DC current: $\Delta i_{dc,i}$.

The AC voltage ($\boldsymbol{\Delta v_{AC,i}}$) and the current injection ($\boldsymbol{\Delta i_{conv,AC,i}}$) of the converter at the PCC must be written in the system synchronous frame $D-Q$, to be able to incorporate the linearised model of the converter into the linearised model fo the rest of the system. Since the converters are controlled using vector control, their linear models will be derived writing the AC voltages and currents in the converter $d-q$ axes and they will transformed to the synchhronous $D-Q$ axes at the end of the process.

### D.1.1 Inner current control

Since the time constant of the inner controller of the converters is very fast in comparison with the rest of the power system dynamics, the closed-loop response of the current is approximated by a first order system, for angle stability studies (Fig. D.2). Hence, the state-space representation of the inner current loop will be:

$$\begin{aligned} \frac{d\boldsymbol{\Delta x_{cint,i}}}{dt} &= \boldsymbol{A_{cint,i}\Delta x_{cint,i}} + \boldsymbol{B_{cint,i}\Delta u_{cint,i}} \\ \boldsymbol{\Delta i^{dq}_{conv,AC,i}} &= \boldsymbol{C_{cint,i}\Delta x_{cint,i}} + \boldsymbol{D_{cint,i}\Delta u_{cint,i}} \end{aligned} \tag{D.2}$$

where:

$$\begin{aligned} \boldsymbol{\Delta x_{cint,i}} &= [\Delta i_{d,i}, \Delta i_{q,i}]^T, \\ \boldsymbol{\Delta u_{cint,i}} &= [\Delta i^{ref}_{d,i}, \Delta i^{ref}_{q,i}]^T, \\ \boldsymbol{\Delta i^{dq}_{conv,AC,i}} &= [\Delta i_{d,i}, \Delta i_{q,i}]^T = \boldsymbol{\Delta x_{cint}}. \end{aligned} \tag{D.3}$$

and

$$\begin{aligned} &\boldsymbol{A_{cint,i}} = \begin{bmatrix} -1/\tau_{d,i} & 0 \\ 0 & -1/\tau_{q,i} \end{bmatrix},\ \boldsymbol{B_{cint,i}} = \begin{bmatrix} 1/\tau_{d,i} & 0 \\ 0 & 1/\tau_{q,i} \end{bmatrix}, \\ &\boldsymbol{C_{cint,i}} = \boldsymbol{I_{2\times 2}},\ \boldsymbol{D_{cint,i}} = \boldsymbol{0_{2\times 2}}. \end{aligned} \tag{D.4}$$

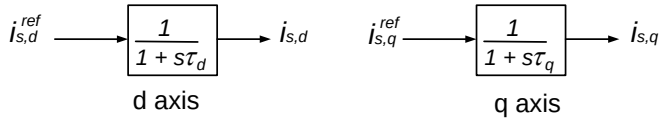


Figure D.2: Approximation of the inner current loop.

### D.1.2 Outer control

The active and reactive power injections of VSC $i$ are given by (see Fig. D.1):

$$p_{s,i} = u_{s,i} i_{d,i}, \quad q_{s,i} = -u_{s,i} i_{q,i}, \tag{D.5}$$

The active power is controlled with the $d$-axis current whilst the reactive power is controlled with the $q$-axis current. The linearised models of the $d$- and $q$- currents are derived independently and, eventually, they are joined together into a single model with the form:

$$\begin{aligned} \frac{d\boldsymbol{\Delta x_{cext,i}}}{dt} &= \boldsymbol{A_{cext,i}\Delta x_{cext,i} + B_{cext,i}\Delta u_{cext,i}}, \\ \boldsymbol{\Delta i_{conv,AC,i}^{dq,ref}} &= \boldsymbol{C_{cext,i}\Delta x_{cext,i} + D_{cext,i}\Delta u_{cext,i}}, \end{aligned} \tag{D.6}$$

where:

$$\boldsymbol{\Delta x_{cext,i}} = [\boldsymbol{\Delta x_{d,i}}, \boldsymbol{\Delta x_{q,i}}]^T, \tag{D.7}$$

$$\boldsymbol{\Delta u_{cext,i}} = [\Delta p_{s,i}^{Ref}, \Delta u_{dc,i}^{Ref}, \Delta q_{s,i}^{Ref}, \Delta u_{s,i}^{Ref}, \Delta u_{s,i}, \Delta u_{dc,i}, \Delta i_{d,i}, \Delta i_{q,i}]^T, \tag{D.8}$$

$$\boldsymbol{\Delta i_{conv,AC,i}^{dq,ref}} = [\Delta i_{d,i}^{ref}, \Delta i_{q,i}^{ref}]^T. \tag{D.9}$$

Notice that the input vector $\boldsymbol{\Delta u_{cext,i}}$ contains redundant reference terms. For example, a converter could be controlling the active power or the DC-voltage, but not both. However, including all the possible references in the input vector helps to write a generalised model. The information about which reference is used for each control model will be in the state matrices of system (D.6).

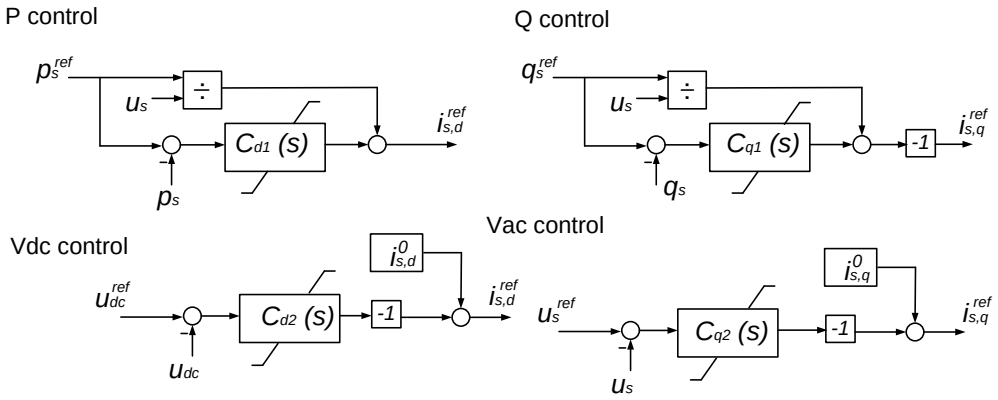


(a) d-axis. (b) q-axis.

Figure D.3: Outer controllers. $C_x(s) = K_{p,x} + K_{i,x}/s$ where $x$ can be $d1$, $d2$, $q1$ or $q2$.

### $d$-axis control

The $d$-axis current is used to control the P injection or the DC voltage, as shown in Fig. D.3a. The linearised model of the outer $d$-axis outer controller will be:

$$\begin{aligned} \boldsymbol{\Delta \dot{x}_{d,i}} &= \boldsymbol{A_{d,i}} \cdot \boldsymbol{\Delta x_{d,i}} + \boldsymbol{B_{d,i}} \cdot \boldsymbol{\Delta u_{cext,i}}, \\ \Delta i_{d,i}^{ref} &= \boldsymbol{C_{d,i}} \cdot \boldsymbol{\Delta x_{d,i}} + \boldsymbol{D_{d,i}} \cdot \boldsymbol{\Delta u_{cext,i}}, \end{aligned} \tag{D.10}$$

The states $\boldsymbol{\Delta x_{d,i}}$ will depend on the controller used, but the inputs will always be $\boldsymbol{\Delta u_{cext,i}}$ and the output will always be $\Delta i_{d,i}^{ref}$, regardless the $d$-axis control mode (P control or DC-voltage control).

The controllers of Fig. D.3a are described below.

d1: Active-power control

The linearised model of the P control of Fig. D.3a is given by:

$$\begin{aligned} \frac{d\Delta m_{d,i}}{dt} &= 0 \cdot \Delta m_{d,i} + K_{I,d1,i}(\Delta p_{s,i}^{Ref} - \Delta p_{s,i}), \\ \Delta i_{d,i}^{ref} &= \left(\frac{1}{u_{s,i}^0}\right)\Delta p_{s,i}^{Ref} + \left(\frac{-p_{s,i}^0}{(u_{s,i}^0)^2}\right)\Delta u_{s,i}, \\ &\quad + K_{P,d1,i}(\Delta p_{s,i}^{Ref} - \Delta p_{s,i}) + \Delta m_{d,i}, \end{aligned} \tag{D.11}$$

where $\Delta m_{d,i}$ is the state variable associated to the integral of the PI controller for P control ($C_{d1}(s)$).

Since $\Delta p_{s,i} = u_{s,i}^0 \Delta i_{d,i} + i_{d,i}^0 \Delta u_{s,i}$, the state-space representation of the $d$-axis outer controller can be written as (D.10) with state matrices:

$$\begin{aligned} \boldsymbol{A_{d,i}} &= 0, \\ \boldsymbol{B_{d,i}} &= \left[\begin{array}{cccccccc} K_{I,d1,i} & 0 & 0 & 0 & -K_{I,d1,i} i_{d,i}^0 & 0 & -K_{I,d1,i} u_{s,i}^0 & 0 \end{array}\right], \\ \boldsymbol{C_{d,i}} &= 1, \\ \boldsymbol{D_{d,i}} &= \left[\begin{array}{cccccccc} (1/u_s^0 + K_{P,d1,i}) & 0 & 0 & 0 & -(p_s^0/(u_s^0)^2 + K_{P,d1,i} i_d^0) & \ldots \\ 0 & -K_{P,d1,i} u_s^0 & 0 \end{array}\right], \end{aligned} \tag{D.12}$$

The $d$-axis current, $i_{d,i}^{ref}$, is often computed simply as $i_{d,i}^{ref} = p_{s,i}^{Ref}/u_{s,i}$. In this case, $K_{P,d1,i} = K_{I,d1,i} = 0$ and there are no state variables in the linear model of the $d$-axis outer controller. Therefore, the system (D.10) si reduced to:

$$\begin{aligned} &\Delta i_{d,i}^{ref} = \boldsymbol{D_{d,i}} \cdot \boldsymbol{\Delta u_{cext,i}}, \\ &\boldsymbol{D_d} = \left[\begin{array}{cccccccc} 1/u_{s,i}^0 & 0 & 0 & 0 & -p_{s,i}^0/(u_{s,i}^0)^2 & 0 & 0 & 0 \end{array}\right]. \end{aligned} \tag{D.13}$$

d2: DC-voltage control

Following the scheme of Fig. D.3a, the linearised model of the DC-voltage control is given by:

$$\begin{aligned} \frac{d\Delta n_{d,i}}{dt} &= 0 \cdot \Delta n_{d,i} + K_{I,d2,i}(\Delta u_{dc,i}^{Ref} - \Delta u_{dc,i}), \\ \Delta i_{d,i}^{ref} &= -K_{P,d2,i}(\Delta u_{dc,i}^{Ref} - \Delta u_{dc,i}) - \Delta n_{d,i}, \end{aligned} \tag{D.14}$$

where $\Delta n_{d,i}$ is the state variable of the PI controller $C_{d2}(s)$.

System (D.14) is equivalent to the one in (D.10) with the state matrices given by:

$$\begin{aligned}
\boldsymbol{A_{d,i}} &= 0, \\
\boldsymbol{B_{d,i}} &= K_{I,d2,i} \cdot \begin{bmatrix} 0 & +1 & 0 & 0 & 0 & -1 & 0 & 0 \end{bmatrix}, \\
\boldsymbol{C_{d,i}} &= -1 \\
\boldsymbol{D_{d,i}} &= K_{P,d2,i} \cdot \begin{bmatrix} 0 & -1 & 0 & 0 & 0 & +1 & 0 & 0 \end{bmatrix}.
\end{aligned} \tag{D.15}$$

**q-axis control**

The $q$-axis controller, used for Q or AC voltage control (Fig. D.3b), takes the form:

$$\begin{aligned}
\boldsymbol{\Delta \dot{x}_{q,i}} &= \boldsymbol{A_{q,i}} \cdot \boldsymbol{\Delta x_{q,i}} + \boldsymbol{B_{q,i}} \cdot \boldsymbol{\Delta u_{cext,i}} \\
\Delta i_{q,i}^{ref} &= \boldsymbol{C_{q,i}} \cdot \boldsymbol{\Delta x_{q,i}} + \boldsymbol{D_{q,i}} \cdot \boldsymbol{\Delta u_{cext,i}}
\end{aligned} \tag{D.16}$$

The state vector $\boldsymbol{\Delta x_{q,i}}$ in (D.16) will depend on the control mode, the input will be the same one used for the $d$-axis control loop, $\boldsymbol{\Delta u_{cext,i}}$ of (D.6), and the output vector will be the $q$-axis current reference $\Delta i_{q,i}^{ref}$.

q1: Reactive-power control

The linearised model of the outer control loop of the reactive power injection (Fig. D.3b) is given by:

$$\begin{aligned}
\frac{d\Delta m_{q,i}}{dt} &= 0 \cdot \Delta m_{d,i} + K_{I,q1,i}(\Delta q_{s,i}^{Ref} - \Delta q_{s,i}), \\
\Delta i_{q,i}^{Ref} &= -\left(\frac{1}{u_{s,i}^0}\right)\Delta q_{s,i}^{Ref} + \left(\frac{q_{s,i}^0}{(u_{s,i}^0)^2}\right)\Delta u_{s,i}, \\
&\quad -K_{P,q1,i}(\Delta q_{s,i}^{Ref} - \Delta q_{s,i}) - \Delta m_{q,i},
\end{aligned} \tag{D.17}$$

where $\Delta m_{q,i}$ is the state variable associated to the integral of the PI controller used in Q control mode ($C_{q1}(s)$).

Since $\Delta q_{s,i} = -u_{s,i}^0 \Delta i_{q,i} - i_{q,i}^0 \Delta u_{s,i}$, the state matrices of system (D.16)

will be given by:

$$\begin{aligned}
\boldsymbol{A_{q,i}} &= 0, \\
\boldsymbol{B_{q,i}} &= K_{I,q1,i}\left[\begin{array}{cccccccc} 0 & 0 & 1 & 0 & i^0_{q,i} & 0 & 0 & K_{I,q1,i}u^0_{s,i} \end{array}\right], \\
\boldsymbol{C_{q,i}} &= -1, \\
\boldsymbol{D_{q,i}} &= [\begin{array}{cccc} 0 & 0 & -(1/u^0_s + K_{P,q1,i}) & 0 \end{array} \quad (q^0_s/(u^0_s)^2 - K_{P,q1,i}i^0_q) \quad \ldots \\
&\qquad \begin{array}{ccc} 0 & 0 & -K_{P,q1,i}u^0_s \end{array}],
\end{aligned} \tag{D.18}$$

As in P control, the gains of the PI controller could be set to zero ($K_{P,q1,i} = K_{I,q1,i} = 0$), leading to $i^{Ref}_{q,i} = -q^{Ref}_{s,i}/u_{s,i}$. In this case, (D.16) will be given by:

$$\begin{aligned}
\Delta i^{ref}_{q,i} &= \boldsymbol{D_{q,i}} \cdot \boldsymbol{\Delta u_{cext,i}}, \\
\boldsymbol{D_{q,i}} &= \left[\begin{array}{cccccccc} 0 & 0 & -1/u^0_s & 0 & q^0_s/(u^0_s)^2 & 0 & 0 & 0 \end{array}\right].
\end{aligned} \tag{D.19}$$

q2: AC-voltage control

If a converter VSC$_i$ is controlling the AC voltage at the PCC using the control diagram of Fig. D.3b, the linearised model of the $q$-axis outer loop is given by:

$$\begin{aligned}
\frac{d\Delta n_{q,i}}{dt} &= 0 \cdot \Delta n_{q,i} + K_{I,q2,i}(\Delta u^{Ref}_{s,i} - \Delta u_{s,i}), \\
\Delta i^{ref}_{q,i} &= -K_{P,q2,i}(\Delta u^{Ref}_{s,i} - \Delta u_{s,i}) - \Delta n_{q,i},
\end{aligned} \tag{D.20}$$

which can be written in matrix form as (D.16), with the state matrices given by:

$$\begin{aligned}
\boldsymbol{A_{q,i}} &= 0, \\
\boldsymbol{B_{q,i}} &= K_{I,q2,i}\left[\begin{array}{cccccccc} 0 & 0 & 0 & 1 & i^0_{q,i} & 0 & 0 & u^0_{s,i} \end{array}\right], \\
\boldsymbol{C_{q,i}} &= -1, \\
\boldsymbol{D_{q,i}} &= [\begin{array}{cccc} 0 & 0 & 0 & -(1/u^0_{s,i} + K_{P,q2,i}) \end{array} \quad (q^0_{s,i}/(u^0_{s,i})^2 - K_{P,q2,i}i^0_q) \quad \ldots \\
&\qquad \begin{array}{ccc} 0 & 0 & -K_{P,q2,i}u^0_{s,i} \end{array}],
\end{aligned} \tag{D.21}$$

The state variable of the PI controller ($\boldsymbol{\Delta x_{cext,i}} = \Delta n_{q,i}$) is the only state of the system, the input vector $\boldsymbol{\Delta u_{cext,i}}$ is the same as in (D.6) and the output signal is the $q$-axis current set point ($\Delta i^{ref}_{q,i}$). The state matrices

of (D.16) will read:

$$\begin{aligned}
\boldsymbol{A_{q,i}} &= 0 \\
\boldsymbol{B_{q,i}} &= K_{I,q2,i} \cdot \begin{bmatrix} 0 & 0 & 0 & +1 & -1 & 0 & 0 & 0 \end{bmatrix} \\
\boldsymbol{C_{q,i}} &= -1 \\
\boldsymbol{D_{q,i}} &= K_{P,q2,i} \cdot \begin{bmatrix} 0 & 0 & 0 & -1 & +1 & 0 & 0 & 0 \end{bmatrix}
\end{aligned} \tag{D.22}$$

**Outer control: $d$-axis and $q$-axis together**

The linearised models of the $d$- and $q$-axis outer controllers, (D.10) and (D.16), respectively, can be put together leading to (D.6) with the state matrices given by:

$$\begin{aligned}
\boldsymbol{A_{cext,i}} &= \left[\begin{array}{c|c} \boldsymbol{A_{d,i}} & \boldsymbol{0} \\ \hline \boldsymbol{0} & \boldsymbol{A_{q,i}} \end{array}\right], \quad \boldsymbol{B_{cext,i}} = \left[\begin{array}{c} \boldsymbol{B_{d,i}} \\ \hline \boldsymbol{B_{q,i}} \end{array}\right], \\
\boldsymbol{C_{cext,i}} &= \left[\begin{array}{c|c} \boldsymbol{C_{d,i}} & \boldsymbol{0} \\ \hline \boldsymbol{0} & \boldsymbol{C_{q,i}} \end{array}\right], \quad \boldsymbol{D_{cext,i}} = \left[\begin{array}{c} \boldsymbol{D_{d,i}} \\ \hline \boldsymbol{D_{q,i}} \end{array}\right],
\end{aligned} \tag{D.23}$$

Notice that, as described at the beginning of Subsection D.1.2, the states of the system are $\boldsymbol{\Delta x_{cext,i}} = [\boldsymbol{\Delta x_{d,i}}, \boldsymbol{\Delta x_{q,i}}]^T$.

### D.1.3 Inner and outer controllers together

Since the $dq$ currents are inputs of the linearised model of the outer controller and states of the inner controller, they should be written explicitely in system (D.6):

$$\begin{aligned}
\frac{d\boldsymbol{\Delta x_{cext,i}}}{dt} &= \boldsymbol{A_{cext,i}\Delta x_{cext,i}} + \boldsymbol{B_{cext,1,i}\Delta u_{cext,1,i}} + \boldsymbol{B_{cext,2,i}} \begin{bmatrix} \Delta i_{d,i} \\ \Delta i_{q,i} \end{bmatrix}, \\
\boldsymbol{\Delta i^{dq,ref}_{conv,AC,i}} &= \boldsymbol{C_{cext,i}\Delta x_{cext,i}} + \boldsymbol{D_{cext,1,i}\Delta u_{cext,1,i}} + \boldsymbol{D_{cext,2,i}} \begin{bmatrix} \Delta i_{d,i} \\ \Delta i_{q,i} \end{bmatrix},
\end{aligned} \tag{D.24}$$

where: [4]

[4] A Matlab-based notation is used. For example: $\boldsymbol{B_{cext,i}}(:,1{:}6)$ denotes a matrix with all the rows of matrix $\boldsymbol{B_{cext,i}}$ and with the columns 1 to 6 of matrix $\boldsymbol{B_{cext,i}}$.

$$\begin{aligned}
&\boldsymbol{B_{cext,1,i}} = \boldsymbol{B_{cext,i}}(:,1{:}6), \quad \boldsymbol{B_{cext,2,i}} = \boldsymbol{B_{cext,i}}(:,7{:}8),\\
&\boldsymbol{D_{cext,1,i}} = \boldsymbol{D_{cext,i}}(:,1{:}7), \quad \boldsymbol{D_{cext,2,i}} = \boldsymbol{D_{cext,i}}(:,8{:}9),\\
&\boldsymbol{\Delta u_{cext,1,i}} = [\Delta p_{s,i}^{Ref}, \Delta u_{dc,i}^{Ref}, \Delta q_{s,i}^{Ref}, \Delta u_{s,i}^{Ref}, \Delta u_{s,i}, \Delta u_{dc,i}]^T.
\end{aligned} \tag{D.25}$$

Then, taking into account all the states of the system, [5]

$$\boldsymbol{\Delta x'_{conv,i}} = [\boldsymbol{\Delta x_{cint,i}}, \boldsymbol{\Delta x_{cext,i}}]^T, \tag{D.26}$$

using $\boldsymbol{\Delta u_{conv,i}} = \boldsymbol{\Delta u_{cext,1,i}}$ as the input vector and writing the $dq$ currents $\boldsymbol{\Delta i^{dq}_{conv,AC,i}}$ as the output vector, the state-space representation of the inner and outer control loops can be put together as:

$$\begin{aligned}
\boldsymbol{\Delta \dot{x}'_{conv,i}} &= \boldsymbol{A'_{conv,i}\Delta x'_{conv,i}} + \boldsymbol{B'_{conv,i}\Delta u_{conv,i}},\\
\boldsymbol{\Delta i^{dq}_{conv,AC,i}} &= \boldsymbol{C'_{conv,AC,i}\Delta x'_{conv,i}} + \boldsymbol{D'_{conv,AC,i}\Delta u_{conv,i}},
\end{aligned} \tag{D.27}$$

with state matrices:

$$\begin{aligned}
\boldsymbol{A'_{conv,i}} &= \left[\begin{array}{c|c} (\boldsymbol{A_{cint}} + \boldsymbol{B_{cint}} \cdot \boldsymbol{D_{cext,2}}) & \boldsymbol{B_{cint}} \cdot \boldsymbol{C_{cext}} \\ \hline \boldsymbol{B_{cext,2}} & \boldsymbol{A_{cext}} \end{array}\right],\\
\boldsymbol{B'_{conv,i}} &= \left[\frac{\boldsymbol{B_{cint}} \cdot \boldsymbol{D_{cext,1}}}{\boldsymbol{D_{cext,1}}}\right],\\
\boldsymbol{C'_{conv,i}} &= \left[\begin{array}{c|c} (\boldsymbol{C_{cint}} + \boldsymbol{D_{cint}} \cdot \boldsymbol{D_{cext,2}}) & \boldsymbol{D_{cint}} \cdot \boldsymbol{C_{cext}} \end{array}\right],\\
\boldsymbol{D'_{conv,i}} &= \boldsymbol{D_{cint}} \cdot \boldsymbol{D_{cext,1}}.
\end{aligned} \tag{D.28}$$

### D.1.4 Including the DC-current injection as an output

Each VSC will be seen as a current injection by the DC grid. Therefore, the DC current injection of each VSC must be included as an output of the linearised model of each VSC, in order to connect the linearised models of the VSCs and the linearised model of the HVDC grid.

**(a) DC current of the VSC:**

According to Fig. D.1, the current injected into the DC grid by each VSC$_i$

[5] Primes (e.g. $\boldsymbol{\Delta x'_{conv,i}}$) are used to denote the states and matrices at intermediate stages of the process of the derivation of the model, in order to obtain the final model of the converter without primes (e.g. $\boldsymbol{\Delta x_{conv,i}}$).

is given by:

$$i_{dc,i} = \frac{p_{dc,i}}{u_{dc,i}} = -\frac{(p_{c,i} + p_{loss,i})}{u_{dc,i}}, \tag{D.29}$$

and the linearised model of (D.29) is given by:

$$\Delta i_{dc,i} = \underbrace{[\frac{(p^0_{c,i} + p^0_{loss,i})}{(u^0_{dc,i})^2} \quad -\frac{1}{u^0_{dc,i}} \quad -\frac{1}{u^0_{dc,i}}]}_{\boldsymbol{D_{a,i}}} \cdot \begin{bmatrix} \Delta u_{dc,i} \\ \Delta p_{c,i} \\ \Delta p_{loss,i} \end{bmatrix}. \tag{D.30}$$

**(b) Active power of the VSC:**
The active power injected by VSC$_i$ into the AC grid (before the connection impedance, see Fig. D.1) is given by:

$$p_{c,i} = e_{c,d,i} i_{d,i} + e_{c,q,i} i_{q,i}. \tag{D.31}$$

The linearised model of (D.32) is:

$$\Delta p_{c,i} = \underbrace{[e^0_{c,d,i} \quad e^0_{c,q,i} \quad i^0_{d,i} \quad i^0_{q,i}]}_{\boldsymbol{D_{b,i}}} \cdot \begin{bmatrix} \Delta i_{d,i} \\ \Delta i_{q,i} \\ \Delta e_{c,d,i} \\ \Delta e_{c,q,i} \end{bmatrix}. \tag{D.32}$$

**(c) VSC losses:**
The converter losses are given by [124]:

$$p_{loss,i} = a_i + b_i \cdot i_{s,i} + c_i \cdot i^2_{s,i}, \tag{D.33}$$

where $c_i = c_{rec,i}$ if VSC$_i$ is working as a rectifier ($p_{c,i} \leq 0$) and $c_i = c_{inv,i}$ if VSC$_i$ is working as a inverter ($p_{c,i} > 0$). If (D.33) is linearised around the operating point, one has:

$$\Delta p_{loss,i} = \underbrace{[(b_i + 2 \cdot c_i \cdot i^0_{d,i}) \quad (b_i + 2 \cdot c_i \cdot i^0_{q,i})]}_{\boldsymbol{D_{c,i}}} \cdot \begin{bmatrix} \Delta i_{d,i} \\ \Delta i_{q,i} \end{bmatrix} \tag{D.34}$$

**(d) Internal voltage of the VSC:**
The internal voltage of VSC$_i$ is given by (Fig. D.1)

$$\bar{e}_{c,i} = \bar{u}_{s,i} + \bar{z}_{s,i} \cdot \bar{i}_{s,i} \;\Rightarrow\; \begin{cases} d-\text{axis: } e_{c,d,i} = u_{s,i} + r_{s,i} i_{d,i} - x_{s,i} i_{q,i}, \\ q-\text{axis: } e_{c,q,i} = 0 + x_{s,i} i_{d,i} + r_{s,i} i_{q,i}, \end{cases} \tag{D.35}$$

and linearising (D.35):

$$\begin{bmatrix} \Delta e_{c,d,i} \\ \Delta e_{c,q,i} \end{bmatrix} = \underbrace{\begin{bmatrix} 1 & r_{s,i} & -x_{s,i} \\ 0 & x_{s,i} & r_{s,i} \end{bmatrix}}_{\boldsymbol{D_{d,i}}} \cdot \begin{bmatrix} \Delta u_{s,i} \\ \Delta i_{d,i} \\ \Delta i_{q,i} \end{bmatrix}. \tag{D.36}$$

**(e) Writing the DC current injections as functions of the states and inputs of the VSC model**

Once subsystems (D.30) , (D.32) and (D.33) have been written, the linearised model of the DC-current injection of VSC$_i$ can be obtained making use of the algorithm described in Section E.1, leading to:

$$\Delta i_{dc,i} = \boldsymbol{C'_{conv,DC,i}\Delta x'_{conv,i} + D'_{conv,DC,i}\Delta u_{conv,i}}. \tag{D.37}$$

Therefore, the state-space system of VSC$_i$ will be now:

$$\begin{aligned} \boldsymbol{\Delta \dot{x}'_{conv,i}} &= \boldsymbol{A'_{conv,i}\Delta x'_{conv,i} + B'_{conv,i}\Delta u_{conv,i}}, \\ \boldsymbol{\Delta i^{dq}_{conv,AC,i}} &= \boldsymbol{C'_{conv,AC,i}\Delta x'_{conv,i} + D'_{conv,AC,i}\Delta u_{conv,i}}, \\ \Delta i_{dc,i} &= \boldsymbol{C'_{conv,DC,i}\Delta x'_{conv,i} + D'_{conv,DC,i}\Delta u_{conv,i}} \end{aligned} \tag{D.38}$$

### D.1.5 Spliting the inputs: set-point values, AC voltage and DC voltage

The input vector in (D.38) can be split as:

$$\boldsymbol{\Delta u_{conv,i}} = [\underbrace{\Delta p^{Ref}_{s,i}, \Delta u^{Ref}_{dc,i}, \Delta q^{Ref}_{s,i}, \Delta u^{Ref}_{s,i}}_{\boldsymbol{\Delta r_{conv,i}}} | \Delta u_{s,i} | \Delta u_{dc,i}]^T. \tag{D.39}$$

Then, (D.38) becomes:

$$\begin{aligned} \boldsymbol{\Delta \dot{x}'_{conv,i}} &= \boldsymbol{A''_{conv,i} \cdot \Delta x'_{conv,i} + B''_{conv,R,i} \cdot \Delta r_{conv,i}} \\ &\quad \boldsymbol{+B''_{conv,A,i} \cdot \Delta u_{s,i} + B''_{conv,D,i} \cdot \Delta u_{dc,i}}, \\ \boldsymbol{\Delta i_{conv,AC,i}} &= \boldsymbol{C''_{conv,A,i} \cdot \Delta x'_{conv,i} + D''_{conv,AR,i} \cdot \Delta r_{conv,i}} \\ &\quad \boldsymbol{+D''_{conv,AA,i} \cdot \Delta u_{s,i} + D''_{conv,AD,i} \cdot \Delta u_{dc,i}}, \\ \boldsymbol{\Delta i_{conv,DC,i}} &= \boldsymbol{C''_{conv,D,i} \cdot \Delta x'_{conv,i} + D''_{conv,DR,i} \cdot \Delta r_{conv,i}} \\ &\quad \boldsymbol{+D''_{conv,DA,i} \cdot \Delta u_{s,i} + D''_{conv,DD,i} \cdot \Delta u_{dc,i}}. \end{aligned} \tag{D.40}$$

where:

$$\begin{aligned}
&\boldsymbol{A''_{conv,i}} = \boldsymbol{A'_{conv,i}},\ \ \boldsymbol{C''_{conv,A,i}} = \boldsymbol{C'_{conv,AC,i}},\ \ \boldsymbol{C''_{conv,D,i}} = \boldsymbol{C'_{conv,DC,i}},\\
&\boldsymbol{B''_{conv,R,i}} = \boldsymbol{B'_{conv,i}}(:, 1:4),\ \ \boldsymbol{B''_{conv,A,i}} = \boldsymbol{B'_{conv,i}}(:, 5),\\
&\boldsymbol{B''_{conv,R,i}} = \boldsymbol{B'_{conv,i}}(:, 6),\\
&\boldsymbol{D''_{conv,AR,i}} = \boldsymbol{D'_{conv,AC,i}}(:, 1:4),\ \ \boldsymbol{D''_{conv,AA,i}} = \boldsymbol{D'_{conv,AC,i}}(:, 5),\\
&\boldsymbol{D''_{conv,AD,i}} = \boldsymbol{D'_{conv,AC,i}}(:, 6),\\
&\boldsymbol{D''_{conv,DR,i}} = \boldsymbol{D'_{conv,DC,i}}(:, 1:4),\ \ \boldsymbol{D''_{conv,DA,i}} = \boldsymbol{D'_{conv,DC,i}}(:, 5),\\
&\boldsymbol{D''_{conv,DD,i}} = \boldsymbol{D'_{conv,DC,i}}(:, 6),
\end{aligned} \tag{D.41}$$

Notice that in (D.40) and (D.41), the subscripts $AC$ and $DC$ have been changed to $A$ and $D$, respectively, for the sake of clarity in the formulation.

### D.1.6 Transformation from VSC $d-q$ axes to system synchronous $D-Q$ axes

The AC voltage and the current injection of VSC$_i$ at the PCC can be written in the system $D-Q$ axes:

$$\bar{u}_{s,i} = u_{s,i}\angle\delta_{s,i} = u_{s,D,i} + ju_{s,Q,i},\ \ \bar{i}_{s,i} = i_{D,i} + ji_{Q,i}, \tag{D.42}$$

Since the local VSC $d-q$ axes (rotating at the frequency at the PCC of the VSC station) are aligned with the AC voltage at the PCC of the converter ($\bar{u}_{s,i} = u_{s,i} + j0$), then:

$$\Delta u_{s,i} = \underbrace{[(u^0_{s,D,i}/u^0_{s,i})\ \ (u^0_{s,Q,i}/u^0_{s,i})]}_{\boldsymbol{M_{V1,i}}} \cdot \begin{bmatrix} \Delta u_{s,D,i} \\ \Delta u_{s,Q,i} \end{bmatrix}, \tag{D.43}$$

$$\Delta\delta_{s,i} = \underbrace{\cos^2\delta^0_{s,i}[-u^0_{s,Q,i}/(u^0_{s,D,i})^2\ \ 1/u^0_{s,D,i}]}_{\boldsymbol{M_{V2,i}}} \cdot \begin{bmatrix} \Delta u_{s,D,i} \\ \Delta u_{s,Q,i} \end{bmatrix}, \tag{D.44}$$

$$\begin{aligned}
\begin{bmatrix} \Delta i_{d,i} \\ \Delta i_{q,i} \end{bmatrix} &= \underbrace{\begin{bmatrix} \cos\delta^0_{s,i} & \sin\delta^0_{s,i} \\ -\sin\delta^0_{s,i} & \cos\delta^0_{s,i} \end{bmatrix}}_{\boldsymbol{M_{I1,i}}} \cdot \begin{bmatrix} \Delta i_{D,i} \\ \Delta i_{Q,i} \end{bmatrix} \\
&+ \underbrace{\begin{bmatrix} (-i^0_{D,i}\sin\delta^0_{s,i} + i^0_{Q,i}\cos\delta^0_{s,i}) \\ (-i^0_{D,i}\cos\delta^0_{s,i} - i^0_{Q,i}\sin\delta^0_{s,i}) \end{bmatrix}}_{\boldsymbol{M_{I2,i}}} \cdot \underbrace{\boldsymbol{M_{V2,i}} \cdot \begin{bmatrix} \Delta u_{s,D,i} \\ \Delta u_{s,Q,i} \end{bmatrix}}_{\Delta\delta_{s,i}}.
\end{aligned} \tag{D.45}$$

Therefore, the linearised model of each VSC$i$, written in the system $D-Q$ reference frame, is given by

$$\begin{aligned}
\boldsymbol{\Delta\dot{x}'_{conv,i}} &= \boldsymbol{A'''_{conv,i}} \cdot \boldsymbol{\Delta x'_{conv,i}} + \boldsymbol{B'''_{conv,R,i}} \cdot \boldsymbol{\Delta r_{conv,i}} \\
&\quad + \boldsymbol{B'''_{conv,A,i}} \cdot \boldsymbol{\Delta v_{AC,i}} + \boldsymbol{B'''_{conv,D,i}} \cdot \Delta u_{dc,i}, \\
\boldsymbol{\Delta i_{conv,AC,i}} &= \boldsymbol{C'''_{conv,A,i}} \cdot \boldsymbol{\Delta x'_{conv,i}} + \boldsymbol{D'''_{conv,AR,i}} \cdot \boldsymbol{\Delta r_{conv,i}} \\
&\quad + \boldsymbol{D'''_{conv,AA,i}} \cdot \boldsymbol{\Delta v_{AC,i}} + \boldsymbol{D'''_{conv,AD,i}} \cdot \Delta u_{dc,i} \\
\Delta i_{dc,i} &= \boldsymbol{C'''_{conv,D,i}} \cdot \boldsymbol{\Delta x'_{conv,i}} + \boldsymbol{D'''_{conv,DR,i}} \cdot \boldsymbol{\Delta r_{conv,i}} \\
&\quad + \boldsymbol{D'''_{conv,DA,i}} \cdot \boldsymbol{\Delta v_{AC,i}} + \boldsymbol{D'''_{conv,DD,i}} \cdot \Delta u_{dc,i}
\end{aligned} \tag{D.46}$$

with state matrices:

$$\begin{aligned}
&\boldsymbol{A'''_{conv,i}} = \boldsymbol{A''_{conv,i}}, \\
&\boldsymbol{B'''_{conv,R,i}} = \boldsymbol{B''_{conv,R,i}}, \quad \boldsymbol{B_{conv,A,i}} = \boldsymbol{B''_{conv,A,i}} \cdot \boldsymbol{M_{V1,i}}, \\
&\boldsymbol{B'''_{conv,D,i}} = \boldsymbol{B_{conv,D,i}}, \\
&\boldsymbol{C'''_{conv,A,i}} = \boldsymbol{M_{I1}^{-1}} \cdot \boldsymbol{C''_{conv,A,i}}, \quad \boldsymbol{C_{conv,D,i}} = \boldsymbol{C''_{conv,D,i}},
\end{aligned} \tag{D.47}$$

$$\begin{aligned}
&\boldsymbol{D'''_{conv,AR,i}} = \boldsymbol{M_{I1}^{-1}} \cdot \boldsymbol{D''_{conv,AR,i}}, \\
&\boldsymbol{D'''_{conv,AA,i}} = \boldsymbol{M_{I1}^{-1}} \cdot (\boldsymbol{D''_{conv,AA,i}} \cdot \boldsymbol{M_{V1,i}} - \boldsymbol{M_{I2}} \cdot \boldsymbol{M_{V2}}),
\end{aligned} \tag{D.48}$$

$$\begin{aligned}
&\boldsymbol{D'''_{conv,AD,i}} = \boldsymbol{M_{I1}^{-1}} \cdot \boldsymbol{D''_{conv,AD,i}}, \\
&\boldsymbol{D'''_{conv,DR,i}} = \boldsymbol{D''_{conv,DR,i}}, \\
&\boldsymbol{D'''_{conv,DA,i}} = \boldsymbol{D''_{conv,DA,i}} \cdot \boldsymbol{M_{V1,i}}, \\
&\boldsymbol{D'''_{conv,DD,i}} = \boldsymbol{D''_{conv,DD,i}},
\end{aligned} \tag{D.49}$$

### D.1.7 Frequency measurement at the PCC

The frequency seen each converter will be required by the control algorithm (for angle-stability improvement). Therefore, it is included in the linearised model using a filter, as depicted in Fig. D.4. Since the AC-side frequency is the derivative of the angle of the voltage measured at the connection point of the VSC, the latter is used as state variable:

$$\Delta\dot{\delta}_{vsc,i} = A_{f,i}\Delta\delta_{vsc,i} + \boldsymbol{B_{f,i}}\boldsymbol{\Delta v_{AC,i}}, \tag{D.50}$$

where:

$$A_{f,i} = (-1/\tau_{f,i}),\ \boldsymbol{B_{f,i}} = (-1/\tau_{f,i})\boldsymbol{M_{V2,i}}, \tag{D.51}$$

and matrix $\boldsymbol{M_{V2,i}}$ is defined in (D.44).

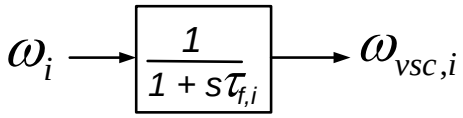


Figure D.4: Model frequency measurement at the PCC of the VSC.

hence, the frequency measurement at the operating point, in p.u, is given by:

$$\Delta\omega_{vsc,i} = \frac{\Delta\dot{\delta}_{vsc,i}}{\omega_0}. \tag{D.52}$$

The state of the voltage angle measured at the PCC is included in the state vector of the VSC station: $\boldsymbol{x_{vsc,i}} = [\boldsymbol{x_{vsc,i}},\ \delta_{vsc,i}]^T$. Therefore, the linearised moel of the VSC station is given by (D.1) (see the beginning of Section D.1) with state matrices:

$$\begin{aligned}
&\boldsymbol{A_{conv,i}} = \mathrm{diag}(\boldsymbol{A'''_{conv,i}}, A_{f,i}),\\
&\boldsymbol{B_{conv,R,i}} = \begin{bmatrix} \boldsymbol{B'''_{conv,R,i}} \\ 0\cdots 0 \end{bmatrix},\ \ \boldsymbol{B_{conv,A,i}} = \begin{bmatrix} \boldsymbol{B'''_{conv,A,i}} \\ B_{f,i} \end{bmatrix},\\
&\boldsymbol{B_{conv,D,i}} = \begin{bmatrix} \boldsymbol{B'''_{conv,D,i}} \\ 0\cdots 0 \end{bmatrix},
\end{aligned} \tag{D.53}$$

$$\boldsymbol{C_{conv,A,i}} = \left[\begin{array}{c|c} \boldsymbol{C'''_{conv,A,i}} & \begin{matrix} 0 \\ 0 \end{matrix} \end{array}\right],\ \ \boldsymbol{C_{conv,D,i}} = \left[\begin{array}{c|c} \boldsymbol{C'''_{conv,D,i}} & 0 \end{array}\right], \tag{D.54}$$

$$\begin{aligned}
&\boldsymbol{D_{conv,AR,i}} = \boldsymbol{D'''_{conv,AR,i}},\ \ \boldsymbol{D_{conv,AA,i}} = \boldsymbol{D'''_{conv,AA,i}},\\
&\boldsymbol{D_{conv,AD,i}} = \boldsymbol{D'''_{conv,AD,i}},\\
&\boldsymbol{D_{conv,DR,i}} = \boldsymbol{D'''_{conv,DR,i}},\ \ \boldsymbol{D_{conv,DA,i}} = \boldsymbol{D'''_{conv,DA,i}},\\
&\boldsymbol{D_{conv,DD,i}} = \boldsymbol{D'''_{conv,DD,i}}.
\end{aligned} \tag{D.55}$$

## D.2 Including all the VSCs of an MTDC system in a single model (without the HVDC grid model)

After the linearised model of each VSC of an MTDC system has been obtained, the next step is to put all VSCs together in a single model. The states, inputs and outputs of the resulting model will be: [6]

- states:
  - $\boldsymbol{\Delta x_{vscs}} = [\boldsymbol{\Delta x_{conv,1}}, \ldots, \boldsymbol{\Delta x_{conv,n_{vsc}}}]^T$
- inputs:
  - $\boldsymbol{\Delta v_{vscs,AC}} = [\boldsymbol{\Delta v_{conv,AC,1}}, \ldots, \boldsymbol{\Delta v_{conv,AC,n_{vsc}}}]^T$
  - $\boldsymbol{\Delta v_{vscs,DC}} = [\Delta u_{dc,1}, \ldots, \Delta u_{dc,n_{vsc}}]^T$
- outputs:
  - $\boldsymbol{\Delta i_{vscs,AC}} = [\boldsymbol{\Delta i_{conv,AC,1}}, \ldots, \boldsymbol{\Delta i_{conv,AC,n_{vsc}}}]^T$
  - $\boldsymbol{\Delta i_{vscs,DC}} = [\Delta i_{dc,1}, \ldots, \Delta i_{dc,n_{vsc}}]^T$

The resulting linearised system will include all the converters together and looks like:

$$\begin{aligned}
\boldsymbol{\Delta \dot{x}_{vscs}} &= \boldsymbol{A_{vscs}} \cdot \boldsymbol{\Delta x_{vscs}} + \boldsymbol{B_{vscs,R}} \cdot \boldsymbol{\Delta r_{vscs}} \\
&\quad + \boldsymbol{B_{vscs,A}} \cdot \boldsymbol{\Delta v_{vscs,AC}} + \boldsymbol{B_{vscs,D}} \cdot \boldsymbol{\Delta v_{vscs,DC}}, \\
\boldsymbol{\Delta i_{vscs,AC}} &= \boldsymbol{C_{vscs,A}} \cdot \boldsymbol{\Delta x_{vscs}} + \boldsymbol{D_{vscs,AR}} \cdot \boldsymbol{\Delta r_{vscs}} \\
&\quad + \boldsymbol{D_{vscs,AA}} \cdot \boldsymbol{\Delta v_{vscs,AC}} + \boldsymbol{D_{vscs,AD}} \cdot \boldsymbol{\Delta v_{vscs,DC}}, \\
\boldsymbol{\Delta i_{vscs,DC}} &= \boldsymbol{C_{vscs,D}} \cdot \boldsymbol{\Delta x_{vscs}} + \boldsymbol{D_{vscs,DR}} \cdot \boldsymbol{\Delta r_{vscs}} \\
&\quad + \boldsymbol{D_{vscs,DA}} \cdot \boldsymbol{\Delta v_{vscs,AC}} + \boldsymbol{D_{vscs,DD}} \cdot \boldsymbol{\Delta v_{vscs,DC}},
\end{aligned} \tag{D.56}$$

with state matrices:

$$\begin{aligned}
&\boldsymbol{A_{vscs}} = \mathrm{diag}(\boldsymbol{A_{conv,i}}), \quad \boldsymbol{B_{vscs}} = \mathrm{diag}(\boldsymbol{B_{conv,i}}), \\
&\boldsymbol{C_{vscs,A}} = \mathrm{diag}(\boldsymbol{C_{conv,A,i}}), \quad \boldsymbol{C_{vscs,D}} = \mathrm{diag}(\boldsymbol{C_{conv,D,i}}), \\
&\boldsymbol{D_{vscs,AA}} = \mathrm{diag}(\boldsymbol{D_{conv,AA,i}}), \quad \boldsymbol{D_{vscs,AR}} = \mathrm{diag}(\boldsymbol{D_{conv,AR,i}}), \\
&\boldsymbol{D_{vscs,AD}} = \mathrm{diag}(\boldsymbol{D_{conv,AD,i}}), \\
&\boldsymbol{D_{vscs,DA}} = \mathrm{diag}(\boldsymbol{D_{conv,DA,i}}), \quad \boldsymbol{D_{vscs,DR}} = \mathrm{diag}(\boldsymbol{D_{conv,DR,i}}), \\
&\boldsymbol{D_{vscs,DD}} = \mathrm{diag}(\boldsymbol{D_{conv,DD,i}}),
\end{aligned} \tag{D.57}$$

[6] *vscs* refer to all the VSC stations of an MTDC system.

## D.3 HVDC grid

An example of a 3-terminal HVDC grid is shown in Figure D.5. A general HVDC grid will have:

- $n$ DC buses.
- $n_L$ DC lines.
- $n_{vsc}$ converters ($n_{vsc}$ DC buses of the total $n$ DC buses will have a VSC connected).

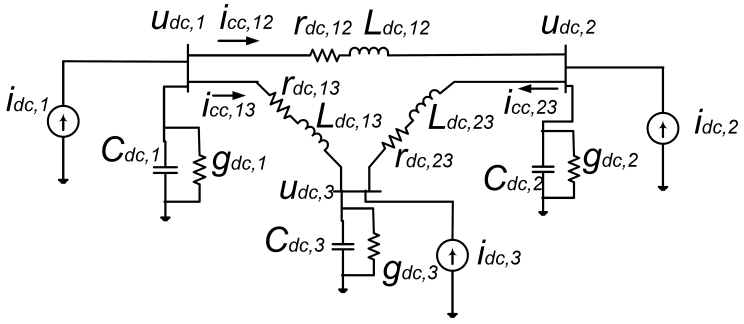


Figure D.5: Dynamic model of the DC grid.

As discussed in Section 6.1, the dynamics of the DC grid is fast in comparison to the electromechanical oscillations and a concentrated $\pi$ model for the DC lines has been used, as shown in Fig. D.5. Nevertheless, if long overhead DC lines or submarine/underground DC cables are consided, the frequency dependent model proposed in [130] (with $\pi$ sections with parallel branches) might be more appropriated. Such models could be easily included in the linearised model defining additional buses and lines in the DC grid.

The state variables of the system are the DC voltages and the currents through the DC lines: [7]

$$\boldsymbol{\Delta x_{DC}} = [\boldsymbol{\Delta v_{DC}}, \boldsymbol{\Delta i_{cc}}]^T, \tag{D.58}$$

[7] *DC* refers to an HVDC grid.

where:

$$\begin{aligned}\boldsymbol{\Delta v_{DC}} &= [\Delta u_{dc,1}, \ldots, \Delta u_{dc,n}]^T \in \mathbb{R}^{n\times 1},\\ \boldsymbol{\Delta i_{cc}} &= [\Delta i_{cc,L1}, \ldots, \Delta i_{cc,Ln_L}]^T \in \mathbb{R}^{n_L\times 1}.\end{aligned} \tag{D.59}$$

The inputs of the system are the current injections in the DC buses:

$$\boldsymbol{\Delta i_{DC}} = [\Delta i_{dc,1}, \ldots, \Delta i_{dc,n}]^T \in \mathbb{R}^{n\times 1}. \tag{D.60}$$

Each converter takes the form of a current injection $i_{dc,i}$ from the DC grid viewpoint. If no converter is connected to a DC bus $i$, the current injection will be zero: $i_{dc,i} = 0$.

The DC voltages, $\boldsymbol{\Delta v_{DC}}$, are selected as outputs of the DC-grid model. This choice will be useful when coupling the linearised models of the VSCs and the DC grid.

Therefore, the linear model of the DC grid is given by:

$$\begin{aligned}\boldsymbol{\Delta \dot{x}_{DC}} &= \boldsymbol{A_{DC}} \cdot \boldsymbol{\Delta x_{DC}} + \boldsymbol{B_{DC}} \cdot \boldsymbol{\Delta i_{DC}},\\ \boldsymbol{\Delta v_{DC}} &= \boldsymbol{C_{DC}} \cdot \boldsymbol{\Delta x_{DC}},\end{aligned} \tag{D.61}$$

with state matrices:

$$\boldsymbol{A_{DC}} = \left[\begin{array}{c|c} -\boldsymbol{C_{dc}^{-1}}\boldsymbol{G_{dc}} & -\boldsymbol{C_{dc}^{-1}}\boldsymbol{A_c} \\ \hline \boldsymbol{L_{dc}^{-1}}\boldsymbol{A_c^T} & -\boldsymbol{L_{dc}^{-1}}\boldsymbol{R_{dc}} \end{array}\right] \in \mathbb{R}^{(n+n_L)\times(n+n_L)}, \tag{D.62}$$

$$\boldsymbol{B_{DC}} = \left[\begin{array}{c} \boldsymbol{C_{dc}^{-1}} \\ \hline \boldsymbol{0}_{n_L\times n} \end{array}\right] \in \mathbb{R}^{(n+n_L)\times n}, \tag{D.63}$$

$$\boldsymbol{C_{DC}} = [\boldsymbol{I}_{n\times n} | \boldsymbol{0}_{n\times n_L}] \in \mathbb{R}^{n\times(n+n_L)}, \tag{D.64}$$

where:

$$\boldsymbol{R_{dc}} = \mathrm{diag}(r_{dc,L1}, \ldots, r_{dc,Ln_L}) \in \mathbb{R}^{n_L\times n_L}, \tag{D.65}$$

$$\boldsymbol{L_{dc}} = \mathrm{diag}(L_{dc,L1}, \ldots, L_{dc,Ln_L}) \in \mathbb{R}^{n_L\times n_L}, \tag{D.66}$$

$$\boldsymbol{G_{dc}} = \mathrm{diag}(g_{dc,1}, \ldots, g_{dc,n}) \in \mathbb{R}^{n\times n}, \tag{D.67}$$

$$\boldsymbol{C_{dc}} = \mathrm{diag}(C_{dc,1}, \ldots, C_{dc,n}) \in \mathbb{R}^{n\times n}, \tag{D.68}$$

and $\boldsymbol{A_c} = (a_{i\ell}) \in \mathbb{R}^{n\times n_L}$ is the incidence matrix of the DC grid, whose

elements are:

$$a_{i\ell} = \begin{cases} +1 & \text{if line } \ell \text{ is defined leaving node } i. \\ -1 & \text{if line } \ell \text{ is defined entering node } i. \\ 0 & \text{if line } \ell \text{ is not connected to node } i. \end{cases} \tag{D.69}$$

## D.4 Complete model of the VSC-MTDC system: converters + HVDC grid

Once the models of the VSCs (D.56) and the model of the HVDC grid (D.61) have been obtained, they must be connected, leading to the complete linearised model of the VSC-MTDC system.

Fisrt of all, a matrix $\boldsymbol{M_{DC}} \in \mathbb{R}^{n \times n_{vsc}}$ is defined with the information of which DC buses have a converter connected. The terms of $\boldsymbol{M_{DC}} = (m_{DC,ij})$ are:

$$m_{DC,ij} = \begin{cases} 1 & \text{if DC-bus } i \text{ is connected to VSC}j. \\ 0 & \text{otherwise.} \end{cases} \tag{D.70}$$

The current injection at each DC bus can be written from the current injections of the VSCs:

$$\boldsymbol{\Delta i_{DC}} = \boldsymbol{M_{DC}} \cdot \boldsymbol{\Delta i_{vscs,DC}}. \tag{D.71}$$

Replacing (D.71) into (D.61),

$$\begin{aligned} \boldsymbol{\Delta \dot{x}_{DC}} &= \boldsymbol{A_{DC}} \cdot \boldsymbol{\Delta x_{DC}} + \boldsymbol{B_{DC}} \cdot \boldsymbol{\Delta i_{DC}} \\ &= \boldsymbol{A_{DC}} \cdot \boldsymbol{\Delta x_{DC}} + \boldsymbol{B_{DC}} \cdot (\boldsymbol{M_{DC}} \cdot \boldsymbol{i_{vscs,DC}}) \\ &= \boldsymbol{A_{DC}} \cdot \boldsymbol{\Delta x_{DC}} + (\boldsymbol{B_{DC}} \boldsymbol{M_{DC}} \boldsymbol{C_{vscs,D}}) \boldsymbol{\Delta x_{vscs}} \\ &\quad + (\boldsymbol{B_{DC}} \boldsymbol{M_{DC}} \boldsymbol{D_{vscs,DR}}) \boldsymbol{\Delta r_{vscs}} \\ &\quad + (\boldsymbol{B_{DC}} \boldsymbol{M_{DC}} \boldsymbol{D_{vscs,DA}}) \boldsymbol{\Delta v_{vscs,AC}} \\ &\quad + (\boldsymbol{B_{DC}} \boldsymbol{M_{DC}} \boldsymbol{D_{vscs,DD}}) \boldsymbol{\Delta v_{scs,DC}}. \end{aligned} \tag{D.72}$$

Replacing $\boldsymbol{\Delta v_{DC}} = \boldsymbol{C_{DC}} \cdot \boldsymbol{\Delta x_{DC}}$ from (D.61) in (D.72) and in (D.56), $\boldsymbol{\Delta v_{vscs,DC}}$ can be eliminated from the state-space model of the MTDC,

obtainig:

$$\begin{bmatrix} \boldsymbol{\Delta \dot{x}_{vscs}} \\ \boldsymbol{\Delta \dot{x}_{DC}} \end{bmatrix} = \left[\begin{array}{c|c} \boldsymbol{A_{vscs}} & \boldsymbol{B_{vscs,D} M_{DC}} \\ \hline \boldsymbol{B_{DC} M_{DC} C_{vscs,D}} & \boldsymbol{A_{DC} + B_{DC} M_{DC} D_{vscs,DD} C_{DC}} \end{array}\right] \cdot \begin{bmatrix} \boldsymbol{\Delta x_{vscs}} \\ \boldsymbol{\Delta x_{DC}} \end{bmatrix} + \begin{bmatrix} \boldsymbol{B_{vscs,R}} \\ \boldsymbol{B_{DC} M_{DC} D_{vscs,DR}} \end{bmatrix} \cdot \boldsymbol{\Delta r_{vsc}} + \begin{bmatrix} \boldsymbol{B_{vscs,A}} \\ \boldsymbol{B_{DC} M_{DC} D_{vscs,DA}} \end{bmatrix} \cdot \boldsymbol{\Delta v_{vscs,AC}}. \tag{D.73}$$

The outputs of the MTDC model will be the currents injected by the VSCs into the AC grid of (D.56), which can be written as:

$$\begin{aligned} \boldsymbol{\Delta i_{vscs,AC}} &= [\boldsymbol{C_{vscs,A}} \quad 0] \cdot \begin{bmatrix} \boldsymbol{\Delta x_{vscs}} \\ \boldsymbol{\Delta x_{DC}} \end{bmatrix} + \boldsymbol{D_{vscs,AR}} \cdot \boldsymbol{\Delta r_{vscs}} + \\ &\quad + \boldsymbol{D_{vscs,AA}} \cdot \boldsymbol{\Delta v_{vscs,AC}} + \boldsymbol{D_{vsc,AD}} \cdot \boldsymbol{\Delta v_{vscs,DC}} \\ &= [\boldsymbol{C_{vscs,A}} \quad \boldsymbol{D_{vsc,AD} C_{DC}}] \cdot \begin{bmatrix} \boldsymbol{\Delta x_{vscs}} \\ \boldsymbol{\Delta x_{DC}} \end{bmatrix} \\ &\quad + \boldsymbol{D_{vscs,AR}} \cdot \boldsymbol{\Delta r_{vscs}} + \boldsymbol{D_{vscs,AA}} \cdot \boldsymbol{\Delta v_{vscs,AC}}. \end{aligned} \tag{D.74}$$

Therefore, defining [8] $\boldsymbol{\Delta x_{mtdc}} = [\boldsymbol{\Delta x_{vscs}}, \quad \boldsymbol{\Delta x_{DC}}]^T$, the complete linearised model of an MTDC system can be written as:

$$\begin{aligned} \boldsymbol{\Delta \dot{x}_{mtdc}} &= \boldsymbol{A_{mtdc}} \cdot \boldsymbol{\Delta x_{mtdc}} \\ &\quad + \boldsymbol{B_{mtdc,R}} \cdot \boldsymbol{\Delta r_{vscs}} + \boldsymbol{B_{mtdc,A}} \cdot \boldsymbol{\Delta v_{vscs,AC}}, \\ \boldsymbol{\Delta i_{vscs,AC}} &= \boldsymbol{C_{mtdc,A}} \cdot \boldsymbol{\Delta x_{mtdc}} \\ &\quad + \boldsymbol{D_{mtdc,AR}} \cdot \boldsymbol{\Delta r_{vscs}} + \boldsymbol{D_{mtdc,AA}} \cdot \boldsymbol{\Delta v_{vscs,AC}}, \end{aligned} \tag{D.75}$$

with state matrices:

$$\boldsymbol{A_{mtdc}} = \left[\begin{array}{c|c} \boldsymbol{A_{vscs}} & \boldsymbol{B_{vscs,D} M_{DC}} \\ \hline \boldsymbol{B_{DC} M_{DC} C_{vscs,D}} & \boldsymbol{A_{DC} + B_{DC} M_{DC} D_{vscs,DD} C_{DC}} \end{array}\right],$$

$$\boldsymbol{B_{mtdc,R}} = \begin{bmatrix} \boldsymbol{B_{vscs,R}} \\ \boldsymbol{B_{DC} M_{DC} D_{vscs,DR}} \end{bmatrix}, \tag{D.76}$$

[8] *mtdc* refers to a multi-terminal VSC-HVDC system.

$$\boldsymbol{B_{mtdc,A}} = \begin{bmatrix} \boldsymbol{B_{vscs,A}} \\ \boldsymbol{B_{DC} M_{DC} D_{vscs,DA}} \end{bmatrix}, \tag{D.77}$$

$$\boldsymbol{C_{mtdc,A}} = [\boldsymbol{C_{vscs,A}} \quad \boldsymbol{D_{vscs,AD} C_{DC}}], \tag{D.78}$$

$$\boldsymbol{D_{mtdc,AR}} = \boldsymbol{D_{vscs,AR}}, \quad \boldsymbol{D_{mtdc,AA}} = \boldsymbol{D_{vscs,AA}}. \tag{D.79}$$

## D.5 Including several VSC-MTDC systems

If the hybrid system has more than one VSC-MTDC system ($n_{mtdc}$), the individual linearised models can be put together into a single model. The states, inputs, outputs and state matrices of the linearised model of a generic VSC-MTDC $k$ (D.76)-(D.79) will be identified, from now on, with a superscript $^{(k)}$. The linearised model of all the VSC-MTDCs together is given by: [9]

$$\begin{aligned} \boldsymbol{\Delta \dot{x}_{MTDC}} &= \boldsymbol{A_{MTDC}} \cdot \boldsymbol{\Delta x_{MTDC}} \\ &\quad + \boldsymbol{B_{MTDC,R}} \cdot \boldsymbol{\Delta r_{MTDC}} + \boldsymbol{B_{MTDC,A}} \cdot \boldsymbol{\Delta v_{MTDC,AC}}, \\ \boldsymbol{\Delta i_{MTDC,AC}} &= \boldsymbol{C_{MTDC,A}} \cdot \boldsymbol{\Delta x_{MTDC}} \\ &\quad + \boldsymbol{D_{MTDC,AR}} \cdot \boldsymbol{\Delta r_{MTDC}} + \boldsymbol{D_{MTDC,AA}} \cdot \boldsymbol{\Delta v_{MTDC,AC}}, \end{aligned} \tag{D.80}$$

where the states, inputs and outputs are defined as:

$$\boldsymbol{\Delta x_{MTDC}} = [\boldsymbol{\Delta x_{mtdc}^{(1)}}, \ldots, \boldsymbol{\Delta x_{mtdc}^{(n_{mtdc})}}]^T, \tag{D.81}$$

$$\boldsymbol{\Delta r_{MTDC}} = [\boldsymbol{\Delta r_{vscs}^{(1)}}, \ldots, \boldsymbol{\Delta r_{vscs}^{(n_{mtdc})}}]^T, \tag{D.82}$$

$$\boldsymbol{\Delta v_{MTDC,AC}} = [\boldsymbol{\Delta v_{vscs,AC}^{(1)}}, \ldots, \boldsymbol{\Delta v_{vscs,AC}^{(n_{mtdc})}}]^T, \tag{D.83}$$

$$\boldsymbol{\Delta i_{MTDC,AC}} = [\boldsymbol{\Delta i_{vscs,AC}^{(1)}}, \ldots, \boldsymbol{\Delta i_{vscs,AC}^{(n_{mtdc})}}]^T, \tag{D.84}$$

and the state matrices are:

$$\boldsymbol{A_{MTDC}} = \text{diag}(\boldsymbol{A_{mtdc}^{(1)}}, \ldots, \boldsymbol{A_{mtdc}^{(n_{mtdc})}}), \tag{D.85}$$

[9] *mtdc* refers to a single VSC-MTDC system and *MTDC* refers to several VSC-MTDC systems.

$$\boldsymbol{B_{MTDC,R}} = \text{diag}(\boldsymbol{B^{(1)}_{mtdc,R}}, \ldots, \boldsymbol{B^{(n_{mtdc})}_{mtdc,R}}), \tag{D.86}$$

$$\boldsymbol{B_{MTDC,A}} = \text{diag}(\boldsymbol{B^{(1)}_{mtdc,A}}, \ldots, \boldsymbol{B^{(n_{mtdc})}_{mtdc,A}}), \tag{D.87}$$

$$\boldsymbol{C_{MTDC,A}} = \text{diag}(\boldsymbol{C^{(1)}_{mtdc,A}}, \ldots, \boldsymbol{C^{(n_{mtdc})}_{mtdc,A}}), \tag{D.88}$$

$$\boldsymbol{D_{MTDC,R}} = \text{diag}(\boldsymbol{D^{(1)}_{mtdc,R}}, \ldots, \boldsymbol{D^{(n_{mtdc})}_{mtdc,R}}), \tag{D.89}$$

$$\boldsymbol{D_{MTDC,A}} = \text{diag}(\boldsymbol{D^{(1)}_{mtdc,A}}, \ldots, \boldsymbol{D^{(n_{mtdc})}_{mtdc,A}}), \tag{D.90}$$

For constant reference values, $\boldsymbol{\Delta r_{conv,i}} = \mathbf{0}$. The linearised model representing all the VSC-MTDC systems can, therefore, be included in the linearised overall model of the system as was described in Section 6.3.

## D.6 DC-voltage droop control

So far, the set points for the outer controllers $\boldsymbol{\Delta r_{conv,i}}$ are treated as inputs, which makes it possible to test the dynamic response of the system under set-point changes. For linerisation purposes, the set points will have constant values leading to $\boldsymbol{\Delta r_{conv,i}} = \mathbf{0}$. Nevertheless, if supplementary set-point values are added to the outer controllers, such as the DC-voltage droop control, they should be included in the set-point vector $\boldsymbol{\Delta r_{conv,i}}$.

In a converter $i$ with the DC-voltage droop implemented, its $d$-axis outer controller will be in active-power control mode (see Subsection D.1.2) and its active-power set-point value will be given by:

$$\Delta p^{Ref}_{s,i} = \frac{1}{k_{dc,i}} \Delta u_{dc,i}. \tag{D.91}$$

Eq. (D.91) can be written relating the set-point vector of the VSC with its DC voltage:

$$\boldsymbol{\Delta r_{conv,i}} = \begin{bmatrix} \Delta p^{Ref}_{s,i} \\ \Delta u^{Ref}_{dc,i} \\ \Delta q^{Ref}_{s,i} \\ \Delta u^{Ref}_{s,i} \end{bmatrix} = \boldsymbol{D_{conv,dc,i}} \cdot \Delta u_{dc,i}, \quad \boldsymbol{D_{conv,dc,i}} = \frac{1}{k_{dc,i}} \begin{bmatrix} 1 \\ 0 \\ 0 \\ 0 \end{bmatrix}. \tag{D.92}$$

If $\boldsymbol{\Delta r_{conv,i}}$ of (D.92) is replaced in (D.1), one has:

$$\begin{aligned}
\boldsymbol{\Delta \dot{x}_{conv,i}} &= \boldsymbol{A_{conv,i}} \cdot \boldsymbol{\Delta x_{conv,i}} + \boldsymbol{B_{conv,A,i}} \cdot \boldsymbol{\Delta v_{AC,i}} \\
&\quad + \boldsymbol{B^{dcdroop}_{conv,D,i}} \cdot \Delta u_{dc,i}, \\
\boldsymbol{\Delta i_{conv,AC,i}} &= \boldsymbol{C_{conv,A,i}} \cdot \boldsymbol{\Delta x_{conv,i}} + \boldsymbol{D_{conv,AA,i}} \cdot \boldsymbol{\Delta v_{AC,i}} \\
&\quad + \boldsymbol{D^{dcdroop}_{conv,AD,i}} \cdot \Delta u_{dc,i} \\
\Delta i_{dc,i} &= \boldsymbol{C_{conv,D,i}} \cdot \boldsymbol{\Delta x_{conv,i}} + \boldsymbol{D_{conv,DA,i}} \cdot \boldsymbol{\Delta v_{AC,i}} \\
&\quad + \boldsymbol{D^{dcdroop}_{conv,DD,i}} \cdot \Delta u_{dc,i}, \qquad \text{(D.93)}
\end{aligned}$$

where most vectors and matrices are as in (D.1), except the matrices multipliying $\Delta u_{dc,i}$, which are given by:

$$\begin{aligned}
\boldsymbol{B^{dcdroop}_{conv,D,i}} &= \boldsymbol{B_{conv,D,i}} + \boldsymbol{B_{conv,R,i}} \boldsymbol{D_{conv,dc,i}}, \\
\boldsymbol{D^{dcdroop}_{conv,AD,i}} &= \boldsymbol{D_{conv,AD,i}} + \boldsymbol{D_{conv,AR,i}} \boldsymbol{D_{conv,dc,i}}, \\
\boldsymbol{D^{dcdroop}_{conv,DD,i}} &= \boldsymbol{D_{conv,DD,i}} + \boldsymbol{D_{conv,DR,i}} \boldsymbol{D_{conv,dc,i}}. \qquad \text{(D.94)}
\end{aligned}$$

Once the DC-voltage droop control has been included in the linearised model of each VSC, the process of building the complete model of the VSC-MTDC systems must follow the steps described in Sections D.2-D.5 and matrices $\boldsymbol{B_{conv,D,i}}$, $\boldsymbol{D_{conv,AD,i}}$ and $\boldsymbol{D_{conv,DD,i}}$ of those converters with DC-voltage droop must be replaced by matrices $\boldsymbol{B^{dcdroop}_{conv,D,i}}$, $\boldsymbol{D^{dcdroop}_{conv,AD,i}}$ and $\boldsymbol{D^{dcdroop}_{conv,DD,i}}$ of (D.94), respectively. Naturally, the VSCs with DC-voltage droop will not have any independent set-point vector $\boldsymbol{\Delta r_{conv,i}}$ any more.

## D.7 Supplementary control strategies

Supplementary control strategies with a general structure are included in the model in this Section. The DC-voltage droop control strategies are a particular case of the control strategies analysed in this Section. However, they were described in Section D.6 due to their simplicity.

Supplementary control strategies at the VSC stations will manipulate the set-point vector $\boldsymbol{\Delta r_{conv,i}}$ of the outer controllers. The linearised model of generic supplementary control strategies for P and Q injections for the $i$th VSC can be written as:

- P control strategy:

$$\begin{aligned} \boldsymbol{\Delta \dot{x}_{CS,P,i}} &= \boldsymbol{A_{CS,P,i}} \cdot \boldsymbol{\Delta x_{CS,P,i}} + \boldsymbol{B_{CS,P,i}} \cdot \boldsymbol{\Delta u_{CS,P,i}}, \\ \Delta p_{s,i}^{Ref} &= \boldsymbol{C_{CS,P,i}} \cdot \boldsymbol{\Delta x_{CS,P,i}} + \boldsymbol{D_{CS,P,i}} \cdot \boldsymbol{\Delta u_{CS,P,i}}, \end{aligned} \tag{D.95}$$

- Q control strategy:

$$\begin{aligned} \boldsymbol{\Delta \dot{x}_{CS,Q,i}} &= \boldsymbol{A_{CS,Q,i}} \cdot \boldsymbol{\Delta x_{CS,Q,i}} + \boldsymbol{B_{CS,Q,i}} \cdot \boldsymbol{\Delta u_{CS,Q,i}}, \\ \Delta q_{s,i}^{Ref} &= \boldsymbol{C_{CS,Q,i}} \cdot \boldsymbol{\Delta x_{CS,Q,i}} + \boldsymbol{D_{CS,Q,i}} \cdot \boldsymbol{\Delta u_{CS,Q,i}}, \end{aligned} \tag{D.96}$$

Therefore, the linearised model of the P and Q supplementary control strategies is given by:

$$\begin{aligned} \boldsymbol{\Delta \dot{x}_{CS,i}} &= \boldsymbol{A_{CS,i}} \cdot \boldsymbol{\Delta x_{CS,i}} + \boldsymbol{B_{CS,i}} \cdot \boldsymbol{\Delta u_{CS,i}}, \\ \boldsymbol{\Delta r_{conv,i}} &= \boldsymbol{C_{CS,i}} \cdot \boldsymbol{\Delta x_{CS,i}} + \boldsymbol{D_{CS,i}} \cdot \boldsymbol{\Delta u_{CS,i}}, \end{aligned} \tag{D.97}$$

where

$$\begin{aligned} \boldsymbol{\Delta x_{CS,i}} &= [\boldsymbol{\Delta x_{CS,P,i}},\ \boldsymbol{\Delta x_{CS,Q,i}}]^T, \\ \boldsymbol{\Delta u_{CS,i}} &= [\boldsymbol{\Delta u_{CS,P,i}},\ \boldsymbol{\Delta u_{CS,Q,i}}]^T, \\ \boldsymbol{\Delta r_{conv,i}} &= [\Delta p_{s,i}^{Ref},\ \Delta u_{dc,i}^{Ref},\ \Delta q_{s,i}^{Ref},\ \Delta u_{s,i}^{Ref}]^T, \end{aligned} \tag{D.98}$$

and

$$\begin{aligned} &\boldsymbol{A_{CS,i}} = \mathrm{diag}(\boldsymbol{A_{CS,P,i}}, \boldsymbol{A_{CS,Q,i}}), \quad \boldsymbol{B_{CS,i}} = \mathrm{diag}(\boldsymbol{B_{CS,P,i}}, \boldsymbol{B_{CS,Q,i}}), \\ &\boldsymbol{C_{CS,i}} = \boldsymbol{M_{CS}} \cdot \mathrm{diag}(\boldsymbol{C_{CS,P,i}}, \boldsymbol{C_{CS,Q,i}}), \\ &\boldsymbol{D_{CS,i}} = \boldsymbol{M_{CS}} \cdot \mathrm{diag}(\boldsymbol{D_{CS,P,i}}, \boldsymbol{D_{CS,Q,i}}). \end{aligned} \tag{D.99}$$

The generic set-point vector $\boldsymbol{\Delta r_{conv,i}}$ is used in (D.98)-(D.99), with all possible set-point values of the VSCs, instead of using P and Q set-point values, only. This is to preserve the flexibility of the model. Matrix $\boldsymbol{M_{CS}}$ of (D.99) is used to include P and Q set-point values into vector $\boldsymbol{\Delta r_{conv,i}}$. The DC- and AC-voltage set point values, which are not used, will be filled with zeros.

Therefore, matrix $\boldsymbol{M_{CS}}$ is defined as:

$$M_{CS} = \begin{bmatrix} 1 & 0 \\ 0 & 0 \\ 0 & 1 \\ 0 & 0 \end{bmatrix}. \tag{D.100}$$

### D.7.1 VSC model + supplementary control strategies

The states of the supplementary control strategies are included in the model of the VSC:

$$\boldsymbol{\Delta x^{CS}_{conv,i}} = [\boldsymbol{\Delta x_{conv,i}},\ \boldsymbol{\Delta x_{CS,i}}]^T, \tag{D.101}$$

Hence, the linearised model of the supplementary control strategies (D.97) is assembled into the state-space representation of VSC$_i$ in (D.1), giving:

$$\begin{aligned}
\boldsymbol{\Delta \dot{x}^{CS}_{conv,i}} &= \boldsymbol{A^{CS}_{conv,i}} \cdot \boldsymbol{\Delta x^{CS}_{conv,i}} + \boldsymbol{B^{CS}_{conv,CS,i}} \cdot \boldsymbol{\Delta u_{CS,i}} \\
&\quad + \boldsymbol{B^{CS}_{conv,A,i}} \cdot \boldsymbol{\Delta v_{AC,i}} + \boldsymbol{B^{CS}_{conv,D,i}} \cdot \Delta u_{dc,i}, \\
\boldsymbol{\Delta i_{conv,AC,i}} &= \boldsymbol{C^{CS}_{conv,A,i}} \cdot \boldsymbol{\Delta x^{CS}_{conv,i}} + \boldsymbol{D^{CS}_{conv,A,CS,i}} \cdot \boldsymbol{\Delta u_{CS,i}} \\
&\quad + \boldsymbol{D^{CS}_{conv,AA,i}} \cdot \boldsymbol{\Delta v_{AC,i}} + \boldsymbol{D^{CS}_{conv,AD,i}} \cdot \Delta u_{dc,i} \\
\Delta i_{dc,i} &= \boldsymbol{C^{CS}_{conv,D,i}} \cdot \boldsymbol{\Delta x^{CS}_{conv,i}} + \boldsymbol{D^{CS}_{conv,D,CS,i}} \cdot \boldsymbol{\Delta u_{CS,i}} \\
&\quad + \boldsymbol{D^{CS}_{conv,DA,i}} \cdot \boldsymbol{\Delta v_{AC,i}} + \boldsymbol{D^{CS}_{conv,DD,i}} \cdot \Delta u_{dc,i}.
\end{aligned} \tag{D.102}$$

The model of the VSC-MTDC system is obtained following the steps described in Sections D.2-D.4, but now the model includes the input vector of the supplementary control strategies of all the VSCs ($\boldsymbol{\Delta u_{vscs,CS}}$):

$$\begin{aligned}
\boldsymbol{\Delta \dot{x}_{mtdc}} &= \boldsymbol{A'_{mtdc}} \cdot \boldsymbol{\Delta x_{mtdc}} \\
&\quad + \boldsymbol{B'_{mtdc,CS}} \cdot \boldsymbol{\Delta u_{vscs,CS}} + \boldsymbol{B'_{mtdc,A}} \cdot \boldsymbol{\Delta v_{vscs,AC}}, \\
\boldsymbol{\Delta i_{vscs,AC}} &= \boldsymbol{C'_{mtdc,A}} \cdot \boldsymbol{\Delta x_{mtdc}} \\
&\quad + \boldsymbol{D'_{mtdc,A,CS}} \cdot \boldsymbol{\Delta u_{vscs,CS}} + \boldsymbol{D'_{mtdc,AA}} \cdot \boldsymbol{\Delta v_{vscs,AC}}.
\end{aligned} \tag{D.103}$$

### D.7.2 Input signals of the control strategies

The loop is closed selecting the input vector of the control strategies ($\boldsymbol{\Delta u_{vscs,CS}}$) as a linear combination of the desired output vector of the linearised model of the VSC-MTDC system ($\boldsymbol{\Delta y_{mtdc}}$):

$$\boldsymbol{\Delta u_{vscs,CS}} = \boldsymbol{H}\boldsymbol{\Delta y_{mtdc}}, \tag{D.104}$$

where matrix $\boldsymbol{H}$ will depend on the control law used and any output vector $\boldsymbol{\Delta y_{mtdc}}$ can be written as:

$$\boldsymbol{\Delta y_{mtdc}} = \boldsymbol{C}\boldsymbol{\Delta x_{mtdc}} + \boldsymbol{D}\boldsymbol{\Delta v_{vscs,AC}}, \tag{D.105}$$

Therefore, if (D.104) and (D.105) are replaced in (D.103), the closed-loop system is given by:

$$\begin{aligned} \boldsymbol{\Delta \dot{x}_{mtdc}} &= \boldsymbol{A_{mtdc}} \cdot \boldsymbol{\Delta x_{mtdc}} + \boldsymbol{B_{mtdc,A}} \cdot \boldsymbol{\Delta v_{vscs,AC}}, \\ \boldsymbol{\Delta i_{vscs,AC}} &= \boldsymbol{C_{mtdc,A}} \cdot \boldsymbol{\Delta x_{mtdc}} + \boldsymbol{D_{mtdc,AA}} \cdot \boldsymbol{\Delta v_{vscs,AC}} \end{aligned} \tag{D.106}$$

with state matrices:

$$\begin{aligned} \boldsymbol{A_{mtdc}} &= \boldsymbol{A'_{mtdc}} + \boldsymbol{B'_{mtdc,CS}}\boldsymbol{H} \cdot \boldsymbol{C}, \\ \boldsymbol{B_{mtdc}} &= \boldsymbol{B'_{mtdc}} + \boldsymbol{B'_{mtdc,CS}}\boldsymbol{H} \cdot \boldsymbol{D}, \\ \boldsymbol{C_{mtdc,A}} &= \boldsymbol{C'_{mtdc,A}} + \boldsymbol{D'_{mtdc,A,CS}}\boldsymbol{H} \cdot \boldsymbol{C}, \\ \boldsymbol{D_{mtdc,AA}} &= \boldsymbol{D'_{mtdc,AA}} + \boldsymbol{D'_{mtdc,A,CS}}\boldsymbol{H} \cdot \boldsymbol{D}. \end{aligned} \tag{D.107}$$

Finally, it is worth pointing out that the input signal of the supplementary control strategy of every VSC can include, among others,

- The DC voltage at the DC side of the VSC station.
- The frequency measurement at AC side of the VSC station.
- The frequency measurement of all the VSC stations of the VSC-MTDC.

Therefore, all the control strategies proposed in Chapters 3-5 for transient stability improvement and any other variants can be implemented in the model. Supplementary control strategies for power oscillation damping have been analysed in Chapter 7.

# Appendix E

# Small-signal analysis

## E.1 Building complex linear state-space models from simple models

This section describes a systematic methodology to build a large-scale state-space system from simple linear models, following the guidelines of [181].

The following linear system is considered:

$$\boldsymbol{\Delta \dot{x}} = \boldsymbol{A}\boldsymbol{\Delta x} + \boldsymbol{B}\boldsymbol{\Delta u} \tag{E.1}$$

$$\boldsymbol{\Delta y} = \boldsymbol{C}\boldsymbol{\Delta x} + \boldsymbol{D}\boldsymbol{\Delta u} \tag{E.2}$$

with $N$ states, $N_{in}$ inputs and $N_{out}$ outputs.

Assume that the system is composed of $N_{sub}$ simple linear subsystems with the form (Fig. E.1):

$$\boldsymbol{\Delta \dot{x}_i} = \boldsymbol{A_i}\boldsymbol{\Delta x_i} + \boldsymbol{B_i}\boldsymbol{\Delta u_i} \tag{E.3}$$

$$\boldsymbol{\Delta y_i} = \boldsymbol{C_i}\boldsymbol{\Delta x_i} + \boldsymbol{D_i}\boldsymbol{\Delta u_i} \tag{E.4}$$

where $i = 1, \ldots, N_{sub}$.

Then, the following system, composed of the simple subsystems, can be built:

$$\boldsymbol{\Delta \dot{x}_s} = \boldsymbol{A_s}\boldsymbol{\Delta x_s} + \boldsymbol{B_s}\boldsymbol{\Delta u_s} \tag{E.5}$$

$$\boldsymbol{\Delta y_s} = \boldsymbol{C_s}\boldsymbol{\Delta x_s} + \boldsymbol{D_s}\boldsymbol{\Delta u_s} \tag{E.6}$$

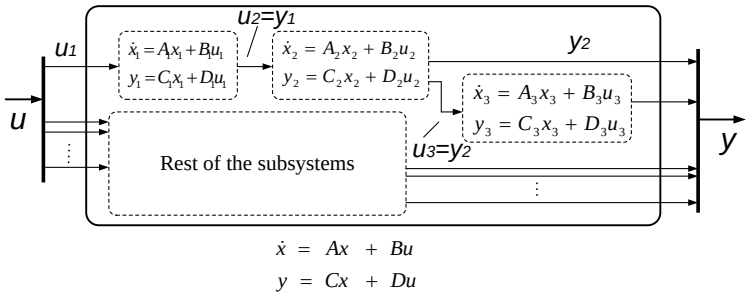


Figure E.1: Linear model composed of subsystems.

where:

$$\boldsymbol{\Delta x_s} = [\boldsymbol{\Delta x_1}, \ldots, \boldsymbol{\Delta x_{N_{sub}}}]^T \tag{E.7}$$
$$\boldsymbol{\Delta u_s} = [\boldsymbol{\Delta u_1}, \ldots, \boldsymbol{\Delta u_{N_{sub}}}]^T \tag{E.8}$$
$$\boldsymbol{\Delta y_s} = [\boldsymbol{\Delta y_1}, \ldots, \boldsymbol{\Delta y_{N_{sub}}}]^T \tag{E.9}$$

where $N_s$ is the number of states, $N_{in,s}$ is the number of inputs and $N_{out,s}$ is the number of outputs.

Assuming that:

$$\boldsymbol{\Delta x} = \boldsymbol{\Delta x_s} \tag{E.10}$$
$$\boldsymbol{\Delta u_s} = \boldsymbol{L\Delta y_s} + \boldsymbol{M\Delta u} \tag{E.11}$$
$$\boldsymbol{\Delta y} = \boldsymbol{N\Delta y_s} \tag{E.12}$$

Then, the following complete system can be obtained [181]:

$$\boldsymbol{\Delta \dot{x}} = \boldsymbol{A\Delta x} + \boldsymbol{B\Delta u} \tag{E.13}$$
$$\boldsymbol{\Delta y} = \boldsymbol{C\Delta x} + \boldsymbol{D\Delta u} \tag{E.14}$$

where:

$$\boldsymbol{A} = \boldsymbol{A_s} + \boldsymbol{B_s}(\boldsymbol{I} - \boldsymbol{LD_s})^{-1}\boldsymbol{C_s} \tag{E.15}$$
$$\boldsymbol{B} = \boldsymbol{B_s}(\boldsymbol{I} - \boldsymbol{LD_s})^{-1}\boldsymbol{M} \tag{E.16}$$
$$\boldsymbol{C} = \boldsymbol{N}(\boldsymbol{I} - \boldsymbol{LD_s})^{-1}\boldsymbol{C_s} \tag{E.17}$$
$$\boldsymbol{D} = \boldsymbol{N}(\boldsymbol{I} - \boldsymbol{LD_s})^{-1}\boldsymbol{M} \tag{E.18}$$

## E.2 Modal observability and controllability factors of VSCs

The output voltage and the current injection of VSC$j$, at the PCC, written in the system $D-Q$ frame, are given by:

$$\bar{v}_j = v_{Dj} + jv_{Qj} \tag{E.19}$$

$$\bar{i}_j = i_{Dj} + ji_{Qj} \tag{E.20}$$

and the P and Q injections of VSC$j$ at the PCC are:

$$\bar{s}_{s,i} = \bar{v}_i \bar{i}_i^* = p_{s,j} + jq_{s,j} \tag{E.21}$$

Fig. E.2 [1] shows a hybrid representation of the linearised model of a power system with a POD controller (transfer function $F(s,q)$). In the PSS controllers proposed in Chapter 7, the output signals ($u$) can be either the active- or reactive-power set points of each VSC station, while the input signal ($y$) is the frequency error, when using the weighted-average frequency as set-point value. Hence, the frequency error at VSC station $j$ is defined as:

$$\bar{e}_j = \bar{\omega} - \omega_j \tag{E.22}$$

where $\bar{\omega}$ is the weighted-average frequency:

$$\bar{\omega} = \sum_{k=1}^{n} \alpha_k \omega_k \tag{E.23}$$

This section describes the calculation of the observability factor of $\bar{e}_j$ and the controllability factors of $\Delta p_{s,j}$ and $\Delta q_{s,j}$ (of the mode of interest $i$). They were used to computed the residues and sensitivities in Chapter 7.

### E.2.1 Observability factor

The observability factor of mode $i$ in the frequency deviation of AC bus $j$ ($\Delta\omega_j$) is given by [181]:

$$obs_{\Delta\omega_j,i} = \boldsymbol{c}^{\boldsymbol{T}}_{\boldsymbol{\Delta\omega_j}} \boldsymbol{v}_{\boldsymbol{\Delta v_j,i}} = \frac{\lambda_i}{\omega_0} \frac{1}{v_{j0}^2} [-v_{Qj0} \quad v_{Dj0}] \begin{bmatrix} v_{\Delta v_{Dj},i} \\ v_{\Delta v_{Qj},i} \end{bmatrix} \tag{E.24}$$

[1] Fig. E.2 was obtained from [181].

where $\boldsymbol{v_i}$ is the extended right eigenvector associated to mode $i$, $\boldsymbol{c^T_{\Delta\omega_j}}$ is matrix $\boldsymbol{c}$ in Fig. E.2, when the frequency at the AC side of VSC$j$ is selected as output signal of the state system and $v_{j0}$ is the magnitude of the output voltage of VSC$j$ at the PCC. All these calculated at the operating point:

$$v_{j0} = \sqrt{v_{Dj0}^2 + v_{Qj0}^2} \tag{E.25}$$

The error of the weighted-average frequency seen by VSC$j$ is defined as:

$$\bar{e}_j = \bar{\omega} - \omega_j = \sum_{k=1}^{n} (\alpha_k \omega_k) - \omega_j \tag{E.26}$$

where $\alpha_k$'s are the weighting factors used to compute the frequency set-point value of the controller.

Therefore, the observability factor of mode $i$ in the error of the WAF at AC bus $j$ ($\Delta\bar{e}_j$) is:

$$obs_{\Delta\bar{e}_j,i} = \sum_{k=1}^{n} (\alpha_k obs_{\Delta\omega_k,i}) - obs_{\Delta\omega_j,i} \tag{E.27}$$

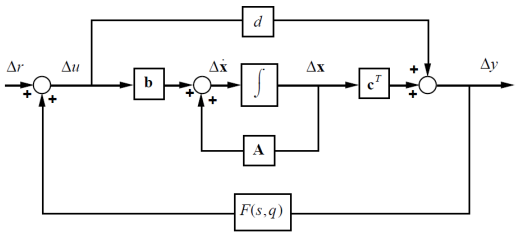


Figure E.2: Hybrid representation of a linear system.

### E.2.2 Controllability factors

The controllability factor of mode $i$ by the P and Q injections of VSC$j$ ($\Delta p_{s,j}$ and $\Delta q_{s,j}$, respectively) are given by [181]:

$$con_{\Delta p_{s,j},i} = \boldsymbol{w_i^T b_{\Delta p_{s,j}}} = [w_{\Delta v_{Dj,i}} \quad w_{\Delta v_{Qj,i}}] \frac{1}{v_{j0}^2} \begin{bmatrix} v_{Dj0} \\ v_{Qj0} \end{bmatrix} \tag{E.28}$$

$$con_{\Delta q_{s,j},i} = \boldsymbol{w_i^T b_{\Delta q_{s,j}}} = [w_{\Delta v_{Dj,i}} \quad w_{\Delta v_{Qj,i}}] \frac{1}{v_{j0}^2} \begin{bmatrix} v_{Qj0} \\ -v_{Dj0} \end{bmatrix} \tag{E.29}$$

where $\boldsymbol{w_i}$ is the extended left eigenvector associated to mode $i$ and $\boldsymbol{b_{\Delta p_{s,j}}}$ and $\boldsymbol{b_{\Delta q_{s,j}}}$ are matrices $\boldsymbol{b}$ of Fig. E.2 when P and Q injections of VSC$j$ are used as input signals of the state system, respectively.

# Appendix F

# Additional results on the SSA of control strategies

The Noridc32A test system with a VSC-MTDC system in a heavily loaded scenario, as described in Section A.3.2, is considered.

The impact of the transient-stability-tailored control strategies (proposed in chapters 3-5) on the electromechanical modes with low damping will be analysed now (modes A-H of Table 7.1 of Chapter 7). Special attention will be given to inter-area modes.

As in chapters 3-5, the gains in strategies P-WAF, P-LF, Q-WAF and Q-LWAF will be computed here as:

$$k_{P,i} = \alpha_i k_{P,T}, \;\; k_{P,T} = \sum_{j=1}^{n} k_{P,j}, \tag{F.1}$$

$$k_{Q,i} = \alpha_i k_{Q,T}, \;\; k_{Q,T} = \sum_{j=1}^{n} k_{Q,j}, \tag{F.2}$$

where $\alpha_i$ is the weighting factor used to compute the weighted-average frequency. Factor $\alpha_i$ will be kept constant and with the same value for each VSC (i.e. $\alpha_i = 1/3$). Therefore the analysis will be restricted to the value of the gains for P and Q modulation, $k_{P,i}$ and $k_{Q,i}$, which will have the same value for all converters ($k_{P,i} = k_{P,j}$, $\forall i,\ j$). In other words, $k_{P,T}$ and $k_{Q,T}$ in (F.1) & (F.2) are changed. The impact of gains within the range $[0, 500]$ p.u (in p.u. referred to the converter rating) will be analysed.

## F.1 Strategy P-WAF

The system eigenvalues with strategy P-WAF using different values of $k_{P,i}$ are shown in Fig. F.1. Modes which are closer to the imaginary axis are shown in Fig. F.1-(b). All system modes have negative real part for all $k_{P,i} \in [0, 500]$ p.u (gains in p.u. referred to the converter rating). Therefore, strategy P-WAF does not produce undesirable instabilities.

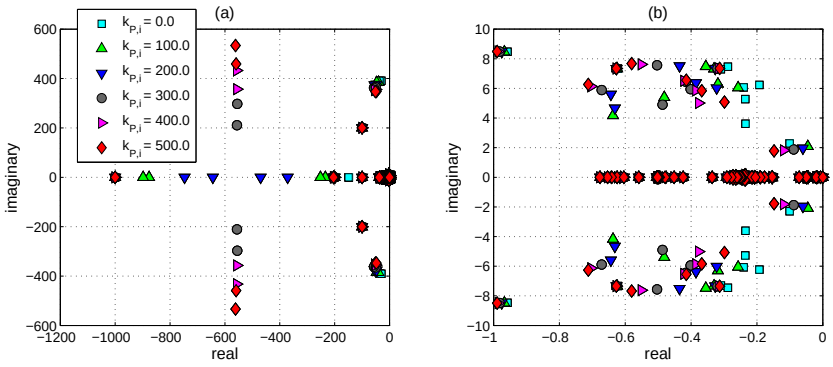


Figure F.1: System eigenvalues with P-WAF.

The impact of gains $k_{P,i}$ (strategy P-WAF) on the electromechanical modes of Table 7.1 (A-H) is analysed now in detail. Gains $k_{P,i}$ have been changed from 0 to 500 p.u using a step of 5 p.u. The effect on each electromechanical mode is shown in Fig. F.2, where the damping ratio of each mode versus the gain values in strategy P-WAF is represented. The following conclusions can be drawn from the results:

- Initially, the damping factor of mode B increases significantly as gains $k_{P,i}$ increase. It reaches a maximum between $k_{P,i} = 120 - 130$ p.u and it decreases from that point.
- Initially, the damping factor of mode A decreases as gains $k_{P,i}$ increase. It reachs a minimum for $k_{P,i} = 100$ p.u, approximately, and it increases from that point.
- The damping factor of mode C increases as gains $k_{P,i}$ increase but it saturates in 11 % for gains 250-300 p.u, approximately.
- The damping factors of modes D, E and F increase slightly as gains $k_{P,i}$ increase.

- The damping factors of modes F and G remain almost constant.

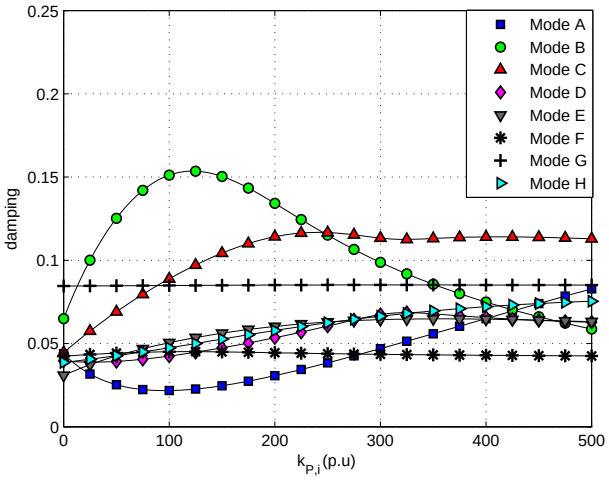


Figure F.2: P-WAF. Damping ratio versus gains $k_{P,i}$ (modes A-H).

## F.2 Strategy P-LF

As shown in Chapter 3, local strategy P-LF cannot help much to improve transient stability, since high gain values produce undesirable DC-voltage fluctuations, which could reach their limits. If this strategy is used for transient stability improvement, the gains should be in the range $k_{P,i} = 10 - 50$ p.u. However, for estimation purposes in strategy Q-LWAF (Chapter 5), gains in the range of $k_{P,i} = 5 - 10$ p.u should be used. This application of strategy P-LF justifies its SSA.

The system eigenvalues obtained using strategy P-LF with different gain values are shown in Fig. F.3. In all cases, the system is stable.

The damping ratios of the electromechanical modes of interest of Table 7.1 versus the gain values are shown in Fig. F.4. For small gains, the effect of strategy P-LF on the electromechanical modes is similar to the effect of strategy P-WAF, which is consistent with the analysis of Chapter 3 (see Subsection 3.4.1 and Figs. 3.6 and 3.7 of Chapter 3). If gains $k_{P,i}$ are high enough, strategies P-LF and P-WAF behave differently, since dynamics of the

AC-side control strategy becomes faster and comparable to the dynamics of the DC grid and the DC droop.

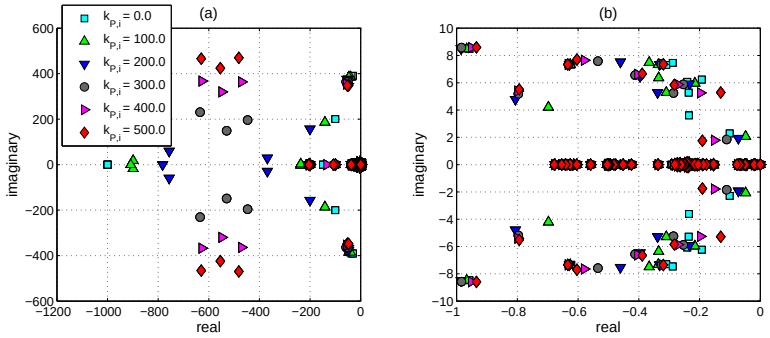


Figure F.3: System eigenvalues with P-LF.

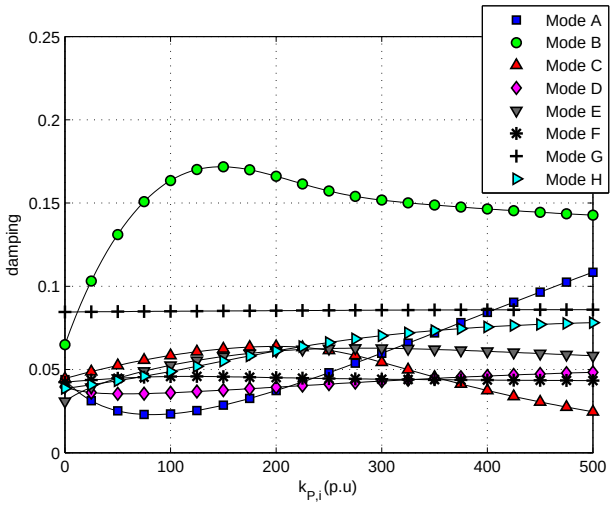


Figure F.4: P-LF. Damping ratio versus gains $k_{P,i}$ (modes A-H).

## F.3 Strategy Q-WAF

The system modes obtained for different values of the gains $k_{Q,i}$ in strategy Q-WAF are shown in Fig. F.5. The system is always stable for $k_{Q,i} \in [0, 500]$ p.u.

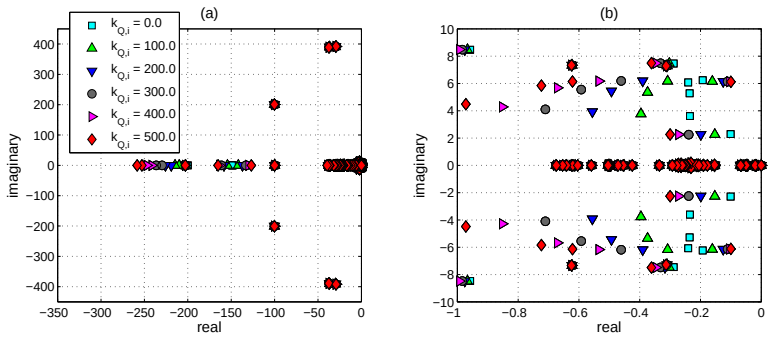


Figure F.5: System eigenvalues with Q-WAF.

The damping ratios of electromechanical modes A-H versus the gains used in Q-WAF, $k_{Q,i}$, are shown in Fig. F.6. The following conclusions can be drawn from the results:

- The damping ratio of mode B increases significantly as $k_{Q,i}$ increases.
- Damping ratios of modes A, C and D also increase as $k_{Q,i}$ increases. Notice that strategy Q-WAF is much more effective to damp mode A than strategy P-WAF.
- Damping ratios of modes F and G remain almost constant for different values of $k_{Q,i}$, which confirms that neither P nor Q modulation can help to damp those local modes.
- The effect of strategy Q-WAF on mode H is also very small.
- Unfortunately, the damping ratio of mode E deteriorates slightly with strategy Q-WAF.

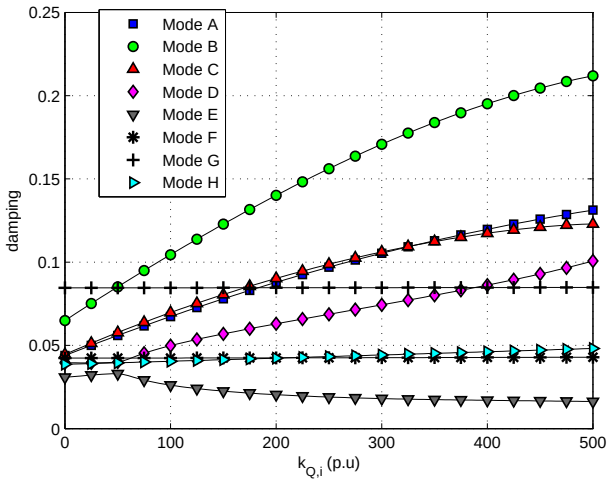


Figure F.6: Q-WAF. Damping ratio versus gains $k_{Q,i}$ (modes A-H).

## F.4 Strategy Q-LWAF

System modes using local strategy Q-LWAF, proposed in Chapter 5, with different gains $k_{Q,i}$ are shown in Fig. F.7. The system is stable for all the values of $k_{Q,i} \in [0, 500]$ p.u, discarding potential instabilities.

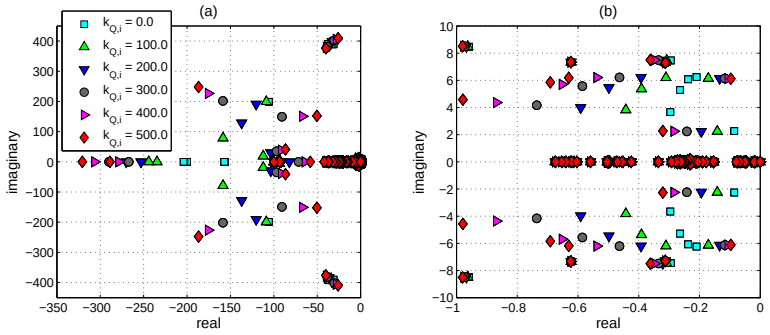


Figure F.7: System eigenvalues with Q-LWAF.

Damping ratios of the electromechanical modes of interest versus gain values are shown in Fig. F.8. Results show that the effect of local strategy

Q-LWAF on the electromechanical modes is remarkably similar to the effect of global strategy Q-WAF (expected from Chapter 5). Therefore, local strategy Q-LWAF could also help to damp electromechanical oscillations using local measurements, only.

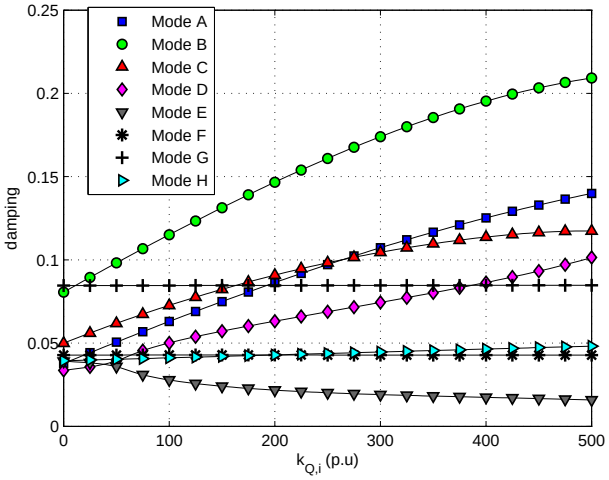


Figure F.8: Q-LWAF. Damping ratio versus gains $k_{Q,i}$ (modes A-H).

## F.5 Strategies P-WAF and Q-WAF simultaneously (PQ-WAF)

The results of Section F.1 proved that modulating the active-power injections with strategy P-WAF could help to damp inter-area oscillations. However, gains $k_{P,i}$ should be designed to compromise the required damping ratio of inter-area modes A and B, because their sentitivities with respect the $k_{P,i}$ are non linear. For example, mode B is damped as $k_{P,i}$ increases but it reaches a maximum and the damping decreases after that point. On the other hand, the damping ratio of mode A decreases as $k_{P,i}$ increases and after a certain gain value, it increases. This phenomenon was not present when using strategy Q-WAF, which could damp efficiently modes A, B and C. Finally, strategy Q-WAF reduces the damping ratio of local mode E, slightly, which could be damped (slightly too) with strategy P-WAF (see Figs. F.2 and F.6 for details).

The results of Subsections F.1 and F.3 suggest to study the implementation of strategies P-WAF and Q-WAF together (PQ-WAF, for short) to investigate if all the electromechanical modes of interest of Table 7.1 can be damped by modulating simultaneously P and Q injections.

Gains in strategy Q-WAF were set to $k_{Q,i} = 200$ p.u and gains $k_{P,i}$ in strategy P-WAF were changed from 0 to 500 p.u. The damping ratios of the electromechanical modes A-H versus the gain values of strategy P-WAF are shown in Fig. F.9. Results show that the use of P-WAF and Q-WAF simultaneously, have a better performance than using P or Q modulation, only.

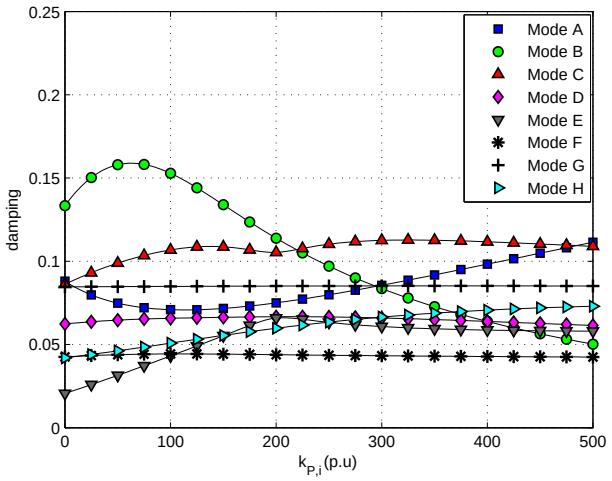


Figure F.9: PQ-WAF. Damping ratio versus gains $k_{P,i}$ (modes A-H).